



**UNIVERSIDAD NACIONAL AUTÓNOMA DE MÉXICO**  
**POSGRADO EN CIENCIAS DE LA TIERRA**  
**INSTITUTO DE GEOFÍSICA**

**EVALUACIÓN DEL RIESGO SOCIAL Y ECONÓMICO POR SUBSIDENCIA EN MÉXICO UTILIZANDO  
SERIES DE TIEMPO INSAR**

QUE PARA OPTAR POR EL GRADO ACADÉMICO DE:  
**DOCTOR EN CIENCIAS DE LA TIERRA**

PRESENTA:  
**Enrique Antonio Fernández Torres**

COMITÉ TUTOR:

Dr. Enrique Cabral Cano (Tutor), Departamento de Geomagnetismo y Exploración Instituto de Geofísica, UNAM

Dr. David Alberto Novelo Casanova, Departamento de Sismología, Instituto de Geofísica, UNAM

Dr. Darío Enmanuel Solano Rojas, División de Ingeniería en Ciencias de la Tierra, Facultad de Ingeniería, UNAM

Ciudad de México, enero 2024



Universidad Nacional  
Autónoma de México



**UNAM – Dirección General de Bibliotecas**  
**Tesis Digitales**  
**Restricciones de uso**

**DERECHOS RESERVADOS ©**  
**PROHIBIDA SU REPRODUCCIÓN TOTAL O PARCIAL**

Todo el material contenido en esta tesis esta protegido por la Ley Federal del Derecho de Autor (LFDA) de los Estados Unidos Mexicanos (México).

El uso de imágenes, fragmentos de videos, y demás material que sea objeto de protección de los derechos de autor, será exclusivamente para fines educativos e informativos y deberá citar la fuente donde la obtuvo mencionando el autor o autores. Cualquier uso distinto como el lucro, reproducción, edición o modificación, será perseguido y sancionado por el respectivo titular de los Derechos de Autor.

**CODIGO DE ÉTICA:**

“Declaro conocer el Código de Ética de la Universidad Nacional Autónoma de México, plasmado en la Legislación Universitaria. Con base en las definiciones de integridad y honestidad ahí especificadas, aseguro mediante mi firma al calce que el presente trabajo es original y enteramente de mi autoría. Todas las citas de, o referencias a, las obras de otros autores aparecen debida y adecuadamente señaladas, así como acreditadas mediante los recursos editoriales convencionales.”

---

Enrique Antonio Fernández Torres

## **Agradecimientos**

Al Posgrado en Ciencias de la Tierra-UNAM por la formación académica.

Al CONAHCYT, por la beca otorgada para la realización de estudios de Doctorado.

Al Dr. Enrique Cabral Cano, por su excelente dirección durante el desarrollo de este trabajo de investigación.

A las Dras. Dora Carreón y Olga Sarychikina y a los Drs. David Novelo y Gil Ochoa por sus importantes contribuciones para mejorar la calidad de este documento.

Al DGTIC, por compartir sus recursos de supercómputo sin los cuales esta investigación no habría sido posible.

A los Drs. Darío Solano y David Novelo por su excelente dirección en el comité de evaluación semestral, lo que permitieron definir objetivos claros y alcanzables en el tiempo.

A los Drs. Sergio Rodríguez, Sébastien Valade, Jesús Pacheco, Antonio Hernández y Darío Solano por su participación y evaluación en el examen de candidatura, lo que permitió discutir las bases y alcances del proyecto.

A Josué García y el Dr. Darío Solano por haberme enseñado las bases del procesamiento InSAR.

A Katia Villarnobo y Daniel Hernández por su colaboración y guía en el manejo de datos de INEGI y DENUÉ, los cuales fueron de gran utilidad en este trabajo.

A la Dra. Shannon Graham, por su colaboración en el artículo de subsidencia urbana en México.

Al programa de apoyo PAEP y de Movilidad Estudiantil por haberme permitido asistir a congresos nacionales e internacionales, así como la compra de equipos.

A mi esposa Sol Moreno, por su apoyo en los momentos y buenos y los no tan buenos. Por siempre brindarme su valiosa compañía, consejo y comprensión.

A mi mamá, papá, hermanos, tíos, primos, suegros y amigos por brindarme su apoyo incondicional y afecto.

Al Ing. Luis Salazar, por su apoyo para aprender las tareas que se desarrollan en campo.

Al proyecto “Elaboración del Atlas de Riesgo por fenómenos de origen natural de la Ciudad de México”, por darme acceso a la información de su base de datos, la cual fue de gran importancia para la generación de mapas de riesgo socioeconómico.

## Índice

### Resumen

### Abstract

<b>1 Revisión de antecedentes (subsistencia del terreno en México)</b> .....	<b>1</b>
<b>2 Hipótesis</b> .....	<b>9</b>
<b>3 Objetivo general</b> .....	<b>9</b>
<b>3.1 Objetivo específicos</b> .....	<b>9</b>
<b>4 Materiales y métodos</b>	
4.1 Radar de apertura sintética (SAR).....	<b>10</b>
4.2 Interferometría de radar de apertura sintética (InSAR).....	<b>10</b>
4.3 Sentinel-1.....	<b>12</b>
4.4 Procesamiento InSAR SBAS.....	<b>12</b>
4.5 Vulnerabilidad socioeconómica.....	<b>13</b>
4.6 Gradiente horizontal de subsistencia.....	<b>13</b>
<b>5 Resultados</b>	
5.1 Country-scale assessment of urban areas, population, and households exposed to land subsidence using Sentinel-1 InSAR and GPS time series.....	<b>14</b>
5.2 Risk assessment of land subsidence and associated faulting in Mexico City using InSAR.....	<b>40</b>
5.3 The Risk Atlas of Mexico City, Mexico: a tool for decision-making and disaster prevention.....	<b>60</b>
5.4 Economic risk to differential subsidence in Mexico City (2014-2022).....	<b>88</b>
5.5 Land Subsidence risk maps and InSAR based angular distortion structural vulnerability assessment: an example in Mexico City.....	<b>110</b>
<b>6 Discusión</b> .....	<b>116</b>
<b>7 Conclusiones</b> .....	<b>118</b>
<b>8 Referencias</b> .....	<b>118</b>

## Resumen

En esta investigación se evaluó el proceso de subsidencia en México mediante el uso de técnicas de geodesia satelital complementadas con información de los censos (2010 y 2020), catastral, geológica, hidrogeológica y la reglamentación de construcción vigente. Entre los resultados obtenidos en este trabajo está la identificación de localidades y áreas urbanas, población y viviendas que están expuestas a velocidades de subsidencia que puedan representar potenciales daños a las construcciones y al terreno, así como la determinación de los factores que favorecen al proceso de subsidencia a nivel país. Los resultados muestran que el área urbanizada que presenta subsidencia con velocidades más rápidas que  $-2.8$  cm/a (1.5 desviaciones estándar de la velocidad) en México, es de  $3,797$  km<sup>2</sup>, generando la exposición de 6.9 millones de viviendas, 17% de la población del país distribuidas en 853 localidades. También se confirmó que la subsidencia del terreno por extracción de agua ocurre sobre depósitos no consolidados y con acuíferos estresados. También se evaluó el riesgo socioeconómico por subsidencia y fallamiento asociado, obteniéndose que, en la Ciudad de México, el 40.4% de la longitud total del fallamiento asociado a subsidencia corresponde un gradiente de subsidencia alto (15.6%) y muy alto (24.8%) y el 9% de las áreas urbanizadas ( $70.7$  km<sup>2</sup>) están expuestas a un riesgo socioeconómico alto y muy alto, donde el 12.6% de la población de la ciudad reside. Las mayores tasas de subsidencia se encuentran hacia el este y sureste de la Ciudad de México, alcanzando velocidades de subsidencia de hasta  $41.1$  cm/a al sureste de la ciudad, en el municipio Tláhuac. En el caso del área metropolitana, la máxima velocidad de subsidencia es de  $52.3$  cm/a en Ciudad Nezahualcóyotl. El mapa de distorsión angular delimita zonas con más de  $0.008$  radianes en las alcaldías al oriente de la ciudad, lo que conlleva una alta probabilidad de generación de fallamiento y por ende afectación a casas habitación e infraestructura urbana. Adicionalmente, se estimó el riesgo económico por subsidencia diferencial con base en los estados límites determinados en la reglamentación de construcción vigente y el valor catastral de los predios de la Ciudad de México. Se consideró la subsidencia diferencial bajo dos escenarios de tipología y se determinó que el 7.6% de las manzanas, 215,000 viviendas y 738,000 habitantes se encuentran en zonas que presentan riesgo alto y muy alto. Esto representa en términos económicos 10,500 millones de dólares americanos, equivalentes al 6.1% del valor catastral total de la Ciudad de México, para un escenario de edificaciones de mampostería y de hasta dos niveles. Asumiendo construcciones de marcos de acero de hasta 4 niveles, se obtuvo que el 2% de las manzanas de la Ciudad de México tienen un riesgo económico alto, que en términos monetarios representa 2,500 millones de dólares americanos, exponiendo a 48 mil viviendas y 169 mil personas.

Los resultados de esta investigación representan un marco de referencia para la identificación de zonas urbanas de México, donde es necesario el desarrollo de medidas que permitan la mitigación del riesgo por subsidencia, tales como la implementación de un manejo eficiente de los recursos hidrogeológicos, el planteamiento de nuevas zonificaciones de uso de suelo y el diseño de infraestructura resiliente a la deformación del terreno en zonas críticas. Así mismo, se demostró que la subsidencia y el fallamiento asociado en zonas de la Ciudad de México presenta una correlación espacial con las áreas con mayor vulnerabilidad socioeconómica, por lo que es necesario la creación de políticas públicas que permitan incrementar la resiliencia de las comunidades más afectadas. Además, esta investigación también proporciona una evaluación en términos económicos de una de las ciudades en el mundo con mayores afectaciones por subsidencia, la Ciudad de México, lo que permite comparar el efecto de la subsidencia con otros fenómenos naturales (p. ej. sismos) y así contextualizar su relevancia, con el fin de promover un marco regulatorio que permita su mitigación de daños.

## Abstract

In this research, land subsidence assessment was performed in Mexico using satellite geodesy techniques complemented with other data sources, such as census (2010 and 2020), cadastral, geological maps, hydrogeological data, and building construction codes. Among this research's results are identifying urban areas and localities, population, and households with exposure to land subsidence velocities, which can represent potential damages in constructions and land, and assessing land subsidence conditional factors at the country-scale level. As a result, we found that the total urban area over land subsidence faster than  $-2.8$  cm/yr (1.5 standard deviations of the land velocity's field of Mexico) is  $3,797$  km<sup>2</sup>, producing an exposure of 6.9 million households, 17% of the total population of Mexico, in 853 urban localities. We also confirmed that land subsidence due to groundwater extraction occurs over unconsolidated sediments and stressed aquifers. Socioeconomic risk due to land subsidence and associated faulting was also evaluated, finding that in Mexico City, 40.4% of the total subsidence-associated faulting length corresponded to a high subsidence gradient (15.6%) and very high (24.8%), and 9% of urban areas ( $70.7$  km<sup>2</sup>) presents exposure to high and very high socioeconomic risk, where 12.6% of the population live in. The highest land subsidence rates were measured in the southeastern of Mexico City, reaching subsidence velocities faster than  $41.1$  cm/yr in Tláhuac municipality. In the Mexico City Metropolitan Area, the maximum subsidence value is  $52.3$  cm/yr in Nezahualcóyotl municipality. An angular distortion map was generated to delimit the areas with more than 0.008 radians of angular distortion in the municipalities of Mexico City, which can produce a high probability of fault generation and household damage to civil structures. Additionally, the economic risk due to differential subsidence in Mexico City was estimated in this research, using Limit States based on a 2014-2022 InSAR analysis, the city's building code, and the property's cadastral values. To assess the economic risk, we considered two typologies' scenarios. We found that 7.6% of the city blocks, 215,000 households, and 738,000 people are in areas with high and very high economic risk. These areas with high and very high risk represent 10,500 million USD, or 6.1% of the total cadastral value of Mexico City, under the scenario of masonry construction with 2 or fewer floors. In another scenario, we assumed constructions made of steel frames with 4 or fewer floors and estimated that 2% of Mexico City's city blocks are at high economic risk, costing 2,500 million USD, producing the exposure of 48,000 households and 169,000 people.

The results of this research are a reference frame to identify urban areas of Mexico undergoing land subsidence where it is necessary to implement actions for subsidence risk mitigation, such as better groundwater management, land use planning, and the design of infrastructure with better resilience to land deformation. Additionally, in Mexico City, we demonstrate that land subsidence and associated faulting have a spatial correlation with urban areas with higher socioeconomic vulnerability; therefore, it is necessary to implement policies to increase the resilience of communities. This research also provides an assessment in economic terms of damages due to land subsidence, which can then be compared to other natural hazards (e.g., seismic activity), and contextualized its relevance to promote a regulatory frame for damage mitigation.

## 1. Revisión de antecedentes (Subsidencia del terreno en México)

En México, se han realizado numerosos estudios del proceso de subsidencia del terreno. Los tópicos que se han estudiado incluyen la determinación de su velocidad, distribución espacial, tipos de subsidencia, identificación de nuevas áreas con subsidencia, fallamiento asociado, susceptibilidad, peligros y riesgos asociados a la subsidencia, evolución temporal de la subsidencia, subsidencia e influencia de las propiedades del subsuelo, subsidencia y sus efectos sobre el sistema acuífero (p. ej. cambios en las propiedades hidráulicas, geotécnicas, contaminación). Otros tópicos estudiados son la subsidencia y modelos para predecir su comportamiento, daños en la infraestructura y pérdidas económicas por subsidencia, medidas de mitigación de la subsidencia, subsidencia y su relación con otros peligros geológicos (p. ej. sismos, inundaciones, deslizamientos), subsidencia por extracción de fluidos geotérmicos, hidrocarburos y minería, jurisprudencia actual con relación a la subsidencia y aspectos técnicos para la determinación de la subsidencia utilizando técnicas de geodesia satelital (p. ej. calibración de velocidades con series de tiempo GPS, nuevos algoritmos de procesamiento y utilización de nuevos sensores SAR).

El estudio de los patrones y magnitudes de subsidencia en México se han centrado en la Faja Volcánica Mexicana (FVM) y el Valle de Mexicali a partir de técnicas satelitales como InSAR, GPS, y técnicas convencionales que incluyen instrumentos geotécnicos y nivelaciones topográficas (p. ej. Calderhead et al. 2010; Glowacka et al. 2010; Sarychikhina et al. 2011, 2018; Cigna and Tapete 2020). Los estudios realizados han mostrado que la distribución espacial de subsidencia está controlada por las características geológicas y estructurales. En la FVM ha predominado desde inicios del Cenozoico un estado de esfuerzos extensionales que ha favorecido el desarrollo de valles que han sido rellenados con depósitos no consolidados con variaciones de depósitos volcánicos, aluviales y lacustres y en los cuales se han desarrollado las ciudades y zonas agrícolas del centro de México (Alaniz-Álvarez et al. 2002; Farina et al. 2008; Ávila-Olivera et al. 2010; Cigna et al. 2012). Por consiguiente, la FVM presenta un comportamiento litológico heterogéneo en el subsuelo, lo que a su vez favorece a la subsidencia diferencial y el potencial desarrollo de fallas asociadas.

A partir de la revisión sobre la subsidencia en México, podemos ver que esta puede ocurrir de dos tipos: el primer tipo está asociado a grandes espesores de sedimentos no consolidados, cuyo ejemplo más claro es la Ciudad de México y el segundo es la subsidencia diferencial con control estructural (Figuroa-Miranda et al. 2018). La subsidencia asociada con grandes espesores de sedimentos se caracteriza porque sus patrones espaciales están controlados por la presencia y espesor de depósitos compresibles y por tener patrones circulares alrededor de las zonas de mayor espesor de sedimentos y/o con mayores tasas de extracción de agua subterránea. En este caso, la velocidad de subsidencia puede alcanzar los 50 cm/a como ocurre en la Ciudad de México, (Gayol 1925; Strozzzi and Wegmuller 1999; Wegmüller et al. 2000; Werner et al. 2000; Strozzzi et al. 2001, 2003, 2005; Cabral-Cano et al. 2008; López-Quiroz et al. 2010; Calderhead et al. 2010; Sowter et al. 2016; Figuroa-Miranda et al. 2018; Chaussard et al. 2021; Ju and Hong 2021). En la Ciudad de México no se presenta evidencias de recargas significativas asociadas a lluvia o recarga artificial (Osmanoğlu et al. 2011; Samsonov and d'Oreye 2017; Cigna and Tapete 2021a).

Por otra parte, la subsidencia diferencial con control estructural se caracteriza por tener bandas bien delimitadas de alto gradiente de velocidad que siguen el rumbo de estructuras geológicas a profundidad, en ocasiones no aflorantes en superficie y por estar cubiertas por sedimentos compresibles más jóvenes (p. ej. Aguascalientes, Querétaro, Celaya, Tepic, Morelia, Valle de Mexicali; Matínez-Reyes and Mitre-Salazar 2010; Cigna et al. 2012; León et al. 2018; Figuroa-Miranda et al. 2018). En este caso, las fallas pueden actuar como barreras al flujo de agua subterránea y/o fluido geotérmico (p. ej. Sarychikhina et al. 2011).

El primer análisis regional de subsidencia se realizó en el Centro de México, cubriendo 200,000 km<sup>2</sup> utilizando la técnica InSAR, con escenas del sensor ALOS y cubriendo la ventana de tiempo 2007-2011 (Chaussard et al. 2014), lo que permitió la identificación 21 localidades con subsidencia, algunas de ellas ya previamente reportadas en la literatura científica (p. ej. Ciudad de México, Aguascalientes, Morelia, Querétaro, Toluca) y otras fueron reportadas por primera vez. Adicionalmente, se han comparado los valores de subsidencia con la densidad de pozos y variaciones en el nivel piezométrico, resultando una relación no muy clara entre la subsidencia del terreno y estos factores (Calderhead et al. 2010; Cigna et al. 2012). En cambio se ha observado que la magnitud y extensión de subsidencia del terreno en zonas con extracción intensiva de agua está controlada por el espesor de los sedimentos compresibles y la heterogeneidad del medio geológico.



En relación con la subsidencia y fallamiento asociado, se han realizado investigaciones en diversas regiones del Centro de México y Valle de Mexicali. En estos estudios, se ha encontrado que el fallamiento asociado al proceso de subsidencia sigue el rumbo del fallamiento tectónico, cuya orientación está determinada por la configuración de la estructura geológica que se encuentra cubierta por intercalaciones de sedimentos volcánicos, lacustres y/o aluviales. La propagación del fallamiento depende de la configuración litoestratigráfica del subsuelo y su comportamiento hidráulico. Este tipo de proceso está presente en Aguascalientes, Querétaro, Celaya, Ciudad Guzmán, Zacatecas, Irapuato, San Luis Potosí, Tepic y Valle de Mexicali (Corona 2004; Barajas-Nigoche et al. 2010; Carreón-Freyre 2010; Pacheco-Martínez et al. 2010; Rodríguez-Castillo and Schroeder-Aguirre 2010; Hernandez-Marin et al. 2017; Murgia et al. 2019; Navarro-Hernández et al. 2020; Muro-Ortega et al. 2021).

Por otra parte, el fallamiento asociado a subsidencia también se puede presentar en la periferia de las zonas de subsidencia máxima o zonas que presentan subsidencia con patrones circulares, como son los casos del Valle de Toluca, oeste del lago de Chapala, Chalco, Ciudad de México, donde el fallamiento se produce en la transición abrupta entre diferentes litologías, generando un escalón hacia la zona más compresible (Carreón-Freyre 2010; Auvinet-Guichard et al. 2013; Hernandez-Marin et al. 2014; Castellazzi et al. 2017). El caso de Morelia presenta un comportamiento híbrido, en otras palabras, en algunas zonas el fallamiento asociado a subsidencia sigue el rumbo de fallas preexistentes y en otras el fallamiento superficial se da en la periferia de las zonas de mayor velocidad de subsidencia (Cabral-Cano et al. 2010a; Cigna et al. 2012).

Para el estudio del fallamiento asociado a subsidencia se han empleado métodos de geodesia satelital (InSAR, GPS), nivelación topográfica, LiDAR, extensómetros, métodos geofísicos (Radar de Penetración Terrestre, refracción sísmica, análisis multicanal de ondas superficiales, tomografía sísmica, ondas sísmicas superficiales, tomografía eléctrica de resistividad), métodos geotécnicos, información hidrogeológica (niveles piezométricos, tasas de bombeo, conductibilidad hidráulica), información geológica de superficie y subsuelos y levantamiento en campo de trazas de fallas (Ávila-Olivera et al. 2008; Barajas-Nigoche et al. 2010; Cabral-Cano et al. 2010a; Pacheco-Martínez et al. 2010; Calderhead et al. 2011; Hernandez-Marin et al. 2017). Esta información ha permitido generar modelos geomecánicos, geológicos y de flujo de agua subterránea. A partir de estos modelos, se realizó la interpretación del comportamiento de los esfuerzos en los planos de falla y el fallamiento, generado diferentes escenarios de manejo de la extracción, evaluando las zonas de máxima subsidencia diferencial y sus desplazamientos (Pacheco et al. 2006; Cabral-Cano et al. 2010b; Ochoa-Gonzalez et al. 2013; Brunori et al. 2015b; Siles et al. 2015b; Auvinet-Guichard et al. 2015; Centeno-Salas et al. 2015; Franceschini et al. 2015; Carreón-Freyre et al. 2016; Ochoa-González et al. 2018). También se han generado mapas de susceptibilidad para el desarrollo potencial de fallamiento asociado, utilizando métodos estadísticos, datos InSAR, Radar de Penetración Terrestre, niveles de abatimiento de pozos y el relieve del basamento (Pacheco-Martínez et al. 2015a; Fernández-Torres et al. 2020; Luna-Villavicencio et al. 2023).

Adicionalmente, en la Ciudad de México se han aplicado otras metodologías para evaluación de fallas asociadas a la subsidencia. Entre las cuales está la identificación de áreas con deformación no lineal, basadas en el modelado de la componente de velocidad vertical de deformación del terreno usando una función cuadrática, encontrando zonas con aceleraciones y desaceleraciones máximas de  $8 \text{ mm/a}^2$  y  $-9 \text{ mm/a}^2$  respectivamente (Siles et al. 2015b). También se realizó un estudio sobre la variación de compresibilidad del subsuelo, la cual es producto de la alta heterogeneidad a nivel mineralógico de la fracción limo-arcillosa del subsuelo. En este estudio se concluyó que el fallamiento no es un fenómeno aleatorio, sino es producto de las propiedades de los materiales (Carreón-Freyre and Cerca 2006). Además, se han explicado los mecanismos desencadenantes y de propagación de fallas asociadas a subsidencia mediante enfoques multidisciplinarios que involucran geología local, prospección geofísica de alta resolución, correlación estratigráfica, caracterización geotécnica y análisis hidrogeológico, para luego analizar los resultados espacialmente y poder desplegarlos en productos cartográficos (Carreón-Freyre 2010).

En cuanto a la evaluación de susceptibilidad, peligros y riesgos asociados a la subsidencia del terreno por extracción de agua subterránea, se han realizado investigaciones en Aguascalientes, Morelia y la Ciudad de México. En Aguascalientes se desarrolló un mapa de susceptibilidad al desarrollo de fallas asociadas a subsidencia utilizando métodos estadísticos y cuatro capas de entrada, las cuales fueron el campo de velocidades, el gradiente horizontal de subsidencia, las profundidades del basamento y los niveles piezométricos (Luna-Villavicencio et al. 2023). Este mapa de susceptibilidad fue validado con el reconocimiento de fallas en campo.

En cuanto a mapas de peligro por fallamiento asociado a subsidencia, en Aguascalientes se desarrolló un producto que muestra la zonificación al desarrollo de fallas. Esta cartografía fue desarrollada utilizando los espesores de los

sedimentos no consolidados obtenidos con gravimetría y el campo de velocidades de desplazamiento del terreno obtenidos con InSAR (Pacheco-Martínez et al. 2015b, a). En la Ciudad de México, se generó un mapa de peligro por subsidencia asociado al gradiente horizontal de subsidencia. En este se dividió la porción nororiental de la Zona Metropolitana de la Ciudad de México en tres categorías de peligros en función de los valores de gradiente horizontal de subsidencia encontrados (Cabral-Cano et al. 2011).

Para la evaluación de la exposición de las propiedades a la subsidencia, en Morelia se utilizó una matriz que involucra la distorsión angular y la densidad de propiedades, obteniéndose que 24,570 propiedades y 48,700 habitantes están en zonas de exposición alta y muy alta (Cigna and Tapete 2022b). Por otra parte, en Aguascalientes se evaluó la evolución de la exposición asociada a subsidencia utilizando dos series de tiempo InSAR. La primera 2003-2010 y la segunda 2015-2020, obteniéndose que el 2% (12,000 viviendas y 39,000 habitantes) y el 6% (25,600 viviendas y 39,000 habitantes) de las áreas urbanas presentan exposición alta y muy alta, respectivamente (Cigna and Tapete 2021b). Para el mapa de exposición de Aguascalientes, utilizaron matrices que involucran la distorsión angular y deformaciones horizontales como peligros y los impactos sobre la población y propiedades como vulnerabilidad. En la Ciudad de México se generó un mapa de exposición, donde esta matriz considera a la distorsión angular y la densidad de propiedades (propiedades/km<sup>2</sup>), obteniendo que alrededor de 470,000 viviendas y 1.5 millones de personas viven en exposición alta y muy alta, ubicados principalmente en Iztapalapa y Tláhuac (Cigna and Tapete 2021a). También se encontró que los máximos valores de distorsión angular presentan una banda de máxima deformación de alrededor de 250 m y sus valores máximos se encuentran en los alrededores de la Sierra de Santa Catarina, Sierra de Chichinautzin, Peñón del Márquez y Peñón de los Baños, donde existe una transición abrupta entre materiales de comportamiento mecánicos contrastantes (Cigna and Tapete 2021a).

Para estudiar la evolución de la subsidencia del terreno debido a la extracción de agua se han empleado series de tiempo largas, utilizando múltiples sensores SAR. Entre los resultados obtenidos tenemos el comportamiento lineal de la subsidencia en las ciudades de Toluca y Ciudad Guzmán. Para el caso de Toluca, se han empleado los sensores SAR a bordo de ERS-1, RADARSAT, Envisat para el periodo 1995-2008, Envisat, RADARSAT-2 y Sentinel-1 para el periodo 2003-2016 obteniéndose una velocidad máxima de subsidencia de 15 cm/a, con un importante desarrollo espacial de subsidencia en la zona del corredor industrial de Toluca (Calderhead et al. 2010, 2011; Castellazzi et al. 2017). En Ciudad Guzmán, se han empleado los sensores Envisat, COSMO-SkyMed y Sentinel-1 para el periodo 2003-2018 y Envisat y RADARSAT-2 para el periodo 2003-2012 encontrándose un comportamiento lineal de la subsidencia y una velocidad máxima de 6.5 cm/a (Brunori et al. 2015a; Bignami et al. 2018; Murgia et al. 2019). En la Ciudad de México, también se ha encontrado que la subsidencia presenta un comportamiento generalmente lineal (Osmanoğlu et al. 2011) alcanzando una máxima velocidad de 50 cm/a (Chaussard et al. 2021), este comportamiento también fue corroborado por Du et al. (2019a) utilizando múltiples sensores SAR cuya serie de tiempo InSAR presenta algunos huecos temporales (Du et al. 2019a, b). La subsidencia en la mayor parte de la Ciudad de México presenta una correlación directa y lineal con el espesor del acuitardo superior y un comportamiento inelástico (Chaussard et al. 2021).

Por otro lado, se ha logrado detectar variaciones en la velocidad de subsidencia en Aguascalientes, Morelia y Querétaro. En Aguascalientes, se han medido velocidades máximas de subsidencia de 14 cm/a (ERS-1/2, 1996-2002), 10 cm/a (Envisat, 2003-2010) y 12 cm/a (Sentinel-1, 2014-2020); adicionalmente, se muestra la aceleración de subsidencia de 0.7 cm/a<sup>2</sup> para el periodo 2014-2020 en zonas con desarrollo de nuevas plantas industriales y nuevo distrito de viviendas (Cigna and Tapete 2021b). En Morelia, se ha observado que la velocidad máxima de subsidencia ha aumentado de 2.5 cm/a (Envisat, 2003-2010) a 9 cm/a (Sentinel-1, 2014-2021), también se ha observado cambios en los patrones espaciales de subsidencia, ya que ésta se ha extendido hacia las zonas recientemente urbanizadas, las cuales presentan importantes espesores de sedimentos compresibles (Cigna and Tapete 2022b). En Querétaro, utilizando datos de Envisat, ALOS, RADARSAT-2 y Sentinel-1, se encontró una disminución de la velocidad máxima de subsidencia de 5 cm/a en 2004 a 1.5 cm/a en 2020; hecho que se debe al cese del bombeo de la mitad de los pozos de extracción de agua presentes en esta ciudad (Castellazzi et al. 2021a) a consecuencia de la construcción del acueducto de Querétaro (CEA Querétaro 2016).

Durante el periodo 1935-2021, la subsidencia en el centro de la ciudad de México ha presentado un comportamiento no lineal. Para el análisis a detalle, dicho periodo puede dividirse en tres etapas. La primera etapa, de 1935 a 1948, tiene la velocidad máxima de subsidencia de 8 cm/a; la segunda, de 1948 a 1958, 29 cm/a y la tercera, de 1959 al 2021 y entre 5 y 9 cm/a. La desaceleración de la subsidencia durante la tercera etapa se puede atribuir a la veda de pozos impuesta en el centro de la ciudad en 1959 (Ortega-Guerrero et al. 1993). Adicionalmente, al norte de la Ciudad de

México, también se han reconocido zonas con aceleración máxima de  $8 \text{ mm/a}^2$  y desaceleración máxima de  $-9 \text{ mm/a}^2$  de subsidencia para el periodo 1999-2010, las cuales han sido modeladas con un comportamiento cuadrático y además presentan desarrollo de fallas asociadas a subsidencia (Siles et al. 2015b). También en la zona norte de la Ciudad de México, se encontraron mayores tasas de subsidencia en temporadas de sequía que las registradas en periodo de lluvia en zonas con presencia de arcillas expansivas (Siles et al. 2015b).

Aunque se reconoció el proceso de subsidencia en la Ciudad de México desde fines del siglo XIX, no fue hasta la década de los 40's en que se consolidó la teoría que relaciona las propiedades del subsuelo y la subsidencia (Gayol 1925; Marsal and Mazari 1959; Marsal 1992; Ovando-Shelley et al. 2003; Santoyo-Villa et al. 2005; Marsal et al. 2016). La teoría establece que la extracción de agua del subsuelo promueve a la disminución de la presión de poro y el aumento de esfuerzo efectivo, generando la consolidación del terreno (Terzaghi 1925; Carrillo 1948). Se han utilizado datos de nivelación, InSAR, GPS y determinaciones de las propiedades mecánicas de arcillas para hacer la reconstrucción de la historia de subsidencia de la Ciudad de México (Marsal and Mazari 1959; Marsal 1992; Ovando-Shelley et al. 2003; Santoyo-Villa et al. 2005; Marsal et al. 2016). También se ha dividido a la Ciudad de México en tres zonas geotécnicas a partir de las propiedades mecánicas del subsuelo (Marsal and Mazari 1959; GDF 2004; Marsal et al. 2016; GCDMX 2017). Las zonas geotécnicas definidas inicialmente fueron la zona de lomas, ubicada sobre tobas de baja compresibilidad, zona de transición y zona de lago, ubicada sobre arcillas altamente compresibles.

Basado en las perforaciones profundas y la exploración sísmica del subsuelo de la Ciudad de México realizadas a consecuencia del sismo del 1985, Pérez-Cruz (1988) interpreta los espesores de los sedimentos susceptibles a la consolidación extrema. Dichos espesores presentan variaciones espaciales importantes, aunque, de manera general, aumentan de oeste a este. El máximo espesor de sedimentos compresibles obtenido fue de 490 m al sur del aeropuerto de la Ciudad de México, en el pozo Tulyehualco-1 (Pérez-Cruz 1988), en la región del antiguo lago Texcoco. También han sido generadas ecuaciones que tratan de describir el comportamiento de las arcillas en el subsuelo la Ciudad de México. Estas ecuaciones indican que el contenido de agua, densidad, resistencia y compresibilidad de las arcillas cambian debido a la disminución de la presión de poro por extracción de agua (Ovando-Shelley et al. 2003). Adicionalmente, se ha determinado que el índice de compresibilidad ( $C_c$ ) es de gran utilidad para evaluar las variaciones verticales y laterales de los materiales fluvio-lacustres de la Ciudad de México, dado que estos son altamente heterogéneos a consecuencia de las condiciones de formación y evolución, considerando que estos materiales se interdigitan con la actividad volcánica reciente (Carreón-Freyre et al. 2015). Entre las características más relevantes de las arcillas de la Ciudad de México se tiene un índice de plasticidad de 300%, contenido de agua máximo de 420% y una presencia de una variedad importante de microorganismos disueltos en combinación con material volcánico y lacustre (p. ej. Marsal and Mazari 1959; Díaz-Rodríguez 2003; Ovando-Shelley et al. 2003; Santoyo-Villa et al. 2005; Marsal et al. 2016).

En la zona centro del país se han realizado estudios donde se analiza la relación entre la subsidencia del terreno y el comportamiento de los sistemas acuíferos. Entre los puntos estudiados se encuentran los cambios de la capacidad de almacenamiento de agua subterránea debido a la extracción de agua subterránea, para esta evaluación utilizaron InSAR y datos GRACE (Castellazzi et al. 2016). Encontrándose que las áreas destinadas al uso agrícola y urbano presenta cambios significativos en la capacidad de almacenamiento de agua y además señalan que hay una posible atenuación en la disminución de los niveles piezométricos debido a la recarga por aguas residuales, lo que puede afectar la calidad de agua (Castellazzi et al. 2016). También se estableció una relación empírica entre la tasa de compactación y el volumen de agua subterránea extraída (Cigna and Tapete 2022a). De la misma manera se ha evaluado la relación entre la subsidencia y la densidad de pozos y tasas de extracción de agua considerando el espesor de sedimentos no consolidados (Figueroa-Miranda et al. 2020; Villaseñor-Reyes et al. 2022). En la Ciudad de México se observa una correlación positiva entre la subsidencia y el espesor del acuitardo; además, se documentó la baja correlación entre la velocidad de subsidencia y la caída del nivel piezométrico, lo que tiene explicación en la geología del subsuelo (Solano-Rojas et al. 2015). De cualquier manera, los escasos pozos de la Ciudad de México que presentaron recuperación de los niveles piezométricos presentan baja velocidad de subsidencia (Solano-Rojas et al. 2015).

En cuanto a la relación entre el fallamiento asociado a subsidencia y la potencial contaminación del sistema acuífero, se realizó un estudio en Aguascalientes donde se utilizó Tomografía de Resistividad Eléctrica para detectar el flujo de contaminantes a través de una falla generada por el proceso de subsidencia. En este estudio, Acuña-Lara et al. (2020) encontraron que el flujo del contaminante se mueve verticalmente en los primeros 10 metros para después migrar horizontalmente siguiendo una capa de mayor permeabilidad. En esta investigación se concluyó que el proceso de filtración de contaminantes a través de fallas tiene el potencial de contaminar a largo plazo el sistema acuífero; sobre

todo, para aquellas fallas que inducen la fractura de tuberías que transportan aguas residuales (Acuña-Lara et al. 2020). En la zona metropolitana de la Ciudad de México, el fallamiento superficial asociado al proceso de subsidencia ha favorecido el flujo de contaminantes al sistema acuífero (Ortega-Guerrero et al. 1993; Hernández-Espriú et al. 2014; Chaussard et al. 2021).

Para entender el comportamiento del sistema acuífero debido a la extracción de agua en la Ciudad de México, se han realizado estudios sobre las variaciones en las propiedades hidráulicas, geotécnicas y geomecánicas mediante modelos que consideran su variabilidad vertical y temporal, así como un proceso de consolidación no lineal (Rivera and Ledoux 1991; Ortega-Guerrero et al. 1993; Ortega-Guerrero et al. 1999; Zapata-Norberto et al. 2018; Tracy et al. 2022). Los resultados de estos estudios indican que la conductividad hidráulica tiene el mayor efecto sobre el comportamiento del sistema acuífero para la formación de fallas y fracturas (Aguilar-Pérez et al. 2006; Zapata-Norberto et al. 2018). Para el cálculo de la deformación vertical del terreno se ha encontrado que el coeficiente de consolidación y la transmisividad son los parámetros que generan mayores cambios en los resultados obtenidos (Aguilar-Pérez et al. 2006). Estos trabajos han permitido caracterizar el flujo de agua subterránea, calcular la subsidencia total con base en escenarios y subsidencia diferencial como potencial formador de fallamiento asociado a subsidencia (Rivera and Ledoux 1991; Ortega-Guerrero et al. 1999; Aguilar-Pérez et al. 2006). Los modelos generados han sido calibrados mediante la utilización de datos InSAR y de campo (Rivera and Ledoux 1991; Ortega-Guerrero et al. 1999; Herrera-Zamarrón et al. 2006; Calderhead et al. 2009). Se han generado modelos conceptuales para el sistema acuífero del Valle de México, lo que ha permitido definir cuatro unidades hidrogeológicas con interdependencias entre sus niveles piezométricos, sistemas de flujo y propiedades hidráulicas, identificando los sistemas de flujo locales, intermedios y regionales (Palma et al. 2022). También se ha calculado la cantidad de agua subterránea disponible, la respuesta del sistema a la recarga artificial y se estima que tomará 150 años para que el acuitardo superior del sistema acuífero de Ciudad de México alcance la compactación total, añadiendo 30 metros de subsidencia total adicional (Rivera and Ledoux 1991; Chaussard et al. 2021).

En cuanto a la generación de daños en la infraestructura civil debido a la subsidencia en la Ciudad de México, se han utilizado escenas SAR de banda X para generar un mapa de velocidades al que se le aplicó una técnica basada en filtros pasa bandas (Solano-Rojas et al. 2020b). Esta metodología permitió detectar levantamiento a lo largo de los viaductos elevados de las Líneas 1 y B del Metro, así como desplazamientos diferenciales en la estación Pantitlán del Metro (Solano-Rojas et al. 2020b). Al noroeste de la Ciudad de México se evaluó el impacto de la subsidencia sobre el Túnel Emisor Oriente y las vías férreas presentes. En el estudio, se determinó que los valores de subsidencia más importantes están entre el eje L0 y L3 del Túnel Emisor Oriente, con una velocidad máxima de subsidencia de 18.5 cm/a (Siles et al. 2015a). También se encontraron fallas asociadas a subsidencia que podrían afectar el Túnel Emisor Oriente (Siles et al. 2015b). Por otra parte, el estudio de Poreh et al. (2021) utilizó mapas de velocidades InSAR (PSI) y un análisis de *Support Vector Machine* con la finalidad de evaluar la correlación entre la velocidad de subsidencia y la densidad de edificaciones, encontrando que las zonas con velocidades de subsidencia más rápidas que 10 cm/a tienen densidad de edificaciones altas y moderadas.

Las pérdidas económicas derivadas de la subsidencia han sido evaluadas en las ciudades de Morelia, San Luis Potosí y Toluca. Las investigaciones realizadas evaluaron la influencia de las fallas asociadas a subsidencia sobre las edificaciones e infraestructura civil, asumiendo que todas las viviendas tienen el mismo costo unitario por metro cuadrado (\$281 dólares americanos). En San Luis Potosí, se aplicó la metodología de Blong (2003) modificada, ya que la original no contempla la subsidencia del terreno entre los peligros (Blong 2003; Julio-Miranda et al. 2012). La metodología de Blong (2003), consiste en evaluar los daños sobre las edificaciones directamente en campo y estimar la severidad de daño en función del área de afectación para luego calcular las pérdidas económicas asumiendo el costo de una vivienda promedio. Este análisis determinó pérdidas económicas de \$30.2 millones de pesos para las más de 200 casas evaluadas (Julio-Miranda et al. 2012). En Morelia y Toluca, la evaluación de las pérdidas económicas por subsidencia se realizó utilizando una ecuación que estima la depreciación por fallamiento asociado a subsidencia en función de relación espacial, obteniendo pérdidas económicas de 23.2 millones de pesos y 13.4 millones de dólares, para Toluca y Morelia, respectivamente (Hernández-Madrigal et al. 2015; Camacho-Sanabria et al. 2020). Sin embargo, esta ecuación no contempla la tipología ni las propiedades geotécnicas del subsuelo (Hernández-Madrigal et al. 2014).

Respecto a la aplicación de medidas para la disminución de la depresión de los niveles piezométricos y la mitigación de la subsidencia, pocos trabajos se han llevado a cabo en México. Querétaro es el único caso de México en el que se ha logrado una reducción considerable de las velocidades de subsidencia, pasando de una velocidad máxima de

subsistencia de 5 cm/a a 1.5 cm/a, como se señaló con anterioridad (Castellazzi et al. 2021a, b). Esto se logró mediante la construcción de un acueducto que transporta agua superficial desde la zona fronteriza entre los estados de Querétaro e Hidalgo a la Ciudad de Querétaro. Sin embargo, esta medida solo disminuyó la velocidad de subsistencia, más no ha mitigado por completo la disminución de los niveles piezométricos debido al creciente aumento de la demanda de agua de la Ciudad de Querétaro. Por otra parte, para la Ciudad de Toluca se generó un modelo que busca el diseño de políticas públicas para un manejo sustentable del sistema acuífero y la mitigación de la subsistencia (Castellazzi et al. 2021a, b). Este modelo utilizó cuatro parámetros, los cuales son la recarga, la exportación de agua a otras cuencas, el consumo local y la reubicación de centros de bombeo y encontrando que la reubicación de los centros de bombeo y una disminución a la mitad de la exportación de agua mitigaría de manera considerable la subsistencia del terreno (Calderhead et al. 2010, 2012).

En el caso de la Ciudad de México, se han generado propuestas geotécnicas, hidrogeológicas y de monitoreo para la mitigación del daño a estructuras civiles debido a la subsistencia total y diferencial. En el caso de las soluciones geotécnicas, se han utilizado diferentes métodos de estabilización para edificaciones con gran valor arquitectónico, generando resultados favorables. Estos métodos de estabilización incluyen la inyección de mortero en suelos arcillosos, la sub-excavación y la construcción de planos con baja resistencia a la cizalla (Ovando-Shelley et al. 2008). También se ha estudiado el desempeño de las cimentaciones piloteadas ante la subsistencia diferencial mediante el uso de elementos finitos, encontrando que la reducción de las asimetrías del diseño puede generar buenos resultados para un diseño de cimentación, promoviendo el incremento de la resistencia a los efectos de asentamientos diferenciales (O'Riordan et al. 2018). En cuanto a las propuestas de mitigación con criterio hidrogeológico, se utilizó un pozo de inyección de agua, el cual no buscaba recuperar el volumen de agua extraída, sino aumentar la presión de poro en el sistema. Los resultados de la inyección de agua indican que hubo una respuesta favorable en el aumento de la presión de poro del sistema acuífero-acuitardo somero (Vázquez-Guillén and Auvinet-Guichard 2019), aunque podría tener efectos secundarios y generar fallamiento inducido por la presión de agua (p. ej. fracturamiento hidráulico; Sun et al. 2019). Respecto al monitoreo de los efectos asociados, se creó una unidad de prevención al riesgo urbano causado por la subsistencia. Esta unidad tiene como principal objetivo el monitoreo de las fallas asociadas a subsistencia en la alcaldía Iztapalapa, al este de la ciudad de México (Carreón-Freyre and Rodríguez-Quiroz 2010; CENAPRED 2017).

La relación entre la subsistencia y la actividad sísmica se ha estudiado, en particular la posible influencia del campo de esfuerzos generado por la extracción de fluidos geotérmico en el Campo Geotérmico de Cerro Prieto sobre el sismo de El Mayor-Cucapah de magnitud 7.2 acontecido el 4 de abril de 2010. En este estudio, Trugman y colaboradores (2014) encontraron una influencia sustancial del campo de esfuerzos local que pudo haber contribuido al desarrollo del sismo, dado que el epicentro del sismo se encontró a escasos 15 km al noreste de la mayor zona de producción del Campo Geotérmico de Cerro Prieto y que el sistema de fallas que origino este sismo se consideraba inactivo. Adicionalmente, se realizó una modelación de la subsistencia tectónica y antropogénica donde se evalúa el cambio de esfuerzos producidos por la extracción de fluidos geotérmicos y por el movimiento tectónico y se discute la relación entre la extracción y la sismicidad (Glowacka et al. 2005). En Aguascalientes se encontró una relación sustancial entre la subsistencia del terreno y el movimiento vertical de fallas activas que han generado sismos de baja magnitud ocurridos en el año 2019 (Hernandez-Marin et al. 2020).

En la Ciudad de México, se ha determinado que los grandes sismos pueden generar la aceleración de la subsistencia, dado que promueven al deslizamiento rápido a lo largo de las fallas generadas por subsistencia diferencial (Solano-Rojas et al. 2020a). Una observación de relevancia ha sido que la subsistencia por extracción de agua modifica el comportamiento sísmico del subsuelo, acortando el periodo de resonancia del terreno y favoreciendo a las estructuras de periodos de resonancia más largos, pero perjudicando las estructuras civiles cuyo periodo es más corto que el periodo de sitio actual (Avilés et al. 2006; Avilés and Pérez-Rocha 2010; Albano et al. 2016). Se ha estimado que para la ventana de tiempo 2005-2013, la subsistencia total es ente 0.5 a 3 m, lo que ha generado una disminución de los periodos de resonancia de 0.1 a 0.4 segundos. Este cambio de los periodos del suelo tiene un gran impacto en el espectro de respuesta usado para el diseño de estructuras, por lo que su evolución debería ser considerado en las reglamentaciones futuras (Albano et al. 2016).

Las altas tasas de subsistencia del terreno medidas en la Zona Metropolitana de la Ciudad de México ha fomentado la formación de depresiones del relieve que han favorecido a la formación de un nuevo lago en Chalco y la exposición a inundaciones de una porción importante del área urbanizada. En Chalco, al sureste de la Ciudad de México, entra en operación en 1984 el sistema de bombeo de agua Mixquic-Santa Catarina, el cual ha generado tasas de subsistencia de hasta 40 cm/a y promovido las inundaciones de zonas agrícolas y urbanas, generando encharcamientos y la formación

de un nuevo lago cuya extensión y geometría está controlada por la intercalación en el subsuelo de coladas basálticas de la Sierra de Santa Catarina (Ortega-Guerrero et al. 1993; Ortega-Guerrero et al. 1999; Ortiz-Zamora and Ortega-Guerrero 2007). Por otra parte, Cigna y Tapete (2021a), determinaron la exposición a inundaciones de la Zona Metropolitana de la Ciudad de México, con base en las velocidades de subsidencia vertical, determinando que 751,000 viviendas y 2.7 millones de personas viven en zonas de alta y muy alta exposición a inundaciones o áreas con velocidades de subsidencia más rápidas que 20 cm/a. Además, señalan que la mayor parte de exposición a subsidencia es debido a la generación de encharcamientos poco profundos sobre las depresiones topográficas generadas por la subsidencia en lugares donde la capacidad de drenaje es excedida durante la temporada de lluvias.

Hacia el este de la Ciudad de México, se han realizado estudios que relacionan el proceso de subsidencia con deslizamientos ubicados al norte del municipio Iztapalapa, en la localidad El Edén y en los alrededores del Peñón del Márquez. Estos deslizamientos se caracterizan por la presencia de zonas de fracturas circulares en la parte alta y media del flanco deslizante, topografía irregular, deformación compresiva en la zona distal y pendientes importantes (Cerca et al. 2010; González-Hernández et al. 2015). Los mayores daños en la infraestructura se dan en la zona de compresión, donde se han observado levantamientos, los cuales han generado daños en la infraestructura civil. Los sitios que presentan subsidencia y deslizamientos se caracterizan por presentar pendientes pronunciadas, valores de subsidencia altos y contraste litológico de los aparatos volcánicos que son subyacentes por materiales lacustres compresibles (Cerca et al. 2010; González-Hernández et al. 2015). Para la caracterización de los deslizamientos se ha utilizado cartografía de campo, Radar de Penetración Terrestre y mediciones por muestreo directo de propiedades físicas de los materiales.

La subsidencia del terreno asociada a la extracción de fluidos para la generación de energía geotérmica en México se ha estudiado en dos áreas. La primera es el Complejo Volcánico los Humeros, alcanzando velocidades de subsidencia de 1.1 cm/a usando escenas de Envisat (2003-2010) (Cigna et al. 2019) y la segunda es en el Campo Geotérmico de Cerro Prieto, cuya máxima subsidencia registrada es de 18 cm/a y se encuentra sobre la zona denominada como zona de recarga, fuera de los límites del campo geotérmico (Sarychikhina et al. 2018).

El Campo Geotérmico de Cerro Prieto se encuentra en el límite oeste de la cuenca *pull-apart* Cerro Prieto, el cual ha sido creado por el movimiento tectónico de las fallas Cerro Prieto e Imperial. Entre límite este del campo geotérmico y falla Imperial/Salttillo se encuentra la zona de recarga que presenta los valores máximos de subsidencia de hasta 18 cm/a en los años 2005-2009, como se mencionó con anterioridad (Sarychikhina et al. 2018). En el límite este de la cuenca Cerro Prieto y de la zona con subsidencia está la falla Saltillo (una rama de la falla imperial). Esta falla presenta un deslizamiento (*creep*) asísmico continuo y en forma de eventos de *creep* causados por subsidencia, presentando velocidades de 5 cm/a entre los años 1996-1999, la cual registró un aumento a poco más de 7 cm/a para el periodo 2004-2010 relacionado con el desarrollo del campo geotérmico. En este campo geotérmico, se han empleado métodos geodésicos (InSAR, nivelación) y observaciones estructurales (comportamiento de las fallas Imperial y Cerro Prieto) para modelar la subsidencia del terreno (Carnece and Fabriol 1999; Glowacka et al. 2010). A partir de esta información, se ha establecido que la causa principal de la subsidencia es la extracción de fluidos geotérmicos.

La subsidencia del terreno causada posiblemente por la extracción de hidrocarburos solo ha sido estudiada en la Ciudad de Villahermosa, Tabasco. Para esta investigación se usaron escenas de Sentinel-1 que cubrieron el periodo de tiempo 2018-2019, encontrando velocidades máximas de subsidencia de 6 cm/a en el Paraíso, al noroeste de Villahermosa, Tabasco. Adicionalmente, se observó una relación espacial entre la subsidencia registrada al suroeste de Villahermosa en procesos de inundación que han acontecido en esta misma área. También han localizado zonas de subsidencia sobre tres campos de extracción de hidrocarburos ubicados al oeste y suroeste de Villahermosa (Pérez-Falls et al. 2022).

En la Ciudad de México se ha estudiado la subsidencia generada sobre antiguas minas que eran utilizadas para extracción de agregados para la construcción, las cuales fueron utilizadas durante el siglo XX (Cárdenas-Soto et al. 2020). Muchas de estas minas se encuentran hacia el oeste de la ciudad y no fueron totalmente rehabilitadas, por lo que permanecen con potencial peligro de desarrollo de subsidencia del terreno. Para estudiar estas minas, Cárdenas-Soto et al. (2020) utilizaron la anomalía de velocidad sísmica generada por ruido sísmico ambiental, en combinación con tomografía de resistividad eléctrica, permitiendo la caracterización de las zonas que presentan potenciales cavidades así como la profundidad de la saturación de agua subterránea.

Gutiérrez-Yurrita (2010) realizó una revisión de la jurisprudencia mexicana y determinó que no existe una pena que contemple la responsabilidad del daño ambiental debido al fenómeno de subsidencia producto de actividades antropogénicas. En este trabajo, se revisaron los códigos civiles y criminales y se encontró que no existe en la

legislación delito relacionado con los daños a edificaciones civiles producto de la subsidencia del terreno (Gutiérrez-Yurrita 2010).

En México se han calibrado las velocidades de desplazamiento del terreno obtenidas con InSAR mediante la comparación con observaciones obtenidas en campo. Para la calibración de las mediciones de InSAR en áreas donde la deformación horizontal es cercana a cero, se ha propuesto una metodología que compara los datos InSAR con mediciones in-situ mediante la utilización de parámetros estadísticos como *Root Mean Square Error*, el cual es normalizado según el rango y magnitudes del campo de velocidades presente y luego es combinado con el coeficiente de correlación de Pearson, para a continuación generar un esquema de clasificación en función de la precisión de los datos InSAR, esta metodología fue aplicada en San Luis Potosí (Navarro-Hernández et al. 2022). En la Ciudad de México, también se han calibrado las series de tiempo InSAR mediante comparación de los resultados de nivelación topográfica, obteniendo velocidades similares (Cabral-Cano et al. 2008). Por otra parte, en Aguascalientes se ha evaluado la precisión de las velocidades verticales y horizontales mediante la comparación de series de tiempo InSAR con mediciones de GPS y nivelación. Para la componente vertical obtuvieron diferencias de 0.9 a 1 cm/a (GPS) y 0.8 cm/a (nivelación topográfica). En la componente horizontal (E-W) las diferencias entre InSAR y GPS de 0.1 a 0.2 mm/a. Las soluciones GPS fueron obtenidas utilizando *Precise Point Positioning* y el software GPSPACE desarrollado por el Servicio Geodésico de Canadá, utilizando los datos de las estaciones estáticas de adquisición continua INEG y AUGU (Cigna et al. 2021). Además, señalan que las mayores discrepancias de velocidades se obtuvieron en zonas cercanas a las fallas normales presentes en el área de estudio (Cigna et al. 2021). Por otra parte, Yalvac (2020) realizó una evaluación de la precisión de las velocidades de InSAR comparando las velocidades con series de tiempo GPS, obteniendo una diferencia promedio de entre 7 y 8 mm de desplazamiento, registrándose un máximo de diferencia de 2 cm. En el Campo Geotérmico de Cerro Prieto, Sarychikhina et al. 2018 realizaron la comparación entre InSAR y nivelación topográfica, así como un análisis de errores de estimación de la velocidad de subsidencia a partir de los datos InSAR, tomando el desplazamiento horizontal igual a cero para los periodos 1993-1997 y 2012-2014 a lo largo de 3 perfiles, obteniendo una correlación razonablemente buena en magnitud y tendencia.

Las características particulares de la señal de subsidencia de la Ciudad de México (p. ej. altas tasas de subsidencia y amplia extensión espacial) han permitido que haya sido el área de estudio para el desarrollo de nuevas técnicas de procesamiento InSAR y la utilización de nuevos sensores SAR. Entre los nuevos algoritmos InSAR cuyo funcionamiento ha sido probado en la Ciudad de México se encuentran GEOS (Geoscience and Earth Observing Systems Group)-ATSA (Advance Time-Series Analysis), GEOS-SBAS (Small Baseline Subset) y ComSAR (Du et al. 2019a, b; Tong-Minh and Ngo 2021). Estos algoritmos fueron calibrados con datos GPS y contrastados con resultados previos obteniendo resultados similares. Además, se han desarrollado técnicas que permiten invertir redes de interferogramas que no están completamente conectadas, obteniendo resultados de velocidades similares a investigaciones previas (López-Quiroz et al. 2009). Por otra parte, en la Ciudad de México, se utilizó por primera vez el procesamiento PSI utilizando escenas de Sentinel-1A definiendo estrategias de procesamiento pioneras para este sensor SAR (Crosetto et al. 2015).

A pesar de que México es uno de los países con mayor número de trabajos y tópicos relacionados con el estudio del proceso de subsidencia del terreno (Herrera-García et al. 2021; Raspini et al. 2022), aún quedan preguntas a ser respondidas para tener una visión más amplia que permita el manejo sustentable de sus sistemas acuíferos, en especial considerando los escenarios actuales de cambio climático, y mitigar sus efectos.

Entre las interrogantes a resolver que este trabajo aborda y que se describen en los siguientes capítulos tenemos:

- a) la identificación y catálogo de todas las localidades urbanas en México que están expuestas a velocidades de subsidencia que generan daños a la infraestructura y al terreno (Capítulo 5.1).
- b) conocer el riesgo socioeconómico de la subsidencia considerando las características de la población (Capítulos 5.2 y 5.3).
- c) evaluar el riesgo económico por subsidencia, considerando los estados límites de la reglamentación de construcción vigente Capítulo 5.4)
- d) la determinación de la por distorsión angular y la evaluación de la exposición estructural de la Ciudad de México (Capítulo 5.5).

Otros tópicos relevantes que no serán tratados en la presente investigación son: determinar a nivel país la relación entre la subsidencia y el uso de suelo, modelar el comportamiento de la subsidencia e inundaciones en zonas costeras

considerando escenarios de cambio climático, generar modelos en zonas detectadas con subsidencia que expliquen el comportamiento de la subsidencia y que sean calibrados con la deformación medida con métodos geodésicos, evaluar el riesgo socioeconómico y económico debido a la subsidencia a nivel país y como esta ha variado en las últimas décadas, determinar los costos directos e indirectos debido a la subsidencia y fallamiento asociado, generar estudios detallados de geología superficial, geología de subsuelo, hidrogeológicos y geotécnicos en zonas previamente detectadas con subsidencia para poder investigar las causas y generar escenarios del comportamiento de la subsidencia, evaluar a nivel país la subsidencia asociada a otros procesos tales como extracción de hidrocarburos y minería, y evaluar el riesgo de las edificaciones a nivel predio mediante el uso de curvas de fragilidad y vulnerabilidad estructural.

## 2. Hipótesis

En esta investigación se contemplan cuatro hipótesis que son:

1. La evaluación de la subsidencia del terreno en parte norte de México y sus costas resultará en un aumento de las localidades urbanas con subsidencia detectadas en el país, dado que estas zonas también presentan condiciones propicias para su desarrollo, tales como, la presencia de materiales compresibles y explotación intensiva de los sistemas acuíferos.
2. Si la vulnerabilidad socioeconómica es mayor en las zonas con subsidencia y fallamiento asociado, entonces el riesgo socioeconómico será mayor hacia el este de la Ciudad de México.
3. La estimación del valor catastral de los predios en conjunto con la subsidencia diferencial y sus estados límite, permitirán conocer las zonas con mayor riesgo económico y el valor catastral que ello representa.
4. La estimación de la distorsión angular permitirá la ubicación de las construcciones que se exponen a subsidencia diferencial y potencial fallamiento.

## 3. Objetivo general

Evaluar el proceso de subsidencia en México mediante el uso de técnicas de geodesia satelital e información del censo, catastral, geológica, hidrogeológica y de la reglamentación de construcciones vigente.

### 3.1 Objetivos específicos

Los objetivos de este trabajo son:

- a) Identificar las localidades y áreas urbanas, población, y viviendas que están expuestas a velocidades de subsidencia que puedan representar posibles daños a la infraestructura y al terreno, así como los factores condicionantes.
- b) Conocer el riesgo socioeconómico por subsidencia y fallamiento asociado considerando las características de la población.
- c) Evaluar el riesgo económico por subsidencia, considerando los estados límites de la reglamentación de construcción vigente.
- d) Evaluar la exposición a la que están sometidas las construcciones mediante el uso de la distorsión angular.



## 4. Materiales y métodos

### 4.1 Radar de apertura sintética (SAR)

Los sensores SAR son sensores activos, ya que tienen su propia fuente de potencia a diferencia de los sensores pasivos que utilizan la luz del Sol (Moreira et al. 2013). La información adquirida con los sensores SAR se obtiene en línea de vista del sensor y estos pueden viajar a bordo de plataformas satelitales, aeronaves o sobre la superficie terrestre (Osmanoğlu et al. 2016). Los sensores SAR emiten ondas electromagnéticas a la superficie terrestre en frecuencia de microondas. Los SAR operan en diversas bandas (p. ej. banda L: 2-1 GHz, banda C: 7.5-3.75 GHz, banda X: 12-7.5 GHz; Moreira et al. 2013). La interacción de las ondas electromagnéticas con la superficie de la Tierra permite la determinación de la topografía, medir características dieléctricas y determinar rugosidad, entre otras propiedades del terreno (Ferretti et al. 2007). Para el procesamiento de las imágenes SAR se utilizan técnicas de procesamiento de señales e información de las órbitas satelitales.

Los sensores SAR obtienen información de la superficie bajo cualquier condición climática, adquiriendo información bidimensional de amplitud y fase (Moreira et al. 2013). La amplitud mide la reflectividad de material y presenta valores máximos en rocas expuestas en superficie y edificaciones (Bamler and Hartl 1998; Bürgmann et al. 2000). La amplitud permite obtener información de las propiedades electromagnéticas del terreno, así como su forma y orientación (Ferretti et al. 2007). Por otra parte, los sistemas SAR tienen la capacidad de registrar de manera muy precisa los cambios de fase. Los sensores SAR, mediante la utilización de al menos dos escenas tomadas de aproximadamente la misma área y en tiempos distintos de adquisición, permite determinar cambios en la superficie, mediante la generación de interferogramas, cuya resolución espacial y temporal dependerá de la longitud de onda y las características del sensor utilizado (Osmanoğlu et al. 2016). La información de fase se encuentra envuelta entre  $-\pi$  y  $\pi$  radianes.

### 4.2 Interferometría de radar de apertura sintética (InSAR)

La técnica InSAR utiliza el cambio de fase registrada en los interferogramas, permitiendo medir deformaciones con una precisión centimétrica a milimétrica, dependiendo la técnica empleada en el procesamiento. La diferencia de fase de un área en específico se puede medir de manera simultánea (dos sensores a bordo de la misma plataforma) o en tiempos diferentes con ángulos de inclinación y azimut ligeramente diferentes (Ferretti et al. 2007).

La técnica InSAR permite la generación de series de tiempo mediante la medición de las diferencias de fases interferométricas utilizando múltiples interferogramas. Las diferencias de fase deben estar sujetas a un desenvolvimiento espacio-temporal para que la información generada tenga significado físico (Osmanoğlu et al. 2016). Para el desenvolvimiento de fase existen múltiples algoritmos (p. ej. SNAPHU; Chen and Zebker 2002). Las mediciones InSAR son especialmente sensibles a la deformación del terreno, cambios en la atmósfera (troposfera e ionosfera), diferencias en la geometría de adquisición de las imágenes, y cambios en las propiedades retrodispersivas de la superficie terrestre o su cobertura (Ferretti et al. 2001). La diferencia de fase, por tanto, involucra múltiples contribuciones, las cuales pueden considerarse como ruido dependiendo de la aplicación. Por ejemplo, si el estudio es sobre la deformación del terreno, las contribuciones de topografía y troposfera serán ruido, pero si la investigación es sobre la topografía, las contribuciones de deformación y troposfera serán consideradas ruido.

La diferencia de fase o fase interferométrica puede ser expresada mediante la ecuación 1 (Osmanoğlu et al. 2016).

$$\Delta\varphi = \varphi_{flat} + \varphi_{topo} + \varphi_{orbit} + \varphi_{defo} + \varphi_{tropo} + \varphi_{iono} + \varphi_{scat} + \varphi_{noise} \quad (\text{ecuación 1})$$

Donde:

$\Delta\varphi$  es la fase interferométrica que es la diferencia de fase existente entre las escenas SAR empleadas y sus valores se encuentran comprendidos entre  $-\pi$  y  $\pi$ . La fase interferométrica es la suma de múltiples contribuciones. Todas las contribuciones de la fase interferométrica están medidas en LOS (línea de vista del sensor).

$\varphi_{flat}$  es la contribución de una superficie de referencia, su valor depende de la línea base paralela (Figura 1).

$\varphi_{topo}$  es la contribución de la topografía, está relacionada con la topografía sobre el elipsoide de referencia, su valor dependerá de la línea base perpendicular y la altura del terreno (Figura 1).

$\varphi_{orbit}$  es la contribución inducida por errores en la información de la órbita.

$\varphi_{defo}$  es la contribución debido a la deformación del terreno ocurrida entre la adquisición de las escenas.

$\varphi_{tropo}$  es la contribución atmosférica debido a los cambios en la troposfera entre la adquisición de las escenas.

$\varphi_{iono}$  es la contribución atmosférica debido a los cambios en la ionosfera entre la adquisición de las escenas. Dicha contribución puede generar problemas en el corrección de las escenas, reducir la coherencia y pérdidas de definición en dirección del rango y azimut. Depende de la diferencia en el número de electrones en la ionosfera y la longitud de onda utilizada por el sistema SAR.

$\varphi_{scat}$  es la contribución de fase debido a los cambios de propiedades retrodispersadas en la escena en el intervalo de tiempo para el cual se genera el interferograma diferencial. Es debido a esta contribución la decorrelación temporal. En áreas con abundante vegetación, el coeficiente de retrodispersión cambia según la estación del año o por el movimiento de la vegetación por efecto del viento. La decorrelación temporal es mayor cuando la longitud de onda de la señal es menor.

$\varphi_{noise}$  es la contribución por ruido instrumental del sensor. Esta contribución puede ser usualmente ignorada.

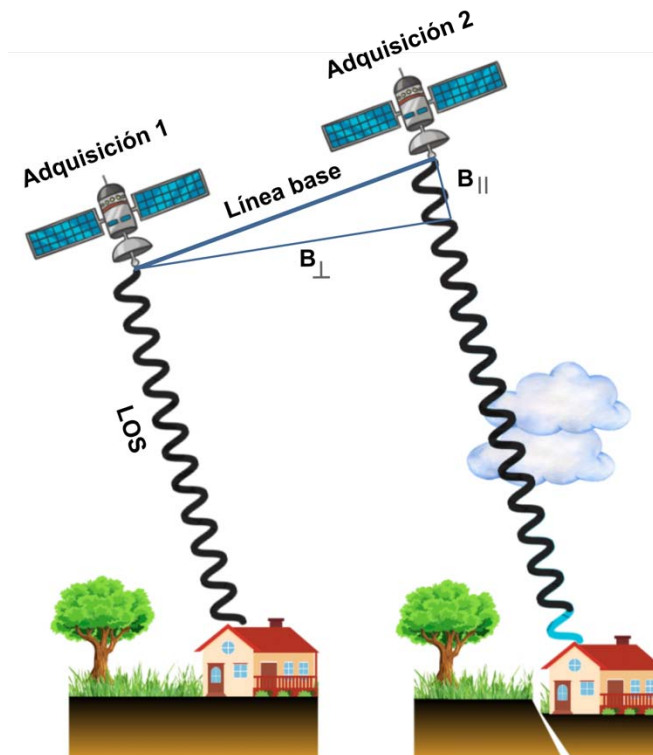


**Figura 1** Geometría de la interferometría SAR por paso repetido (modificado de Osmanoğlu et al. 2016).  $B_{\parallel}$  y  $B_{\perp}$  representan las líneas base paralela y perpendicular, respectivamente.

Las técnicas utilizadas para el análisis de series de tiempo InSAR fueron desarrolladas con la finalidad de sobreponerse a la decorrelación (Zebker and Villasenor 1992) y los efectos atmosféricos (Zebker et al. 1997). Las series de tiempo InSAR, permiten el análisis de la evolución de la deformación de la superficie terrestre en el tiempo. Estas presentan múltiples aplicaciones tales como: estudio de subsidencia del terreno, ciclo sísmico, actividad volcánica, procesos de remoción de masa, flujos glaciares y cambios en la superficie de sistemas geotérmicos (Ferretti et al. 2007; Moreira et al. 2013). Las series de tiempo InSAR se pueden generar mediante la utilización de dos grandes familias de algoritmos: *Persistent Scatterer Interferometry* (PSI) y *Small Baseline Subset* (SBAS). Cada uno de este conjunto de métodos está diseñado para un tipo específico de mecanismos de dispersión. Los algoritmos que utilizan PSI permiten la identificación de los dispersores estables (permanentes) o aquellos puntos que mantienen sus propiedades de retrodispersión a lo largo del tiempo, tales como infraestructura urbana y afloramientos en zonas áridas (Ferretti et al. 2001) o no estables. Para la determinación de los dispersores estables se han planteado diferentes metodologías (p. ej. Werner et al. 2003; Hooper et al. 2004; Kampes 2006; Costantini et al. 2008). En los algoritmos PSI, los interferogramas se forman usando una única imagen máster, sin importar la dimensión de su línea base. En estos algoritmos se debe asumir un cierto tipo de modelo de deformación, ya sea lineal (más común), sinusoidal, etc. Con

estos modelos se intenta simular la evolución del movimiento del terreno pixel a pixel. Por su parte los algoritmos que usan SBAS, el criterio para evaluar la estabilidad de la fase interferométrica, se basa en la coherencia espacial (Berardino et al. 2002) los puntos que se muestran más coherentes son los reflectores o blancos distribuidos, es decir, zonas relativamente grandes que se mantienen inalteradas. Los tipos de reflectores que utiliza SBAS son más sensibles a la longitud de la componente perpendicular de la línea de la línea base (Figura 1), por lo que la red de interferogramas se genera respetando ciertos límites de línea base espaciales y perpendiculares. Para la familia SBAS se han generado también varias versiones (p. ej. Usai 2003; Schmidt and Bürgmann 2003; Cavalie et al. 2007; López-Quiroz et al. 2009). Estas dos familias de algoritmos (PSI, SBAS) han permitido la generación de series tiempo InSAR con precisión sub-centimétrica mediante la reducción de la decorrelación de la señal.

### 4.3 Sentinel-1

Sentinel-1 es una constelación conformada por dos satélites SAR, Sentinel-1A y B, que orbitan en el mismo plano orbital. Esta constelación es operada por la *European Space Agency* (ESA) y es parte del programa Copernicus (Torres et al. 2012). El sensor Sentinel-1A fue lanzado el 3 de abril de 2014 y entro en su fase de operaciones en junio de 2015; por su parte, el satélite Sentinel-1B fue lanzado el 25 de abril de 2016 (Kalia et al. 2017) y cesó operaciones por problemas técnicos en diciembre de 2021, debido a un fallo en la unidad de alimentación de la antena del sensor. En abril del 2024 y 2026 se espera el lanzamiento de Sentinel-1C y Sentinel-1D, respectivamente. Los sensores de Sentinel-1 orbitan a unos 700 km de altitud y fueron diseñados para tener una vida útil de al menos 7 años, con un periodo de duración de la constelación Sentinel-1 de 15-20 años (Torres et al. 2012).

Sentinel-1 orbita en órbitas casi polares, adquiriendo en órbitas ascendentes y descendentes, lo que permite descomponer el vector de velocidades en sus componentes este y vertical, pero está imposibilitando a obtener información en la componente norte. Sentinel-1 tiene una cobertura 45 grados norte y -45 grados sur, opera en la banda C permitiendo darle continuidad temporal a otros sensores de banda C como los son ERS/Envisat, haciendo posible la generación de series de tiempo con información de hasta tres décadas, permitiendo estudiar de manera sinóptica la evolución del campo de velocidades (Torres et al. 2012).

Sentinel-1 tiene un tiempo de paso de entre 6 a 12 días, un tubo orbital de 200 m, lo que permite aumentar la coherencia temporal y espacial (Fletcher and European Space Agency 2012). Posee una antena que tiene vista hacia la derecha y adquiere la información en línea de vista de sensor, con un ángulo de incidencia que oscila entre 31°-46° con respecto a la vertical. El ancho de *swath* de Sentinel-1 es de 250 km en el modo de operación *Interferometric Wide swath* (IW) y presenta una resolución espacial de 5 x 20 m lo que permite la detección de desplazamientos rápidos no lineales (Torres et al. 2012). También es posible activar otros modos de adquisición como *Stripmap*, en el caso de que se quieran monitorear áreas de gran magnitud, o el modo *Extra-Wide swath* el cual es usado para el monitoreo costa afuera de masas de hielo (Torres et al. 2012). Para adquirir la información SAR, Sentinel-1 utiliza como modo de operación el *Terrain Observation by Progressive Scan* (TOPS; De Zan and Monti Guarnieri 2006), el cual necesita un correregistro muy preciso, por lo que se suelen utilizar algoritmos como el *Network-Based Enhanced Spectral Diversity* (NESD; Fattahi et al. 2017). Sentinel-1 tiene una política de generación de escenas SLC de libre costo, lo que ha permitido ser ampliamente utilizadas para la evaluación de peligros naturales, vigilancia de barcos y monitoreo de flujos glaciares.

En esta investigación se utilizó los sensores de Sentinel-1 debido a que sus escenas son de libre costo y a sus características técnicas, tales como tiempo de paso de 6 a 12 días, banda C y tubo orbital de 200 m lo que permite cubrir amplias zonas del país con una resolución espacial, coherencia espacial y temporal adecuada permitiendo la detección de nuevas áreas urbanas con subsidencia, así como la evaluación de la exposición de construcciones civiles a la subsidencia diferencial.

### 4.4 Procesamiento InSAR SBAS

Las escenas Sentinel-1 *Single Look Complex* (SLC) y la información orbital fueron descargadas del repositorio del *European Space Agency* utilizando la plataforma de *Alaska Satellite Facility*. Para el procesamiento de las escenas SAR TOPS de Sentinel-1 y generación de interferogramas utilizamos el software *Interferometric Synthetic Aperture Radar Scientific Computing Environment* ISCE-2 (Rosen et al. 2012). En el correregistro de las escenas Sentinel-1 SAR TOPS utilizamos el flujo de trabajo de *Network-Based Enhanced Spectral Diversity* (NESD; Fattahi et al. 2017). Para todos los interferogramas removimos la contribución topográfica utilizando los modelos digitales de elevación de

*Shuttle Radar Topography Mission* (SRTM; Farr et al. 2007). En el desenvolvimiento de la fase utilizamos el algoritmo *Statiscal-cost Network-flow Algorithm for PHase Unwrapping* (SNAPHU; Chen and Zebker 2002). Para la red de interferogramas se utilizó 3 conexiones, la cuales fueron generadas utilizando el algoritmo *Small BAseline Subsets* (SBAS; Berardino et al. 2002). También utilizamos un *multilook* en azimut y *range* para mejorar la coherencia espacial.

Una vez obtenidos los interferogramas desenvueltos con ISCE-2, se procedió a la generación de las series de tiempo InSAR y mapa de velocidad promedio utilizando el software *Miami InSAR Time-series Python* software (MintPy, Yunjun et al. 2019). Para la corrección de errores de desenvolvimiento de la fase se utilizó el algoritmo *phase-closure technique* (Usai 2003). Los puntos de referencia de los mapas de velocidades se establecieron manualmente en lugares con coherencia temporal mayor 0.85, y con deformación nula o cercana a cero. Para la corrección troposférica utilizamos la correlación empírica entre troposfera y topografía (Doin et al. 2009). Los errores relacionados a modelos digitales del terreno fueron removidos siguiendo el método de Fattahi and Amelung (2013). También se calcularon el *Root Mean Square* (RMS) de la fase residual para cada adquisición de la serie de tiempo, eliminando de la estimación de las velocidades las escenas ruidosas (Yunjun et al. 2019). Para la identificación de las escenas ruidosas utilizamos la *Median Absolute Deviation* (MAD) y marcamos como escenas ruidosas a aquellas donde su valor de RMS es mayor a 3 MAD. Las adquisiciones ruidosas no se toman en cuenta en el cálculo de las velocidades promedio ni en las series de tiempo InSAR. Para la generación del mapa de velocidades promedio aplicamos una máscara de agua y de coherencia temporal mayor a 0.7 con la finalidad de solo mostrar las velocidades de pixeles confiables (Pepe and Lanari 2006). En la estimación de la tasa de deformación, la velocidad es estimada como la pendiente de mejor ajuste a la serie de tiempo del desplazamiento.

#### 4.5 Vulnerabilidad socioeconómica

Se denomina vulnerabilidad al conjunto de condiciones o características que puedan presentar una comunidad que aumente su susceptibilidad a ser afectada por un peligro (Novelo-Casanova, comunicación personal). El caso de vulnerabilidad socioeconómica se medirá en función de parámetros económicos y sociales que aumenten la vulnerabilidad de la población a determinado peligro. En esta investigación se utilizaron 13 indicadores cuya información fue obtenida a nivel AGEB y con base a los datos del censo de población y vivienda 2010 (INEGI 2010), como fue descrito en Novelo-Casanova et al. (2022). La selección de los indicadores socioeconómicos estuvo a cargo de especialistas en diferentes peligros geológicos pertenecientes al Instituto de Geofísica de la Universidad Nacional Autónoma de México (UNAM) y del Centro Nacional de Prevención de Desastres (CENAPRED), cuyo criterio se basó en los parámetros relacionados con el poder adquisitivo que puedan incrementar la vulnerabilidad de la población. Para la evaluación de los pesos de cada indicador socioeconómico se asignaron pesos mediante la comparación de estos mediante la aplicación de la metodología denominada Proceso Analítico Jerárquico (Saaty 1980), cuya evaluación estuvo a cargo de especialistas en peligros geológicos pertenecientes a los institutos de Geología y Geofísica de la UNAM y del CENAPRED. La vulnerabilidad socioeconómica nos permitió obtener el riesgo socioeconómico debido a subsidencia a nivel AGEB como está descrito en (Novelo-Casanova et al. 2022, Fernández-Torres et al. 2022).

#### 4.6 Gradiente horizontal de subsidencia

El gradiente horizontal de subsidencia permite calcular la máxima tasa de cambio de un píxel central de velocidad vertical del terreno con respecto a una vecindad de píxeles en las direcciones horizontales ( $dz/dx$ ) y verticales ( $dz/dy$ ). Para su estimación utilizamos el algoritmo *Neighborhood Slope Algorithm* (NSA; Burrough et al. 2015). En el cálculo del gradiente horizontal utilizamos el algoritmo Pendiente disponible en QGIS 3.22. El algoritmo NSA fue aplicado sobre un ráster de velocidades verticales y para la estimación del máximo cambio del píxel central es necesario de que al menos 7 píxeles tengan velocidades distintas de NAN dentro en una ventana móvil de 3 por 3 píxeles. El gradiente horizontal de subsidencia puede ser expresado en radianes y representa el cambio de velocidad en una distancia horizontal, concepto análogo a la distorsión angular  $\beta$  (p. ej. Skempton and Macdonald 1956). A partir de la distorsión angular se puede calcular la subsidencia diferencial, como el producto entre la distorsión angular y el tamaño del píxel (ecuación 2). Donde  $\beta$  es la distorsión angular,  $ds$  es la subsidencia diferencial y  $l$  es el tamaño de píxel.

$$\beta = \frac{ds}{l} \quad \text{(ecuación 2)}$$

# Capítulo 5.1 Country-scale assessment of urban areas, population, and households exposed to land subsidence using Sentinel-1 InSAR and GPS time series

## Contents

---

### **Abstract**

### **1 Introduction**

### **2 Study area**

### **3 Methodology**

#### **3.1 SAR dataset and InSAR processing**

#### **3.2 Urban areas exposed to land subsidence and classification of land subsidence regions**

#### **3.3 Calibration**

### **4 Results**

#### **4.1 Spatial pattern and time series of land subsidence**

#### **4.2 Urban localities with land subsidence and land subsidence regions**

#### **4.3 Relationship between land subsidence and conditional factors**

#### **4.4 InSAR and GPS Comparison**

### **5 Discussion**

### **6 Conclusion**

### **References**

---

**Fernández-Torres EA, Cabral-Cano E, Solano-Rojas D, et al (2023)** Country-scale assessment of urban areas, population, and households exposed to land subsidence using Sentinel-1 InSAR, and GPS time series. Nat Hazards. <https://doi.org/10.1007/s11069-023-06259-5>



# Country-scale assessment of urban areas, population, and households exposed to land subsidence using Sentinel-1 InSAR, and GPS time series

Enrique Antonio Fernández-Torres<sup>1,2</sup> · Enrique Cabral-Cano<sup>2</sup> · Darío Solano-Rojas<sup>3</sup> · Luis Salazar-Tlaczani<sup>2</sup> · Josue García-Venegas<sup>3</sup> · Bertha Marquez-Azúa<sup>4</sup> · Shannon Graham<sup>5</sup> · Katia Michelle Villarnobo-Gonzalez<sup>6</sup>

Received: 2 November 2022 / Accepted: 27 September 2023  
© The Author(s) 2023

## Abstract

The increased need for water resources in urban sprawls and intense droughts has forced more aggressive groundwater extraction resulting in numerous urban areas undergoing land subsidence. In most cases, only some large metropolitan areas have been well-characterized for subsidence. However, there is no existing country-wide assessment of urban areas, population, and households exposed to this process. This research showcases a methodology to systematically evaluate urban localities with land subsidence higher than  $-2.8$  cm/year throughout Mexico. We used Interferometric Synthetic Aperture Radar (InSAR) tools with a dataset of 4611 scenes from European Space Agency's Sentinel-1 A/B SAR sensors acquired from descending orbits from September 2018 through October 2019. This dataset was processed at a supercomputer using InSAR Scientific Computing Environment and the Miami InSAR Time Series software in Python software. The quality and calibration of the resulting velocity maps are assessed through a large-scale comparison with observations from 100 continuous GPS sites throughout Mexico. Our results show that an urban area of  $3797$  km<sup>2</sup>, 6.9 million households, and 17% of the total population in Mexico is exposed to subsidence velocities of faster than  $-2.8$  cm/year, in more than 853 urban localities within 29 land subsidence regions. We also confirm previous global potential estimations of subsidence occurrence in low relief areas over unconsolidated deposits and where groundwater aquifers are under stress. The presented research demonstrates the capabilities for surveying urban areas exposed to land subsidence at a country-scale level by combining Sentinel-1 velocities with spatial national census data.

**Keywords** InSAR · Sentinel-1 · Urban land subsidence · GPS · Mexico · Nation-wide

## 1 Introduction

Since the industrial revolution, the planet has suffered a constant increase in the release of greenhouse gases resulting in an increasing trend in the temperature and changes in the precipitation patterns (IPCC 2021). These changes in climate behavior have had

---

Extended author information available on the last page of the article

Published online: 29 October 2023

Springer

considerable alterations in the hydrological system, causing a rise in the intensity and frequency of floods and droughts. As result of the surface water scarcity, aggressive groundwater extraction rates result in stressed aquifers, and loss of storage capacity that may ultimately land subsidence (Herrera-García et al. 2021). Ground subsidence, a natural or human-induced phenomena caused by underground materials movement producing topographic level decrease (e.g., Galloway et al. 1999), generates substantial economic loss in urban areas due to damage to infrastructure and/or increase flooding probability. In human-induced subsidence, surface lowering mainly due to surface loading and extraction of underground fluids and/or solid materials (Galloway et al. 1999) and its velocity can be ten times higher than the natural surface level decrease (Meckel 2008).

Ground-level decrease due to groundwater extraction occurs as a response to the reduction in pore water stress and the resulting increase in effective pressure, generating compaction of unconsolidated sediments (Carrillo 1948). The physical behavior of land subsidence may be controlled by subsoil composition and stress history, which can have an elastic or inelastic response (Terzaghi 1925). The elastic deformation occurs when the preconsolidation stress in the aquifer system is not exceeded. The preconsolidation stress is the maximum vertical effective stress that the subsoil has suffered due to its own weight or external loading (Casagrande 1936). The preconsolidation stress is influenced by several factors such as environmental conditions, hydrology, secondary compression, chemical alteration, variation in overburden pressure, sedimentation rate, sediment age, and tectonic conditions (e.g., Brumund et al. 1976). Small displacements on the surface characterize the elastic deformation, the deformation is recoverable, and it can have seasonal behavior depending on the water table fluctuations (e.g., Galloway et al. 1999). In contrast, in the inelastic deformation, the aquitard skeleton may suffer significant and permanent reorganization and occurs when the load exceeds the preconsolidation stress. In the inelastic deformation, pore fluids move into the aquifers; as a result, pore volume irreversibly decreases (e.g., Galloway et al. 1999). Inelastic land subsidence can produce very fast land subsidence rates (e.g., Chaussard et al. 2014). In this case, the ground subsidence process has important consequences as aquifer storage capacity severely decreases, eventually restricting the long-term viability of urban areas that depend on aquifers/aquitards for their water supply.

InSAR techniques have been satisfactorily applied to detect land subsidence in many cities worldwide (e.g., Raspini et al. 2022), and the land movement precision measurement mainly depends on the decorrelation of the SAR signal, phase unwrapping errors, and atmospheric delays. To overcome errors related to SAR signal decorrelation, two families of InSAR time series techniques were developed, PS and DS. The PS algorithm is based on the phase-stable point scatterers (PS), which mainly correspond to man-made structures and bare rocks surfaces (e.g., Ferretti et al. 2001). The second family is distributed scatterers (DS); these algorithms include areas with decorrelation using a redundant network of interferograms (e.g., Berardino et al. 2002). Several algorithms are available for reducing unwrapping errors, such as the bridging method, phase closures method, coherence-based network to exclude interferograms with coherent phase unwrapping errors, and iterative spatial bridging (Yunjun et al. 2019; Oliver-Cabrera et al. 2022). In the case of tropospheric delay, we can use the empirical relationship between stratified troposphere delay and topography (Doin et al. 2009) or using global atmospheric models, such as ERA-I (Dee et al. 2011). Moreover, in recent years, modern SAR satellites (e.g., PAZ, ALOS-2/PALSAR-2, Sentinel-1), new InSAR process algorithms, and powerful computation resources are available, allowing to measure land surface deformation at a country-level with high accuracy (Manunta et al. 2019; Morishita 2021).

The ESA's Sentinel-1 A and B SAR C-band constellation can accurately measure land movement deformation. These sensors have improved capabilities such as an orbital tube of 200 m, revisit time of 6 days (12 for a single sensor), nearly worldwide coverage, free data policy, the TOPS (Terrain Observations by Progressive Scan) image acquisition mode that allows reaching 250 km of swath width, and a spatial resolution of  $5 \times 20 \text{ m}^2$  (interferometric wide swath mode; Torres et al. 2012). As a result, Sentinel-1 data have been used for a wide spectrum of applications, including mapping of natural hazards, monitoring of glacier flows, and surveillance of ship routes (Torres et al. 2012). In addition, Sentinel-1 C-band sensors provide data time continuity with previous C-band SAR sensors (i.e., Envisat and ERS missions), making possible to generate InSAR long time series deformation assessment which can include several decades (e.g., Chaussard et al. 2021). Therefore, several studies have used Sentinel-1 data to monitor land movement on a regional scale (e.g., Crosetto et al. 2020). However, a few country-scale studies measure land subsidence occurrence and their spatial patterns, magnitudes, urban areas, population, and households exposed to ground subsidence.

This work is aimed at providing a country-scale assessment of urban areas, population, and households exposed to land subsidence and how they can be grouped into land subsidence regions. Relationships were evaluated between conditional factors (e.g., lithology and groundwater health) and urban areas with land subsidence. Finally, we also provide an extensive quality assessment by comparing InSAR time series and permanent GPS stations.

## 2 Study area

The main factors that increase the potential of land subsidence due groundwater extraction in Mexico are the spatial distribution of compressible deposits and population density (e.g., Chaussard et al. 2014). As a result, we used the information of the spatial distribution of unconsolidated deposits (Fig. 1a, modified from SGM 1998), the distribution of urban areas (Fig. 1b, modified from INEGI 2020), and groundwater condition (Fig. 1c, d, modified from CONAGUA 2020) to define the potential area to land subsidence.

Mexico lacks cartographic products with thickness, compressibility index, and porosity values of unconsolidated sediments. Consequently, we used a criterion based on surface lithology with the potential to develop land subsidence. This criterion assumes that unconsolidated surface lithology poses high compressibility and porosity values; therefore, there is a high potential for land subsidence velocity (Chaussard et al. 2014). Under this broad category of compressible-unconsolidated deposits, we grouped all alluvial, lacustrine, colluvial, eolian, littoral, and palustrine lithologies from the *Servicio Geológico Mexicano* cartographic database (SGM 1998). Figure 1a shows the spatial distribution of unconsolidated deposits with high compressibility and porosity potential. This figure also shows that unconsolidated-compressible deposits are present in well-defined regions that include a central east–west region, a central north–south and the coastal plains in the Gulf of Mexico, northwestern Mexico, and portions of the Baja California Peninsula (Fig. 1a). In the first two areas, the extensional Cenozoic stress regime favored developing of grabens that promoted the accumulation of unconsolidated-compressible materials (e.g., Henry and Aranda-Gomez 1992; García-Palomo et al. 2000; Nieto-Samaniego et al. 2005).

In Mexico, 79% of the total population live in urban areas (INEGI 2020); moreover, land subsidence is a significant problem in affected urban localities because of the resulting damage to buildings and urban infrastructure. Therefore, in this study, we used the spatial



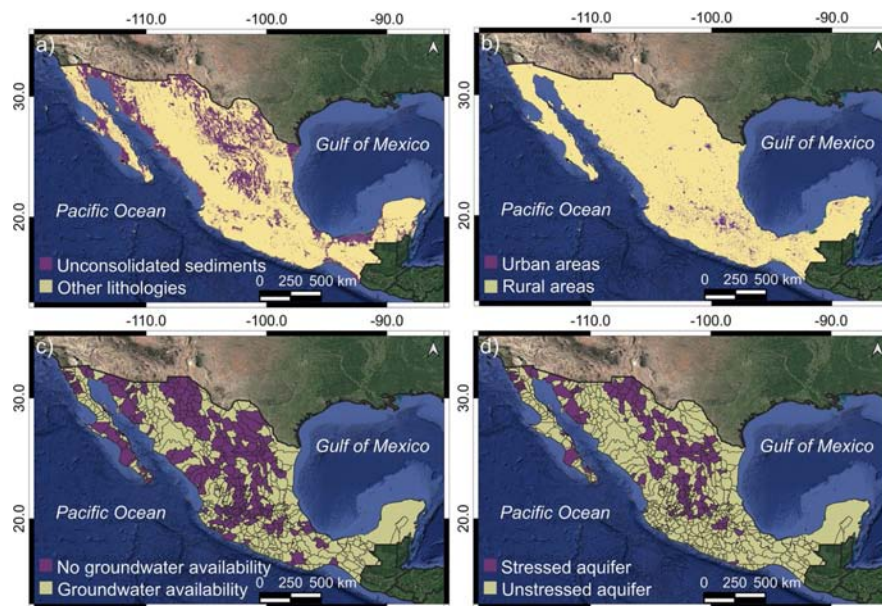


**Fig. 1** Spatial distribution of factors that define urban areas with land subsidence. **a** Distribution of unconsolidated deposits based on (SGM 1998). **b** Urban AGEBs of Mexico (modified from INEGI 2020). **c** Groundwater availability. **d** Groundwater stress. (Modified from CONAGUA 2020). Google Earth imagery was used as the base map in Figs. 1, 3, 4, 5, and 7, and QGIS 3.22 software to compose the maps (<https://www.qgis.org/es/site/>)

distribution of urban *Áreas Geoestadísticas Básicas* (AGEBs) shapefiles from the 2020 Housing and Population Census (INEGI 2020), as an area of interest. The urban AGEBs are composed of street blocks (usually ~1–50) that are grouped in geographically delimited polygons (INEGI 2020; Figs. 1b, 4b) to optimize the nation-wide statistical analysis. Consequently, the higher the density of urban AGEB, the higher the groundwater extraction to cover the population needs. The AGEB spatial distribution shows that most of the urban areas are located in central Mexico along an east–west corridor that coincides with the Mexican Volcanic Belt (Figs. 1b, 4b); subsequently, this area of Mexico has the highest potential to develop land subsidence (Chaussard et al. 2014). However, there are also urban areas that spatially overlap with compressible-unconsolidated deposits, such as the central plateau in northern Mexico and along the northwestern Mexico and Gulf of Mexico coastal areas (Fig. 1a, b).

For the distribution of groundwater, we used the *Comisión Nacional del Agua* groundwater availability and stress map (Fig. 1c, d; CONAGUA 2020). CONAGUA analysis indicates that 205 out of 653 of Mexico's aquifers have no additional groundwater availability (Fig. 1c). Meanwhile, 105 out of 653 of Mexico's aquifers have an extraction rate exceeding their natural recharge (CONAGUA 2020, Fig. 1d). Only southeastern Mexico has both groundwater availability and unstressed aquifers (Fig. 1c, d). The region east of the Tehuantepec isthmus currently has a low potential of developing land subsidence associated with groundwater extraction and thus was not considered in our current analysis (Fig. 3). Nevertheless, there are reports of ground subsidence due to hydrocarbon

extraction in Villahermosa, Tabasco, in southeastern Mexico (Pérez-Falls and Martínez-Flores 2020) although they are spatially restricted.

Previous research on subsidence by groundwater withdrawal only covered the east–west central Mexico and Cerro Prieto regions [initially described by Carnec and Fabriol (1999), Cabral-Cano et al. (2008), Chaussard et al. (2014)] but at the same time still missing its reconnaissance over broad regions of Mexico with high potential for land subsidence. In consequence, in this research, we evaluated the land subsidence in urban areas located over the intersection of high compressible deposits with stressed aquifers and no additional groundwater available, thus covering large areas of the country that have not been previously analyzed for subsidence.

### 3 Methodology

To estimate the urban areas exposed to land subsidence in Mexico, we first narrow the area of interest using the spatial distribution of aquifer health (potential urban areas land subsidence; see Sect. 2). We then performed an InSAR analysis to systematically identify and characterize velocity fields and InSAR time series. Subsequently, we applied a temporal coherence mask for quality control, and then thresholds for velocity and slope were utilized. We also overlapped the urban AGEB regions with the InSAR velocity field to find the urban localities with land subsidence which were classified according to their spatial distribution using the Gaussian mixture algorithm (Fig. 2). Then, we analyzed relationships between urban areas with land subsidence and conditional factors (i.e., lithology, aquifer condition, land subsidence causes; Fig. 2). Finally, we compared InSAR and GPS time series velocities to calibrate the accuracy of our results (Fig. 2; calibration).

#### 3.1 SAR dataset and InSAR processing

The Synthetic Aperture Radar (SAR) data consists of 4,611 Single Look Complex (SLC) scenes acquired by the Sentinel-1 A/B sensors. The SAR SLC images were obtained from September 1, 2018, to October 30, 2019, along 12 descending orbits (Fig. 3; Table 1) and covering 1.7 million km<sup>2</sup> (Fig. 4a, b). The SAR scenes were processed with interferometric networks of three connections using the Small Baseline Subset algorithm (Berardino et al. 2002). The InSAR processing was carried out with a multilooking of 20 by 60 looks in azimuth and range orientations, resulting in a size of  $\sim 300 \times 300$  m<sup>2</sup>. We used SBAS (DS) algorithm because it used an interferometric network with a small spatial and temporal baseline reaching a higher spatial coverage than PS algorithms and allowing to measure land deformation with millimetric precision over thousands of square kilometers (i.e., regional studies, e.g., Manunta et al. 2019; Morishita 2021). Besides, Sentinel-1 scenes have a small orbital tube (i.e., 200 m) and high revisit time frequency to reduce spatial decorrelation effects.

To process the SAR acquisitions, we used the JPL/Caltech ISCE software (Rosen et al. 2012), obtaining 4302 unwrapped interferograms, which were then processed using the MintPy (Yunjun et al. 2019) to compute the average velocity and the deformation time series of each pixel. In this InSAR processing we also applied the network-based enhanced spectral diversity (NESD; Fattahi et al. 2017) and the empirical correlation between troposphere and topography (Doin et al. 2009), for a precise interferogram co-registration and corrected tropospheric errors, respectively. The noisy scenes were estimated using the

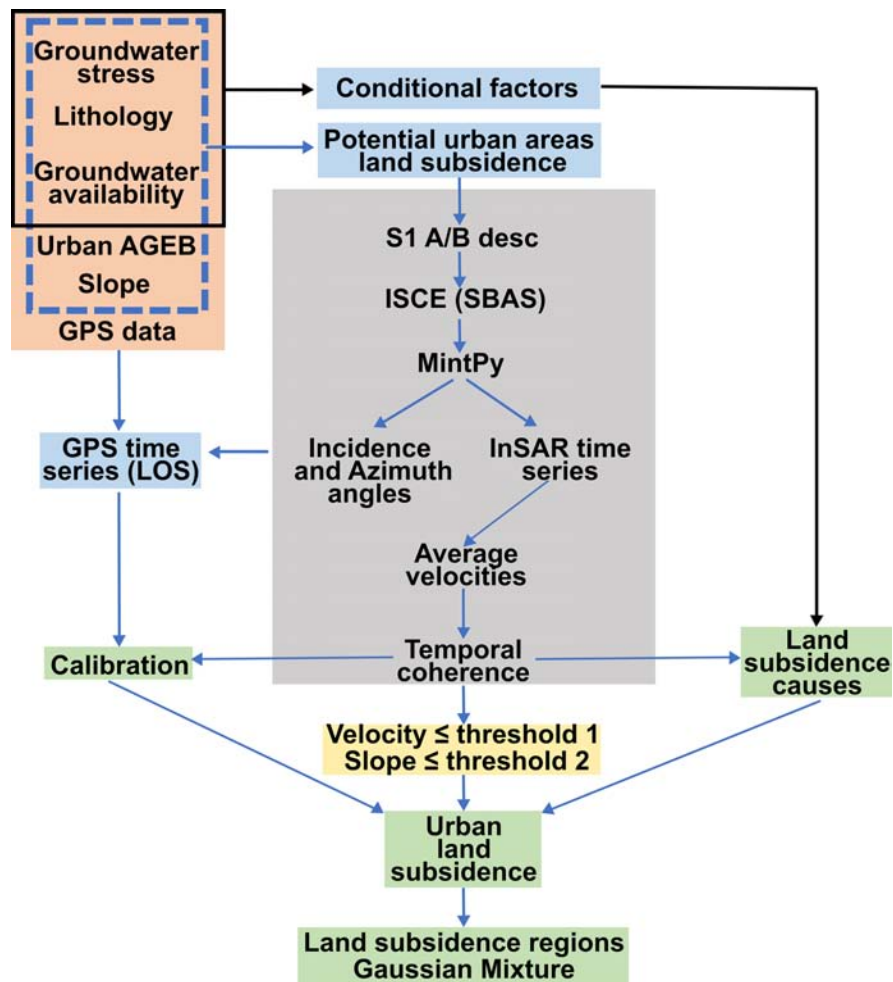


**Fig. 2** Workflow to detect urban areas with land subsidence. Orange polygon represents input data. Light blue polygons are intermediate products. InSAR-SBAS methodology is inside gray polygon. Yellow polygon has the velocity and slope thresholds 1 and 2, respectively. Light green polygons are final products

root-mean-square (RMS) approach from Yunjun et al. (2019) and a temporal coherence mask of 0.7 was implemented to keep only high-quality pixels (Pepe and Lanari 2006).

To compare our results with previous research and considering that in Mexico most of the cGPS the vertical displacement component is higher than the horizontal components (e.g., Blewitt et al. 2018; Cabral-Cano et al. 2018), the resulting InSAR average velocities maps were projected from LOS deformation ( $d_{los}$ ) into vertical deformations ( $d_v$ ) using the incidence angle of the sensors  $\theta$  ( $d_v = d_{los} / \cos \theta$ ), assuming that there is no lateral displacement. We also processed a longer InSAR time series (January 2018–June 2021) in some places with remarkable land subsidence velocities (i.e., Mexico City Metropolitan Area, Jocotepec Jalisco, Torreón Coahuila, and Chaparroza Zacatecas; Supplementary file 1) to compare with the one-year observation velocities used for the entire country. These

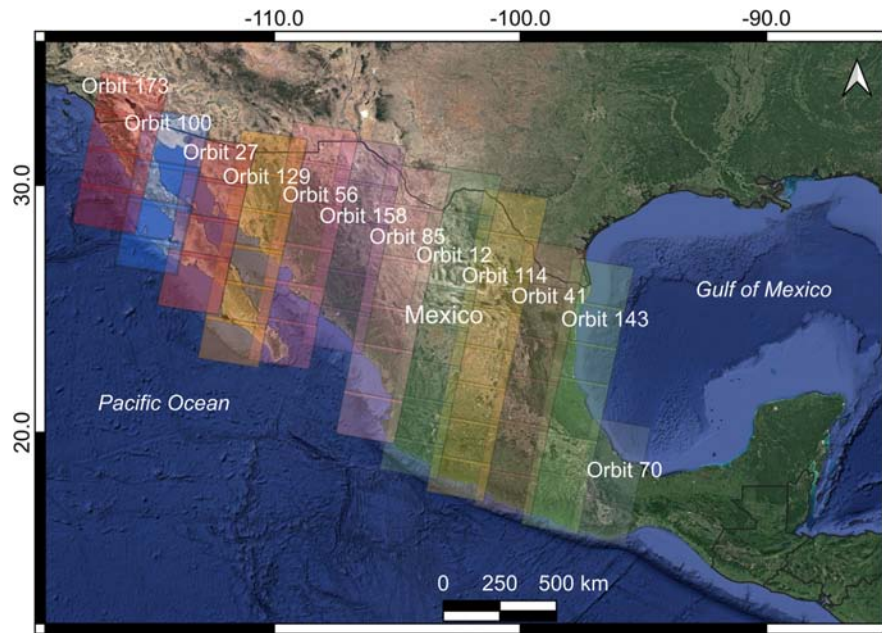


**Fig. 3** Relative orbits that cover the subsiding areas of interest in descending path from Sentinel-1

**Table 1** Relative orbits, observation periods, and number of dates used in this study

Relative orbit	Date (yyyymmdd) Start–End	# SLC	# IFG
173	20180902–20191027	123	116
100	20180909–20191022	245	198
27	20181115–20191029	105	78
129	20180911–20191024	385	396
56	20180906–20191019	392	396
158	20180901–20191026	403	408
85	20180908–20191021	344	276
12	20180903–20191028	539	405
114	20180910–20191023	455	396
41	20180905–20191030	661	699
143	20180906–20191025	543	480
70	20180901–20191026	416	454
Total		4611	4302

more extended InSAR time series were obtained using 1020 Sentinel-1 A/B SLC scenes acquired in descending relative orbits (i.e., 41, 114, and 12). The Sentinel-1 A/B SLC January 2018–June 2021 scenes were processed with the same methodology applied to process the smaller InSAR time series (i.e., September 2018–October 2019).

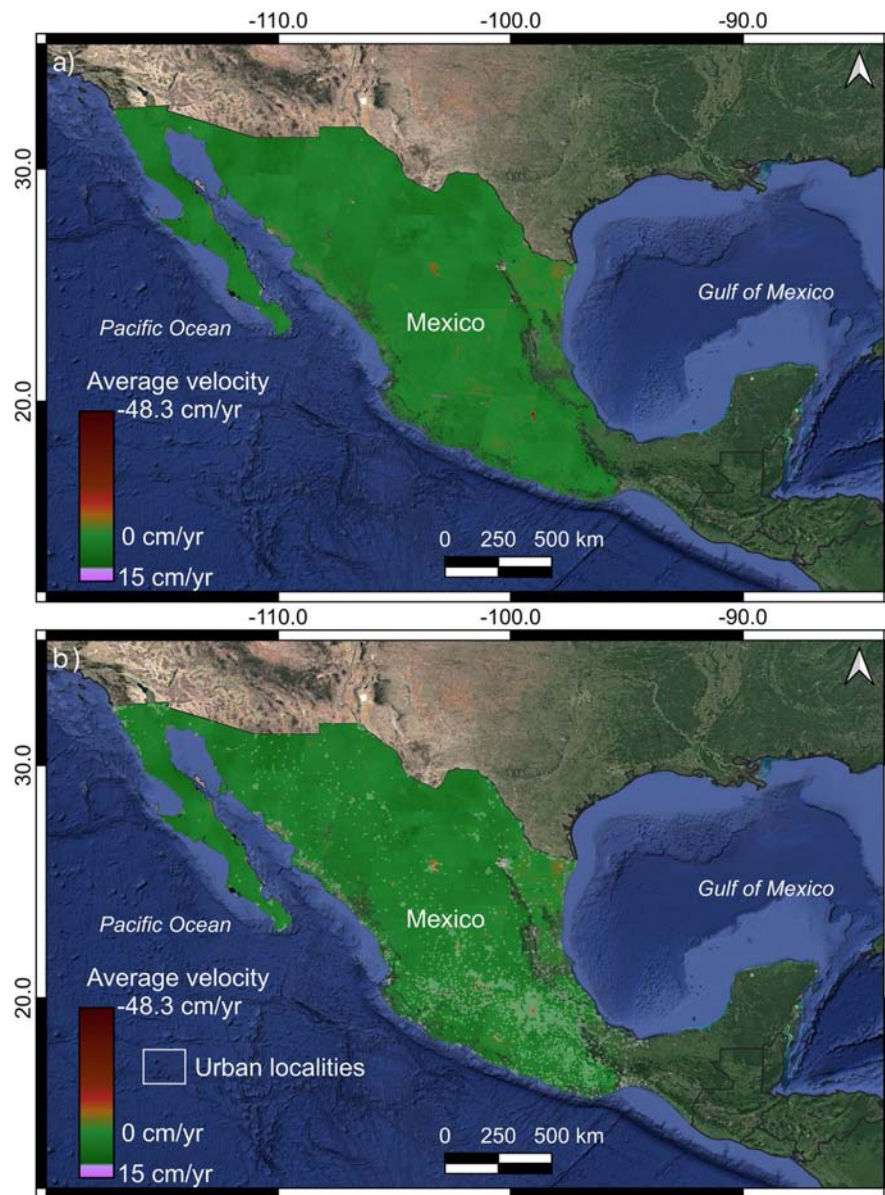


**Fig. 4** Velocity maps and urban AGBEB of Mexico. **a** Mosaic map of ground subsidence associated with groundwater extraction in Mexico. **b** Average velocity map mosaic with the urban localities' polygons superimposed

Due to the size of the data and computer requirements, the InSAR processing of the entire country was divided into forty sub-areas and was performed at a supercomputing facility. We required 19 TB for SAR scenes FTP downloads, 108.1 TB to generate

unwrapped interferograms, and 0.1 TB for velocity maps and time series generation (Table 2).

### 3.2 Urban areas exposed to land subsidence and classification of land subsidence regions

To identify urban areas exposed to land subsidence, we overlapped urban AGEBS polygons over the InSAR velocity map (Fig. 4a, b). AGEBS provide the basic unitary information from the INEGI's national Housing and Population 2020 census, available at street-block scale and with multiple parameters such as population, number of households, total area, states, municipalities, urban localities, and others which can be grouped as urban localities (Fig. 4b). Then, we identify all AGEBS with a maximum subsidence velocity faster than or equal to  $-2.8$  cm/year.

The velocity threshold is based on the value of 1.5 standard deviations (SD) of velocity pixels of the study area (1.7 million km<sup>2</sup>), following previously defined criteria which pointed out that the SD of velocity is an indicator of the level of noise (e.g., Tomás et al. 2019). Moreover, using a relatively high threshold prevents overestimating the total urban areas exposed to land subsidence. The second threshold, slope values lower than 5 degrees, was used considering that land subsidence occurs where the negative vertical velocity overcomes horizontal rates and over very flat topography (e.g., Tomás et al. 2019).

In the next step, AGEBS of the same states and municipalities were grouped using INEGI's polygons of urban localities (INEGI 2020). The urban localities were grouped following similar velocity categories used by Chaussard et al. (2014). These categories are low [ $-2.8$  to  $-5$  cm/year], intermediate ( $-5$  to  $-10$ ] cm/year, and high with a subsidence rate faster than  $-10$  cm/year. Next, we measured the areas, population, and households between each category and identified the latitude and longitude of the polygon's centroid of the AGEBS with maximum average subsidence velocity (Supplementary file 2).

The Gaussian mixture model (GMM) was then used to spatially classify urban areas undergoing land subsidence. This probabilistic approach can be implemented as an unsupervised machine learning technique. For the GMM classification, we employed the Scikit-learn machine learning library (Pedregosa et al. 2011). We implemented the GMM over the spatial distribution of land subsidence urban location polygon centroids to group them into clusters ( $k$ ). To determine the optimal number of  $k$ , we applied the Bayesian information criterion (BIC) over a different number of clusters to find the number of  $k$  that minimizes the theoretical information criterion. In other words, the number of  $k$  that better fits our data. We also determined the best value of the covariance type hyperparameter according to the spatial distribution of the data. Our best model parameters (i.e.,  $k$  and covariance type) were then used to fit the GMM to our data (i.e., the latitude and longitude values of land subsidence urban location centroids).

**Table 2** Supercomputing resources

Parameter	Total storage (TB)	Time (hh:mm)
FTP SLCs	19	57:20
ISCE	108.1	284:01
Mintpy	0.1	07:45
Total	127.2	347:10

and obtained each cluster parameters including weights, means, and covariance matrices of each  $K$ . Finally, to identify the relationship between urban areas with land subsidence and conditional factors (Fig. 2), we created an intersection table between urban localities with land subsidence and aquifer units (CONAGUA 2020) and lithology (SGM 1998) (Supplementary file 2).

### 3.3 Calibration

The area of interest was divided into forty sub-areas and where there is at least one continuous GPS station that presents a null vertical velocity that is used as reference points in 34 out of 40 InSAR-processed Sentinel-1 relative orbit zones (Figs. 3, 5). In those six cases where there are no continuous GPS permanent stations available inside the area, we assigned the reference point in a coherence pixel located on a rock outcrop (and presumably) a stable, non-subsiding area.

To investigate the accuracy of the generated InSAR time series, we compared the InSAR time series results with those from 100 continuous GPS stations that include all the TLALOCNet GPS stations (Cabral-Cano et al. 2018) and other time series solutions available at the Nevada Geodetic Laboratory (Blewitt et al. 2018). In this comparison, we considered the following:

1. We used those continuous GPS stations with an average time overlap of 1.03 years with the InSAR time series (see Supplementary file 3).

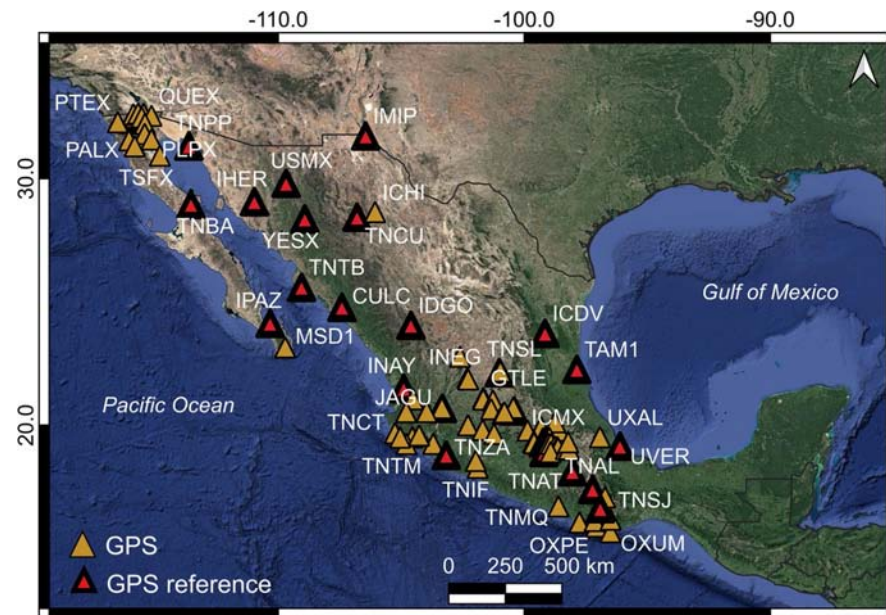


**Fig. 5** Location map of the 100 continuous GPS stations that include all the TLALOCNet GPS stations (Cabral-Cano et al. 2018) and other time series solution available at the Nevada Geodetic Laboratory (Blewitt et al. 2018) used for calibration and accuracy assessment of the InSAR velocities

2. GPS coordinate components time series (i.e., north–south, west–east, and vertical) were projected into line-of-sight direction by considering the InSAR-processed based incidence and azimuthal angles at each GPS's position (e.g., Catalao et al. 2011).
3. For both continuous GPS and InSAR time series, the average velocity was computed using a linear regression analysis using the time window of InSAR data (September 2018 to October 2019).
4. GPS measurements were assumed as reference.
5. GPS stations are those located in InSAR velocity coherence pixels.

To assess the accuracy, we calculated the difference between cGPS and InSAR time series velocities and measured the correlation between InSAR and GPS velocities (Fig. 11; Table 5).

## 4 Results

### 4.1 Spatial pattern and time series of land subsidence

The average velocity map mosaic is presented as a vertical component in Fig. 4a. This map displays only pixels with temporal coherence higher than 0.7 providing the time series of 188.8 million coherence pixels and covering an area of about 1.7 million km<sup>2</sup>. Pixels with red colors represent the areas with higher displacement away from the satellite (e.g., subsidence), pixels with green colors velocity represent areas with lower and null displacement away from the satellite, and areas with purple color show areas with movement toward the satellite (e.g., uplift).

In Fig. 4b, we can observe that urban areas with land subsidence below  $-2.8$  cm/year are along a central east–west region, a central north–south, along the coastal plains in the Gulf of Mexico, northwestern Mexico, and portions of the Baja California Peninsula. One of the most evident areas is the well-documented case of Mexico City (e.g., Solano-Rojas et al. 2020; Chaussard et al. 2021; Fernández-Torres et al. 2022), although some other prominent large areas either with a large subsidence footprint and/or with very fast rates are present (e.g., Sarychikhina et al. 2011; Chaussard et al. 2014).

### 4.2 Urban localities with land subsidence and land subsidence regions

The distribution of maximum subsidence velocity per urban localities (presented in Fig. 6a) indicates that 3149 urban localities are subsiding, and 75% of the urban localities have a subsidence velocity faster than  $-0.9$  cm/year and mean and median velocity values of  $-2.7$  cm/year and  $-1.9$  cm/year, respectively (Table 3). Additionally, the fastest land subsidence recorded in an urban area is  $-42.8$  cm/year at Ciudad Nezahualcoyotl, which is part of the Mexico City Metropolitan Area (Fig. 6a; Table 3). Nevertheless, the maximum land subsidence velocity recorded in Mexico is  $-48.3$  cm/year in the northeast sector of the Mexico City Metropolitan Area in a not urbanized area within the Ciudad Nezahualcoyotl municipality (Fig. 4a, b).

However, to better compare our results with previous regional observations and to keep low level of noise, we only consider those urban areas with land subsidence velocity faster than  $-2.8$  cm/year and slope lower than 5 degrees. We detected 853 urban localities within this subsidence velocity and slope thresholds (Figs. 6b, 7; Supplementary file



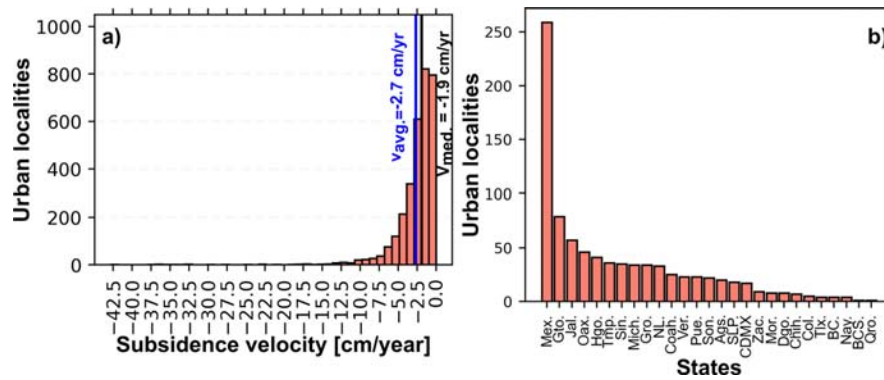


**Fig. 6** Number of urban localities according to velocities and states. **a** Analysis of maximum subsidence velocity observed in urban localities located inside potential areas with land subsidence in Mexico in 2018–2019. **b** The number of urban localities per state with land subsidence faster than  $-2.8$  cm/year and slope lower than 5 degrees

**Table 3** Basic statistics of maximum subsidence velocity observed in urban localities located inside of potential areas with land subsidence in Mexico in 2018–2019

Parameter	Value
Count	3.149
Mean	$-2.7$ cm/year
Standard deviation	$3.4$ cm/year
Minimum	$-42.8$ cm/year
25%	$-3.3$ cm/year
50%	$-1.9$ cm/year
75%	$-0.9$ cm/year

2). As a result, the State of Mexico (Mex.) has the highest number of urban localities with ground subsidence rates faster than  $-2.8$  cm/year, representing 30.3% of the total localities detected (Fig. 6b). We divided urban localities undergoing subsidence into three categories: (a) low  $-2.8$  to  $-5$  cm/year, (b) intermediate  $-5$  to  $-10$  cm/year, and (c) high faster than  $-10$  cm/year. The highest number of localities and the highest magnitude of subsidence are located within the Mexican Volcanic Belt (MVB; Fig. 7). This geological province has 59.3% of the total number of urban localities undergoing land subsidence. In the Mexican Volcanic Belt, numerous urban areas have developed over flat surfaces, which are, in most cases, the surface expression of endorheic basins or tectonic valleys (grabens and semi-grabens) filled with variable thickness, compressible lacustrine and fluvial sediments interbedded with pyroclasts and lava flows within an extensional tectonic regime (e.g., García-Palomo et al. 2000; Carreón-Freyre and Cerca 2006). The MVB presents compressible deposits that can reach hundreds of meters in thickness which spatially correspond with the higher recorded velocities rates (e.g., Chaussard et al. 2021). In addition, the geomechanical properties of silt and clay compressible deposits indicate low shear strength, variable compression index, and water content that can reach 300%, which promotes the ground subsidence process (e.g., Marsal et al. 2016). The MVB also has the 23.5% of aquifers under stress, in part because this region of Mexico has 90% of irrigated

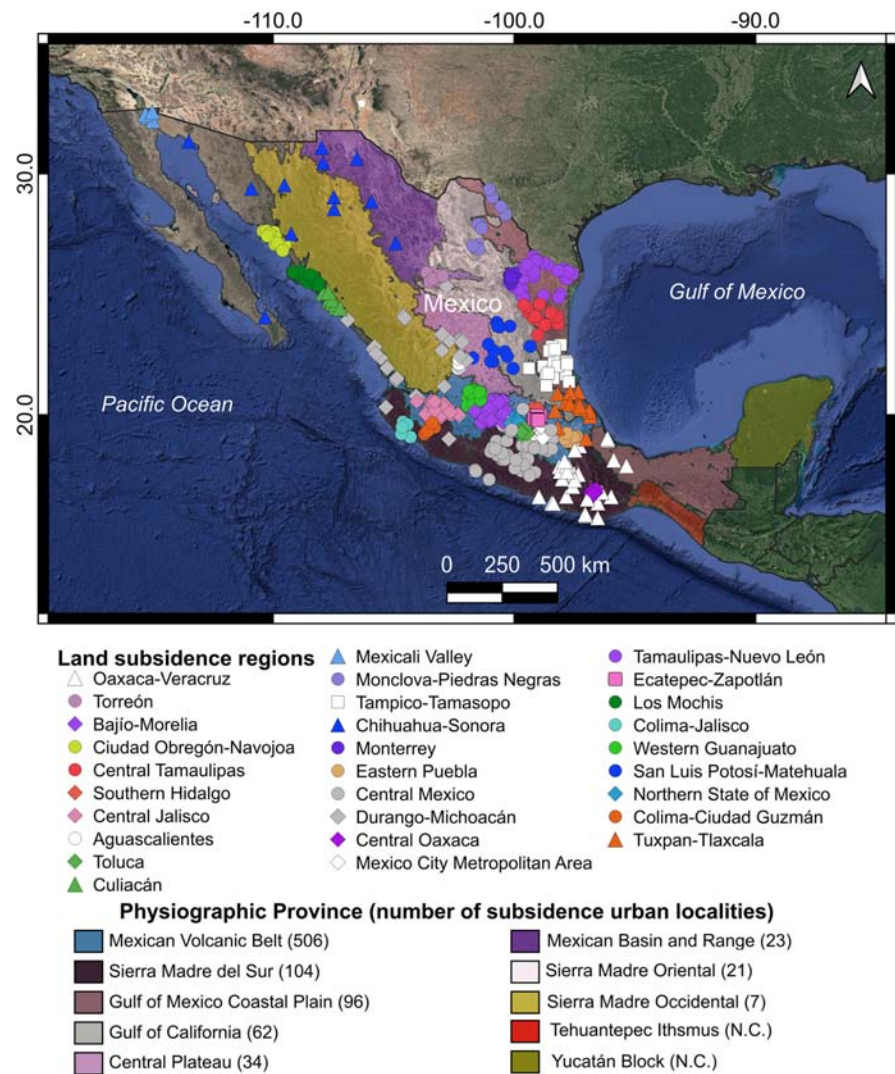


**Fig. 7** Map of urban localities undergoing land subsidence grouped by regions. Colored polygons are Mexico's physiographic provinces. N.C., not considered

agricultural areas and 76% of Mexico's population; however, this region only receives 20% of Mexico's total rain precipitation. (Hernandez 2003). This largely populated region has undergone a rapid development period in the past 40 years and thus groundwater use, and large subsidence velocities.

According to our observations, 27 out of 32 states in Mexico have urban areas with velocities faster or equal to  $-2.8$  cm/year over slope lower than 5 degrees (Figs. 6b, 8). As a result, the country has a total area of 3797 km<sup>2</sup> exposed to subsidence (Fig. 8d), where the State of Mexico (Mex.) and Mexico City (CDMX) comprise 53.3% of this subsiding

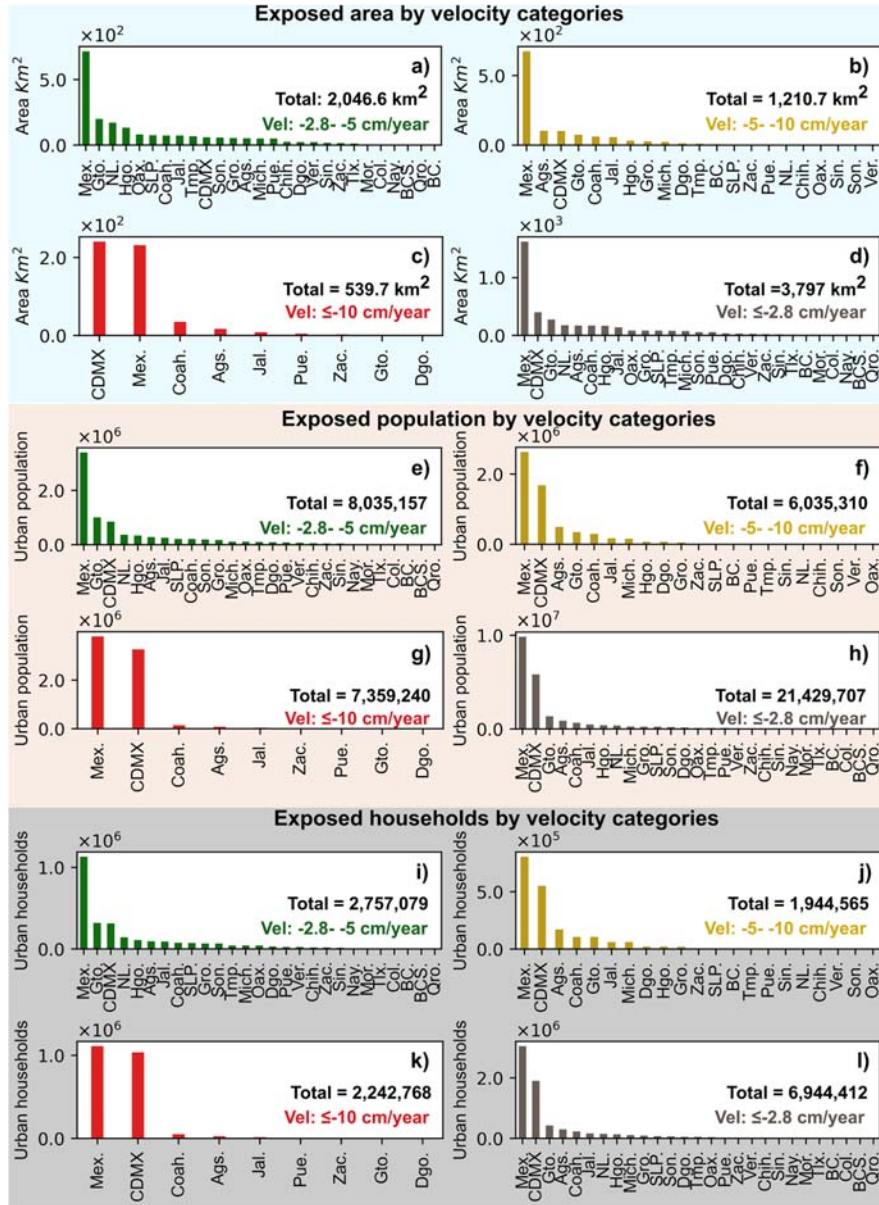


**Fig. 8** Total area, population and households exposed to land subsidence ( $\leq -2.8$  cm/year) and slope lower than 5 degrees in Mexico

area (Fig. 8d). Due to high population density in this area, 21.4 million people (Fig. 8h) or 17% of the country’s total population in 2020 (INEGI 2020) live in areas exposed to land subsidence faster than  $-2.8$  cm/year. This population spread throughout 6,944,412 households (Fig. 8l).

The  $-2.8$  to  $-5$  cm/year subsidence velocity interval has a total area of  $2046.6$  km<sup>2</sup> with a population of  $8,035,157$ , and  $2,757,079$  households within it (Fig. 8a, e, i respectively). If we consider the subsidence velocity between  $-5$  and  $-10$  cm/year, its exposed urban area, population, and households are  $1210.7$  km<sup>2</sup>,  $6,035,310$ , and  $1,944,585$ , respectively (Fig. 8b, f, j, respectively). The fastest land subsidence interval ( $\leq -10$  cm/year) has a total area of  $539.7$  km<sup>2</sup>, exposing  $7,359,240$  people and  $2,242,768$  households (Fig. 8c, g, k, respectively) to ground subsidence.

All urban subsiding locations were be grouped into 29 regions (see Fig. 7 and Table 4). Nine of these ground subsidence regions are located within the Mexican Volcanic Belt geologic province (Bajío-Morelia, Southern Hidalgo, Central Jalisco, Toluca, Eastern Puebla, Mexico City Metropolitan Area, Ecatepec-Zapotlán, Western Guanajuato, Northern State of Mexico) and five additional regions are partly located in this physiographic province (Oaxaca-Veracruz, Central Mexico, Durango-Michoacán, Colima-Ciudad Guzman, Tuxpan-Tlaxcala). Consequently, the Mexican Volcanic Belt geologic province has the highest number of land subsidence clusters (Fig. 7). The number of urban localities per land subsidence region ranges from 92 (in Toluca) to 5 (Mexicali Valley) (Table 4). The maximum subsidence velocity found was  $-42.8$  cm/year located in the Mexico City Metropolitan Area (MCMA). The MCMA land subsidence region has the highest urban area ( $781.3$  km<sup>2</sup>), population ( $11,141,364$ ), and households ( $3,501,957$ ) with exposure to land subsidence (see Fig. 7 and Table 4).

### 4.3 Relationship between land subsidence and conditional factors

We evaluated the relationship between land subsidence and three variables that generate favorable conditions for land subsidence development associated with groundwater extraction. These variables are lithology, groundwater availability, and aquifer stress (Fig. 9).

To evaluate groundwater depletion's influence over land subsidence in urban areas, we considered groundwater availability and whether the aquifers were stressed. These variables showed that  $76.9\%$  and  $65.9\%$  of the urban areas with velocities faster than  $-2.8$  cm/year and slope lower than  $5$  degrees have no groundwater availability and an underlying stressed aquifer, respectively (Fig. 9). As a result, land subsidence generally occurred in water-stressed basins, where groundwater withdrawal rate is higher than the natural recharge.

Our results show that  $73.9\%$  ( $\sim 2919.9$  km<sup>2</sup>) of the urban areas with land subsidence are developed over unconsolidated sediments,  $8.5\%$  of the urban areas developed over sandstones-polygenic conglomerate (SPC),  $1.9\%$  are over andesitic-basalt (AB),  $1.9\%$  in rhyolitic tuff (RT),  $1.7\%$  are over polygenic conglomerate, and  $12.1\%$  over other lithologies (e.g., andesitic tuff, shale, limestones, among others). These results indicate that most exposed urban areas are located over unconsolidated sediments, although we also notice a large lithological heterogeneity (see Fig. 9).

### 4.4 InSAR and GPS comparison

InSAR and GPS time series velocities (LOS) comparisons were carried out to assess the accuracy of our InSAR results. These comparisons are shown in Fig. 10, and the Supplementary material (Supplementary file 4). In this analysis, we used 100 permanent GPS stations located on high coherence pixels (temporal coherence  $> 0.7$ ) (Figs. 5, 10; Supplementary file 3, Supplementary file 4, and Supplementary file 5). Furthermore, due to the

**Table 4** Urban regions with urban land subsidence in Mexico and their total area, population, households, and maximum subsidence velocity

ID	Region name	# Urban localities	Velocity $\leq -2.8$ cm/year			Maximum subsidence velocity cm/year
			Urban area (km <sup>2</sup> )	Population	Households	
0	Oaxaca-Veracruz	29	34.3	40.637	16.244	-5.3
1	Torreón	18	178.3	784.736	272.697	-14.3
2	Bajío-Morelia	66	151.6	539.216	196.529	-12.7
3	Ciudad Obregón-Navojoa	17	52.4	184.823	64.076	-5.9
4	Central Tamaulipas	13	21.8	26.209	11.415	-5.5
5	Southern Hidalgo	35	157	392.795	124.986	-9.9
6	Central Jalisco	47	133.5	411.005	148.692	-16.5
7	Aguascalientes	20	171.5	865.082	291.471	-11.1
8	Toluca	92	624.9	2.186.719	662.530	-11.6
9	Culiacán	12	7.9	18.766	4.967	-3.9
10	Mexicali Valley	5	7.5	9.762	3.734	-9.1
11	Monclova-Piedras Negras	12	24	17.971	6.847	-5
12	Tampico-Tamasopo	19	32.1	70.219	26.251	-6.4
13	Chihuahua-Sonora	12	35.9	64.539	24.213	-7
14	Monterrey	18	115.1	281.102	108.056	-3.9
15	Eastern Puebla	17	51.9	82.881	25.026	-14.3
16	Central Mexico	58	117.3	294.503	110.672	-7.9
17	Durango-Michoacán	27	58.1	249.477	90.655	-19.3
18	Central Oaxaca	24	56.9	82.652	31.440	-4.8
19	Mexico City Metropolitan Area	65	781.3	11.141.364	3.501.957	-42.8
20	Tamaulipas-Nuevo León	31	96.3	130.892	55.710	-6.7
21	Ecatepec-Zapotlán	78	321.2	1.846.946	649.590	-12.9
22	Los Mochis	19	8.3	23.286	7.166	-5.2
23	Colima-Jalisco	7	2.8	6.802	2.683	-4.2
24	Western Guanajuato	32	151.5	890.096	265.169	-9.2
25	San Luis Potosí-Matehuala	13	73.5	214.330	73.154	-6.5
26	Northern State of Mexico	41	296.1	469.884	134.124	-6.6
27	Colima-Ciudad Guzmán	10	17.3	66.635	22.323	-7.6
28	Tuxpan-Tlaxcala	16	16.4	36.378	12.035	-4.3

overlapping nature between relative orbits of Sentinel-1 (Figs. 3, 11) those 100 GPS locations provide 130 calibration points on the InSAR velocity maps.

InSAR time series accuracy was obtained by computing the differences between InSAR and GPS in LOS velocities (Fig. 11a; Table 5). Our results show that the differences are very close to a normal distribution where mean and median values are  $-1$  mm/year

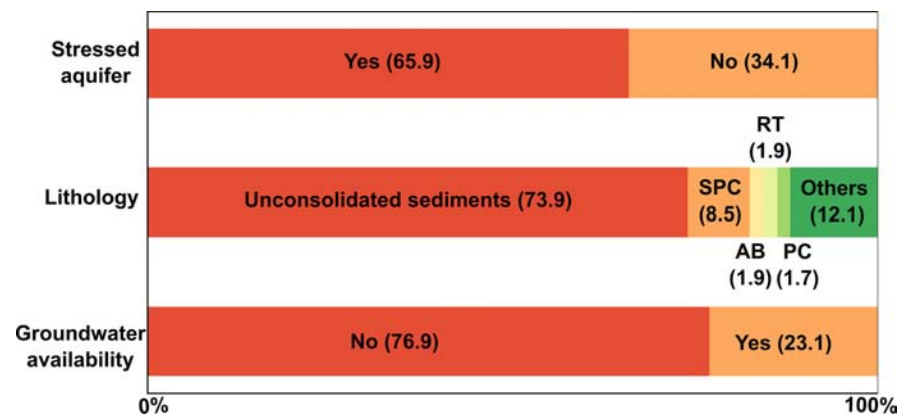


**Fig. 9** Spatial distribution of land subsidence conditional factors. SPC, sandstone-polygenic conglomerate; AB, andesite-basalt; RT, rhyolite tuff; PC, polygenic conglomerate; other lithologies (e.g., andesitic tuff, limestone, shale, among others)

and  $-2$  mm/year, respectively. Thus, most of the velocity differences are near  $0$  cm/year (Table 5). We also found the correlation between GPS (LOS) and InSAR (LOS) velocities shows a coefficient ( $R^2$ ) of  $0.82$  (Fig. 11b), indicating a very high correlation. Besides, using the three GPS components to project into LOS to assess the accuracy of LOS InSAR measurements, as has been previously used elsewhere (e.g., Manunta et al. 2019). Obtaining  $-1$  mm/year in the mean difference velocities suggests that the LOS InSAR measurements are accurate, and GPS horizontal velocity components are negligible; thus, the projection of InSAR LOS as a vertical component is a valid assumption.

## 5 Discussion

We performed a country-wide assessment of areas, population, and households exposed to land subsidence using InSAR-SBAS in Mexico and an extensive comparison between InSAR and GPS velocities to calibrate our results. Our primary objective was to identify urban subsidence; thus, this assessment did not account for all agricultural areas that also undergo subsidence. If we consider a threshold detection limit of  $-2.8$  cm/year and slope lower than  $5$  degrees,  $3797$  km<sup>2</sup> of urbanized areas are affected by land subsidence, and consequently,  $21.4$  million people and  $6.9$  million households are exposed to significant land subsidence. In context, more than  $15.7\%$  out of  $24,227$  km<sup>2</sup> urban AGEB area of Mexico probably exceed the tolerable limits of settlement that a civil structure may undergo under current building codes (e.g., Gaceta Oficial de la Ciudad de México 2017). This result indicates that a considerable proportion of the critical urban infrastructure (e.g., roads, hospitals, schools, surface and underground transportation and underground hydraulic lines, etc.), as well as households, are affected by land subsidence, and therefore a sharp decrease in their useful life is expected with long-term financial consequences. However, building damage severity due to ground subsidence not only depends on a high subsidence rate, but also on the differential settlement, angular distortion, construction quality, foundations type, and other underlying lithological and geomechanical properties (e.g., Peduto et al. 2017).

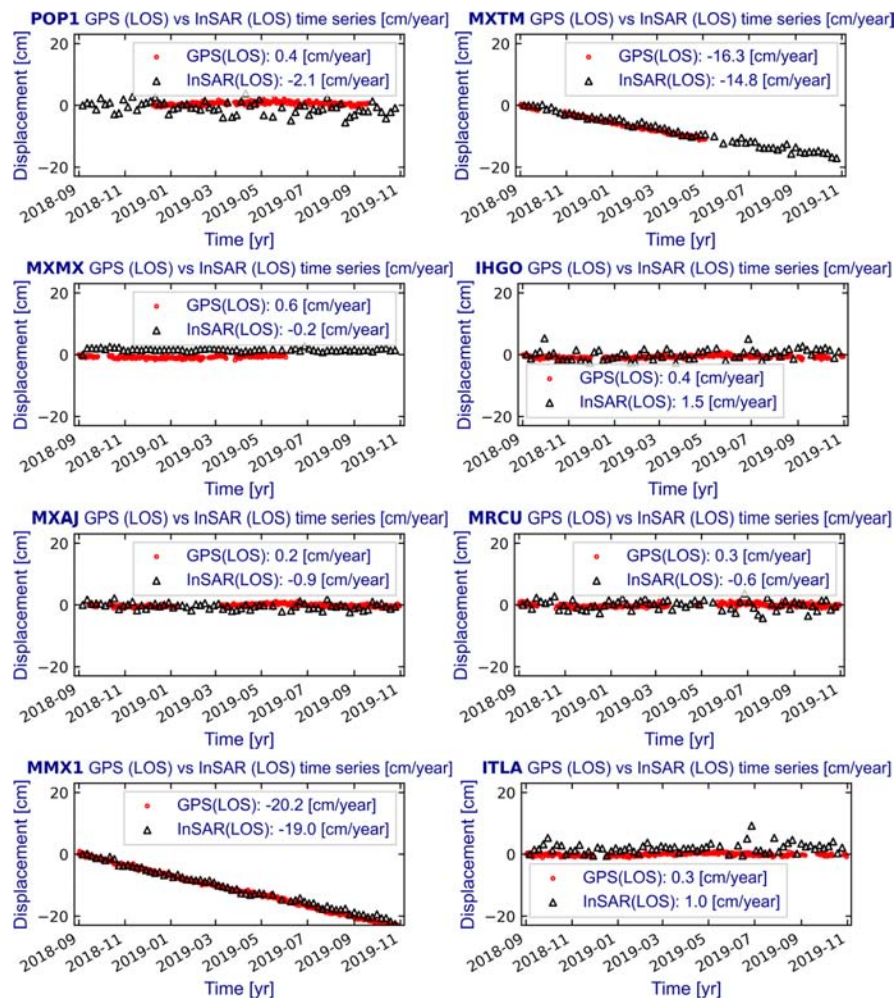


**Fig. 10** Comparison between the InSAR (LOS; black triangles) and the LOS-projected GPS (red dots) surface deformation time series for 14 out of 100 GPS stations identified in Fig. 5

All detected urban areas with ground subsidence faster than  $-2.8$  cm/year were grouped into 29 land subsidence regions, and these are in the central east–west trending Mexican Volcanic Belt, the central highland plateau, along the coastal plains in the Gulf of Mexico, the northwestern Mexico coastal plains, and in some portions of the Baja California Peninsula (Figs. 4, 7 and Table 4). The conditional factors for this spatial pattern are high population density, the prevalence of unconsolidated sediment, and underlying groundwater-stressed basins (Fig. 1). These results bear strong similarities with the Potential Global subsidence map (Herrera-García et al. 2021). However, this map only shows high and very high land subsidence potential in the northwestern portion of the Gulf of Mexico and some small areas inside the central portion of Mexico. Possible reasons for differences between our results and the Herrera-García et al. (2021)

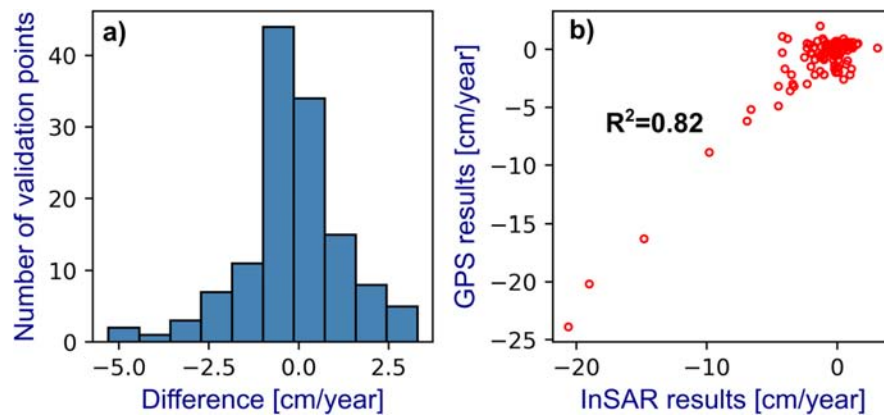


**Fig. 11** Statistics of the differences between InSAR and GPS velocities. **a** Histogram of the velocity's differences between InSAR and GPS. **b** Scatter plot with the correlation among InSAR and GPS velocities

**Table 5** Basic statistics of the differences between InSAR and GPS velocities

Parameter	Value
Count	130
Mean (cm/year)	-0.1
Std. (cm/year)	1.4
Min. (cm/year)	-5.3
25% (cm/year)	-0.8
50% (cm/year)	-0.2
75% (cm/year)	0.6
Max. (cm/year)	3.3

work is their worldwide scope and, consequently, the inherently lower spatial resolution of global datasets used. Nevertheless, there is a general good agreement.

Our land subsidence magnitude observations show that several of the Mexican urban localities fall within the highest ground subsidence rates registered around the world (e.g., Galloway and Burbey 2011) such as Ciudad Nezahualc6yotl, part of the Mexico City metropolitan area [-42.8 cm/year], Chaparrosa, Zacatecas [-19.3 cm/year], Jocotepec, Jalisco [-16.5 cm/year], La Partida, Coahuila [-14.3 cm/year], La Purisima, Puebla [-14.3 cm/year], Santa Rosa, Guanajuato [-12.7 cm/year] (Supplementary file 1).

Spatial pattern and subsidence rates evolution can be evaluated by comparing our results with previously reported subsidence areas (e.g., the east–west central Mexico and Cerro Prieto regions; see Supplementary file 6 for details) and evaluation of the spatial distribution and velocity rate consistency throughout a longer time span (Supplementary file 1). For most of all the previously recognized subsiding areas, we observe very similar magnitudes and overall spatial distribution (Supplementary file 6). The subsidence rates and spatial consistency indicate that most of the localities present a linear subsidence behavior, and their velocities are largely unchanged. The only exception is the city of Quer6taro, where changes in the water sources have made possible a



3× reduction after 2011, where subsidence rates dropped from  $\sim -5$  cm/year to the current rates of  $\sim -1.5$  cm/year. This subsidence deceleration implies that water management modifications can indeed mitigate land subsidence due to groundwater extraction (e.g., Morishita 2021). On the other hand, we also record some differences (although far fewer locations) between our results and previous reported maximum average ground subsidence rates (e.g., Ahucatlán, Ciudad Guzmán, Mexicali; Supplementary file 6) that may be caused by multiple factors. Other than a simple increase in the extraction rate that triggers changes in subsidence velocity or spatial distribution, we compared the InSAR time series of prominent subsidence areas with longer time series (3.5 years), obtaining similar velocity values and spatial distribution (see Supplementary file 1); consequently, the September 2018–October 2019 present consistency when comparing with longer time series.

We have also investigated the possible conditional factors for all ground subsidence and found that urban areas with subsidence rates faster than  $-2.8$  cm/year were preferably developed over unconsolidated sediments (73.9%), without excess groundwater availability (76.9%), and over an underlying stressed aquifer (65.9%). These unconsolidated sediments are primarily deposited over coastal plains, or over structurally controlled or endorheic lacustrine basins where a low relief is dominant. These sedimentary environments favor ground subsidence because of the compressible mechanical behavior of the infills and where these unconsolidated materials are more prone to compaction due to their decreasing pore water pressure (e.g., Carrillo 1948). Water pressure decreasing over deformable unconsolidated deposits is, by far, the main trigger of ground lowering (e.g., Motagh et al. 2017); consequently, non-groundwater availability and stressed spatial distribution, as we have documented, exhibit a very close relationship with urban areas undergoing land subsidence. Our land subsidence assessment in Mexico and the conditional factors are very well-aligned and (at least regionally) corroborate previous large-scale subsidence potential distribution (e.g., Herrera-García et al. 2021).

The precision of our InSAR-SBAS analysis was assessed through an extensive comparison with 100 cGPS stations throughout Mexico. The mean velocity differences of  $-1$  mm/year were obtained when we compared the GPS (LOS) and InSAR (LOS) time series (Table 5); therefore, our results show a millimetric accuracy level and is similar to results than analogous surveys (e.g., Manunta et al. 2019). Three main factors benefit the higher obtained accuracy:

1. Target urban areas and a large portion of GPS stations are in low relief areas that retain long-term spatial coherence and are thus less susceptible to topography removal and phase unwrapping errors, (e.g., Morishita 2021).
2. Pixels with temporal coherence lower than 0.7 were masked from our average velocity maps and time series (e.g., Pepe and Lanari 2006).
3. The Sentinel-1 SAR free data policy and small spatial and temporal baseline (e.g., Torres et al. 2012) allow InSAR analysis at the country-scale level with high temporal resolution.

This study constitutes the most extensive land subsidence assessment that has been performed in Mexico to date; as a result, we detected well over one order of magnitude more localities than all preceding studies (see Supplementary file 2). Perhaps most relevant is the significant increase in the number of detected localities with ground subsidence.

## 6 Conclusion

Detection of urban localities with land subsidence is a necessary step to an adequate and sustainable groundwater and land-use management. This InSAR-SBAS based on Sentinel-1 analysis is the first systematic nation-wide inventory of urban areas, population, and household exposed to land subsidence. We detected 853 urban localities exposed to land subsidence (faster than  $-2.8$  cm/year and slope lower than 5 degrees) which were clustered into 29 land subsidence regions. These subsiding urban centers cover of 3797 km<sup>2</sup>, or about 15.7% of the total urban area of Mexico. Moreover, land subsidence areas expose 21.4 million people and 6.9 million households.

Our results also show that detected land subsidence velocities have the same rate and spatial distribution that have been previously reported smaller coverage studies in central Mexico (e.g., Chaussard et al. 2014, indicating that any subsidence mitigation efforts have been insufficient) except for the city of Querétaro, where subsidence rates have decreased from  $\sim -5$  to  $\sim -1.5$  cm/year due to changes in water management (Castellazzi et al. 2021). The obtained urban subsidence rates are among the highest in the world (e.g., Galloway and Burbey 2011), and we also found that it is spatially controlled by groundwater and geological setting conditions. Regarding groundwater, we found that (65.9%) and (76.9%) of the urban area with land subsidence is over-stressed aquifers and no groundwater availability, respectively (Fig. 9). In the case of geological conditions, our results show that (73.9%) of the total urban area with land subsidence faster than  $-2.8$  cm/year are on unconsolidated sediments (mainly lacustrine and alluvial deposits; Fig. 9). In other words, around 7 of each 10 km<sup>2</sup> of the urban area with land subsidence occurs where the water table considerably decreases and with highly compressible deposits, which in some cases can reach several hundreds of meters. The obtained urban land subsidence panorama may be a consequence of the no planning for city growth that Mexico has experienced in the last 40 years because of accelerated population growth (INEGI 2020), causing an increase in the probability of groundwater contamination and damages in building and infrastructure (Hernández-Espriú et al. 2014; Solano-Rojas et al. 2020). In addition, if no effective strategies are applied, the current land subsidence status can continue or even can be worst in the following decades, considering the possible growth in groundwater dependency because of climate change scenarios which forecast a rise in intensity and duration of drought (IPCC 2021).

The results of this research have local and general impacts in terms of land subsidence. At the local scale, urban land subsidence detection can be helpful to Civil Protection authorities and decision-makers to improve urban planning, water management strategies, assessment and mitigation of risk associated and subsidence, and to identify urban areas where field measurements and in-depth research is needed. Moreover, this study has covered  $\sim 85\%$  of the Mexican territory, identifying urban areas undergoing ground subsidence that were not previously detected and documented. The spatial relationships between urban land subsidence and triggering factors (i.e., lithology, groundwater stress, and groundwater availability) were assessed and confirmed results of previous works (e.g., Herrera-García et al. 2021).

## 6.1 Supplementary information

*Supplementary file 1* compares September 2018–October 2019, and January 2018–June 2021 InSAR time series in urban areas with prominent land subsidence rates. *Supplementary file 2* contains detailed results and other ancillary information used in the analysis of 853 urban localities in Mexico that undergo land subsidence. *Supplementary file 3* has the time overlap between GPS and InSAR time series. *Supplementary file 4* shows the comparative analysis between 130 InSAR and GPS (LOS) time series. *Supplementary file 5* presents the location and geographic coordinates of the GPS stations used in this study. *Supplementary file 6* has the subsidence velocity comparison in previous reported areas.

**Supplementary Information** The online version contains supplementary material available at <https://doi.org/10.1007/s11069-023-06259-5>.

**Acknowledgements** The authors thank two anonymous reviewers for their valuable contributions to the paper. Copernicus Sentinel-1 IW SAR data were retrieved from Alaska Satellite Facility and the Copernicus Open Access Hub. The GPS data were provided by several data providers, including the Trans-boundary, Land and Atmosphere Long-term Observational and Collaborative Network (TLALOCNet; Cabral-Cano et al. 2018) operated by Servicio de Geodesia Satelital (SGS) at the Instituto de Geofísica-Universidad Nacional Autónoma de México (UNAM) in collaboration with UNAVCO Inc. and Servicio Sismológico Nacional (SSN) also at Instituto de Geofísica-Universidad Nacional Autónoma de México (UNAM). Other GPS Mexican data providers include CICESE-Caltech REGNOM GPS Network, UNAVCO's Network of the Americas (NOTA, formerly PBO), INEGI's Red Geodésica Nacional Activa, US Federal Aviation Administration, SmartNet North America and other unknown providers whose metadata is unavailable at University of Nevada Reno. GPS solutions were accessed at the Nevada Geodetic Laboratory (Blewitt et al. 2018). We are deeply grateful to all personnel from UNAVCO, SSN and SGS and other data providers previously mentioned for station installation, maintenance, data acquisition, IT support and data curation and distribution for these networks. InSAR processing was performed at UNAM-Dirección General de Cómputo y de Tecnologías de Información y Comunicación (DGTIC) Miztli high performance computer. GPS solutions from the Nevada Geodetic Laboratory at University of Nevada Reno were used. The ISCE and MintPy are open-source code freely available at GitHub.

**Author contributions** EAFT and ECC conceptualized the research and developed the methodology. EAFT processed the data and provided formal analysis and writing of the original draft under the supervision of ECC. LST, ECC, BMA, and SG provided GPS data. ECC, DSR, JGV supervised the InSAR processing. EAFT, ECC, and SG performed GPS analysis. EAFT, ECC, LST, SG, and KMGV contributed to the data validation. All authors revised the manuscript.

**Funding** EAFT acknowledges funding from Consejo Nacional de Ciencia y Tecnología (CONACyT) for his doctoral studies. TLALOCNet, SSN-TLALOCNet, and other GPS related operations from SGS were/are supported by the Consejo Nacional de Ciencia y Tecnología (CONACyT) projects 253760, 256012 and 2017-01-5955, UNAM-Programa de Apoyo a Proyectos de Investigación e Innovación Tecnológica (PAPIIT) projects IN104213, IN111509, IN109315-3, IN104818-3, IN107321, National Science Foundation (NSF) grant 2025104, National Aeronautics and Space Administration (NASA)-ROSES grant NNX12AQ08G and supplemental support from UNAM-Instituto de Geofísica. EarthScope's (formerly UNAVCO) initial support for TLALOCNet (some of its stations are now part of NOTA) was performed under EAR-1338091. TLALOCNet and other NOTA stations in northwestern Mexico are supported by the GAGE Facility operated by EarthScope's, Inc. with support from NSF, NASA, and the U.S. Geological Survey under NSF Cooperative Agreement EAR-1724794. Southern Mexico GPS and the TLALOCNet archive operations are supported by NSF grant EAR-2025104 to the College of New Jersey.

## Declarations

**Conflict of interest** The authors declare that they have no known competing financial interests or personal relationships that could have appeared to influence the work reported in this paper.

**Open Access** This article is licensed under a Creative Commons Attribution 4.0 International License, which permits use, sharing, adaptation, distribution and reproduction in any medium or format, as long as you give appropriate credit to the original author(s) and the source, provide a link to the Creative Commons licence, and indicate if changes were made. The images or other third party material in this article are included in the article's Creative Commons licence, unless indicated otherwise in a credit line to the material. If material is not included in the article's Creative Commons licence and your intended use is not permitted by statutory regulation or exceeds the permitted use, you will need to obtain permission directly from the copyright holder. To view a copy of this licence, visit <http://creativecommons.org/licenses/by/4.0/>.

## References


- Berardino P, Fornaro G, Lanari R, Sansosti E (2002) A new algorithm for surface deformation monitoring based on small baseline differential SAR interferograms. *IEEE Trans Geosci Remote Sens* 40:2375–2383. <https://doi.org/10.1109/TGRS.2002.803792>
- Blewitt G, Hammond W, Kreemer C (2018) Harnessing the GPS data explosion for interdisciplinary science. In: *Eos*, 99. Accessed 16 Jun 2021. <https://doi.org/10.1029/2018EO104623>
- Brumund WF, Jonas E, Ladd CC (1976) Estimating in situ maximum past (preconsolidation) pressure of saturated clays from results of laboratory consolidometer tests. Special Report - National Research Council, Transportation Research Board 4–12
- Cabral-Cano E, Dixon T, Miralles-Wilhelm F et al (2008) Space geodetic imaging of rapid ground subsidence in Mexico City. *Geol Soc Am Bull* 120:1556–1566. <https://doi.org/10.1130/B26001.1>
- Cabral-Cano E, Pérez-Campos X, Azúa B et al (2018) TLALOCNet: a continuous GPS-met backbone in Mexico for seismotectonic and atmospheric research. *Seismol Res Lett*. <https://doi.org/10.1785/0220170190>
- Carnec C, Fabriol H (1999) Monitoring and modeling land subsidence at the Cerro Prieto geothermal field, Baja California, Mexico, using SAR interferometry. *Geophys Res Lett* 26:1211–1214. <https://doi.org/10.1029/1999GL900062>
- Carreón-Freyre DC, Cerca M (2006) Fracturing phenomena in two urban areas of Mexico. *IAEG* 291:1–10
- Carrillo N (1948) Influence of Artesian Wells on the Sinking of Mexico City. In: *Proceedings, second international conference on soil mechanics and foundation engineering*, vol 2, pp 156–159
- Casagrande A (1936) The determination of the pre-consolidation load and its practical significance. In: *Proceedings of the 1st international conference on soil mech.* pp 60–64
- Castellazzi P, Garfias J, Martel R (2021) Assessing the efficiency of mitigation measures to reduce groundwater depletion and related land subsidence in Querétaro (Central Mexico) from decadal InSAR observations. *Int J Appl Earth Obs Geoinf* 105:102632. <https://doi.org/10.1016/j.jag.2021.102632>
- Catalao J, Hanssen R, Catita C (2011) Merging GPS and atmospherically corrected InSAR data to map 3-D terrain displacement velocity. *IEEE Trans Geosci Remote Sens* 49:2354–2360. <https://doi.org/10.1109/TGRS.2010.2091963>
- Chaussard E, Wdowinski S, Cabral-Cano E, Amelung F (2014) Land subsidence in central Mexico detected by ALOS InSAR time-series. *Remote Sens Environ* 140:94–106. <https://doi.org/10.1016/j.rse.2013.08.038>
- Chaussard E, Havazli E, Fattahi H et al (2021) Over a century of sinking in Mexico City: no hope for significant elevation and storage capacity recovery. *J Geophys Res Solid Earth* 126:1–18. <https://doi.org/10.1029/2020JB020648>
- CONAGUA (2020) Sistema Nacional de Información del Agua | SINA. In: *Acuíferos (nacional)*. <http://sina.conagua.gob.mx/sina/index.php>. Accessed 2 Dec 2021
- Crosetto M, Solari L, Mróz M et al (2020) The evolution of wide-area DInSAR: From regional and national services to the European Ground motion service. *Remote Sens* 12:2043. <https://doi.org/10.3390/rs12122043>
- Dee DP, Uppala SM, Simmons AJ et al (2011) The ERA-Interim reanalysis: configuration and performance of the data assimilation system. *Q J R Meteorol Soc* 137:553–597. <https://doi.org/10.1002/qj.828>
- Doin M-P, Lasserre C, Peltzer G et al (2009) Corrections of stratified tropospheric delays in SAR interferometry: validation with global atmospheric models. *J Appl Geophys* 69:35–50. <https://doi.org/10.1016/j.jappgeo.2009.03.010>
- Fattahi H, Agram P, Simons M (2017) A network-based enhanced spectral diversity approach for TOPS time-series analysis. *IEEE Trans Geosci Remote Sens* 55:777–786. <https://doi.org/10.1109/TGRS.2016.2614925>

- Fernández-Torres EA, Cabral-Cano E, Novelo-Casanova DA et al (2022) Risk assessment of land subsidence and associated faulting in Mexico City using InSAR. *Nat Hazards*. <https://doi.org/10.1007/s11069-021-05171-0>
- Ferretti A, Prati C, Rocca F (2001) Permanent scatterers in SAR interferometry. *IEEE Trans Geosci Remote Sens* 39:8–20. <https://doi.org/10.1109/36.898661>
- Gaceta Oficial de la Ciudad de México (2017) Normas Técnicas Complementarias sobre Criterios y acciones para el Diseño Estructural de las Edificaciones. NTCCA. Jefatura de Gobierno, CDMX, Mexico
- Galloway DL, Burbey TJ (2011) Review: regional land subsidence accompanying groundwater extraction. *Hydrogeol J* 19:1459–1486. <https://doi.org/10.1007/s10040-011-0775-5>
- Galloway DL, Jones DR, Ingebritsen SE (eds) (1999) Land subsidence in the United States. U.S. Geological Survey, Reston, VA
- García-Palomo A, Macías JL, Garduño VH (2000) Miocene to recent structural evolution of the Nevado de Toluca volcano region, Central Mexico. *Tectonophysics* 318:281–302. [https://doi.org/10.1016/S0040-1951\(99\)00316-9](https://doi.org/10.1016/S0040-1951(99)00316-9)
- Henry CD, Aranda-Gomez JJ (1992) The real southern Basin and Range: mid- to late Cenozoic extension in Mexico. *Geology* 20(8):701
- Hernandez A (2003) Water law in the Republic of Mexico. *U S Mexico Law J* 11:15–28
- Hernández-Espriú A, Reyna-Gutiérrez JA, Sánchez-León E et al (2014) The DRASTIC-Sg model: an extension to the DRASTIC approach for mapping groundwater vulnerability in aquifers subject to differential land subsidence, with application to Mexico City. *Hydrogeol J* 22:1469–1485. <https://doi.org/10.1007/s10040-014-1130-4>
- Herrera-García G, Ezquerro P, Tomás R et al (2021) Mapping the global threat of land subsidence. *Science* 371:34. <https://doi.org/10.1126/science.abb8549>
- INEGI IN de E y G (2020) Censo de Población y Vivienda 2020. [https://www.inegi.org.mx/programas/ccpv/2020/#Datos\\_abiertos](https://www.inegi.org.mx/programas/ccpv/2020/#Datos_abiertos). Accessed 19 Feb 2022
- IPCC (2021) Climate Change 2021: the physical science basis. Contribution of Working Group I to the Sixth Assessment Report of the Intergovernmental Panel on Climate Change, Masson-Delmotte, V., P. Zhai, A. Pirani, S.L. Connors, C. Péan, S. Berger, N. Caud, Y. Chen, L. Goldfarb, M.I. Gomis, M. Huang, K. Leitzell, E. Lonnoy, J.B.R. Matthews, T.K. Maycock, T. Waterfield, O. Yelekçi, R. Yu, and B. Zhou. Cambridge University Press, Cambridge, United Kingdom and New York, NY, USA (In press)
- Manunta M, De Luca C, Zinno I et al (2019) The parallel SBAS approach for Sentinel-1 interferometric wide swath deformation time-series generation: algorithm description and products quality assessment. *IEEE Trans Geosci Remote Sens* 57:6259–6281. <https://doi.org/10.1109/TGRS.2019.2904912>
- Marsal RJ, Mazari M, Auvinet G, et al (2016) El subsuelo de la Ciudad de México: con una revisión de los avances en el conocimiento del subsuelo de la Ciudad de México (1959–2016). Vol. 3: ..., 3a. edición con revisión a avances. UNAM, Instituto de Ingeniería, Ciudad de México
- Meckel TA (2008) An attempt to reconcile subsidence rates determined from various techniques in southern Louisiana. *Quat Sci Rev* 27:1517–1522. <https://doi.org/10.1016/j.quascirev.2008.04.013>
- Morishita Y (2021) Nationwide urban ground deformation monitoring in Japan using Sentinel-1 LiCSAR products and LiCSBAS. *Prog Earth Planet Sci* 8:6. <https://doi.org/10.1186/s40645-020-00402-7>
- Motagh M, Shamshiri R, Haghshenas Haghghi M et al (2017) Quantifying groundwater exploitation induced subsidence in the Rafsanjan plain, southeastern Iran, using InSAR time-series and in situ measurements. *Eng Geol* 218:134–151. <https://doi.org/10.1016/j.enggeo.2017.01.011>
- Nieto-Samaniego ÁF, Alaniz-Álvarez SA, Camprubí-Cano A (2005) La Mesa Central de México: estratigrafía, estructura y evolución tectónica cenozoica. *Bol Soc Geol Mex* 57:285–318. <https://doi.org/10.18268/BSGM2005v57n3a3>
- Oliver-Cabrera T, Jones CE, Yunjun Z, Simard M (2022) InSAR phase unwrapping error correction for rapid repeat measurements of water level change in Wetlands. *IEEE Trans Geosci Remote Sens* 60:1–15. <https://doi.org/10.1109/TGRS.2021.3108751>
- Pedregosa F, Varoquaux G, Gramfort A et al (2011) Scikit-learn: machine learning in Python. *J Mach Learn Res* 12:2825–2830
- Peduto D, Nicodemo G, Maccabiani J, Ferlisi S (2017) Multi-scale analysis of settlement-induced building damage using damage surveys and DInSAR data: a case study in The Netherlands. *Eng Geol* 218:117–133. <https://doi.org/10.1016/j.enggeo.2016.12.018>
- Pepe A, Lanari R (2006) On the extension of the minimum cost flow algorithm for phase unwrapping of multitemporal differential SAR interferograms. *IEEE Trans Geosci Remote Sens* 44:2374–2383. <https://doi.org/10.1109/TGRS.2006.873207>

- Pérez-Falls Z, Martínez-Flores G (2020) Land subsidence in Villahermosa Tabasco Mexico, using radar interferometry. In: Mata-Rivera MF, Zagal-Flores R, Arellano Verdejo J, Lazcano Hernandez HE (eds) GIS LATAM. Springer, Cham, pp 18–29
- Raspini F, Caleca F, Del Soldato M et al (2022) Review of satellite radar interferometry for subsidence analysis. *Earth Sci Rev* 235:104239. <https://doi.org/10.1016/j.earscirev.2022.104239>
- Rosen PA, Gurrola E, Sacco GF, Zebker H (2012) The InSAR scientific computing environment. In: EUSAR 2012; 9th European conference on synthetic aperture radar, pp 730–733
- Sarychikhina O, Glowacka E, Mellors R, Vidal FS (2011) Land subsidence in the Cerro Prieto Geothermal Field, Baja California, Mexico, from 1994 to 2005: an integrated analysis of DInSAR, leveling and geological data. *J Volcanol Geoth Res* 204:76–90. <https://doi.org/10.1016/j.jvolgeores.2011.03.004>
- SGM (1998) Cartas geológico-mineras escala 1:250,000. In: GeoInfoMex, El Banco de Datos del SGM. <https://www.sgm.gob.mx/GeoInfoMexGobMx/>. Accessed 2 Dec 2021
- Solano-Rojas D, Wdowinski S, Cabral-Cano E, Osmanoğlu B (2020) Detecting differential ground displacements of civil structures in fast-subsiding metropolises with interferometric SAR and band-pass filtering. *Sci Rep* 10:15460. <https://doi.org/10.1038/s41598-020-72293-z>
- Terzaghi K (1925) Principles of soil mechanics: IV; settlement and consolidation of clay. *Erdbaummechanik* 95:874–878
- Tomás R, Pagán JI, Navarro JA et al (2019) Semi-automatic identification and pre-screening of geological-geotechnical deformational processes using persistent scatterer interferometry datasets. *Remote Sens* 11:1675. <https://doi.org/10.3390/rs11141675>
- Torres R, Snoeij P, Geudtner D et al (2012) GMES Sentinel-1 mission. *Remote Sens Environ* 120:9–24. <https://doi.org/10.1016/j.rse.2011.05.028>
- Yunjun Z, Fattahi H, Amelung F (2019) Small baseline InSAR time series analysis: unwrapping error correction and noise reduction. *Comput Geosci* 133:1–67. <https://doi.org/10.1016/j.cageo.2019.104331>

**Publisher's Note** Springer Nature remains neutral with regard to jurisdictional claims in published maps and institutional affiliations.

## Authors and Affiliations

Enrique Antonio Fernández-Torres<sup>1,2</sup>  · Enrique Cabral-Cano<sup>2</sup> · Darío Solano-Rojas<sup>3</sup> · Luis Salazar-Tlaczani<sup>2</sup> · Josue García-Venegas<sup>3</sup> · Bertha Marquez-Azúa<sup>4</sup> · Shannon Graham<sup>5</sup> · Katia Michelle Villarnobo-Gonzalez<sup>6</sup>

✉ Enrique Antonio Fernández-Torres  
enrique.30065@comunidad.unam.mx

- <sup>1</sup> Posgrado en Ciencias de la Tierra, Universidad Nacional Autónoma de México, Ciudad Universitaria, 04510 Coyoacán, Mexico City, Mexico
- <sup>2</sup> Departamento de Geomagnetismo y Exploración, Instituto de Geofísica, Universidad Nacional Autónoma de México, Ciudad Universitaria, 04510 Coyoacán, Mexico City, Mexico
- <sup>3</sup> División de Ingeniería en Ciencias de la Tierra, Facultad de Ingeniería, Universidad Nacional Autónoma de México, Ciudad Universitaria, 04510 Coyoacán, Mexico City, Mexico
- <sup>4</sup> Centro de Estudios Estratégicos Para el Desarrollo, Universidad de Guadalajara, Ladrón de Guevara, Tomás V. Gómez 121, 44100 Guadalajara, Jalisco, Mexico
- <sup>5</sup> The College of New Jersey Physics Department, 2000 Pennington Rd, Ewing, NJ 08628, USA
- <sup>6</sup> Departamento de Física, Facultad de Ciencias, Universidad Nacional Autónoma de México, Ciudad Universitaria, 04510 Coyoacán, Mexico City, Mexico

## Capítulo 5.2 Risk assessment of land subsidence and associated faulting in Mexico City using InSAR

### Contents

---

#### **Abstract**

#### **1 Introduction**

#### **2 Study area**

#### **3 Methodology**

##### **3.1 InSAR-SBAS processing**

##### **3.2 Socioeconomic vulnerability assessment**

##### **3.3 Socioeconomic risk map due to land subsidence and associated faulting**

#### **4 Results and discussion**

##### **4.1 Subsidence velocity and subsidence horizontal gradient**

##### **4.2 Relationship between surface faults associated to ground subsidence and the subsidence horizontal gradient (SHG)**

##### **4.3 Socioeconomic vulnerability**

##### **4.4 Socioeconomic risk map due to land subsidence and associated faulting**

#### **5 Conclusions**

### References

---

Fernández-Torres EA, Cabral-Cano E, Novelo-Casanova DA, et al (2022) Risk assessment of land subsidence and associated faulting in Mexico City using InSAR. *Nat Hazards* 112:37–55. <https://doi.org/10.1007/s11069-021-05171-0>



## Risk assessment of land subsidence and associated faulting in Mexico City using InSAR

Enrique Antonio Fernández-Torres<sup>1,2</sup> · Enrique Cabral-Cano<sup>2</sup> · David Alberto Novelo-Casanova<sup>3</sup> · Darío Solano-Rojas<sup>4</sup> · Emre Havazli<sup>5</sup> · Luis Salazar-Tlaczani<sup>2</sup>

Received: 8 May 2021 / Accepted: 10 December 2021 / Published online: 29 January 2022  
© The Author(s), under exclusive licence to Springer Nature B.V. 2021, Corrected publication 2022

### Abstract

Land subsidence and associated faulting have affected Mexico City (CDMX), Mexico, for more than 100 years. However, despite the extensive research on land subsidence in CDMX, very few investigations focus on characterizing its socioeconomic risk due to land subsidence. In this article, we present Mexico City's socioeconomic risk map due to land subsidence and associated faulting, combining our data from a land subsidence characterization based on InSAR processing with a socioeconomic vulnerability assessment. Our results show two high subsidence velocity areas. The largest area is located in the north-east sector of CDMX and the neighboring State of Mexico suburbs, where the maximum subsidence rate reaches up to 423 mm/year. We also found that 40.4% of the total cumulative length of land subsidence-associated faults correspond to high 15.6% and very high 24.8% classes of subsidence horizontal gradient. Our results demonstrate a spatial correlation between areas of high subsidence rate and horizontal gradient with high and very high socioeconomic vulnerability zones. Under this scenario, 9% of the urbanized areas, about 70.7 km<sup>2</sup>, are exposed to high and very high land subsidence socioeconomic risk where approximately 12.6% of the CDMX population lives.

**Keywords** Land subsidence · InSAR · Risk assessment · Socioeconomic vulnerability · Surface faults · México

---

✉ Enrique Antonio Fernández-Torres  
enrique.30065@gmail.com

<sup>1</sup> Posgrado en Ciencias de La Tierra, Universidad Nacional Autónoma de México, Ciudad Universitaria, Coyoacán CDMX 04510, México

<sup>2</sup> Departamento de Geomagnetismo y Exploración, Instituto de Geofísica, Universidad Nacional Autónoma de México, Ciudad Universitaria, Coyoacán CDMX 04510, México

<sup>3</sup> Departamento de Sismología, Instituto de Geofísica, Universidad Nacional Autónoma de México, Ciudad Universitaria, Coyoacán CDMX 04510, México

<sup>4</sup> División de Ingeniería en Ciencias de La Tierra, Facultad de Ingeniería, Universidad Nacional Autónoma de México, Ciudad Universitaria, Coyoacán CDMX 04510, México

<sup>5</sup> Jet Propulsion Laboratory, California Institute of Technology, 4800 Oak Grove Drive, Pasadena, CA 91109-8099, USA



## 1 Introduction

In the last decades, land subsidence has increased its influence as a result of growing groundwater extraction (Vörösmarty et al. 2000) due to the accelerated growth of cities and irrigation-agriculture land use (Dalin et al. 2017). Consequently, aquifers progressively deplete worldwide (Wada et al. 2014), generating compaction of aquifer systems and land subsidence (Herrera-García et al. 2021), affecting large areas spanning years or decades (Galloway and Burbey 2011).

In this context, the Interferometric Synthetic Aperture Radar (InSAR) techniques have proved to be an excellent toolset to characterize spatial and temporal variability of land subsidence (e.g., Galloway et al. 1999; Amelung et al. 1999; Chaussard et al. 2014; Kalia et al. 2017; Ahmad et al. 2019; Solano-Rojas et al. 2020; Chaussard et al. 2021; Aljammaz et al. 2021; Orhan et al. 2021; Morishita 2021). However, the atmospheric delay, phase unwrapping error, and decorrelation of the SAR signal may reduce the accuracy of the InSAR technique (Yunjun et al. 2019). In order to partly mitigate these shortcomings, techniques such as Permanent Scatterers (PS; Ferretti et al. 2001) and Small Baseline Subset (SBAS; Berardino et al. 2002) have been developed and made possible to obtain surface deformation time series with sub-centimeter accuracy (Casu et al. 2006; Yalvac 2020; Orhan 2021). InSAR velocity maps can be used to identify areas with differential vertical subsidence that result in surface faulting (Bouwer 1977; Ferretti et al. 2004; Mazzotti et al. 2009).

Faulting development due to land subsidence is produced when the geological media presents considerable lateral variability in mechanical properties such as compressibility and water content (e.g., Holzer and Pampeyan 1981; Caine et al. 1996; Pacheco et al. 2006; Brunori et al. 2015). Additionally, vertical consolidation of clay and silt materials may produce both vertical and horizontal stress (Carreón-Freyre et al. 2006). Besides, if the horizontal stress is distributed over narrow areas, it may induce shallow fault formation (Brunori et al. 2015). The high horizontal-stress zones can be identified by the presence of horizontal velocity high gradients (Cabral Cano et al. 2011; Brunori et al. 2015).

The subsidence horizontal gradient (SHG) is a dimensionless cartographic tool that is sensitive to significant velocity changes; therefore, it can be used as a tool to detect potential areas for fault development (Cabral-Cano et al. 2011; Cigna et al. 2011). Shallow geophysical surveys have shown a strong correlation between changes in the subsidence gradient and surface faults (Cabral-Cano et al. 2008, 2010; Qu et al. 2014). Therefore, applying an InSAR-based SHG analysis is an excellent proxy to identify areas with high vulnerability to fault development (e.g., Cabral Cano et al. 2010, Fernández-Torres et al. 2020).

In this context, land subsidence and its associated surface faulting fall under the definition of a natural hazard because it can be considered a potentially damaging phenomenon that affects a given area and specific time period (Office of the United Nations Disaster Relief Coordinator 1991). Due to its origin, land subsidence increases its occurrence probability with the confluence of compressible sedimentary strata and aggressive groundwater extraction rates, which in turn are usually tied to high population density urban areas and/or agricultural development (e.g., Pacheco-Martínez et al. 2013; Chaussard et al. 2014; Castellazzi et al. 2016; Putri et al. 2018). Consequently, an essential element to evaluate the effect of land subsidence among the population is their vulnerability. Vulnerability, in the context of risk studies, is defined as potential damage that impacts individuals and the community due to a hazardous event (e.g., Morrow 1999; Cutter et al. 2003). This potential damage includes a set of conditions and processes resulting from physical, social, and

economic factors. In consequence, several parameters can be considered to evaluate vulnerability. However, the measurement of socioeconomic aspects could be regarded as one of the most significant parameters to characterize vulnerability because it represents a community's resiliency or capacity to recover from damage (Novelo-Casanova and Rodríguez-Vangort 2016).

In the case of our study area, extensive research on land subsidence has been carried out for decades. However, very few investigations focus on characterizing risk that includes both hazard and a vulnerability assessment. In this work, we developed Mexico City's land subsidence and its associated fault risk map from a Sentinel-1 subsidence characterization combined with a socioeconomic vulnerability assessment. We used InSAR techniques and previous surveys of surface faults associated with ground subsidence to estimate the hazard related to land subsidence and faulting as well as the CDMX's social vulnerability. By combining hazard and vulnerability, we generated the socioeconomic risk map due to land subsidence and its associated faulting.

## 2 Study area

Mexico City is the capital and largest city of Mexico and the urban center with the largest population in North America (United Nations et al. 2016) located in the Valley of Mexico within a 2200 m high plateau in central Mexico (Fig. 1). According to the Housing and Population 2010 census, CDMX has a population of 8'810,277, and its total urban area is over 790 km<sup>2</sup> (INEGI 2011) distributed in 16 municipalities. However, the larger Mexico City metropolitan area covers 5954 km<sup>2</sup> and has a population of 21'828,944. In this study, we constrain our analysis to CDMX (Fig. 1).

Because of its rapid urban expansion and aggressive groundwater extraction rates from the highly compressible sediments of its underlying aquifer, CDMX has registered for over a century one of the highest land subsidence velocities (Galloway and Burbey 2011), with a maximum subsidence rate of 423 mm/year in satellite line-of-sight (LOS; Fig. 2). Shallow faulting associated with land subsidence has developed where there is a sharp horizontal transition between lithological units with significant differences in thickness and/or mechanical properties (e.g., permeability, thickness, and compressibility; Carreón-Freyre et al. 2006).

Land subsidence is constrained on the eastern and southeastern sectors of CDMX. In fact, in this area, there is a considerable thickness of high-compressible lacustrine and alluvial deposits (Pérez-Cruz 1988) (Units Q1a and Q1a, respectively; see Fig. 1). Moreover, the Sierra de Santa Catarina and the Sierra de Chichinautzin present a sharp transition between high-compressible lacustrine and alluvial deposits and volcanic rock outcrops. Therefore, this portion of the city constitutes the area with high potential for developing faults associated with land subsidence (Fig. 1).

In CDMX, several methodologies have been used to measure spatial and temporal magnitude of land subsidence such as conventional leveling, GNSS, and InSAR (e.g., Cabral-Cano et al. 2008; Osmanoğlu et al. 2011; Solano-Rojas et al. 2015; Marsal et al. 2016; Du et al. 2019; Yalvac 2020; Chaussard et al. 2021; Cigna and Tapete 2021). Multi-temporal InSAR measurements provide well-constrained results of land subsidence in Mexico City because of its high spatial resolution and synoptic view and the coherence maintained over time in the urban environment (e.g., Du et al. 2019; Fernández-Torres et al. 2020; Solano-Rojas et al. 2020; Poreh et al. 2021).

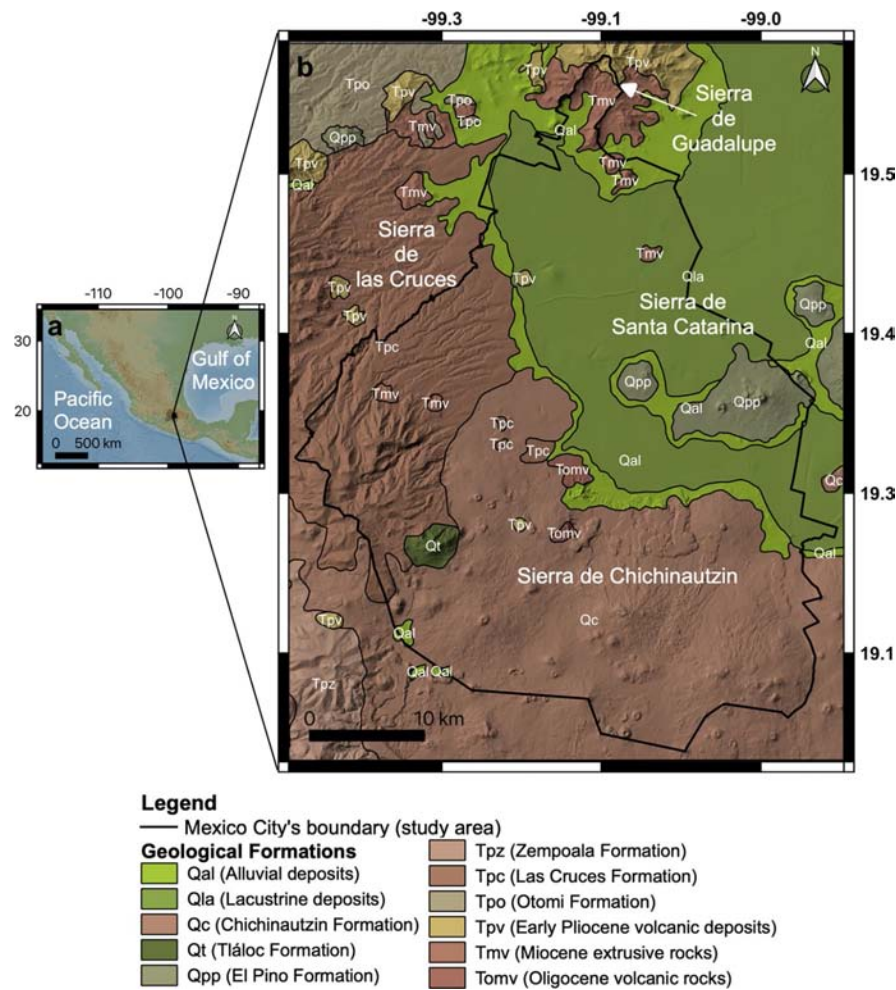


**Fig. 1** **a** Location of the study area. The research focuses exclusively within the Mexico City (CDMX) boundary. **b** Geological map of CDMX (solid black line) and its surroundings after Vázquez-Sánchez and Jaimes-Palomera (1989). The QGIS 3.10 software (<https://www.qgis.org/es/site/>) was used to produce the shaded elevation from *Continuo de Elevaciones Mexicano* data (INEGI 2013) and to compose the maps

### 3 Methodology

To estimate Mexico City's land subsidence and its associated fault risk, we used an InSAR analysis to determine the land subsidence velocity field. Subsequently, we applied a spatial analysis to calculate the SHG (Cabral Cano et al. 2010) and evaluated the relationship between SHG and previously field-surveyed faults associated with ground subsidence. To determine the socioeconomic vulnerability, we used thirteen socioeconomic parameters (Table 1; Novelo-Casanova et al. 2021) and the Analytical Hierarchical Process (AHP) of Saaty (1980). Finally, the risk is the result of the product

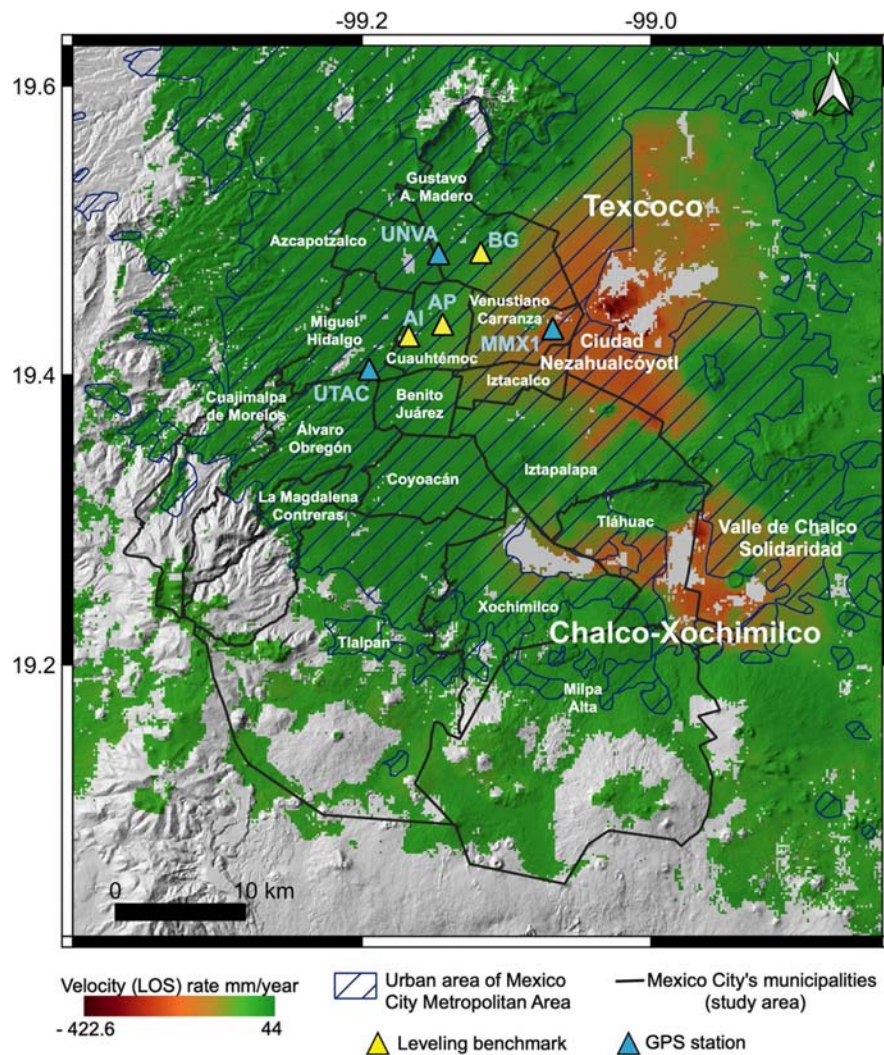


**Fig. 2** Velocity map of land subsidence within Mexico City’s municipalities derived from the SBAS interferometric analysis of Sentinel-1 A/B. The blue hatched area represents the urbanized area of the larger Mexico City Metropolitan Area. The black polygons are the Mexico City municipality’s boundaries. Texcoco and Xochimilco-Chalco represent the two sub-basins with alluvial and lacustrine deposits (see Fig. 1) where the higher velocities of land subsidence occur. The locations of the leveling benchmarks and GPS stations used in Fig. 3 for calibrating the velocity map are shown in yellow and blue triangles, respectively. BG: Basilica of Guadalupe, AP: Alameda Park, AI: The Angel of Independence (see Fig. 3)

between vulnerability and hazard (Varnes 1984; United Nations, Department of Humanitarian Affairs 1991). Thus, to obtain the socioeconomic risk map (Fig. 6) due to land subsidence and its associated faults, we multiply vulnerability (socioeconomic vulnerability) by hazard (land subsidence rate and SHG).

**Table 1** Socioeconomic vulnerability indicators and their weights (From Novelo-Casanova et al., 2021)

Indicator	Description	Weighing ( $w_i$ )
SV <sub>1</sub>	<i>Health</i> Percentage of population with access to public or private health services	0.069
SV <sub>2</sub>	<i>Education and Knowledge</i> Percentage of illiteracy	0.080
SV <sub>3</sub>	Percentage of population between 6 and 14 years old that do not attend school	0.065
SV <sub>4</sub>	Percentage of devices or technology for accessing information	0.110
SV <sub>5</sub>	Level of education	0.107
SV <sub>6</sub>	<i>Housing</i> Percentage of housing without basic services	0.117
SV <sub>7</sub>	Percentage of houses with dirt floor	0.058
SV <sub>8</sub>	Percentage of overcrowding (number of family members/ numbers of rooms)	0.087
SV <sub>9</sub>	<i>Employment</i> Percentage of economic dependency ratio	0.040
SV <sub>10</sub>	<i>Population</i> Population density	0.107
SV <sub>11</sub>	Percentage of indigenous-speaking population	0.055
SV <sub>12</sub>	Percentage of population with disabilities	0.074
SV <sub>13</sub>	Percentage of female-headed households	0.030

### 3.1 InSAR-SBAS processing

The subsidence velocity map was obtained using Synthetic Aperture Radar (SAR) scenes from Sentinel-1A/B sensors. Images were obtained along track 143 in descending orbit at mostly 12-day intervals between 8 November 2014 and 28 November 2017 (125 images in total). These C-band SAR scenes were acquired under the Interferometric Wide Swath (IWS) mode, covering 250 km × 250 km. The processing of the Sentinel-1A/B data set was carried out in two steps that included the generation of unwrapped interferograms following a times series inversion using these unwrapped interferograms.

In the first step, we used the Interferometric Synthetic Aperture Radar Scientific Computing Environment (ISCE) software to generate single interferograms (Rosen et al. 2012). We used an interferogram network with five connections and a multilooking factor of 11 × 31 in azimuth and range directions given a final resolution of ~ 160 m. The digital elevation model from the Shuttle Radar Topography Mission (SRTM) (30 m × 30 m spatial resolution) was used to correct the topographic effects of each interferogram (Farr et al. 2007) and the statistical-cost network-flow algorithm for phase unwrapping (SNAPHU; Hooper 2009). Next, the network was co-registered to a single master interferogram (Chen and Zebker 2001). Phase unwrapping errors were adjusted by using a phase-closure technique (Usai 2003), and the same coherent pixel was used for all phase unwrapping.

The second step consisted in using the Miami INsar Time-series software in Python (MintPy) to generate the map of the velocity of land subsidence of CDMX. This software is based on applying the Small Baseline Subset (SBAS) time series analysis (<http://github.com/insarlab/MintPy>) (Yunjun et al. 2019). MintPy allows us to generate the deformation history of each pixel and calculates the best fitting line to each time series to estimate the associated velocity. In the SBAS technique, interferograms are generated with SAR data pairs characterized by small spatial and temporal baselines between acquisitions

(Berardino et al. 2002). Therefore, SBAS maximizes the reliable measure points by mitigating the noise (e.g., the decorrelation phenomena).

We compared the InSAR time series with three leveling benchmarks and three GPS permanent stations in close proximity or within to the highest subsidence area (Figs. 2 and 3). Due to fact that conventional leveling measures only vertical displacements over benchmarks, we projected the InSAR time series into the vertical component. In this process, we assumed that the horizontal component of deformation is negligible and projected LOS displacements (dLOS) into vertical ( $dv$ ) based on the SAR sensor incidence angle  $\theta$  ( $dv = dLOS / \cos\theta$ ). In this comparison, we used information from *Basilica of Guadalupe* 83-B(N04E02)01, Alameda Park 376—C(N01W01)18, and The Angel of Independence 445—C(S01W03)17 benchmarks (SACMEX 2017; Pino 2018) (Figs. 2 and 3a, c, e). Next, we computed the velocity of InSAR ( $dv$ ) and leveling; we used a linear regression for the InSAR time series, and for the conventional leveling, we calculated the velocity as the slope between the two last points for the 2007–2016 time series as the closest time overlap with the InSAR data (Fig. 3a, c, e). For the comparison between the InSAR time series and permanent GPS stations, we evaluated velocities at MMX1 (Mexico City’s Airport), UNVA, and UTAC continuous GPS stations. Data from GPS time series were obtained in 3D positioning components (Vertical, East, and West) from Blewitt et al. 2018. Then, the 3D GPS components were projected into LOS following Catalao et al. 2011. Finally, a linear regression was used to estimate the velocities of InSAR data (LOS) and GPS (LOS) (Figs. 2 and 3b, d, f).

From the resulting subsidence velocity map, we generated a SHG map (Cabral-Cano et al. 2010). To estimate the SHG, we applied the Neighborhood Slope Algorithm (NSA; Burrough et al. 2015) to the velocity land subsidence map. NSA computes the maximum change rate of each cell with respect to its closest neighbors (Cabral-Cano et al. 2008; Cabral-Cano et al. 2010; Cigna et al. 2011; Qu et al. 2014; Fernández-Torres et al. 2020). The closest neighborhood was defined as square mobile window region of 3 by 3 cells, then the rates of change (delta) of the surface in vertical ( $dz/dy$ ) and horizontal ( $dz/dx$ )

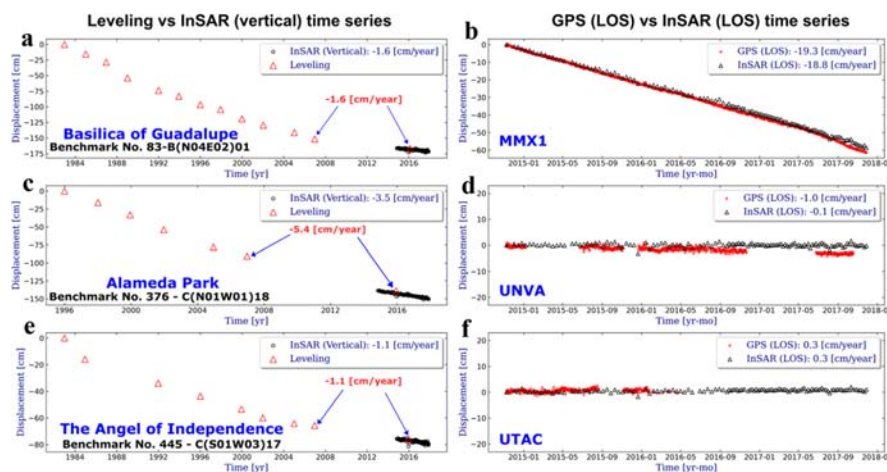


**Fig. 3** Subsidence rates time series as measured by InSAR, leveling, and GPS [cm/year] at six different locations (see locations on Fig. 2). Panels a, c, e illustrate the comparison between conventional leveling and InSAR in vertical projection. Panels b, d, g show the correlation between GPS and InSAR in LOS

directions from the center cell determine the slope (SHG; see Eq. 1). Conceptually, the output of NSA is the slope of a plane fitting the eight velocity cells values around the central velocity cell pixel.

$$\text{Slope}_{\text{degrees}} = \tan^{-1} \left( \sqrt{[dz/dx]^2 + [dz/dy]^2} \right) * 57.29578 \quad (1)$$

Finally, to determine the spatial correlation between SHG and field surveyed faults (CENAPRED 2017), we first measured each fault's length and calculated a 10 m buffer around each fault and used the Zonal Statistics tool for QGIS 3.10 to estimate the mean SHG value that corresponds to each fault and classified them into five categories (Fig. 4). These SHG categories were defined considering that at least 40% of fault cumulative length correspond to the highest SHG categories (e.g., high and very high; Table 2).

### 3.2 Socioeconomic vulnerability assessment

The socioeconomic vulnerability assessment is from Novelo-Casanova et al. (2021). These authors estimated the spatial distribution of the CDMX's socioeconomic vulnerability considering thirteen parameters that reflect the social characteristics of the population, such as age, access to basic services (electricity, water, drainage, etc.), income, and educational level. Each parameter was weighed using the Analytical Hierarchical Process (AHP; Saaty

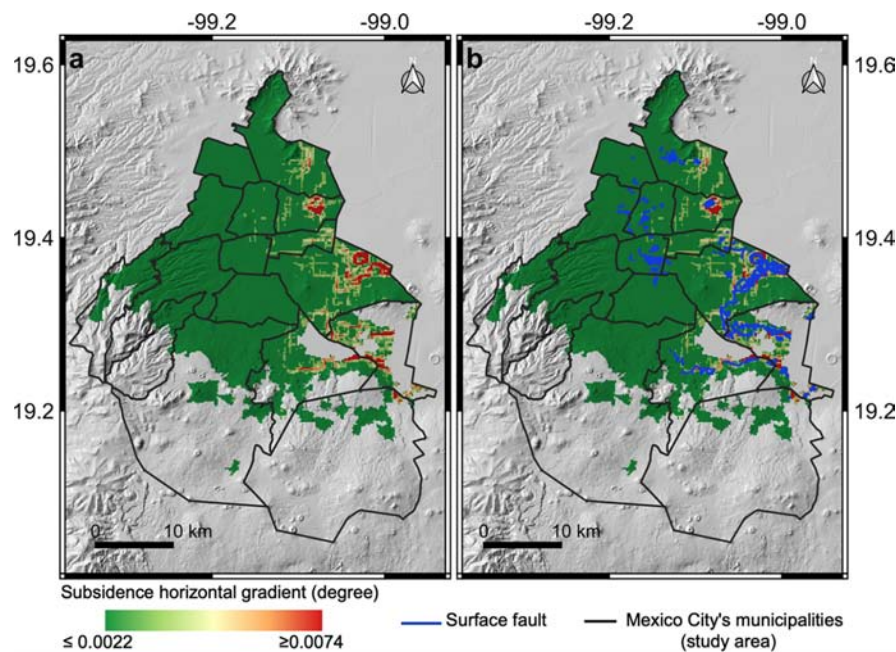


**Fig. 4** **a** Spatial distribution of the Mexico City subsidence horizontal gradient obtained considering the land subsidence velocity map (Fig. 2) and the subsidence horizontal gradient approach (Cabral-Cano et al. 2015). **b** Spatial distribution of CDMX's subsidence horizontal gradient and surface faults (blue lines; CENAPRED 2017)

**Table 2** Correlation of subsidence horizontal gradient class intervals and cumulative length of shallow faults in CDMX

Category	Subsidence horizontal gradient (degree)	Fault cumulative length (km)	Fault cumulative length (%)
Very low	$\leq 0.0022$	61.4	30.9
Low	0.0022–0.0041	38.7	19.5
Intermediate	0.0041–0.0054	18.3	9.2
High	0.0054–0.0074	30.9	15.6
Very high	$> 0.0074$	49.1	24.8
Total		198.4	

1980) (Table 1). Because the thirteen socioeconomic indicators' heterogeneity, it was necessary to normalize these parameters based on each parameter's maximum and minimum values. In this way, each parameter was given a relative weight and then correlated with the other twelve parameters (Novelo-Casanova et al. 2021). The spatial distribution of the socioeconomic vulnerability level was calculated considering the average results for each AGEB polygon (Fig. 5) from INEGI (2010). The AGEB definition was established by the Institute of Geography and Statistics (INEGI) and consists of a geographic area with a group of city blocks (1–50) where housing, commerce, industry, and other urban areas are the primary land use. The socioeconomic vulnerability results were validated on the field and are closely tied to the average socioeconomic level of the population (Novelo-Casanova et al. 2021).

In this work, in order to compute the mean level of socioeconomic vulnerability per municipality, we used the socioeconomic vulnerability polygon raster and the zonal statistics plugin available in QGIS (Table 4).

### 3.3 Socioeconomic risk map due to land subsidence and associated faulting

Risk can be defined as the estimated influence that a specific hazard would have on people, facilities, services, structures, and assets (Ponce-Pacheco and Novelo-Casanova 2018). In this work, we define risk as an expression with the following considerations:

- Both hazard (e.g., SHG and Subsidence Land Velocity) and vulnerability parameters (e.g., socioeconomic vulnerability) was normalized to its highest value
- We consider that the three parameters that define the risk are equally important; therefore, to avoid any bias, SLV, SHG, and SEV are assigned each one the same the weight
- Areas showing high hazard values due to SHG, subsidence rate, and socioeconomic vulnerability imply high risk

As a result, socioeconomic risk due to land subsidence and associated faulting is defined by:

$$\text{Risk} = \frac{\text{SHG}}{\text{SHG}_{\max}} \times \frac{\text{SLV}}{\text{SLV}_{\max}} \times \frac{\text{SEV}}{\text{SEV}_{\max}} \quad (2)$$

where: Risk: Socioeconomic risk due to land subsidence and associated faulting; SHG: Subsidence Horizontal Gradient; SLV: Subsidence Land Velocity; SEV: Socioeconomic Vulnerability.



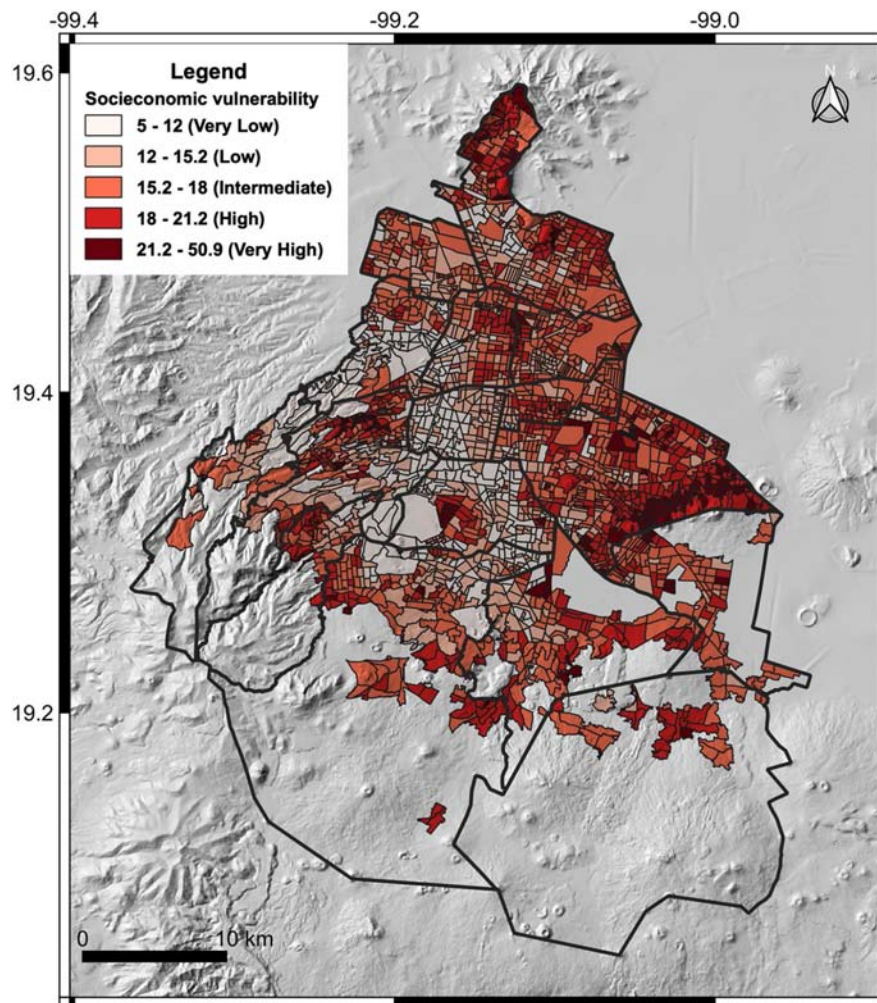


**Fig. 5** Socioeconomic vulnerability of Mexico City (CDMX). The different categories were obtained using the Natural Breaks classification (Jenks 1967) Modified from Novelo-Casanova et al. (2021)

## 4 Results and discussion

### 4.1 Subsidence velocity and subsidence horizontal gradient

The subsidence map obtained from the analysis of Sentinel-1A/B data from November 2014 to November 2017 shows two high subsidence rate patches (Fig. 2). The largest patch is placed in the northeast of CDMX and the Ciudad Nezahualc6yotl and Texcoco municipalities of the State of Mexico, where up to 423 mm/year of subsidence velocity is reached in LOS. Within CDMX, the maximum subsidence is located in the municipalities of Iztapalapa, Venustiano Carranza, Iztacalco, and Gustavo A. Madero with

258 mm/year, 201 mm/year, 177 and 173 mm/year, respectively. The second subsidence path is located in the southeast of CDMX with subsidence rates as high as 307 mm/year in Valle de Chalco Solidaridad municipality, State of Mexico, and 273 mm/year and 224 in Tláhuac and Xochimilco within CDMX (Fig. 2). To corroborate the obtained velocities map, we compared the InSAR time series with conventional leveling data and GPS stations at six different locations (Figs. 2 and 3). The absolute differences in the vertical velocities from InSAR and Leveling are  $\sim 0$ –1.9 cm/year, and between GPS and InSAR time series in LOS are  $\sim 0$ –0.9 cm/year (Fig. 3). These correspondences show good agreement, and therefore, we consider our InSAR measured velocities as accurate.

In CDMX, the expansion of the urbanized area in the eastern sector of the city was followed by land subsidence. The city's eastern sector was gradually exposed to the newly developed subsiding area due to the perforation of new water wells (Marsal et al. 2016). The currently observed velocity field is consistent with previous observations, even considering those that used different sensors and time windows (e.g., Cabral-Cano et al. 2008; López-Quiroz et al. 2009; Osmanoglu et al. 2011, 2016; Chaussard et al. 2014; Du et al. 2019). Under this circumstance, the land subsidence process still represents a hazard to Mexico City's urban infrastructure.

As described in Sect. 3.1, the information on land subsidence velocity also enables calculating the SHG that estimates those areas with the potential to develop faults associated with land subsidence (Fig. 4; Cabral-Cano et al. 2011). The CDMX municipalities with the highest SHG values are Venustiano Carranza, Tláhuac, Iztapalapa, and Xochimilco.

The SHG exhibits its largest patch in the southeast of CDMX suggesting that the zone with the highest potential to develop faults due to land subsidence is located on the outskirts of Sierra de Santa Catarina (Figs. 1; 4). The transitional zone juxtaposes the high-compressible lacustrine sediments with non-compressible volcanic structures with null or low subsidence rates ( $< -30$  mm/yr.) in this area over a short distance, developing a high subsidence horizontal gradient. Also, our SHG estimations agree with the spatial distribution of previous analyses (Cabral-Cano et al. 2008, 2010, 2015; Hernández-Espriú et al. 2014; Fernández-Torres et al. 2020; Solano-Rojas et al. 2020).

In this context, the highest values of land subsidence rate and horizontal gradient in the Valley of Mexico are mainly controlled by two factors:

1. Local stratigraphy (Fig. 1). Because the highly compressible lacustrine and alluvial deposits (water content: 200–400%, porosity: 70–90%; compression index: 3–6; void ratio: 6–11) are present in the central and eastern sectors surrounding high relief volcanic structures (e.g., Marsal et al. 2016).
2. The sediment thickness of the aquitard (Pérez-Cruz 1988; Cabral-Cano et al. 2008; Hernández-Espriú et al. 2014). According to the poroelastic theory of Biot (1941), the highly compressible lacustrine and alluvial deposits located in the city's eastern sector suffer plastic deformation when undergoing loading or stress.

Deformation occurs because water pumping-induced stress is stronger than the pre-compression strength, and the particles are rearranged. Therefore, fine sediments may undergo weak chemical bonding resulting in non-recoverable deformation (Sneed et al. 2003). Besides, once these clays have been deformed and water content is removed, they may shrink 25–30% of their original volume (Jaime and Méndez-Sánchez 2010). In the case of the sediment thickness of the aquitard, several studies support the idea that the

thicker parts of the CDMX's aquitard show the highest land subsidence rates (Pérez-Cruz 1988; Cabral-Cano et al. 2008; Hernández-Espriú et al. 2014; Solano-Rojas et al. 2015).

#### 4.2 Relationship between surface faults associated to ground subsidence and the subsidence horizontal gradient (SHG)

The resulting map with faults superimposed over the five SHG categories indicates that high values of SHG are correlated with a high density of faults associated with subsidence in the southeastern sector of CDMX (Fig. 4). According to this scenario, about 40.4% of the total cumulative length of field surveyed faults correspond to high 15.6% and very high 24.8% SHG categories (Table 2). Therefore, SHG is a suitable tool to identify shallow fault development areas associated with ground subsidence. Moreover, this deformation pattern may be used to map locations where fault systems are likely to develop in future.

The CDMX's central-east region has low SHG values associated with low fault density because in this zone there are compressible lacustrine deposits interbedded with volcanic ash and pumice deposits (e.g., Santoyo-Villa et al. 2005). In this region the uppermost lacustrine deposits are 20–60 m thick in contrast with 70–110 m of lacustrine strata in the southern sector of Sierra de Santa Catarina (Hernández-Espriú et al. 2014; Lozano-García et al. 2017). As a result, the sharp transition between clay-rich strata and volcanic rocks is crucial for developing high differential subsidence and high subsidence horizontal gradients.

The spatial relationship between the horizontal gradient and faults allowed us to establish a quantitative criterion to determine class intervals of SHG that may prove useful for evaluating subsidence hazard in other cities with similar soil conditions. Besides, this procedure allows us to identify areas where the highest values of SHG can produce significant damages in vital infrastructures that are susceptible to elevation changes of surface such as sewage system, gas stations, roads, and subway system (Hernández-Espriú et al. 2014, Fernández-Torres et al. 2020).

#### 4.3 Socioeconomic vulnerability

About 24.1% of the urbanized area of CDMX has high and very high levels of vulnerability with an extension of approximately 191 km<sup>2</sup> and affects approximately 3'254,672 inhabitants (Table 3; Fig. 5). In this scenario, the Iztapalapa, Milpa Alta, and Venustiano Carranza

**Table 3** Areas and number of inhabitants within the five socioeconomic vulnerability categories of Fig. 5

Categories of socioeconomic vulnerability	Area (km <sup>2</sup> )	Area (%)	Inhabitants	Inhabitants (%)
5–12 (Very low)	153.0	19.4	836,266	9.5
12– 15.2 (Low)	165.6	21.0	1,694,773	19.2
15.2–18 (Intermediate)	279.7	35.4	3,024,566	34.3
18–21.2 (High)	155.9	19.7	2,541,321	28.8
21.2–50.9 (Very high)	35.1	4.4	713,351	8.1
Total	789.2		8,810,277	

**Table 4** Mexico City municipalities (see Fig. 2) with a higher mean level of socioeconomic vulnerability

Municipality	Socioeconomic vulnerability
Iztapalapa	18.3
Milpa Alta	17.4
Venustiano Carranza	17.3
Xochimilco	16.9
Iztacalco	16.7

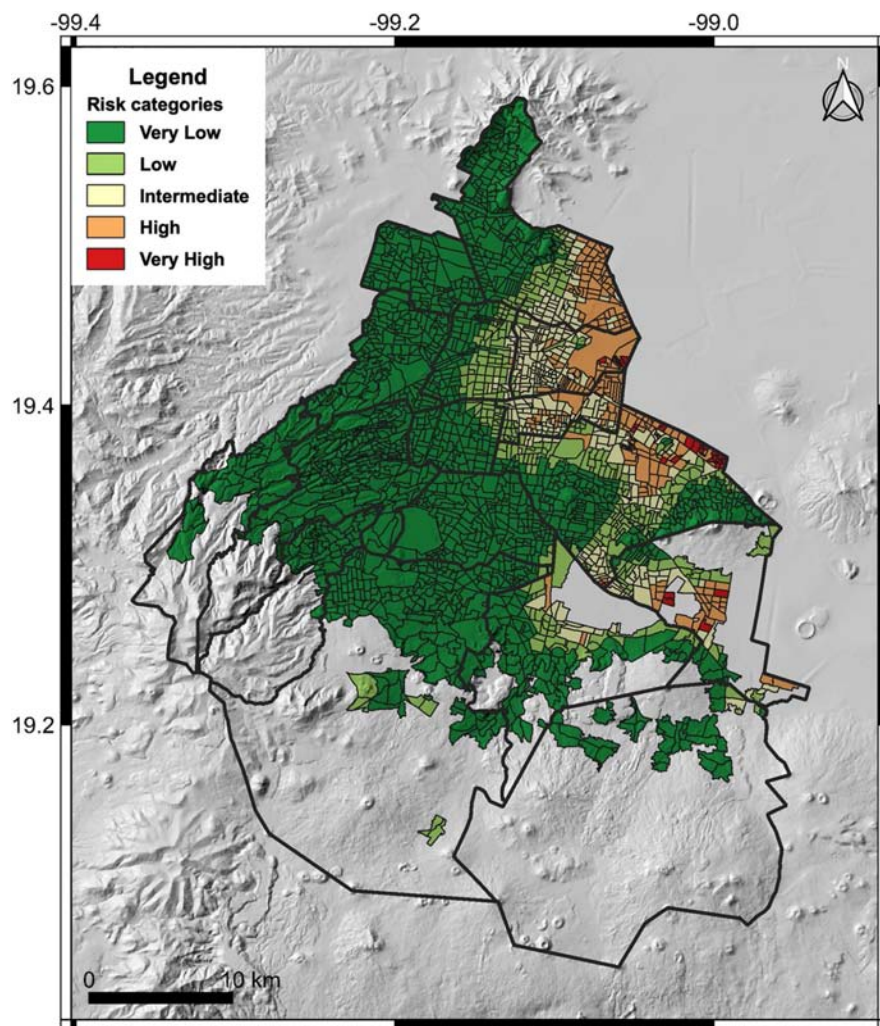


**Fig. 6** Socioeconomic risk map due to land subsidence and associated faulting in Mexico City. Socioeconomic risk categories were divided following Natural Breaks (Jenks 1967)

**Table 5** Socioeconomic risk due land subsidence and associated faulting according to Fig. 6

Risk Category	Area (km <sup>2</sup> )	Percentage of area	Number of inhabitants	Percentage of inhabitants
Very low	548.5	69.5	4,930,537	56.0
Low	96.2	12.2	1,378,416	15.6
Intermediate	73.8	9.4	1,395,817	15.8
High	65.2	8.3	1,001,463	11.4
Very high	5.5	0.7	104,044	1.2
Total	789.2		8,810,277	

municipalities have the highest socioeconomic vulnerability levels (Table 4). Thus, we can conclude that:

1. More than a third of the city's population has a low socioeconomic level. Thus, this population may not have an adequate ability to anticipate, resist or respond to the impact of land subsidence and the resulting damage to housing.
2. Low-income populations live in the city sectors with very high subsidence velocities and with a high potential for the development of associated faulting (Figs. 2, 4, and 5).

These conditions support the idea that socioeconomic vulnerability may be a consequence of widespread urbanization with poor planning and rapid population growth and disregard for the land subsidence consequences.

#### 4.4 Socioeconomic risk map due to land subsidence and associated faulting

The percentage of the urban area with high and very high subsidence risk is 9% (about 70.7 km<sup>2</sup>; Table 5; Fig. 6). Additionally, the population living in this risk level is 1'105,507 inhabitants, equivalent to 12.6% of the total population in CDMX (*Censo de Población y Vivienda*; INEGI 2010).

The expression used to compute risk considers three factors (see Eq. 2). The first two parameters constitute the hazard due to land subsidence (SLV) and its associated faults (SHG), and the last parameter is vulnerability (SEV). Those zones with high and very high socioeconomic risk represent areas where both subsidence and surface faults may produce considerable damage to critical urban infrastructure and housing, and the community's capacity to damage recovery is the lowest. Consequently, the socioeconomic risk map is a valuable tool for mitigating effects due to land subsidence and associated faulting and to develop better policies for land use management.

## 5 Conclusions

Land subsidence risk management is needed for proper land-use planning and optimizing areas where mitigation and prevention plans are required. Our results provide elements for local authorities and non-governmental organizations to develop mitigation and prevention strategies and long-term plans to establish better public policies for disaster reduction and environmental restoration due to land subsidence and its associated faulting.

Our results show that the current rate of land subsidence has the same spatial distribution and velocities that have been reported in previous studies despite using different time windows, sensors, and software (Cabral-Cano et al. 2008; López-Quiroz et al. 2009; Osmanoglu et al. 2011; Chaussard et al. 2014; Osmanoglu et al. 2016; Du et al. 2019; Solano-Rojas et al. 2020). Subsequently, the northeast sector of Mexico City and the neighboring State of Mexico suburbs undergo one of the highest land subsidence velocities in the world.

The definition of the categories of horizontal gradient subsidence in CDMX based on the correlation with based field faults represents an essential contribution to defining a quantitative criterion to identify potential areas to develop land subsidence-associated faulting and infrastructure damage.

Our results indicate that the CDMX's municipalities with high socioeconomic vulnerability have also high land subsidence velocities and large SHG values. Thus, more than 12% of the population of CDMX (1'105,500 inhabitants; *Censo de Población y Vivienda*; INEGI 2010) live in areas with high and very high socioeconomic risk due to land subsidence and associated faulting. Besides, the urbanization process will likely continue in the southern flank of the Sierra de Santa Catarina and the north flank of the Sierra of Chichinautzin (Fig. 1) because the real estate value in this zone is one of the lowest in the city (Agencia Digital de Innovación Pública). Consequently, areas and populations affected by land subsidence and associated faults will likely grow in future.

**Acknowledgements** The author would like to thank two anonymous reviewers for their insightful comments on the paper. We also thank for the GPS data provided by the Trans-boundary, Land and Atmosphere Long-term Observational and Collaborative Network (TLALOCNet; Cabral-Cano et al., 2018) operated by the Servicio de Geodesia Satelital (SGS) at the Instituto de Geofísica-Universidad Nacional Autónoma de México (UNAM) in collaboration with UNAVCO Inc. and Servicio Sismológico Nacional (SSN). Data from other network operators in Mexico, including INEGI was also used. We are deeply grateful to all personnel from UNAVCO, SGS and SSN for station installation, maintenance, data acquisition, IT support and data curation and distribution for these networks and in particular to the following individuals and institutions and those whose hard fieldwork and resourcefulness were central to the success of this project and our partners that kindly host continuous GPS stations: Jesus Pacheco-Martínez at Universidad Autónoma de Aguascalientes, Bertha Marquez-Azúa and personnel at the Universidad de Guadalajara at campus Guadalajara, Mascota and Ameca, Protección Civil de Jalisco, Lenin Avila Barrientos at CICESE, Universidad de Colima at campus Colima and campus El Naranjo and Centro de Geociencias, Centro de Ciencias de la Atmosfera and Instituto de Biología Estación Chamela at UNAM. This work was done as a private venture and not in the author's capacity as an employee of the Jet Propulsion Laboratory, California Institute of Technology.

**Author contributions** EAFT and ECC conceptualized the research. EAFT, ECC and DANC developed the methodology. EAFT provided formal analysis and writing of the original draft. DSR and EH provided parts of the InSAR data processing and LST provided data calibration. All authors reviewed and edited the original manuscript.

**Funding** EAFT is supported by a fellowship from Consejo Nacional de Ciencias y Tecnología (CONACyT), México. The Secretaría de Educación, Ciencia, Tecnología e Innovación (SECTEI) of Ciudad de México (CDMX) funded the socioeconomic vulnerability assessment under Grant SECITI/112/2017 to DANC. We acknowledge support for the high-performance computing resources from LANCAD-UNAM-DGTIC-362 project. TLALOCNet and other GPS related operations from Servicio de Geodesia Satelital have been supported by the Consejo Nacional de Ciencia y Tecnología (CONACyT) projects 253760, 256012 and 2017–01-5955. UNAM-Programa de Apoyo a Proyectos de Investigación e Innovación Tecnológica (PAPIIT) projects IN104213, IN111509, IN109315-3, IN104818-3, IN107321, National Science Foundation (NSF) Grant 2025104, National Aeronautics and Space Administration (NASA)-ROSES Grant NNX12AQ08G and supplemental support from UNAM-Instituto de Geofísica. UNAVCO's initial support for TLALOCNet was performed under EAR-1338091 and is currently supported by NSF and NASA under NSF Cooperative Agreement EAR-1724794.

**Data availability** Sentinel-1A/B SAR open access scenes were provided by the European Space Agency via the Alaska Satellite Facility SAR Data Center at <https://datapool.asf.alaska.edu> and the Copernicus Open Access Hub at <https://scihub.copernicus.eu>. Rinex GPS data was obtained from the TLALOCNet archive (<http://tlalocnet.udg.mx>), the UNAVCO archive and INEGI's Red Geodesica Nacional Activa. GPS solutions were obtained from the Nevada Geodetic Laboratory at <http://geodesy.unr.edu>.

**Code availability** ISCE and MintPy open access codes are available <https://github.com/isce-framework/isce2> and <https://github.com/insarlab/MintPy>. QGIS software is available from the QGIS project at <https://qgis.org>

## Declarations

**Conflict of interest** The authors declare that they have no conflict of interest. The content has not been approved or adopted by NASA, JPL, or the California Institute of Technology. Any views and opinions expressed herein do not necessarily state or reflect those of NASA, JPL, or the California Institute of Technology.

## References

- Agencia Digital de Innovación Pública Sistema Abierto de Información Geográfica (SIGCDMX). <http://sig.cdmx.gob.mx/>. Accessed 2 May 2021
- Ahmad W, Choi M, Kim S, Kim D (2019) Detection of land subsidence and its relationship with land cover types using ESA Sentinel satellite data: a case study of Quetta Valley, Pakistan. *Int J Remote Sens* 40(24):9572–9603. <https://doi.org/10.1080/01431161.2019.1633704>
- Aljammaz A, Sultan M, Izadi M, Abotalib AZ, Elhebiry MS, Emil MK, Abdelmohsen K, Saleh M, Becker R (2021) Land subsidence induced by rapid urbanization in arid environments: a remote sensing-based investigation. *Remote Sens* 13(6):1109. <https://doi.org/10.3390/rs13061109>
- Amelung F, Galloway DL, Bell JW, Zebker HA, Laczniak RJ (1999) Sensing the ups and downs of Las Vegas: InSAR reveals structural control of land subsidence and aquifer-system deformation. *Geology* 27(6):483–486
- Berardino P, Fornaro G, Lanari R, Sansosti E (2002) A new algorithm for surface deformation monitoring based on small baseline differential SAR interferograms. *IEEE Trans Geosci Remote Sens* 40(11):2375–2383. <https://doi.org/10.1109/TGRS.2002.803792>
- Biot M (1941) General theory of three-dimensional consolidation. *J Appl Phys* 12:155–165
- Blewitt G, Hammond W, Kreemer C (2018) Harnessing the GPS Data Explosion for Interdisciplinary Science. In: *Eos*, 99. <https://doi.org/10.1029/2018EO104623>. Accessed from 16 Jun 2021
- Bouwer H (1977) Land subsidence and cracking due to ground-water depletion. *Groundwater* 15(5):358–364. <https://doi.org/10.1111/j.1745-6584.1977.tb03180.x>
- Brunori CA, Bignami C, Zucca F, Gropelli G, Norini G, Davila Hernández N, Stramondo S (2015) Ground fracturation in urban area: monitoring of land subsidence controlled by buried faults with InSAR techniques (Ciudad Guzmán: Mexico). In: Lollino G, Manconi A, Guzzetti F, Culshaw M, Bobrowsky P, Luino F (eds) *Engineering geology for society and territory*, vol 5. Springer International Publishing, New York, pp 1027–1031
- Burroughs PA, McDonnell RA, Lloyd CD (2015b) *Principles of geographical information systems*. OUP Oxford, Oxford
- Cabral-Cano E, Dixon T, Miralles-Wilhelm F, Diaz-Molina O, Sanchez Zamora O, Carande R (2008) Space geodetic imaging of rapid ground subsidence in Mexico City. *Geol Soc Am Bull.* <https://doi.org/10.1130/B26001.1>
- Cabral-Cano E, Osmanoglu B, Dixon T, Wdowinski S, DeMets C, Cigna F, Díaz Molina O (2010a) Subsidence and fault hazard maps using PSInSAR and permanent GPS networks in central Mexico. IAHS Press, Wallingford
- Cabral-Cano E, Díaz Molina O, Delgado Granados H (2011) Subsidence and hazard maps: an example in the northeast of Mexico City Metropolitan Zone. *Bol Soc Geol Mex* 63(1):53–60
- Cabral-Cano E, Solano-Rojas D, Oliver-Cabrera T, Wdowinski S, Chaussard E, Salazar-Tlaczani L, Cigna F, DeMets C, Pacheco-Martínez J (2015) Satellite geodesy tools for ground subsidence and associated shallow faulting hazard assessment in central Mexico. *Proc Int Assoc Hydrol Sci* 372:255–260. <https://doi.org/10.5194/piahs-372-255-2015>

- Cabral-Cano E, Pérez-Campos X, Azúa B, Sergeeva M, Salazar-Tlaczani L, Demets C, Adams D, Galetzka J, Hodgkinson K, Feaux K, Serra Y, Mattioli G, Miller M (2018) TLALOCNet: a continuous GPS-met backbone in Mexico for seismotectonic and atmospheric research. *Seismol Res Lett.* <https://doi.org/10.1785/0220170190>
- Caine J, Evans J, Forster C (1996) Fault zone architecture and permeability structure. *Geology* 18(11):1025–1028
- Carreón-Freyre DC, Hidalgo-Moreno CM, Hernández-Marín M (2006) Mecanismos de fracturamiento de depósitos arcillosos en zonas urbanas. Caso de deformación diferencial en Chalco, Estado de México. *Bol Soc Geol Mex* 58(2):237–250. <https://doi.org/10.18268/bsgm2006v58n2a6>
- Castellazzi P, Arroyo-Dominguez N, Martel R, Calderhead AI, Normand JCL, Garfias J, Rivera A (2016) Land subsidence in major cities of Central Mexico: Interpreting InSAR-derived land subsidence mapping with hydrogeological data. *Int J Appl Earth Obs Geoinf* 47:102–111. <https://doi.org/10.1016/j.jag.2015.12.002>
- Casu F, Manzo M, Lanari R (2006) A quantitative assessment of the SBAS algorithm performance for surface deformation retrieval from DInSAR data. *Remote Sens Environ* 102(3):195–210. <https://doi.org/10.1016/j.rse.2006.01.023>
- Catalao J, Hanssen R, Catita C (2011) Merging GPS and atmospherically corrected InSAR data to Map 3-D Terrain displacement velocity. *IEEE T Geosci Remote Sens* 49:2354–2360. <https://doi.org/10.1109/TGRS.2010.2091963>
- CENAPRED (2017) Análisis de la Vulnerabilidad Física a la Subsistencia y Agrietamiento en la Ciudad de México. Mexico, p 23
- Chaussard E, Wdowinski S, Cabral-Cano E, Amelung F (2014) Land subsidence in central Mexico detected by ALOS InSAR time-series. *Remote Sens Environ* 140:94–106. <https://doi.org/10.1016/j.rse.2013.08.038>
- Chaussard E, Havazli E, Fattahi H, Cabral-Cano E, Solano-Rojas D (2021) Over a century of sinking in Mexico city: no hope for significant elevation and storage capacity recovery. *J Geophys Res Solid Earth.* <https://doi.org/10.1029/2020JB020648>
- Chen CW, Zebker HA (2001) Two-dimensional phase unwrapping with use of statistical models for cost functions in nonlinear optimization. *J Opt Soc Am A JOSAA* 18(2):338–351. <https://doi.org/10.1364/JOSAA.18.000338>
- Cigna F, Cabral-Cano E, Osmanoglu B, Dixon TH, Wdowinski S (2011) Detecting subsidence-induced faulting in Mexican urban areas by means of persistent scatterer interferometry and subsidence horizontal gradient mapping. pp 2125–2128
- Cigna F, Tapete D (2021b) Present-day land subsidence rates, surface faulting hazard and risk in Mexico City with 2014–2020 Sentinel-1 IW InSAR. *Remote Sens Environ.* <https://doi.org/10.1016/j.rse.2020.112161>
- Cutter SL, Boruff BJ, Shirley WL (2003) Social vulnerability to environmental hazards\*. *Soc Sci Q* 84(2):242–261. <https://doi.org/10.1111/1540-6237.8402002>
- Dalin C, Wada Y, Kastner T, Puma MJ (2017) Groundwater depletion embedded in international food trade. *Nature* 543(7647):700–704. <https://doi.org/10.1038/nature21403>
- Du Z, Ge L, Ng AH-M, Zhu Q, Zhang Q, Kuang J, Dong Y (2019) Long-term subsidence in Mexico City from 2004 to 2018 revealed by five synthetic aperture radar sensors. *Land Degrad Dev* 30(15):1785–1801. <https://doi.org/10.1002/ldr.3347>
- Farr TG, Rosen PA, Caro E, Crippen R, Duren R, Hensley S, Kobrick M, Paller M, Rodriguez E, Roth L, Seal D, Shaffer S, Shimada J, Umland J, Werner M, Oskin M, Burbank D, Alsdorf D (2007) The shuttle radar topography mission. *Rev Geophys.* <https://doi.org/10.1029/2005RG000183>
- Fernández-Torres E, Cabral-Cano E, Solano-Rojas D, Havazli E, Salazar-Tlaczani L (2020) Land Subsidence risk maps and InSAR based angular distortion structural vulnerability assessment: an example in Mexico City. In: *Proceedings of the International Association of Hydrological Sciences*. Copernicus GmbH, pp 583–587
- Ferretti A, Prati C, Rocca F (2001) Permanent scatterers in SAR interferometry. *IEEE Trans Geosci Remote Sens* 39(1):8–20. <https://doi.org/10.1109/36.898661>
- Ferretti A, Novali F, Bürgmann R, Hilley G, Prati C (2004) InSAR permanent scatterer analysis reveals ups and downs in San Francisco Bay Area. *EOS Trans Am Geophys Union* 85(34):317–324. <https://doi.org/10.1029/2004EO340002>
- Galloway DL, Burbey TJ (2011) Review: regional land subsidence accompanying groundwater extraction. *Hydrogeol J* 19(8):1459–1486. <https://doi.org/10.1007/s10040-011-0775-5>
- Galloway DL, Jones DR, Ingebritsen SE (eds) (1999) *Land subsidence in the United States*. US Geological Survey, Reston, VA



- Hernández-Espriú A, Reyna-Gutiérrez JA, Sánchez-León E, Cabral-Cano E, Carrera-Hernández J, Martínez-Santos P, Macías-Medrano S, Falorni G, Colombo D (2014) The DRASTIC-Sg model: An extension to the DRASTIC approach for mapping groundwater vulnerability in aquifers subject to differential land subsidence, with application to Mexico City. *Hydrogeol J* 22(6):1469–1485. <https://doi.org/10.1007/s10040-014-1130-4>
- Herrera-García G, Ezquerro P, Tomás R, Béjar-Pizarro M, López-Vinielles J, Rossi M, Mateos RM, Carreón-Freyre D, Lambert J, Teatini P, Cabral-Cano E, Erkens G, Galloway D, Hung W-C, Kakar N, Sneed M, Tosi L, Wang H, Ye S (2021) Mapping the global threat of land subsidence. *Science* 371(6524):34–36. <https://doi.org/10.1126/science.abb8549>
- Holzer TL, Pampeyan EH (1981) Earth fissures and localized differential subsidence. *Water Resour Res* 17:223227
- Hooper A (2009) A statistical-cost approach to unwrapping the phase of InSAR time series 6
- INEGI (2010) Censo de Población y Vivienda 2010. In: INEGI. <https://www.inegi.org.mx/programas/ccpv/2010/>. Accessed from 5 Apr 2021
- INEGI (2013) Continuo de Elevaciones Mexicano (CEM). <https://www.inegi.org.mx/app/geo2/elevacionesmex/index.jsp>. Accessed from 21 Oct 2019
- INEGI IN de E y G (2011) Instituto Nacional de Estadística y Geografía. INEGI. <https://www.inegi.org.mx/default.html>. Accessed from 17 Oct 2019
- Jaime A, Mendes-Sanchez E (2010) Evolution of Mexico City clay properties affected by land subsidence. In: IAHS-AISH publication. pp 232–234
- Jenks GF (1967) The data model concept in statistical mapping. *Int Yearb Cartogr* 7:186–190
- Kalia AC, Frei M, Lege T (2017) A Copernicus downstream-service for the nationwide monitoring of surface displacements in Germany. *Remote Sens Environ* 202:234–249. <https://doi.org/10.1016/j.rse.2017.05.015>
- López-Quiroz P, Doin M-P, Tupin F, Briole P, Nicolas J-M (2009) Time series analysis of Mexico City subsidence constrained by radar interferometry. *J Appl Geophys* 69(1):1–15. <https://doi.org/10.1016/j.jappge.2009.02.006>
- Lozano-García S, Brown ET, Ortega B, Caballero M, Werne J, Fawcett PJ, Schwab A, Valero-Garcés BL, Schnurrenberger D, O'Grady R, Stockhecke M, Steinman B, Cabral-Cano E, Caballero C, Sosa-Nájera S, Soler AM, Pérez L, Noren A, Myrbo A, Bücker M, Watrus B, Arciniega A, Wonik T, Watt S, Kumar D, Acosta C, Martínez I, Cossio R, Ferland T, Vergara-Huerta F (2017b) Perforación profunda en el lago de Chalco: reporte técnico. *BSGM* 69(2):299–311. <https://doi.org/10.18268/BSGM2017v69n2a2>
- Marsal RJ, Mazari M, Auvinet G, Méndez E, Juárez M (2016) El subsuelo de la Ciudad de México: con una revisión de los avances en el conocimiento del subsuelo de la Ciudad de México (1959–2016). Vol. 3: ..., 3a. edición con revisión a avances. UNAM, Instituto de Ingeniería, Ciudad de México
- Mazzotti S, Lambert A, Van der Kooij M, Mainville A (2009) Impact of anthropogenic subsidence on relative sea-level rise in the Fraser River delta. *Geology* 37(9):771–774. <https://doi.org/10.1130/G25640A.1>
- Morishita Y (2021) Nationwide urban ground deformation monitoring in Japan using Sentinel-1 LiCSAR products and LiCSBAS. *Prog Earth Planet Sci* 8(1):6. <https://doi.org/10.1186/s40645-020-00402-7>
- Morrow BH (1999) Identifying and mapping community vulnerability. *Disasters* 23(1):1–18. <https://doi.org/10.1111/1467-7717.00102>
- Novelo-Casanova DA, Rodríguez-Vangort F (2016b) Flood risk assessment case of study: Motozintla de Mendoza, Chiapas, Mexico. *Geomat Natl Hazards Risk* 7(5):1538–1556. <https://doi.org/10.1080/19475705.2015.1089327>
- Novelo-Casanova DA, Suárez G, Cabral-Cano E, Fernández-Torres EA, Fuentes-Mariles OA, Havazli E, Jaimes MÁ, López-Espinoza ED, Martín-Del Pozzo AL, Morales-Barrera WV, Morales-Rodríguez HL, Nieto-Torres A, Rodríguez-Elizarrarás SR, Solano-Rojas D, Velasco-Herrera VM (2021) The risk atlas of Mexico City, Mexico: a tool for decision-making and disaster prevention. *Nat Hazards*. <https://doi.org/10.1007/s11069-021-05059-z>
- Office of the United Nations Disaster Relief Co-ordinator (1991) Mitigating natural disasters: phenomena, effects and options: a manual for policy makers and planners. United Nations, New York
- Orhan O (2021) Monitoring of land subsidence due to excessive groundwater extraction using small baseline subset technique in Konya, Turkey. *Environ Monit Assess* 193(4):174. <https://doi.org/10.1007/s10661-021-08962-x>
- Orhan O, Oliver-Cabrera T, Wdowinski S, Yalvac S, Yakar M (2021) Land subsidence and its relations with sinkhole activity in Karapinar region, Turkey: a multi-sensor InSAR time series study. *Sensors* 21(3):774. <https://doi.org/10.3390/s21030774>
- Osmanoğlu B, Dixon TH, Wdowinski S, Cabral-Cano E, Jiang Y (2011) Mexico City subsidence observed with persistent scatterer InSAR. *Int J Appl Earth Obs Geoinf* 13(1):1–12. <https://doi.org/10.1016/j.jag.2010.05.009>

- Osmanoğlu B, Sunar F, Wdowinski S, Cabral-Cano E (2016) Time series analysis of InSAR data: methods and trends. *ISPRS J Photogramm Remote Sens* 115:90–102. <https://doi.org/10.1016/j.isprsjprs.2015.10.003>
- Pacheco J, Arzate J, Rojas E, Arroyo M, Yutsis V, Ochoa G (2006) Delimitation of ground failure zones due to land subsidence using gravity data and finite element modeling in the Querétaro valley, México. *Eng Geol* 84(3):143–160. <https://doi.org/10.1016/j.enggeo.2005.12.003>
- Pacheco-Martínez J, Hernández-Marín M, Burbey TJ, González-Cervantes N, Ortíz-Lozano JÁ, Zermeño-De-Leon ME, Solís-Pinto A (2013) Land subsidence and ground failure associated to groundwater exploitation in the Aguascalientes Valley, México. *Eng Geol* 164:172–186. <https://doi.org/10.1016/j.enggeo.2013.06.015>
- Peréz-Cruz GA (1988) Estudio sismológico de reflexión del subsuelo de la Ciudad de México. Universidad Nacional Autónoma de México, México
- Pino YL (2018b) Evolución de la respuesta sísmica de la ciudad de México. Universidad Nacional Autónoma de México, México
- Ponce-Pacheco AB, Novelo-Casanova DA (2018) Vulnerabilidad y riesgo en el valle de Chalco Solidaridad, Estado de México, Mexico. Caso de Estudio: El Triunfo, Avándaro and San Isidro. *Investigaciones geográficas*. <https://doi.org/10.14350/riig.59675>
- Poreh D, Pirasteh S, Cabral-Cano E (2021) Assessing subsidence of Mexico City from InSAR and LandSat ETM+ with CGPS and SVM. *Geoenviron Disasters* 8(1):7. <https://doi.org/10.1186/s40677-021-00179-x>
- Putri RF, Wibirama S, Sukamdi GSR (2018) Population condition analysis of Jakarta land deformation area. *IOP Conf Ser Earth Environ Sci* 148:012007. <https://doi.org/10.1088/1755-1315/148/1/012007>
- Qu F, Zhang Q, Lu Z, Zhao C, Yang C, Zhang J (2014) Land subsidence and ground fissures in Xi'an, China 2005–2012 revealed by multi-band InSAR time-series analysis. *Remote Sens Environ* 155:366–376. <https://doi.org/10.1016/j.rse.2014.09.008>
- Rosen PA, Gurrola E, Sacco GF, Zebker H (2012) The InSAR scientific computing environment. In: *EUSAR 2012; 9th European Conference on Synthetic Aperture Radar*. pp 730–733
- Saaty TL (1980) *The analytical hierarchy process*. McGraw-Hill, New York
- SACMEX S de A de la C de M (2017) Nivelación de bancos superficiales. Secretaría de Obras y Servicios, Mexico City (Mexico)
- Santoyo-Villa E, Ovando-Shelley E, Mooser F, León-Plata E (2005) Síntesis Geotécnica de la Cuenca del Valle de México. México
- Sneed M, Ikehara ME, Stork SV, Amelung F, Galloway D (2003) Detection and measurement of land subsidence using interferometric synthetic aperture radar and global positioning system, san Bernardino County, Mojave Desert, California. *US Geological Survey* 69
- Solano-Rojas D, Cabral-Cano E, Hernández-Espriú A, Wdowinski S, DeMets C, Salazar-Tlaczani L, Falorni G, Bohane A (2015) The relationship of InSAR-GPS land subsidence and the groundwater level decrease in wells of the Mexico City Metropolitan Area. *Bol Soc Geol Mex* 67(2):273–283
- Solano-Rojas D, Wdowinski S, Cabral-Cano E, Osmanoğlu B (2020) Detecting differential ground displacements of civil structures in fast-subsiding metropolises with interferometric SAR and band-pass filtering. *Sci Rep* 10(1):15460. <https://doi.org/10.1038/s41598-020-72293-z>
- United Nations (2016) *The World's Cities in 2016*. UN
- United Nations, Department of Humanitarian Affairs (1991) *Mitigating natural disasters: phenomena, effects and options—a manual for policy makers and planners*. United Nations, New York
- Usai S (2003) A least squares database approach for SAR interferometric data. *IEEE Trans Geosci Remote Sens* 41(4):753–760. <https://doi.org/10.1109/TGRS.2003.810675>
- Varnes DJ (1984) *Landslide Hazard Zonation: A Review of Principle and Practice*. UNESCO, Paris
- Vázquez-Sánchez E, Jaimes-Palomera R (1989) Geología de la Cuenca de México. *Rev Unión Geofís Mex* 28:1–57
- Vörösmarty CJ, Green P, Salisbury J, Lammers RB (2000) Global water resources: vulnerability from climate change and population growth. *Science* 289(5477):284–288. <https://doi.org/10.1126/science.289.5477.284>
- Wada Y, Wisser D, Bierkens MFP (2014) Global modeling of withdrawal, allocation and consumptive use of surface water and groundwater resources. *Earth Syst Dyn* 5(1):15–40. <https://doi.org/10.5194/esd-5-15-2014>
- Yalvac S (2020) Validating InSAR-SBAS results by means of different GNSS analysis techniques in medium- and high-grade deformation areas. *Environ Monit Assess* 192(2):120. <https://doi.org/10.1007/s10661-019-8009-8>
- Yunjun Z, Fattahi H, Amelung F (2019) Small baseline InSAR time series analysis: Unwrapping error correction and noise reduction. *Comput Geosci* 133:104331. <https://doi.org/10.1016/j.cageo.2019.104331>

**Publisher's Note** Springer Nature remains neutral with regard to jurisdictional claims in published maps and institutional affiliations.

## Capítulo 5.3 The Risk Atlas of Mexico City, Mexico: a tool for decision-making and disaster prevention

### Contents

---

#### Abstract

#### 1 Introduction

#### 2 Development of hazard reduction efforts in Mexico City and the Risk Atlas

#### 3 Earthquake hazard

##### 3.1 Seismic micro-zonation

##### 3.2 Evaluation of seismic hazard

#### 4 Volcanic hazard in Mexico City

##### 4.1 Eruption of a new volcano in the Younger Chichinautzin Monogenetic Field

#### 5 Subsidence of the ground in CDMX

##### 5.1 Horizontal subsidence gradient

##### 5.2 Angular distortion

#### 6 Floods

##### 6.1 Return period and volume

##### 6.2 Flood area

#### 7 Forest fires

#### 8 Landslide hazards in Mexico City

#### 9 Social vulnerability of CDMX

#### 10 Exposure

#### 11 Social risk

#### 12 Examples of seismic risk scenarios

#### 13 Retrospective

#### References

---

Novelo-Casanova DA, Suárez G, Cabral-Cano E, **Fernández-Torres EA**, et al (2022) The Risk Atlas of Mexico City, Mexico: a tool for decision-making and disaster prevention. Nat Hazards 111:411–437.  
<https://doi.org/10.1007/s11069-021-05059-z>



## The Risk Atlas of Mexico City, Mexico: a tool for decision-making and disaster prevention

David A. Novelo-Casanova<sup>1</sup> · Gerardo Suárez<sup>1</sup> · Enrique Cabral-Cano<sup>2</sup> · Enrique A. Fernández-Torres<sup>3</sup> · Oscar A. Fuentes-Mariles<sup>4</sup> · Emre Havazli<sup>5</sup> · Miguel Á. Jaimes<sup>6</sup> · Erika D. López-Espinoza<sup>7</sup> · Ana Lillian Martin-Del Pozzo<sup>8</sup> · Wendy V. Morales-Barrera<sup>9</sup> · Hipólito L. Morales-Rodríguez<sup>4</sup> · Amiel Nieto-Torres<sup>3</sup> · Sergio R. Rodríguez-Elizarrarás<sup>9</sup> · Darío Solano-Rojas<sup>10</sup> · Victor M. Velasco-Herrera<sup>11</sup>

Received: 23 May 2021 / Accepted: 27 September 2021 / Published online: 8 October 2021  
© The Author(s) 2021

### Abstract

We present a Risk Atlas of Mexico City based on a Geographical Information System (RA-GIS). We identified the prevalent social risk to the more relevant hazards in Mexico City (CDMX): earthquakes, volcanic eruptions, floods, landslides, forest fires, and land subsidence. A total of 274 shape-file maps were generated in this project. Seismic hazard was estimated for return periods (RP) of 20, 125, 250, and 475 years. Three areas in central and northwestern CDMX were identified along the Younger Chichinautzin Monogenetic Volcanic Field with a high probability of forming a new volcano. Subsidence is concentrated to the east and southeast of CDMX, where subsidence rates are among the highest worldwide. Flooding events were estimated for RP of 2, 5, 10, 50, and 100 years, and most of them are concentrated in the central and northern sectors of the city. During the dry season (December–April), southern CDMX has very high probability of forest fire occurrence. There is high susceptibility of landslides on the west and southwest of the city. The goals of this RA-GIS are to provide a tool to the local and federal authorities and all organizations responsible for disaster prevention and mitigation to: (1) improve the knowledge of the potential physical and social impact of local hazards; (2) provide elements for disaster prevention, mitigation, preparedness, and response; (3) benefit decision-makers with robust risk data; (4) provide information for land-use planning; and (5) support further research to reduce the impact of disasters caused by natural phenomena.

**Keywords** Mexico City · Hazard · Vulnerability · Risk · Risk Atlas · Disaster prevention · Mexico

---

✉ David A. Novelo-Casanova  
dnovelo@geofisica.unam.mx

Extended author information available on the last page of the article

## 1 Introduction

The reason behind Mexico City's high level of exposure to natural phenomena lies at the core of its history. Mexico City (CDMX) sits in an endorheic basin, where precipitation formed a set of interconnected lakes fed by rivers flowing from the surrounding mountains (Santoyo et al. 2005; Sosa-Rodríguez 2010). CDMX was founded on the remains of the old Aztec capital. The Aztecs built their city on an island in the middle of the lake. After the Spanish conquest, the Spaniards decided to build the new capital on the ruins of the old Aztec city and began to drain and landfill the surrounding lakes. They also disregarded maintenance of the system of dikes and aqueducts built by the original inhabitants to control flooding (Levi 1990; Sosa-Rodríguez 2010). As a result, the newly founded city suffered frequent inundations in 1555, 1604, 1607, and 1629 (Hoberman 1974). After the 1607 catastrophic floods, the authorities ordered the construction of a channel to the northeast of the city to drain the lakes and to provide an outlet during heavy rains (Boyer 1975; Scaletti Cárdenas 2018).

Since those early days, major engineering projects have been undertaken to alleviate flooding of the city. Most of the original lakes have been drained, and CDMX gradually grew on the soft clay sediments of the old lakebed. This soft, water-saturated subsoil is the cause behind many of the hazards now faced by the city. For example, although CDMX lies about 350 km from the subduction zone, where the largest and more frequent earthquakes originate, it is severely affected by strong shaking due to the local amplification of seismic waves (e.g., Ordaz and Singh 1992). Also, the subsidence rates observed in CDMX, considered to be among the largest in the world, are due to the sinking of the lakebed due to water extraction (López-Quiroz et al. 2009; Cabral-Cano et al. 2008; Osmanoglu et al. 2011). Additionally, soil fractures result from the differential subsidence of the ground (Auvinet et al. 2013).

As a result of the subsoil characteristics, the population, infrastructure, and critical facilities are highly exposed to earthquakes, land subsidence and flooding. In addition, CDMX is in the Trans-Mexican Volcanic Belt (TMVB) and is affected by volcanic activity. Thus, CDMX faces important challenges to contend with future disastrous situations. Digital maps are important interactive tools to visualize and compare the spatial distribution of the population, buildings, and infrastructure exposed to various hazards.

The purpose here is to present a digital atlas of hazards and social risk of CDMX developed in a Geographic Information System that from now on we call RA-GIS. Also, because risk is a spatially dependent phenomenon, emergency managers and the public require a proper visualization instrument such as a GIS. The main objectives of the RA-GIS are to make authorities, citizens, and the media aware of the levels of natural hazards and risks to which the city is exposed with the purpose of providing the necessary elements to establish preventive and remedial actions. This RA-GIS can also serve as a guide for future land use and development plans, to promote scientific research on the subject and to strengthen the culture of disaster prevention in society.

We present the methodologies used to assess hazard, social vulnerability, and risk at the scale of CDMX and several examples of the studies and maps that constitute the RA-GIS. We also include an electronic supplement that shows the hazard, vulnerability, and risk maps in PDF format generated or updated during this research (Online Resource 1). Although maps at the CDMX level is a small scale for the development of proper civil protection actions, the GIS maps will allow local authorities to intervene at the dwelling and neighborhood level. On the other hand, our database includes information about the

footprint of buildings, density of population and housing, critical infrastructure as hospitals and schools of CDMX as well as the location of gas station, main markets, among other types of infrastructures (see Online Resource 1).

## 2 Development of hazard reduction efforts in Mexico City and the Risk Atlas

After the destructive earthquake of September 19, 1985 ( $M_w$  8.1) (UNAM Seismology Group 1986), the Mexican authorities promoted various initiatives to build a nation-wide civil protection system to prevent disasters caused by natural phenomena and anthropogenic activity. Important early contributions were the creation of the National Civil Protection System (SINAPROC) in 1986 and the Mexican National Center for Disaster Prevention (CENAPRED). Also, the installation of civil protection offices was mandated at all levels of government.

An additional response was the development of the Seismic Early Warning System in 1989. Given the location of the city, large earthquakes in the subduction zone allow approximately 60 s of warning before the arrival of damaging seismic waves (Espinosa-Aranda et al. 1995; Suárez et al. 2009, 2018). Although these initiatives have achieved considerable progress, the local authorities recognized the need to continue improving disaster risk management based on preventive actions. As part of these efforts, the Secretariat of Education, Science, Technology, and Innovation (SECTEI) of the Mexico City government funded the present project to develop the RA-GIS. In this first phase, the main purpose is to identify the levels of hazard associated with earthquakes, volcanic eruptions, floods, landslides, forest fires, and land subsidence. Social vulnerability is also evaluated to estimate the risk posed by these natural hazards.

## 3 Earthquake hazard

Mexico has a long history of destructive earthquakes originating in the subduction zone (García-Acosta and Suárez 1996). Although the September 19, 1985 ( $M_w$  8.1), earthquake was located ~350 km away from CDMX, the city suffered considerable damage and loss of life (Aguilar et al. 1989; Rosenblueth and Meli 1986; UNAM Seismology Group 1986; Stone et al. 1987). The city is also vulnerable to earthquakes located beneath the continent that reflect the deformation of the subducted Cocos plate. The more recent example occurred on September 19, 2017, when an intraplate earthquake  $M_w$  7.1 was strongly felt by several communities in Mexico including CDMX. Its epicenter was located ~150 km from the city at a depth of 55 km. In Mexico City, more than 40 buildings collapsed, and 370 people perished.

An additional source of seismic hazard is represented by the crustal faults located on the Trans-Mexican Volcanic Belt (TMVB). Two large crustal earthquakes took place in the TMVB in the early twentieth century: the Acambay earthquake of November 19, 1912 ( $M_w$  6.9) (Urbina and Camacho 1913), and the Xalapa event of January 4, 1920 ( $M_w$  6.4) (Flores and Camacho 1922; Suárez and Novelo-Casanova 2018). Historical records also show a large number of crustal earthquakes in the TMVB in the last 450 years of written history (Suárez et al. 2019).

### 3.1 Seismic micro-zonation

The CDMX building code classifies the local soil conditions into three seismic zones (Gobierno del Distrito Federal 2004): Zone I (hill zone) constituted mainly of basaltic and rhyolitic lava and compact pyroclastic flows; Zone II (transition zone) composed of sands and pyroclastic material from the surrounding volcanic deposits; Zone III (lakebed zone) composed of silt and volcanic clay sediments with a very high water content that suffer large ground amplification with passing seismic waves (Ordaz and Singh 1992; Lermo and Chávez-García 1994). Zone III is subdivided further into three zones. The stark contrasts of the geotechnical conditions of the soil in CDMX show that micro-zonation based on the natural period of the ground is an essential element in the evaluation of seismic hazard and in the design of building codes and regulations.

The spatial seismic response of the CDMX's subsoil was estimated using the spectral ratio technique developed by Nakamura (1989). It is considered that this spectral technique gives an approximation of the soil's transfer function, its amplification, and the natural period of vibration (Bard 1999). We used the following data: (a) new measurements made in 75 sites (Fig. 1); (b) records from 84 sites, previously obtained by different authors; and (c) recordings from 53 stations of the Accelerographic Network of Mexico City (RACM), operated by the Instrumentation Center and Seismic Recording (CIRES; Centro de Instrumentación y Registro Sísmico, in Spanish). These 212 measurements were interpolated using a thin plate spline (Duchon 1977) to outline the spatial distribution of the dominant periods of the soil in Mexico City (Fig. 1).

### 3.2 Evaluation of seismic hazard

Seismic hazard in CDMX was estimated for the return periods prescribed by CENAPRED of 20, 125, 250, and 475 years. The methodology considers the following steps (Jaimes and Niño 2017): (a) characterization of the different seismic sources potentially affecting CDMX (subduction, intraslab, and crustal); (b) use of appropriate ground motion models depending on the types of earthquakes (Abrahamson and Silva 1997; Jaimes et al. 2006, 2015; Jaimes and García-Soto 2020); (c) convolution of the response spectral ratios (Rosenblueth and Arciniega 1992) with the ground motion predictions; and (d) probability estimation of shaking intensity for the different return periods.

There is a univocal correlation between the thickness of the soft and water-saturated clays and the areas where the probability of high peak ground acceleration is observed. Areas in the central part of the ancient lakes are more heavily impacted by soil amplification. The estimated PGA values in the lakebed zone (Zone III) vary from a possible maximum 0.09 g for a return period of 20 years (Fig. 2a) up to 0.53 g for 475 years (Fig. 2d). These areas are concentrated in municipalities located in the central, southern, and eastern zones of the city (Fig. 2).

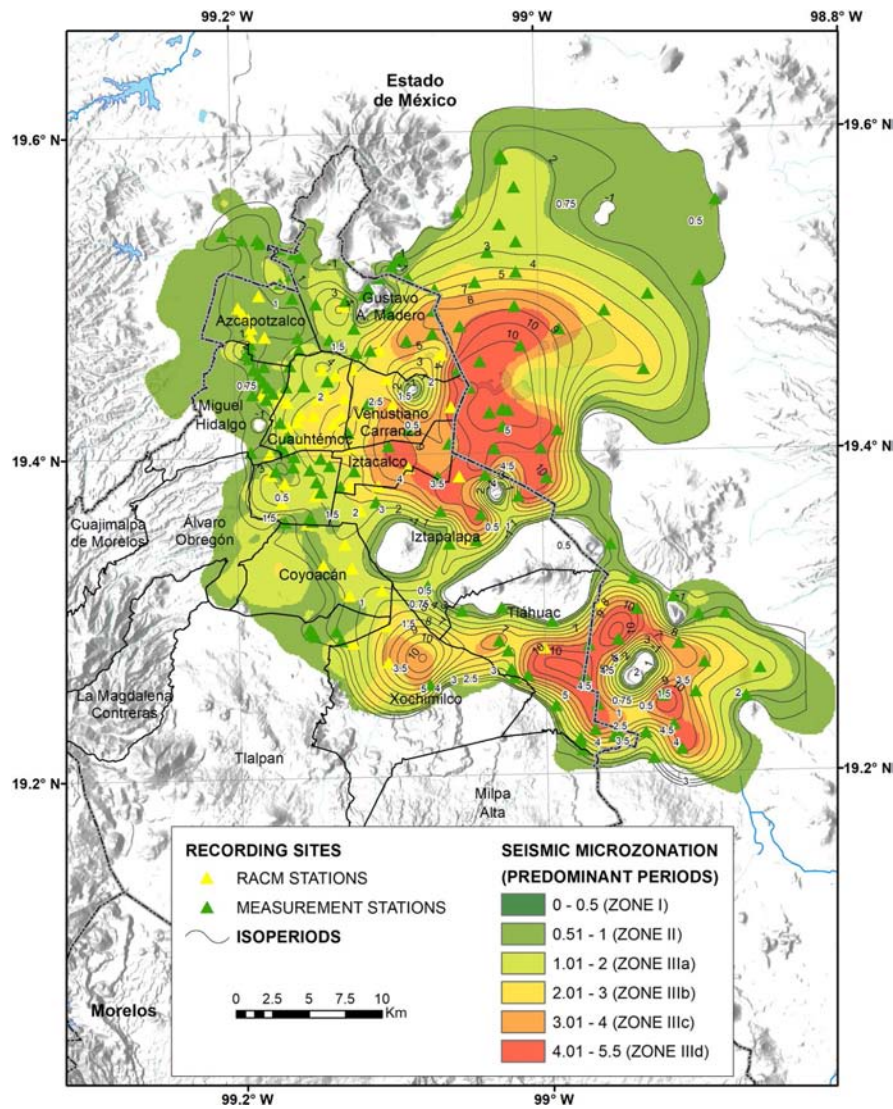


**Fig. 1** Seismic micro-zonation of CDMX. Recording sites data of the Accelerographic Network of Mexico City (RACM) and stations’ locations of new measurements indicated by yellow and green triangles, respectively

## 4 Volcanic hazard in Mexico City

### 4.1 Eruption of a new volcano in the Younger Chichinautzin Monogenetic Field

CDMX lies in the Trans-Mexican Volcanic Belt, an active Miocene to recent geological structure that spans central Mexico from the Pacific Ocean to the Gulf of Mexico (e.g., Ferrari et al. 2012). Unlike most volcanic arcs associated with subduction processes,



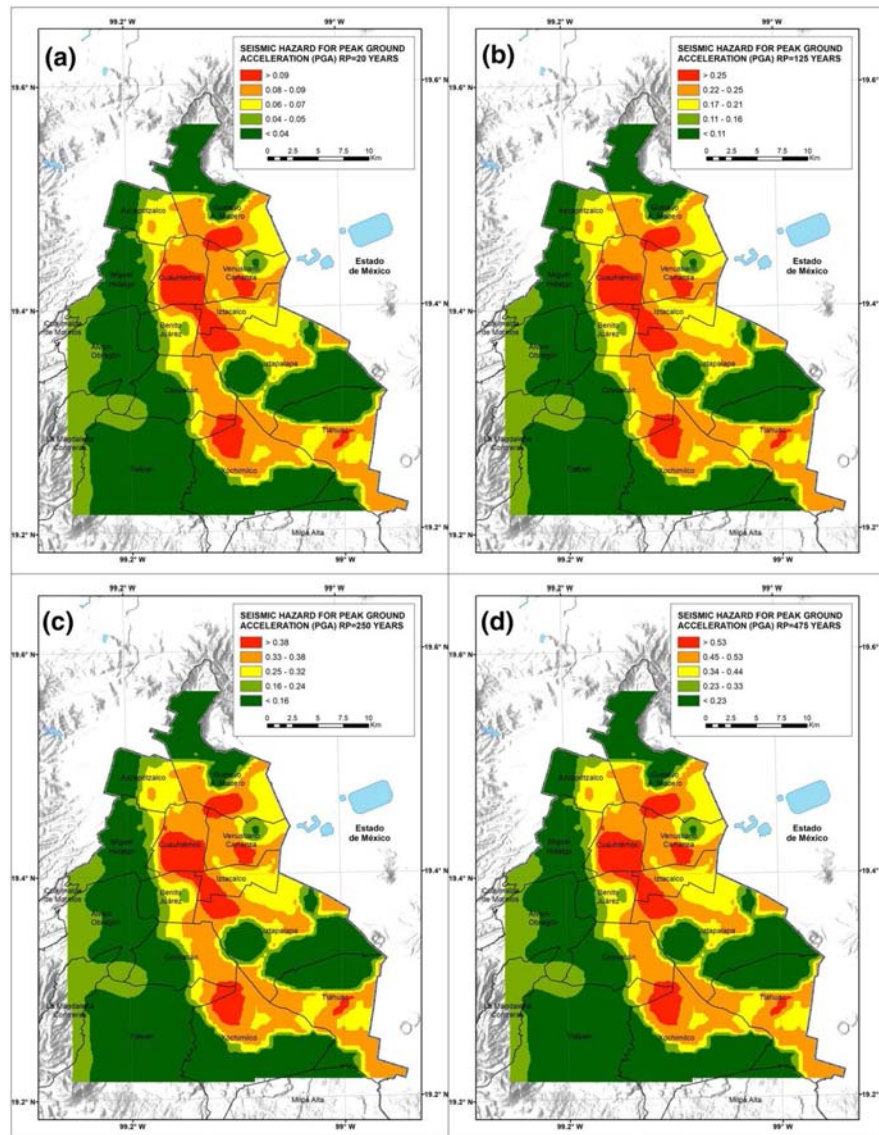


**Fig. 2** Seismic hazard for peak ground acceleration (PGA) (g) for return periods of 20, 125, 150, and 475 years

the TMVB is oblique and not parallel to the trench where the Cocos and Rivera plates subduct beneath North America (Pardo and Suárez 1995). In this geological context, the CDMX is exposed to hazards presented by the surrounding volcanic structures.

One of these volcanic hazards stems from the Younger Chichinautzin Monogenetic Field (YCMF). This is a volcanic structure to the south of CDMX that is of particular interest due to its very young age and its potential impact on the city. Historical eruptions of

the YCMF occurred at a time when the region was sparsely inhabited (Martin-Del Pozzo 1982; Córdoba et al. 1994; Martin-Del Pozzo et al. 1997). The lava flows covered an area of 70 km<sup>2</sup> in southern CDMX burying the Cuicuilco civilization (Martin-Del Pozzo et al. 1997; Siebe 2000). Later, the Chichinautzin volcano erupted in 1835 BP covering a very large area of southern CDMX (Martin-Del Pozzo et al. 1997). Clearly, a new eruption in this region would have devastating consequences for the population and infrastructure of CDMX. To extend the existing studies of volcanic hazard in CDMX, we incorporated the recent work of Nieto-Torres and Martin-Del Pozzo (2019) and Nieto-Torres (2020), who estimated probabilistically the hazard associated with the eruption of a new volcano in the YCMF.

The volcanic activity of the YCMF was analyzed to probabilistically forecast future eruptions, assuming that this potential activity would follow a similar pattern in time as past volcanic eruptions. To this end, the monogenetic volcanoes of the YCMF were dated based on morphometric analysis (Wood 1980; Martin-Del Pozzo 1982; Hooper 1995). Wood (1980) proposed that the rate between the volcano's height ( $H$ ) and width ( $W$ ) is a rough indicator of the volcano's age. Thus,  $H/W$  is higher for relatively young volcanoes than for older ones. This rate is called the volcano youth index ( $I_j$ ).  $I_j$  were measured from multispectral images, topographic maps, digital elevation model (DEM), and fieldwork in the area. Nieto-Torres (2020) and Nieto-Torres and Martín-Del Pozzo (2019) used the ages of the volcanic edifices to determine a probability function for future eruptions of the YCMF in a 5 × 5 km grid.

Based on a *Grid Probability Analysis* (Song et al. 2013), three areas (A, B, C) located close to the volcanoes with the most recent eruption history were identified to have a high probability of generating a new volcano in the YCMF (Fig. 3a). The results of the analysis

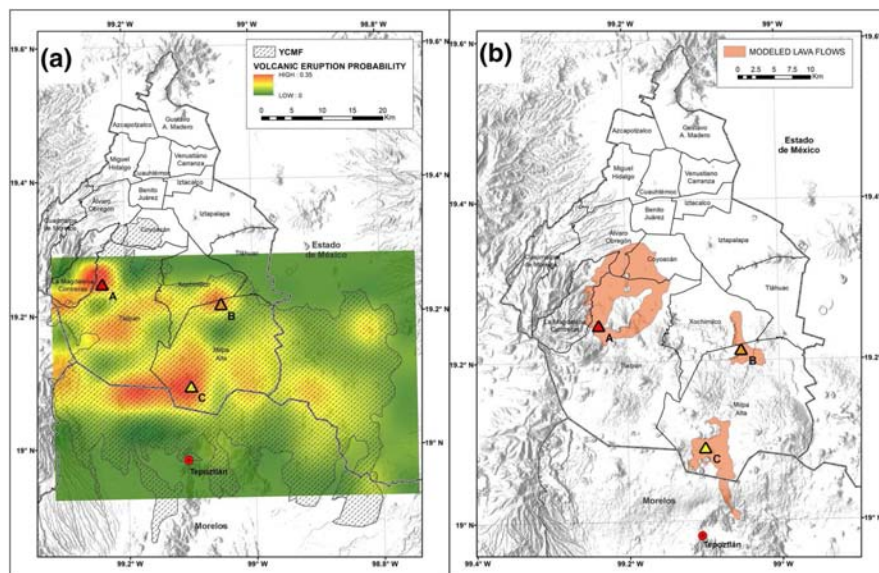


**Fig. 3** a Zones A, B, and C indicate the more probable sites where a new volcano could erupt in the Younger Chichinautzin Monogenetic Field (YCMF). The spatial probability of hosting a future eruption in the YCMF is also indicated; b expected lava flows scenarios for zones A, B, and C (see text). From Nieto-Torres and Martin-Del Pozzo (2019) and Nieto-Torres (2020)

show that there is 0.99 probability that a new eruption could take place in a 2000-year window for the whole YCMF. This value agrees with the observation of Siebe et al. (2004) who suggest that eruptions in the YCMF have recurrence rates of ~1700 years. The hazard posed by this field of monogenetic volcanoes is highlighted by the fact that the last eruption took place 1670–2030 years BP.

Lava flows from each of these A, B, and C volcanic zones were modeled to estimate their potential thickness and areal span (Nieto-Torres 2020). This modeling was performed using the *Etna Lava* (Damiani et al. 2006) and the *Q-LAVHA* models (Mossoux et al. 2016) (Fig. 3b). Eruption in Zone A shows a scenario that would impact deep into Mexico City resulting with 5-m-thick fluid lavas, extending for 12 km; this scenario is to past volcanic activity of Xitle volcano (Nieto Torres and Martin-Del Pozzo 2019). In Zone B, viscous lavas with a thickness of about 150 m and a distance range of 5 km were modeled, considering that the eruption would be as those from the neighboring Xicomulco volcano (Nieto-Torres 2020). In the expected scenarios for Zone C, eruptions would produce fluid lava flows with thickness on the order of 3 m and travel distances in the range of 15 km (Fig. 3b) (Nieto-Torres 2020).

Nieto-Torres (2020) also modeled the spatial distribution of ashfall for volcanic eruptions in zones A and C using the software *Tephra* (Courtland et al. 2012). Ashfall for an eruption in region B was not considered because in this area previous volcanic activity consisted mainly of lava effusion. Nieto-Torres (2020) ashfall scenarios would result in many exposed elements in CDMX (population, houses, and critical infrastructure). Also, about 27 km<sup>2</sup> of agricultural and 23 km<sup>2</sup> of forested areas would be impacted. Primary communication routes in CDMX would be exposed and could delay the delivery of materials and medical supplies, as well as the operation of basic services such as banks, gas stations, hotels, self-service stores, airports, etc. Additionally, these ash deposits would cause health and sanitary effects.

## 5 Subsidence of the ground in CDMX

Land subsidence is generally related to the consolidation of fine-grained materials in response to the extraction of fluids from underground compressible soil (Galloway and Burbey 2011; Herrera et al. 2021). Subsidence in CDMX is a major hazard due to the intensive water extraction rates from its underlying lacustrine, water-saturated sediments. Ground subsidence was first reported in CDMX in the early twentieth century. It is estimated that parts of CDMX have subsided as much as nine meters since the mid nineteenth century (Gayol 1925; Carrillo 1948).

In the past decade, subsidence of the city has been studied with modern geodetic techniques (Cabral-Cano et al. 2008; López-Quiroz et al. 2009; Osmanoglu et al. 2011; Chaussard et al. 2014; Du et al. 2019; Fernández-Torres et al. 2020; Solano-Rojas et al. 2020; Cigna and Tapete 2021). In this study, subsidence in CDMX was analyzed using 125 images recorded between November 2014 and October 2017 by the C-band SAR (Synthetic Aperture Radar) instrument onboard the Sentinel 1-A and B in Interferometric Wide Swath, descending mode (Fig. 4a). The dataset was processed using the *ISCE* software (Rosen et al. 2012) to generate interferometric pairs and SBAS time-series using the program *MintPy* (Yunjun et al. 2019). Following Osmanoglu et al. (2011), the former GPS site UCHI was used as the reference point along with stations UTUL and UFXN that are part of the TLALOC Net GPS network (Cabral-Cano et al. 2008).

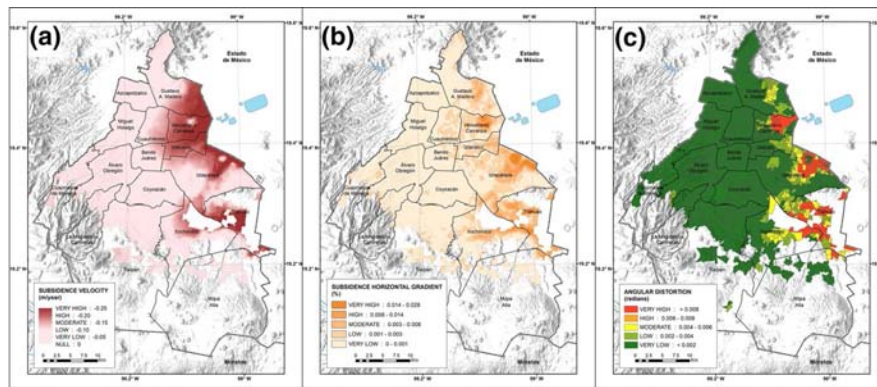


**Fig. 4** Spatial distribution of: **a** subsidence rate; **b** horizontal subsidence gradient; **c** angular distortion for the CDMX

The zones with very high subsidence rates with more than 25 cm/yr (line of sight) are concentrated toward the northeast, southeast, and east of CDMX (Fig. 4a). In some cases, these large subsidence rates result in soil fractures.

### 5.1 Horizontal subsidence gradient

A horizontal subsidence gradient (HSG) was also determined for detecting areas with the potential to generate fractures and faults due to differential subsidence (Cabral-Cano et al. 2008, 2015). Our results are presented within the spatial framework of the Basic Geo-statistical Areas (AGEB). An AGEB is defined by the Mexican Institute of Geography and Statistics (INEGI) as a basic geographic area where a group of city blocks (1–50) are well delimited by streets and avenues or any other easily identified urban feature where the land use is mainly for housing, industry, commerce, and other urban services.

Based on the AGEB spatial distribution, three regions with large HSG (0.014–0.024%) were identified mainly to the east of CDMX (Fig. 4b). These high-gradient zones are located on the abrupt transition between lacustrine sediments undergoing subsidence and the stable volcanic rocks (Cabral-Cano et al. 2008, 2015). In these areas, considerable differences in relative vertical motion develop over short distances, resulting in high horizontal strain and surface faulting that eventually fracture buildings (Burland et al. 2004).

### 5.2 Angular distortion

Angular distortion ( $\beta$ ) is the ratio of the differential subsidence ( $\delta$ ) between two surface points located at a distance ( $L$ ) (Ricceri and Soranzo 1985):

$$\beta = \delta/L \quad (1)$$

Skempton and Macdonald (1956) proposed expected levels of damage due to angular distortion variations based on studies throughout the world (the UK, Austria, Brazil, the USA, and Mexico) (Table 1). These values are now used as a reference for construction design (Meyerhof 1956; Bjerrum 1963; Wahls 1981).

**Table 1** Values of angular distortion and their impact to structures (Skempton and Macdonald 1956)

Angular distortion (radians)	Impact to structures
0.0066	Cracking panels in traditional frame buildings or on the walls of load-walled structures
0.0033	Structural damage to columns and beams
0.0020	Design limit to prevent cracking
0.0010	Design limit to avoid any damage due to subsidence

For a clear representation of the angular distortion worst-case scenario, we assigned its maximum value to each of CDMX's AGEBS (Fig. 4c). As expected, the higher angular distortion rates ( $>0.008$  radians) are observed in the municipalities located to east of the city, near the boundary between the soft soils and the volcanic terrains (Fig. 4c), damaging structures located in this region (Table 1).

## 6 Floods

Despite the intensive and ambitious engineering projects undertaken to drain CDMX during periods of heavy rain, the closed nature of the basin coupled to the continued land subsidence induced by water extraction of the subsoil creates a permanent threat of flooding in several parts of the city.

### 6.1 Return period and volume

To estimate the return period of floods, we analyzed the hydrological characteristics of the greater Metropolitan Zone of the Basin of Mexico (MZBM) that extends beyond the political boundaries of CDMX and was geographically divided into 250 regions "tributary stream areas" that were determined considering the local topography, land use, and drainage. The precipitation data from pluviometric stations were obtained from the Mexican National Water Commission for the period 1920 to 2015 (<http://clicom-mex.cicese.mx>).

The analysis was restricted to pluviometric records comprising twenty or more years and with complete daily rain datasets from June to October, the rain season in Mexico City. For each selected station, we obtained the maximum rainfall per year and a frequency analysis was performed using the software *Ax* developed by CENAPRED that allows the estimation of probability functions for temporal series (Jimenez 1996).

The effective rainfall was obtained multiplying the rainfall sheet for a specific return period by the runoff coefficient of each tributary area considering the type of soil and land use (Goel 2011):

$$h_{ei}^{Tr} = h_i^{Tr} C_{ei} \quad (2)$$

where:

$i = 1, 2, 3, \dots, 250$ : identifies the tributary area.

$h_i^{Tr}$ : rainfall sheet for the tributary area  $i$  and return period  $T_r$ .

$C_{ei}$ : runoff coefficient for tributary area  $i$ .

$h_{ei}^{Tr}$ : effective rainfall sheet (m) for the tributary area  $i$  with return period  $T_r$ .

The flood volume for each tributary area ( $V_{ind_i}^{Tr}$ ) was obtained by multiplying the effective rainfall sheet for a determined return period ( $h_e^{Tr}$ ) by the area of the tributary area ( $A_i$ ) (Goel 2011):

$$V_{ind_i}^{Tr} = A_i h_e^{Tr} \quad (3)$$

Assuming that the flood volume in each tributary area is concentrated in zones of low topographic elevation in a hemisphere, the water volume was estimated from the following equation:

$$V_{inu} = \frac{\pi h^2}{3} (3r - h) \quad (4)$$

where:

$V_{inu}$ : flood's volume ( $m^3$ ).

$h$ : flood's height (m)

$r$ : hemisphere's radius (m).

To estimate the water mirror's area ( $A$ ) and the flood's radius ( $a$ ), we used the following equations:

$$A = \pi a^2 \quad (5)$$

$$a^2 = 2rh - h^2 \quad (6)$$

## 6.2 Flood area

The flood areas were estimated using the following data:

- The water volume database obtained following the procedures described above for each tributary area.
- The vector data of each tributary area.
- The DEM of CDMX.

With this information, the procedure to estimate the flood area is as follows:

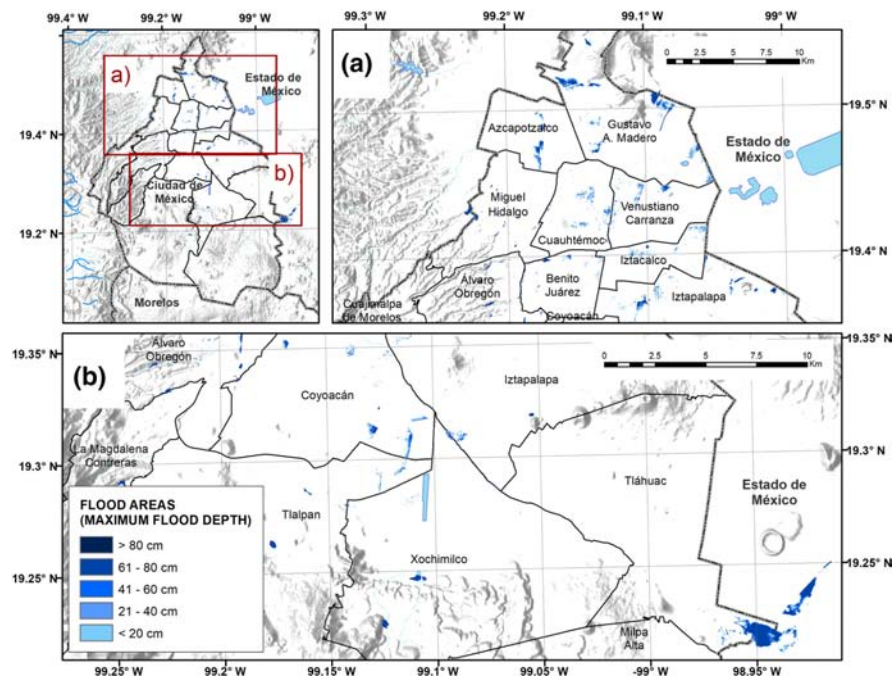
*Step 1:* Flood heights were calculated considering the water volumes resulting from the different return periods. Using the DEM of CDMX, a 3D elevation model was determined with topographic contours every 0.10 m. Based on these data and using the "Polygon Volume" function of ArcGis10.3, we computed the water volume for a specific tributary area. These procedures were repeated until the theoretical volume (described above) was reached for the return periods considered. The topographic contours that contain the estimated volume provide the most probable zones that could potentially be flooded in the MZMV.

*Step 2.* With the tool *Extract by Mask* of ArcGis10.3, the raster of the flooding area was extracted, and a new classification was obtained considering five flood heights where less than 20 cm and greater than 80 cm correspond to very-low and very-high hazard levels, respectively (Table 2).

Following these procedures, floods in CDMX were estimated for return periods of 2, 5, 10, 50, and 100 years, as established by CENAPRED (Fig. 5). Most of the potential flood

**Table 2** Flood hazard according to flood's height

Hazard level	Flood height (cm)
Very low	< 20
Low	20–40
Moderate	40–60
High	60–80
Very high	> 80

**Fig. 5** Flood hazard estimation for a return period of 10 years in the CDMX

areas in MZMV are concentrated in the central and in the northern part of its territory. This is coincident with the flood inventory for the period 1920–2017 compiled as part of this project (Online Resource 1).

The explosive urban growth has dramatically enlarged the impervious zone in Mexico City and increased the volume of rainwater that must be drained out of the basin. In many cases, the local drainage network is insufficient for this task. This situation leads to recurrent large flooding causing serious urban damage in CDMX.

## 7 Forest fires

The Mexican National Forest Commission (CONAFOR) installed in 1999 an early warning system (EWS) to alert for forest fires. This EWS is designed to evaluate and reduce the hazard represented by these fires. It is based on measurements of temperature, relative humidity, precipitation, and wind velocity. Using an index based on the initial propagation velocity and available fuel, the CONAFOR's EWS provides a meteorological index for fire hazard ([http://forestaes.ujed.mx/incendios/inicio/evolucion\\_del\\_peligro.php#](http://forestaes.ujed.mx/incendios/inicio/evolucion_del_peligro.php#)).

In this project, the forest fire EWS was extended to forecast fires in the long term with the purpose of supporting local authorities in the development of preventive actions to reduce risk to the exposed population. We used satellite data from the NASA's Fire Information for Resource Management System (FIRMS) ([https://firms.modaps.eosdis.nasa.gov/active\\_fire/#firms-shapefile](https://firms.modaps.eosdis.nasa.gov/active_fire/#firms-shapefile)) for the period 2000 to 2019. This database provides fire hot-spots locations, including coordinates, temperature, brightness, and resolution.

Fire hazard estimations are based on the *Clustering Machine Learning* tool to group temperature and brightness in clusters (Buduma and Locascio 2017). For our calculations, we used the *boasted trees* algorithm to analyze cluster data (Maloof 2005). This algorithm identifies groups of similar objects and establishes the pattern distribution of large datasets. Decision trees are machine-learning tools where each tree is dependent on previous trees. The algorithm "learns" continuously by fitting the residual of preceding trees.

The probability of fire occurrence was estimated for the rain and dry seasons for the next five years for the eastern, and southern regions of CDMX (Fig. 6a, 6b). During the rainy season (May–November), there is moderate probability (41–60%) of forest fires south of CDMX for the next five years (Fig. 6a). However, during the dry season (December–April), southern CDMX has high probability of forest fires (> 81%) in the forests of the Tlalpan, Xochimilco, and Tláhuac municipalities (Fig. 6b).

Using the *Machine Learning* tool, we also forecast the number of expected forest fires up to the year 2028 (Fig. 6c). We estimated that during the year 2025, there is a high probability that ~1400 forest fires occur in CDMX (Fig. 6c). This number is higher than the number of previous forest fires during the 1970–2020 periods. This forecast is based on the decadal periodicity of wildfires in CDMX. Our model predicted that in 2020 a new high-forest fire season initiated and that it will reach its peak around 2025.

## 8 Landslide hazards in Mexico City

Several municipalities of CDMX are located on the volcanic deposits that form the Las Cruces, Guadalupe, and Chichinautzin (LCGC) ridges to the west and southern areas of the city. These volcanic edifices constitute the limits of the lacustrine basin. Besides the natural instability associated with the steep slopes of the terrain, land alteration due to urban growth and erosion has increased the susceptibility for the occurrence of landslides and rock falls in these regions. In addition, several communities are irregular settlements, increasing the exposure to landslides.

As a first step to estimate landslide susceptibility, an inventory was compiled for the period 1972 to 2018. The database was constructed from local newspapers reports, the Internet platform *Desinventar* (<https://www.desinventar.org>), and information provided by municipalities of CDMX. *Desinventar* is a tool containing data of human and material



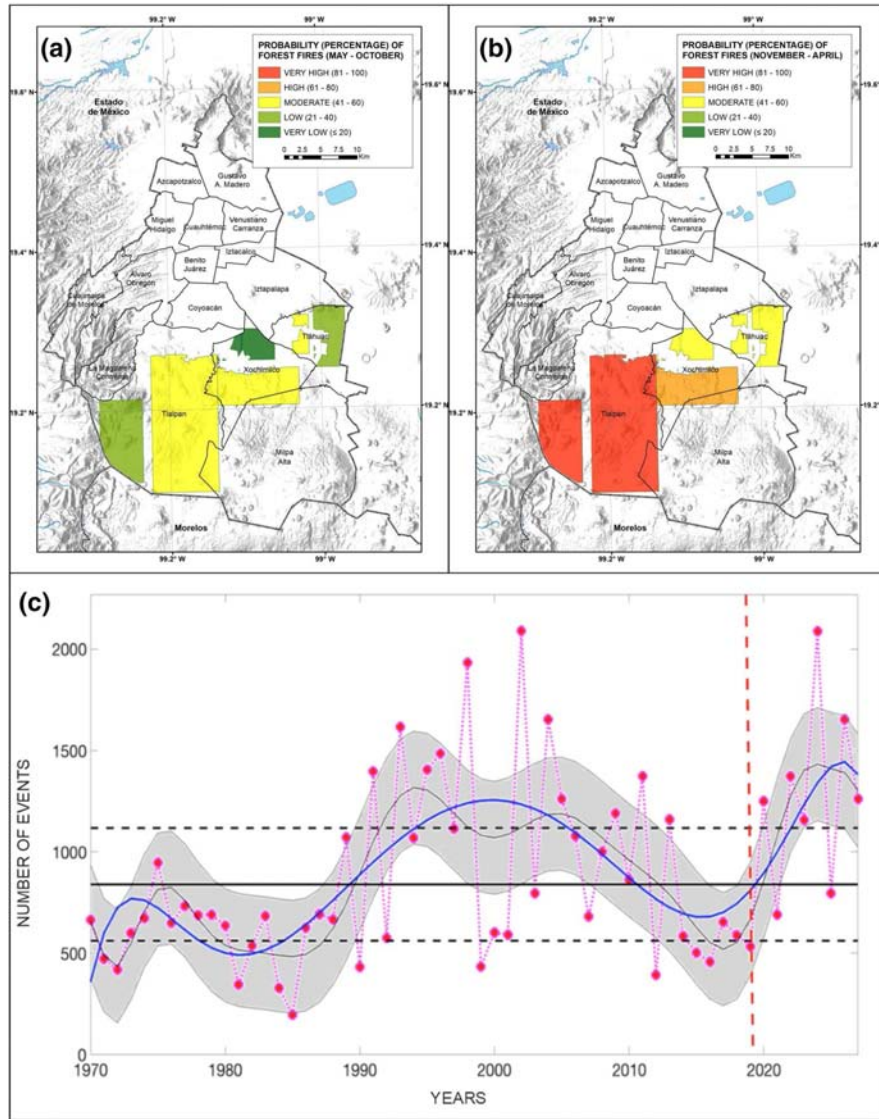


**Fig. 6** **a** Probability of forest fires occurrence in CDMX during the rainy season for the following five years (2021–2025); **b** the same as **a** for the dry season; **c** forest fire forecast from 2020 to 2028. Red dots are the annual number of forest fires reported by the Mexican National Forest Commission until 2020. The blue line approximates the data’s tendency. The vertical red dashed line separates the historical from the forecast data. The horizontal solid and dashed lines indicate the mean and standard deviation, respectively. The shadowed area outlines the 95% confidence interval

losses, damages, disasters, and events that have impacted different countries in Latin American and the Caribbean. Our landslide and rock fall inventory included the location, date of occurrence, size, typology, and damage. However, all this information was not available for some events.

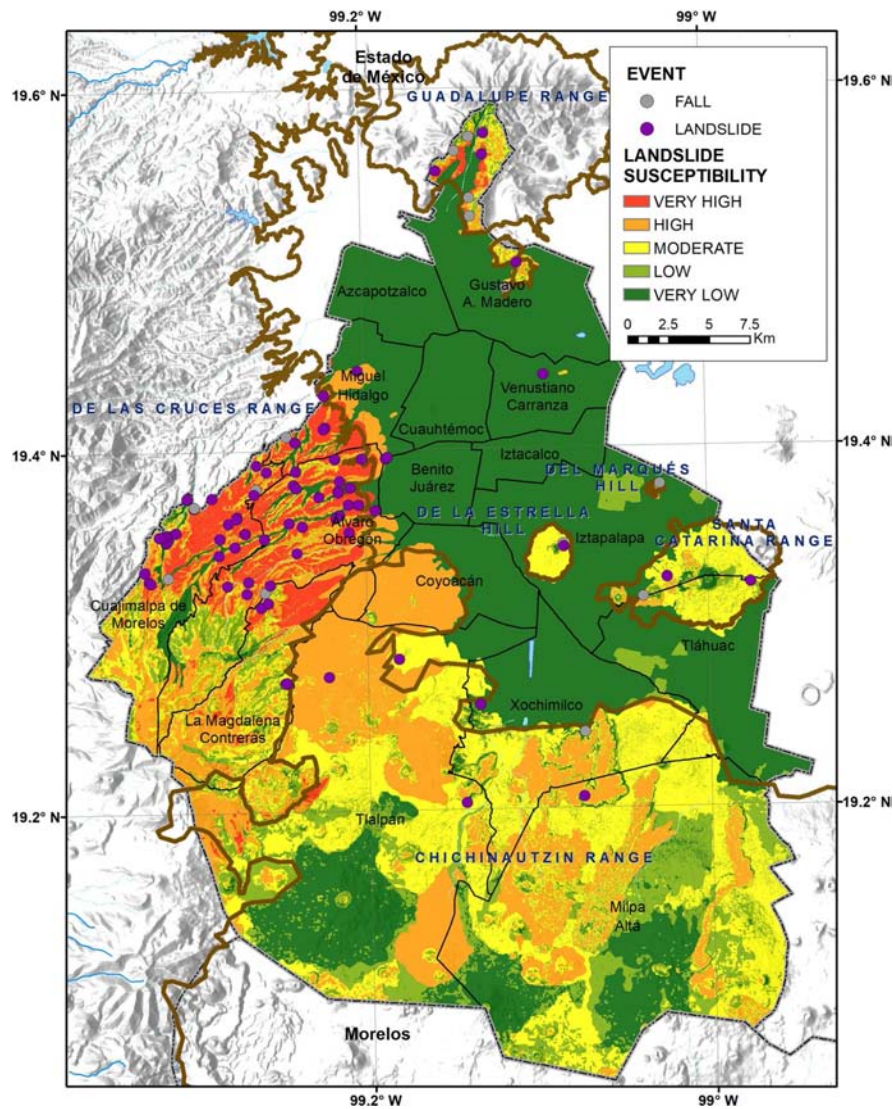


**Fig. 7** Inventory of landslides and rock falls (purple and gray solid circles) and spatial distribution of landslide susceptibility

We recorded more than 100 landslides in the inventory and as expected, most of them occurred during the rainy season, from May to November. Many of these events are concentrated in the western part of CDMX. However, some are also reported around the hills in the eastern part of the city in the LCGC and the Santa Catarina ranges (Fig. 7).

The landslide susceptibility estimation also included fieldwork, interpretation of satellite images, analysis of samples in laboratory, and municipal inventories. We used a 5-m resolution DEM to generate the hypsometric and slope maps. Using the univariate

**Table 3** Weights for parameters used to estimate landslide susceptibility

Parameter	Weight
Geology	0.60
Slope	0.20
Relative height	0.10
Land use and vegetation	0.10
Total	1.00

statistical method (Denis 2020), and after testing different weights to identify those with less uncertainty for different scenarios, we weighed each of these parameters according to their assumed importance for a landslide to occur. We considered geology as the principal parameter that conditions the characteristics of landslide susceptibility, followed by the slope, relative height, land use, and type of vegetation (Table 3). Also, each variable within each parameter was weighed considering relative values from 1 to 5 to indicate how much that variable increases the landslide susceptibility with 1: very-low and 5: very-high (Table 4). To geology, values of 5 were given to very altered rocks with fractures and faults of andesite, dacite, and lahar deposits as well as pumice flow, volcanic ash, and alluvial deposits. To slope  $> 60^\circ$ , relative heights  $> 100$  m, and human settlements parameters, we also assigned values of 5 (Table 4). The results were classified in five categories of susceptibility (Fig. 7): very low, low, moderate, high, and very high.

The results of this study are intended to support the development of preventive actions and land use policies designed to avoid the catastrophes and loss of life associated with landslides and rock falls in the past 50 years (García-Palomo 2006).

## 9 Social vulnerability of CDMX

Social vulnerability is an intrinsic characteristic of society that is independent of its exposure to natural and man-made hazards. However, social vulnerability is the most complicated component of risk to measure. This is because the concept is given varying interpretations and conceptual frameworks by different authors (Cutter et al. 2003; Rashed and Weeks 2003).

We consider thirteen indicators that reflect the social characteristics of the population, such as age, access to basic services (electricity, water, drainage, etc.), income, and educational level (Table 5). These indicators were obtained from the 2010 Mexican Census of Population and Housing (Instituto Nacional de Estadística, Geografía e Informática 2010; <https://www.inegi.org.mx/programas/ccpv/2010/>). We excepted housing's indicators, because this Census lacks information regarding the type of structure or dwelling. Each of the selected indicators was weighed using the *Hierarchical Analytical Process* (HAP) (Saaty 1980). Saaty (1987) pointed out that “*The HAP is a general theory of measurement. It is used to derive ratio scales from both discrete and continuous paired comparisons. These comparisons may be taken from actual measurements or from a fundamental scale that reflects the relative strength of preferences and feelings.*” The HAP was applied considering the opinion of experts from CENAPRED and from the authors of this work (Table 5). As a result of this methodology, the parameters that were given larger weights are population density, access to information, level of education, and availability of basic

**Table 4** Weights for the variables considered to estimate landslide susceptibility

Variable	Weighting
<i>Geology</i>	
Lake alluvial deposits	1
Basalt (Quaternary)	2
Andesite (Quaternary)	2
Basaltic andesite (Quaternary)	2
Alluvial deposits (foothill)	3
Andesite	3
Basalt	3
Andesitic-basaltic (altered lavas)	3
Dacite	3
Basaltic andesite (cones)	3
Andesite (very altered and fractured rocks)	4
Basalt (Very altered and fractured rocks)	4
Basaltic andesite (very altered and fractured rocks)	4
Dacite (very altered and fractured rocks)	4
Basaltic andesite (very altered cones)	4
Basalt (very altered cones)	4
Lahar deposit	4
Pumice flow	4
Avalanche	4
Andesite (very altered rocks with fractures and faults)	5
Dacite (very altered rocks with fractures and faults)	5
Lahar deposit (very altered rocks with fractures and faults)	5
Pumice flow and volcanic ash	5
Alluvial deposits (slope)	5
<i>Slope (degree)</i>	
0°–5°	1
5°–15°	2
16°–30°	3
45°–60°	4
> 60°	5
<i>Relative Height (m)</i>	
0–10	1
11–20	2
20–50	3
50–100	4
> 100	5
<i>Land use and vegetation</i>	
Body of water	1
Hydrophilic and halophilic	1
Tule	1
Oyamel forest	2
Sarcocaulous shrubland	3
Cultivated grassland	3

**Table 4** (continued)

Variable	Weighting
Halophile grassland	3
Induced grassland	3
Secondary shrub vegetation of oyamel forest	3
No apparent vegetation	4
Annual irrigation agriculture	4
Urban Zone	4
Human settlements	5

Very low: 1; low: 2; moderate: 3; high: 4; very high: 5

**Table 5** Weights for indicators used to assess social vulnerability

Indicator	Description	Weighting ( $w_i$ )
SV <sub>1</sub>	<i>Health</i> Percentage of population with access to public or private health services	0.069
SV <sub>2</sub>	<i>Education and Knowledge</i> Percentage of illiteracy	0.80
SV <sub>3</sub>	Percentage of population between 6 and 14 years old that do not attend school	0.065
SV <sub>4</sub>	Percentage of devices or technology for accessing information	0.110
SV <sub>5</sub>	Level of education	0.107
SV <sub>6</sub>	<i>Housing</i> Percentage of housing without basic services	0.117
SV <sub>7</sub>	Percentage of houses with dirt floor	0.058
SV <sub>8</sub>	Percentage of overcrowding (number of family members/ numbers of rooms)	0.087
SV <sub>9</sub>	<i>Employment</i> Percentage of economic dependency ratio	0.040
SV <sub>10</sub>	<i>Population</i> Population density	0.107
SV <sub>11</sub>	Percentage of indigenous-speaking population	0.055
SV <sub>12</sub>	Percentage of population with disabilities	0.074
SV <sub>13</sub>	Percentage of female-headed households	0.030

services (Table 5). To map the spatial distribution of the social vulnerability (SV) of CDMX, the social indicators were processed as follows:

1. For each AGEB in CDMX, we determined the proportional contribution of the following indicators: SV<sub>1</sub>, SV<sub>2</sub>... to SV<sub>13</sub> (Table 5).
2. SV<sub>5</sub> reflects the average of completed education years within each AGEB.
3. SV<sub>10</sub> reflects the population density, and it is estimated as the ratio of the number of inhabitants and the area of each AGEB.
4. SV is then calculated using the following equation:

$$SV = \sum_{i=1}^{13} SV_i * w_i \quad (7)$$

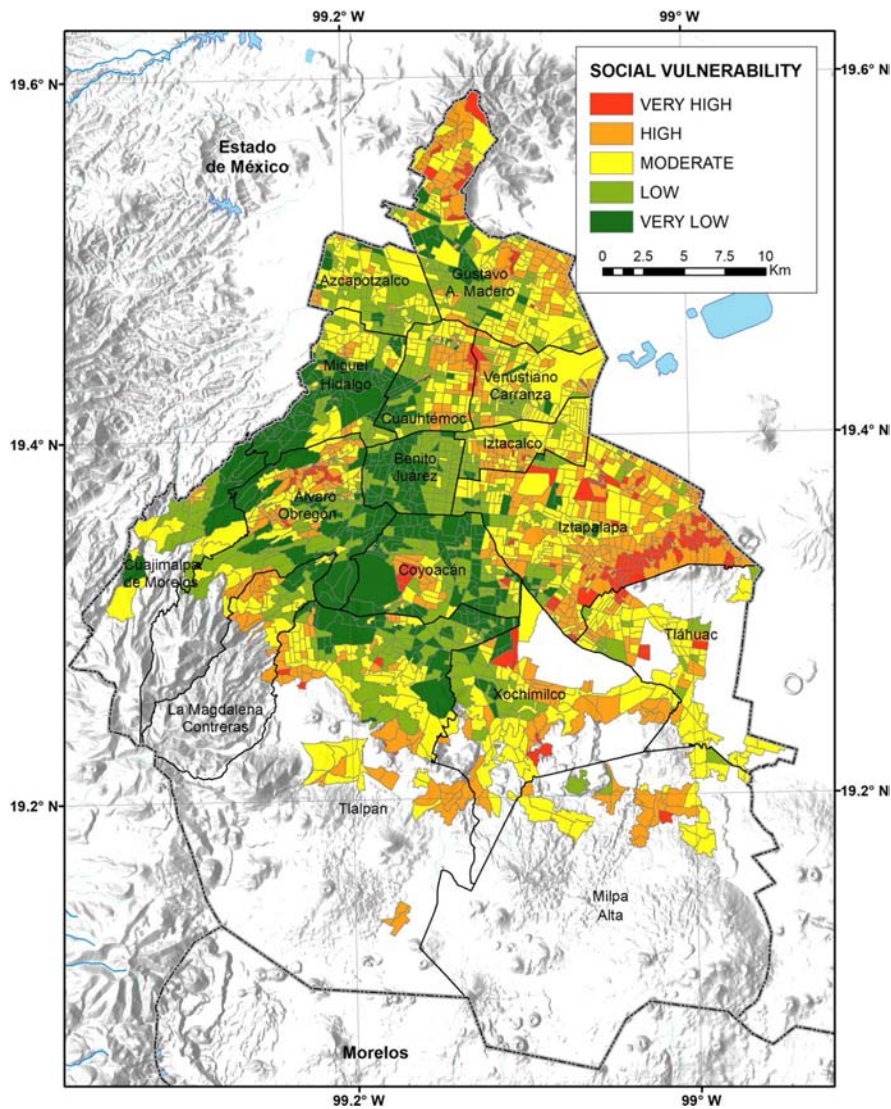


**Fig. 8** Map with the spatial distribution of social vulnerability in CDMX obtained considering the variables of Table 5 and data processing as described in Sect. 9

where  $w_i$  are the weights obtained applying the HAP methodology (Saaty 1987; Table 5). Using Eq. (7) the social vulnerability of CDMX was classified into five levels: very low, low, moderate, high, and very high by utilizing the *Jenks Natural Breaks* classification of the ArcGIS10.3 that reduces the deviation from the class mean (Fig. 8). Our results show that social vulnerability varies between moderate and very high in the north, northeast, east, and central regions of CDMX (Fig. 8). Unfortunately, more than half of the population of CDMX has a level of social vulnerability that varies between

moderate and very high that may be closely tied to the average socioeconomic level of the population.

## 10 Exposure

Exposure refers to the people, communities, and their assets that are predisposed to a particular hazard. The RA-GIS contains GIS layers of the following exposed elements: population, population density, public schools (elementary, high school, college-university), hospitals, markets, fuel and radio stations, free connectivity sites (free internet places), and TV stations. We found a large fraction of the population and of critical infrastructure in CDMX exposed to the different hazards here analyzed (Online Resource 1).

## 11 Social risk

Risk measures the probability of damage considering the combination of three factors: hazard, vulnerability, and exposure (Crichton 1999; Cutter et al. 2003). According to the United Nations Disaster International Strategy for Disaster Reduction (2009), social risk is “*The probability of possible losses (loss of human life, injury, disturbance in economic activities, goods deteriorated or destroyed, alterations of the environment) determined by a certain danger, under some circumstances of exposure and vulnerability*” (UNISDR 2009).

In this work, risk is expressed using a qualitative spatial multi-criteria evaluation technique by superimposing the raster of the social vulnerability over individual hazard rasters. We consider that by using this method we are measuring the “*likelihood of social risk*.” Vulnerability and hazard are classified into five categories, with values from 1 to 5. As a result, a meshing array reflects the likelihood of social risk for specific hazards. Under these considerations, the minimum and maximum values of risk are: 1 (1\*1) and 25 (5\*5). Risk is then classified in five intervals from very low to very high (Table 6) and its spatial distribution is obtained using a Kriging spatial interpolation method (Burrough and McDonnell 1998).

Following these procedures, large extensions in the northeast and east of CDMX show moderate to high levels of social risk due to subsidence (Fig. 9a). On the other hand, seismic social risk also varies from moderate to high in the central as well as the eastern and northeastern region of CDMX (Fig. 9b).

**Table 6** Classification of risk

Level of risk	Score
Very low	1–5
Low	6–10
Moderate	11–15
High	16–20
Very high	21–25

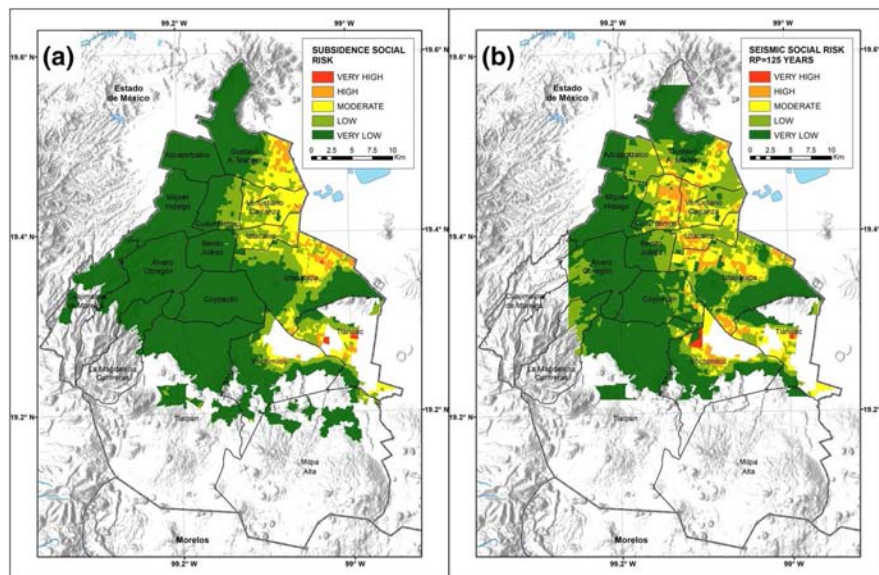


Fig. 9 Social risk in the CDMX for: **a** subsidence; and **b** an earthquake with a return period of 125 years

## 12 Examples of seismic risk scenarios

As an integral part of the Risk Atlas of CDMX, we developed eight seismic risk scenarios (see maps in Online Resource 1). Scenarios 1 and 2 correspond to the September 19, 2017, and September 17, 2017, earthquakes, respectively. Scenarios 7 and 8 reflect the potential damage expected from an earthquake similar to the Acambay earthquake ( $M_w$  6.9) that took place on November 19, 1912, at distances of 80 and 40 km from CDMX (Online Resource 1). Details about the procedures and the results from these scenarios will be presented in subsequent publications.

## 13 Retrospective

In general, there are three phases to mitigate and manage risk: (1) assessment and analysis; (2) implementation of mitigation and preventive actions based on the knowledge of the spatial distribution of risk; (3) design of short- and long-term plans to reduce the social construction of risk (public policies, land-use planning, environmental restoration, etc.). The objective of this paper is to present a tool to assess the level and the spatial distribution of social risk to subsidence, floods, earthquakes, volcanic eruptions, forest fires, and landslides in CDMX. Our results are a contribution to the first phase of risk management by providing hard evidence to local authorities and citizens to develop preventive actions and mitigation procedures to reduce the impact of future disasters in CDMX.

The main functions of this tool are:



- To provide decision and policy makers with appropriate risk information to strengthen their capacity to develop risk management strategies.
- To interactively view and retrieve different hazard, social vulnerability, and risk maps at the CDMX level.
- To view and retrieve the maps of exposed elements to the different hazards analyzed, including both, population, and infrastructure.
- Encourage the development of local case studies of social vulnerability and risk for specific hazards.
- Provide a catalyst for a holistic approach aimed at making CDMX a more resilient community.

Our findings also provide elements for the development of early warning systems. Also, our results point out areas where the relocation of population exposed to very high levels of natural hazards may be considered. Clearly, a complete analysis of the risk posed by man-made hazards (explosions, spills, etc.) and sanitary-ecological hazards (soil and air pollution, etc.) needs be considered in the future.

**Supplementary Information** The online version contains supplementary material available at <https://doi.org/10.1007/s11069-021-05059-z>.

**Acknowledgements** Our sincere gratitude to Aurora Hernández Hernández, Andrea Juárez Sánchez, Patricia Medina Andrade, Ana B. Ponce Pacheco, Alma R. Espinoza Jiménez, Uriel Martínez Ramírez, Guadalupe Hernández Bello, Paola A. Olmedo Velázquez, Omar Huerta Espinoza, Karla E. Escobar Mercado, Magdalena V. Hernández Luna, Diego E. López Maldonado, Nuria D. Vargas Huipe, Amalia E. Macías Rojas, Sabrina E. Espinosa Pacheco, Amayrani Martínez Mendoza, Daniel Ruiz Barón, Susana Rodríguez Padilla, Claudia B. López Venegas, Pamela I. Pedroza Rodríguez, Fernando García Yañez, Esteban Lugo Zavala, Jéssica Atilano Pablo, Heber A. Pacheco Silva, Karla P. Sánchez Albizar, Alma E. Macías Rojas, Sandra K. González Hernández, Brenda A. González Hernández, Mariana Sandoval García, Monserrat Luna Contreras, and Héctor Raúl Estévez Pérez for invaluable support for data acquisition, processing, storage and management, and for logistics coordination in the fieldworks. We thank the civil protection offices of the following CDMX municipalities: Álvaro Obregón, Azcapotzalco, Cuajimalpa, Cuauhtémoc, Gustavo A. Madero, Iztacalco, Iztapalapa, Magdalena Contreras, Miguel Hidalgo, Milpa Alta, Tlahuac, Tlalpan, and Xochimilco for their cooperation during our fieldwork and for providing data for the project. We are grateful to Hugo Delgado Granados, Gerardo A. Galguera Rosas, Vanesa Ayala Perea, and Viviana Torres Valle for their assistance in the administration of the project. We also, acknowledge Enrique Guevara Ortiz, Carlos Valdés González, Oscar Cepeda Ramos, and Leobardo Domínguez Morales of the Centro Nacional de Prevención de Desastres (CENAPRED), for sharing data and for encouraging the development of this research. Data were obtained from the following institutions: Servicio Sismológico Nacional, Instituto Nacional de Estadística y Geografía (INEGI), Secretaría de Comunicaciones y Transporte (SCT), Instituto Federal de Telecomunicaciones, Comisión Nacional del Agua (CONAGUA), Centro de Instrumentación y Registro Sísmico (CIRES), Comisión Nacional Forestal (CONAFOR), Secretaría de Educación Pública (SEP), Secretaría de Desarrollo Económico (SEDECO), Comisión Reguladora de Energía, and Instituto Federal de Telecomunicaciones (IFT). The Secretaría de Educación, Ciencia, Tecnología e Innovación (SECTEI) of CDMX funded this research (Convenio SECITI/12/2017). We also acknowledge the partial support from the National Autonomous University of Mexico under the “Programa de Apoyo a Proyectos de Investigación e Innovación Tecnológica (PAPIIT Projects No. IT102420, IN107321)” and the Consejo Nacional de Ciencia y Tecnología (CONACYT 2017-01-5955).

**Author contributions** D.A. Novelo-Casanova contributed to design, planning, supervision of the Atlas and estimates of social vulnerability, exposure, and risk; G. Suárez contributed to design, planning and supervision of the Atlas and estimation of seismic hazard and scenarios; E. Cabral-Cano, E.A. Fernández-Torres, E. Havazli and D. Solano-Rojas contributed to subsidence hazard; O.A. Fuentes-Mariles, E.D. López-Espinosa, and H.L. Morales-Rodríguez contributed to flood hazard; M.A. Jaimés contributed to seismic risk and scenarios; A.L. Martín-Del Pozzo and A. Nieto-Torres contributed to volcanic hazard and scenarios; S. R. Rodríguez-Elizarrarás and W.V. Morales-Barrera contributed to mass movement processes hazard; V.M. Velasco-Herrera contributed to forest fire hazard.

## Declarations

**Conflict of interest** The authors have no conflicts of interest to declare that are relevant to the content of this article.

**Open Access** This article is licensed under a Creative Commons Attribution 4.0 International License, which permits use, sharing, adaptation, distribution and reproduction in any medium or format, as long as you give appropriate credit to the original author(s) and the source, provide a link to the Creative Commons licence, and indicate if changes were made. The images or other third party material in this article are included in the article's Creative Commons licence, unless indicated otherwise in a credit line to the material. If material is not included in the article's Creative Commons licence and your intended use is not permitted by statutory regulation or exceeds the permitted use, you will need to obtain permission directly from the copyright holder. To view a copy of this licence, visit <http://creativecommons.org/licenses/by/4.0/>.

## References

- Abrahamson NA, Silva WJ (1997) Empirical response spectral attenuation relations for shallow crustal earthquakes. *Seism Res Lett* 68:94–127
- Aguilar J, Juárez H, Ortega R, Iglesias J (1989) The Mexico earthquake of september 19, 1985—statistics of damage and of retrofitting techniques in reinforced concrete buildings affected by the 1985 earthquake. *Earthq Spec* 5(1):145–151
- Auvinet G, Méndez E, Juárez, M (2013) Soil fracturing induced by land subsidence in Mexico City. In Proceedings of the 18th International Conference on Soil Mechanics and Geotechnical Engineering, Paris, 2921–2924
- Bard PY (1999) Microtremor measurements: a tool for site effects estimation? Effect of Surface Geology on Seismic Motion. Proc. 2nd Internat. Symp, Yokohama, Japan 1251–1279
- Bjerrum L (1963) Allowable settlement of structures. Proc European Conference on Soil Mechanic and Foundation Engineering, Wiesbaden, Brighton, England, 135–137
- Boyer ER (1975) *La gran inundación: vida y sociedad en México (1629–1638)*, Secretaría de Educación Pública, México, SepSetentas, 218, 151 p
- Buduma N, Locascio N (2017) *Fundamentals of Deep Learning: Designing Next-Generation Machine Intelligence Algorithms*. O'Reilly Media, Inc
- Burland JB, Mair RJ, Standing JR (2004) Ground performance and building response due to tunnelling. In *Advances in Geotechnical Engineering: The Skempton conference* 291–342
- Burrough PA, McDonnell RA (1998) *Principles of geographical information systems*. Oxford University Press, New York
- Cabral-Cano E, Dixon TH, Miralles-Wilhelm F, Díaz-Molina O, Sánchez-Zamora O, Carande RE (2008) Space geodetic imaging of rapid ground subsidence in Mexico City. *GSA Bull* 120:1556–1566. <https://doi.org/10.1130/B26001.1>
- Cabral-Cano E, Solano-Rojas D, Oliver-Cabrera T, Wdowinski S, Chaussard E, Salazar-Tlaczani L, Cigna F, DeMets C, Pacheco-Martínez J (2015) Satellite geodesy tools for ground subsidence and associated shallow faulting hazard assessment in central Mexico. *Proc IAHS* 372:255–260. <https://doi.org/10.5194/piahs-372-255-2015>
- Carrillo N (1948) Influence of artesian wells on the sinking of Mexico City. *Proc Second Int Conf Soil Mech Found Eng* 2:156–159
- Chaussard E, Wdowinski S, Cabral-Cano E, Amelung F (2014) Land subsidence in central Mexico detected by ALOS InSAR time-series. *Rem Sens Environ* 140:94–106. <https://doi.org/10.1016/j.rse.2013.08.038>
- Cigna F, Tapete D (2021) Present-day land subsidence rates, surface faulting hazard and risk in Mexico City with 2014–2020 Sentinel-1 IW InSAR. *Rem Sens of Environ*. <https://doi.org/10.1016/j.rse.2020.112161>
- Córdova C, Martin-Del Pozzo AL, López CJ (1994) Paleoland forms and volcanic impact on the environment of prehistoric Cuicuilco, southern Mexico City. *J Archaeol Sci* 21:585–596
- Courtland LM, Connor CB, Connor L, and Bonadonna C (2012) Introducing geoscience students to numerical modeling of volcanic hazards: The example of Tephra2 on VHub.org. *Numeracy*, 5(2), Article 6
- Crichton D (1999) The risk triangle. In: Ingleton J (ed) *Natural disaster management*. Tudor Rose, England


- Cutter SL, Boruff BJ, Shirley WL (2003) Social vulnerability to environmental hazards. *Soc Scien Quart* 84:242–261
- Damiani ML, Groppelli G, Norini G, Bertino E, Gigliuto A, Nucita A (2006) A lava flow simulation model for the development of volcanic hazard maps for Mount Etna (Italy). *Comput Geosci* 32:512–526
- Denis DJ (2020) Univariate, bivariate, and multivariate statistics using R: quantitative tools for data analysis and data science. Wiley Online Libr. <https://doi.org/10.1002/9781119549963>
- Du Z, Ge L, Ng AH-M, Zhu Q, Zhang Q, Kuang J, Dong Y (2019) Long-term subsidence in Mexico City from 2004 to 2018 revealed by five synthetic aperture radar sensors. *Land Deg Develop* 30:1785–1801. <https://doi.org/10.1002/ldr.3347>
- Duchon J (1977) Splines minimizing rotation invariant semi-norms in Sobolev spaces. In: *Constructive Theory of Functions of Several Variables*, Springer. Berlin 85–100, doi: <https://doi.org/10.1007/BFb0086566>
- Espinosa Aranda JM, Jiménez A, Ibarrola G, Alcántara F, Aguilar A, Henestroza M, Maldonado S (1995) Mexico City: seismic alert system. *Seismol Res Lett* 66:42–53
- Fernández-Torres E, Cabral-Cano E, Solano-Rojas D, Havazli E, Salazar-Tlaczani L (2020) Land subsidence risk maps and InSAR based angular distortion structural vulnerability assessment: an example in Mexico City. *Proc Int As Hydrol Sci, Copernicus GmbH* 382:583–587. <https://doi.org/10.5194/piahs-382-583-2020>
- Ferrari L, Orozco-Esquivel T, Manea V, Manea M (2012) The dynamic history of the trans-Mexican volcanic belt and the Mexico subduction zone. *Tectonophysics* 522:122–149
- Flores T, Camacho H (1922) Terremoto Mexicano del 3 de enero de 1920. Instituto Geológico Mexicano, Boletín 38. <http://bcct.unam.mx/bogeolpdf/geo38/>
- Galloway DL, Burbey TJ (2011) Review: regional land subsidence accompanying groundwater extraction. *Hydrogeology* 19:1459–1486. <https://doi.org/10.1007/s10040-011-0775-5>
- García-Acosta V, Suárez G (1996). Los sismos en la historia de México, tomo I. Universidad Nacional Autónoma de México/Centro de Investigaciones y Estudios Superiores en Antropología Social. Fondo de Cultura Económica, 719
- García-Palomo A, Carlos-Valerio V, López-Miguel C, Galván-García Concha-Dimas A (2006) Landslide inventory map of Guadalupe range, north of the Mexico Basin. *Bol Soc Geol Mex*. <https://doi.org/10.18268/bsgm2006v58n2a2>
- Gayol R (1925) Estudio de las perturbaciones que en el fondo de la Ciudad de México ha producido el drenaje de las aguas del subsuelo, por las obras del desagüe y rectificación de los errores a que ha dado lugar una incorrecta interpretación de los efectos producidos. *Revista Mexicana De Ingeniería y Arquitectura* 3:96–132
- Gobierno del Distrito Federal (2004) Normas técnicas complementarias para diseño y construcción de cimentaciones. *Gaceta Oficial del Distrito Federal*, v. II, 103-BIS, 11–39
- Goel MK (2011) Runoff Coefficient. In: Singh VP, Singh P, Haritashya UK (eds) *Encyclopedia of snow, ice and glaciers*. Encyclopedia of earth sciences series. Springer, Dordrecht
- Herrera G, Ezquerro P, Tomás R, Béjar-Pizarro M, López-Vinielles J, Rossi M et al (2021) Global threats of a silent hazard: land subsidence due to groundwater extraction. *Science* 371:34–36
- Hoberman L (1974) Bureaucracy and disaster: Mexico City and the flood of 1629. *J Lat Am Stu* 6:211–230
- Hooper DM (1995) Computer-simulation models of scoria cone degradation in the Colima and Michoacán-Guanajuato volcanic field, México. *Geofis Int* 34:321–340
- Jaimes MA, García-Soto AD (2020) Ground-motion duration prediction model from recorded mexican interplate and intermediate-depth intraslab earthquakes. *Bull Seismol Soc Am* 20:1–16
- Jaimes MA, Reinoso E, Ordaz M (2006) Comparison of methods to predict response spectra at instrumented sites given the magnitude and distance of an earthquake. *J Earthq Eng* 10:887–90
- Jaimes MA, Ramírez-Gaytán A, Reinoso E (2015) Ground-motion prediction model from intermediate-depth intraslab earthquakes at the hill and lake-bed zones of Mexico City. *J Earthq Eng* 19:1260–1278. <https://doi.org/10.1080/13632469.2015.1025926>
- Jaimes MA, Niño M (2017) Cost-benefit analysis to assess seismic mitigation options in Mexican public school buildings. *Bull Earthq Eng* 15(19):3919–3945. <https://doi.org/10.1007/s10518-017-0119-5>
- Jiménez-Espinoza M (1996) Programa Ax. Área de Riesgos Hidrometeorológicos. Centro Nacional de Prevención de Desastres. México Instituto Nacional de Estadística, Geografía e Informática (National Institute of Statistics and Geography): Censo de Población y Vivienda [Census of Population and Housing 2010] (<https://www.inegi.org.mx/programas/ccpv/2010/>)
- Lermo J, Chávez-García FJ (1994) Site effect evaluation at Mexico City: dominant period and relative amplification from strong motion and microtremor records. *Soil Dyn Earthq Eng* 13:413–423
- Levi E (1990) History of the drainage of Mexico City. *Int J Wat Res Develop*. <https://doi.org/10.1080/07900629008722472>

- López-Quiroz P, Doin M-P, Tupin F, Briole P, Nicolas J-M (2009) Time series analysis of Mexico City subsidence constrained by radar interferometry. *J App Geophys* 69:1–15. <https://doi.org/10.1016/j.jappgeo.2009.02.006>
- Maloof MA (2005) Machine learning and data mining for computer security: Methods and applications. Advanced Information and Knowledge Processing, Springer
- Martin-Del Pozzo AL (1982) Monogenetic volcanism in Sierra Chichinautzin. *Mexico Bull Volcanol* 45:9–24
- Martin-Del Pozzo AL, Córdova C, Lopez J (1997) Volcanic impact on the southern basin of Mexico during the Holocene. *Quat Int* 43:181–190
- Meyerhof GG (1956) Penetration tests and bearing capacity of cohesionless soils. *J Soil Mech and Found Div* 82:1–19
- Mossoux S, Saey M, Bartolini S, Poppe S, Canters F, Kervyn M (2016) Q-LAVHA: a flexible GIS plugin to simulate lava flows. *Comput Geosci* 97:98–109. <https://doi.org/10.1016/j.cageo.2016.09.003>
- Nakamura Y (1989) A method for dynamic characteristics estimation of subsurface using microtremor on the ground surface. *Quart Rep Rail Tech Res Inst* 30:25–33
- Nieto-Torres A, Martin-Del Pozzo AL (2019) Spatio-temporal hazard assessment of a monogenetic volcanic field, near México City. *J Volcan Geother Res* 371:46–58
- Nieto Torres A (2020) Evaluación del riesgo asociado al vulcanismo monogenético hacia la Ciudad de México. PhD Thesis, Earth Sciences, Universidad Nacional Autónoma de México
- Ordaz M, Singh SK (1992) Source spectra and spectral attenuation of seismic waves from Mexican earthquakes, and evidence of amplification in the hill zone of Mexico City. *Bull Seismol Soc Am* 82:24–43
- Osmanoglu B, Dixon TH, Wdowinski S, Cabral-Cano E, Jiang Y (2011) Mexico City subsidence observed with persistent scatterer InSAR. *Int J App Earth Obs Geoinformation* 13:1–12. <https://doi.org/10.1016/j.jag.2010.05.009>
- Pardo M, Suárez G (1995) Shape of the subducted Rivera and Cocos plates in southern Mexico: seismic and tectonic implications. *J Geophys Res: Solid Earth* 1978–2012(100):12357–12373
- Rashed T, Weeks J (2003) Assessing vulnerability to earthquake hazards through spatial multicriteria analysis of urban areas. *Int J Geo-Inf* 17:47–576
- Ricceri G, Soranzo M (1985) An analysis on allowable settlement of structures. *Rivista Italiana di Geotecnica* 4:177–188
- Rosen PA, Gurrola E, Sacco GF (2012) The InSAR scientific computing environment, Proc 9th European Conference on Synthetic Aperture Radar, 730–733
- Rosenblueth E, Arciniega A (1992) Response spectral ratios. *Earthq Eng Struct Dyn* 21:483–492
- Rosenblueth E, Meli R (1986) The 1985 Mexico earthquake. *Concr Int* 8(5):23–34
- Saaty RW (1980) The analytic hierarchy process, New York: McGraw Hill, Revised editions, Paperback Pittsburgh: RWS Publications
- Saaty RW (1987) The Analytic hierarchy process-what it is and how it is used. *Matem Model* 9:161–176
- Santoyo E, Ovando E, Mooser F, León-Plata E (2005) Síntesis Geotécnica de la Cuenca del Valle de México, TGC Ediciones, Ciudad de México, Mexico, 171pp
- Scaletti Cárdenas A (2018) Capital disasters and suspended moves: Mexico (1629) and Lima (1746). *Quiroga* 14:114–123
- Siebe C (2000) Age and archaeological implications of Xitle volcano, southwestern basin of Mexico-City. *J Volcan Geother Res* 104(1–4):45–64
- Siebe C, Rodríguez-Lara V, Schaaf P, Abrams M (2004) Radiocarbon ages of Holocene Pelado, Guespalapa, and Chichinautzin scoria cones, south of Mexico City: implications for archaeology and future hazards. *Bull Volcan* 66:203–225
- Skempton AW, Macdonald DH (1956) The allowable settlements of buildings. *Proc Inst Civ Eng, London* 50:727–768. <https://doi.org/10.1680/ipeds.1956.12202>
- Solano-Rojas D, Wdowinski S, Cabral-Cano E, Osmanoglu B (2020) Detecting differential ground displacements of civil structures in fast-subsiding metropolises with interferometric SAR and band-pass filtering. *Sci Rep* 10:15460. <https://doi.org/10.1038/s41598-020-72293-z>
- Song Y, Gong J, Niu L, Li Y, Jiang Y, Zhang W, Cui T (2013) A grid-based spatial data model for the simulation and analysis of individual behaviours in micro-spatial environments. *Simul Model Pract Theory* 38:58–68
- Sosa-Rodríguez FS (2010) Impacts of water-management decisions on the survival of a City: from ancient Tenochtitlan to modern Mexico City. *Wat Res Develop* 26:675–687
- Stone WC, Yokel FY, Celebi M, Hanks T, Leyendecker EV (1987) Engineering aspects of the september 19, 1985 Mexico earthquake. *NBS Build Sci Series* 165:207

- Suárez G, Espinosa-Aranda JM, Cuellar A, Ibarrola G, García A, Zavala M, Maldonado S, Islas R (2018) A dedicated seismic early warning network: the mexican seismic alert system (SASMEX). *Seism Res Lett* 89(2A):382–391. <https://doi.org/10.1785/0220170184>
- Suárez G, Novelo-Casanova DA (2018) A pioneering aftershock study of the destructive 4 january 1920 Jalapa, Mexico, earthquake. *Seism Res Lett*. <https://doi.org/10.1785/0220180150>
- Suárez G, Novelo D, Mansilla E (2009) Performance evaluation of the seismic alert system (SAS) in Mexico City: a seismological and social perspective. *Seism Res Lett* 80:707–716
- Suárez G, Caballero-Jiménez GV, Novelo-Casanova DA (2019) Active crustal deformation in the trans-mexican volcanic belt as evidenced by historical earthquakes during the last 450 years. *Tectonics*. <https://doi.org/10.1029/2019TC005601>
- UNAM Seismology Group (1986) The September 1985 Michoacan earthquakes: Aftershock distribution and history of rupture. *Geophys Res Lett* 13 573–576
- United Nations International Strategy for Disaster Reduction: Terminology on disaster reduction (2009). [https://www.unisdr.org/files/7817\\_UNISDRTerminologyEnglish.pdf](https://www.unisdr.org/files/7817_UNISDRTerminologyEnglish.pdf)
- Urbina F, Camacho H (1913) La zona megasísmica Acambay-Tixmadeje, estado de México: conmovida el 19 de noviembre de 1912 (Vol. 32). Imprenta y fototipia de la Secretaría de fomento, Mexico
- Wahls HE (1981) Tolerable settlement of buildings. *J Geotech Eng* 109:1495–1496. [https://doi.org/10.1061/\(ASCE\)0733-9410\(1983\)109:11\(1495.2\)](https://doi.org/10.1061/(ASCE)0733-9410(1983)109:11(1495.2))
- Wood CA (1980) Morphometric evolution of cinder cones. *J Volcanol Geotherm Res* 7:387–413
- Yunjun Z, Fattahi H, Amelung F (2019) Small baseline InSAR time series analysis: unwrapping error correction and noise reduction. *Comput Geosc* 133:104331. <https://doi.org/10.1016/j.cageo.2019.104331>

**Publisher's Note** Springer Nature remains neutral with regard to jurisdictional claims in published maps and institutional affiliations.

## Authors and Affiliations

David A. Novelo-Casanova<sup>1</sup>  · Gerardo Suárez<sup>1</sup> · Enrique Cabral-Cano<sup>2</sup> · Enrique A. Fernández-Torres<sup>3</sup> · Oscar A. Fuentes-Mariles<sup>4</sup> · Emre Havazli<sup>5</sup> · Miguel Á. Jaimes<sup>6</sup> · Erika D. López-Espinoza<sup>7</sup> · Ana Lillian Martin-Del Pozzo<sup>8</sup> · Wendy V. Morales-Barrera<sup>9</sup> · Hipólito L. Morales-Rodríguez<sup>4</sup> · Amiel Nieto-Torres<sup>3</sup> · Sergio R. Rodríguez-Elizarrarás<sup>9</sup> · Darío Solano-Rojas<sup>10</sup> · Victor M. Velasco-Herrera<sup>11</sup>

<sup>1</sup> Departamento de Sismología, Instituto de Geofísica, Universidad Nacional Autónoma de México, Col. Ciudad Universitaria, Alcaldía Coyoacán, 04510 Ciudad de México, México

<sup>2</sup> Departamento de Geomagnetismo y Exploración, Instituto de Geofísica, Universidad Nacional Autónoma de México, Col. Ciudad Universitaria, Alcaldía Coyoacán, 04510 Ciudad de México, México

<sup>3</sup> Posgrado de Ciencias de La Tierra, Instituto de Geofísica, Universidad Nacional Autónoma de México, Col. Ciudad Universitaria, Alcaldía Coyoacán, 04510 Ciudad de México, México

<sup>4</sup> Coordinación de Hidráulica, Instituto de Ingeniería, Universidad Nacional Autónoma de México, Col. Ciudad Universitaria, Alcaldía Coyoacán, 04510 Ciudad de México, México

<sup>5</sup> Rosenstiel School of Marine and Atmospheric Science, University of Miami, 4600 Rickenbacker Cswy, Miami, FL 33149, USA

<sup>6</sup> Coordinación de Ingeniería Estructural, Instituto de Ingeniería, Universidad Nacional Autónoma de México, Col. Ciudad Universitaria, Alcaldía Coyoacán, 04510 Ciudad de México, México

<sup>7</sup> Departamento de Ciencias Atmosféricas, Centro de Ciencias de La Atmósfera, Universidad Nacional Autónoma de México, Col. Ciudad Universitaria, Alcaldía Coyoacán, 04510 Ciudad de México, México

<sup>8</sup> Departamento de Vulcanología, Instituto de Geofísica, Universidad Nacional Autónoma de México, Col. Ciudad Universitaria, Alcaldía Coyoacán, 04510 Ciudad de México, México

- 
- <sup>9</sup> Departamento de Dinámica Terrestre Superficial, Instituto de Geología, Universidad Nacional Autónoma de México, Col. Ciudad Universitaria, Alcaldía Coyoacán, 04510 Ciudad de México, México
- <sup>10</sup> Facultad de Ingeniería, Universidad Nacional Autónoma de México, Col. Ciudad Universitaria, Alcaldía Coyoacán, 04510 Ciudad de México, México
- <sup>11</sup> Sección de Radiación Solar, Instituto de Geofísica, Universidad Nacional Autónoma de México, Col. Ciudad Universitaria, Alcaldía Coyoacán, 04510 Ciudad de México, México

## Capítulo 5.4 Economic risk to differential subsidence in Mexico (2014-2022)

### Contents

---

#### **Abstract**

#### **1 Introduction**

#### **2 Methodology**

##### **2.1 Stage I Cadastral values**

##### **2.2 Stage II, InSAR subsidence velocity map**

###### **2.2.1 InSAR descending and ascending average velocity maps**

###### **2.2.2 Vertical velocity, angular distortion, and differential subsidence**

###### **2.2.3 InSAR time series calibration**

##### **2.3 Stage III, Economic risk**

###### **2.3.1 City block exceeding Limit States due to differential subsidence**

###### **2.3.2 Differential subsidence city block risk**

#### **3 Results and discussion**

##### **3.1 Cadastral values**

###### **3.1.1 Building use, class, and floors distribution**

###### **3.1.2 Cadastral values per city block**

##### **3.2 Mexico City subsidence**

###### **3.2.1 Vertical and horizontal velocity maps**

###### **3.2.2 Angular distortion and differential subsidence**

##### **3.3 Economic risk**

###### **3.3.1 City blocks exceeding Limit States due to differential subsidence**

###### **3.3.2 Economic risk due to differential subsidence**

#### **4 Conclusion**

#### **References**

---

**Fernández-Torres E, Cabral-Cano E, Solano-Rojas S (2023) Economic risk to differential settlement in Mexico (2014-2022). Article submitted to Natural Hazards**

## Economic risk to differential subsidence in Mexico City (2014-2022)

Enrique Antonio Fernández-Torres<sup>a,b</sup>, Enrique Cabral-Cano<sup>b</sup>, Luis Salazar-Tlaczani<sup>b</sup>, Darío Solano-Rojas<sup>c</sup>

<sup>a</sup> Posgrado en Ciencias de la Tierra, Universidad Nacional Autónoma de México. Ciudad Universitaria, Coyoacán, CDMX, 04510, México

<sup>b</sup> Departamento de Geomagnetismo y Exploración, Instituto de Geofísica, Universidad Nacional Autónoma de México. Ciudad Universitaria, Coyoacán, CDMX, 04510, México

<sup>c</sup> División de Ingeniería en Ciencias de la Tierra, Facultad de Ingeniería, Universidad Nacional Autónoma de México. Ciudad Universitaria, Coyoacán, CDMX, 04510, México

Corresponding author:

Enrique Antonio Fernández-Torres  
enrique.30065@gmail.com

### Abstract

Differential ground subsidence associated with groundwater extraction can damage urban infrastructure and housing, producing important economic risk and losses. This paper assessed the economic risk due to differential subsidence in Mexico City. To obtain the economic risk maps, we applied a three-stage methodology. In the first stage, we computed the cadastral value per city block. In the second stage, we obtained the vertical, horizontal, and differential subsidence velocities for the period 2014-2022 using Sentinel-1 SAR scenes. In the last stage, we combined the products of stages I and II to obtain the city blocks exceeding Mexico City's Limit States to differential subsidence and the economic risk maps based on two scenarios of typologies. The first scenario consists of masonry construction with 1-2 floors, and the second of constructions with 1-4 floors with steel frames. In the first scenario of economic risk, we obtained that 7.6% of city blocks, 215,000 properties, and 738,000 people are within high and very high-risk categories, representing an economic cost of \$10.5 billion USD. In the second risk scenario, we obtained that \$2.5 billion USD is the cost of properties with high-risk, exposing 48,000 properties, 169 thousand people, and 2% of city blocks. This paper represents the first time land subsidence is evaluated in Mexico City in economic terms. The obtained results can be useful to local authorities to know the economic impacts of differential land subsidence in the city, which can help to improve land subsidence mitigation strategies in the coming years.

### Keywords

Economic risk, Subsidence, Differential subsidence, Mexico City, Sentinel-1

### 1 Introduction

In Mexico, land subsidence due to groundwater extraction, a phenomenon resulting from the combination of its local characteristics and anthropogenic activities, has increased in rates and extension after the 1980s, exposing people and constructions and producing economic losses and risk. In Mexico City, since the late XIX century, vertical land subsidence has been measured (Gayol 1925; Figueroa-Vega 1976) and has demonstrated a pre-disposition for developing ground subsidence rates faster than -10 cm/year because of compaction of the upper aquitard, which corresponds to a wide Pac-Man shape area located to the eastern and southeastern of the urban metropolitan area, where an ancient lake system was located (e.g., Cabral-Cano et al. 2008; Osmanoglu et al. 2011; Cigna and Tapete 2021a). Among the geotechnical properties that favor the current subsidence rates of the silty clay upper aquitard are very high values of void ratio (6-11), water content (420%), compression index (3-6), porosity (70-90%), and plasticity index (300%) (Marsal and Mazari 1959; Díaz-Rodríguez 2003). Several researchers have also found that the higher the thickness of the upper aquitard, the higher the subsidence rate, finding that for each additional meter of compressible deposits, the rate of subsidence increases by 3 mm/year (Cabral-Cano et al. 2008, Solano-Rojas et al. 2015; Chaussard et al. 2021). The geotechnical and geological characteristics of Mexico City combined with groundwater extraction rates have induced considerable aquifer stress, reduced the pore pressure, and increased the effective stress, producing land subsidence as fast as -50 cm/year.



In this framework, several methodologies have been successfully applied to measure the land subsidence velocity field and spatial distribution characterization, that range from optical leveling, borehole extensometers, to LiDAR, GPS, and InSAR (Cabral-Cano et al. 2008; Calderhead et al. 2011; Osmanoğlu et al. 2011; Auvinet-Guichard et al. 2017a; Hu et al. 2022). InSAR, is a remote sensing technique that can obtain terrain information using SAR microwave radar sensors (e.g., Massonnet et al. 1993; Ferretti et al. 2001; Berardino et al. 2002). Satellite SAR sensors have recorded land surface information for the last 30 years, allowing us to evaluate land subsidence evolution. The InSAR technique measures land deformation in line-of-sight (LOS) direction using the phase difference between at least two SAR scenes acquired in almost the same place at two different times (e.g., Bürgmann et al. 2000). Phase measurement precision is obtained by using the coherences, which depends on the temporal acquisition frequency, orbital separation, atmospheric conditions, radar wavelength, and land cover (Hanssen 2001; Lanari et al. 2004).

Several multitemporal algorithms have been developed to improve the phase displacement measurements and study land deformation for long periods, such as Small Baseline Subset (SBAS; Berardino et al. 2002). SBAS algorithm estimates the land deformation using interferogram networks of differential interferograms with small spatial and temporal baselines, reducing the decorrelation and improving the spatial convergence, obtaining sub-centimetric precision (Manunta et al. 2019). Among the products that have been developed using InSAR to evaluate land subsidence and identify possible associated damages are the characterization of vertical velocity, angular distortion, and differential subsidence (e.g., Fernández-Torres et al. 2020; Cigna and Tapete 2021a).

The vertical land subsidence velocity can be obtained by combining LOS velocities and geometric information of SAR scenes acquired in different path directions (i.e., descending and ascending paths; Cigna et al. 2021a). The methodology to obtain the vertical velocity field allows to separate of the vertical rates from horizontal East-West deformation (Cigna and Tapete 2021a). The InSAR vertical velocity field can also be used to obtain angular distortion by computing the differential velocity in a neighborhood (e.g., Fernández-Torres et al. 2020; Cigna and Tapete 2021a). Angular distortion, which is the ratio of differential subsidence in a distance between two reference points, is a building damageability criterion that has been widely applied in geotechnical engineering (Skempton and Macdonald 1956; Bjerrum 1963; Burland and Wroth 1975). Angular distortion and differential subsidence high values promote the development of surface land subsidence-associated faults. The high rate of differential subsidence and subsidence-associated faulting has been a recurrent problem in Central Mexico because of its lithological and tectonic settings (Ferrari 2000; García-Palomo et al. 2000; Arce et al. 2019). The Central Mexico geological settings contribute to the existence of stable volcanic structures adjacent to lacustrine and alluvial compressible deposits (e.g., the area between the stable volcanic rock of the Santa Catarina Range and the surrounding compressible material in southeast Mexico City). Therefore, constructions within these areas with high differential subsidence rates can suffer damages that lead to economic losses (Julio-Miranda et al. 2012; Auvinet-Guichard et al. 2013; Hernández-Madriral et al. 2015; Solano-Rojas et al. 2020b).

In other Mexican cities undergoing ground subsidence, economic losses due to subsidence-associated faulting have been evaluated under two approaches. The first is a modified version of the Blong (2003) methodology to evaluate economic damage due to subsidence-associated faults. In this approach, the damage severity is evaluated in the field, and estimated the total economic loss in San Luis Potosi households based on the price of an average house (Julio-Miranda et al. 2012). The second approach evaluates the damages due to subsidence-associated faults based on a depreciation factor, which uses a proximity criterion between the ground subsidence associated faults and the constructions. This second approach has been applied considering average construction and land values in Morelia and using both land and cadastral values in Toluca (Hernández-Madriral et al. 2014, 2015; Camacho-Sanabria et al. 2020). However, these two approaches to evaluate economic losses due to differential land subsidence did not consider any risk, which can be a valuable tool for selecting and prioritizing where mitigation measurements are necessary.

On the other hand, in Mexico City, risk assessment due to differential subsidence has previously used the properties density exposure and socioeconomic vulnerability based on population and households census data (Cigna and Tapete 2021a, b, 2022; Novelo-Casanova et al. 2022; Fernández-Torres et al. 2022) but there is no analysis on economic risk due to differential land subsidence yet.

This research evaluates the economic risk due to differential land subsidence in Mexico City, one of the cities with large population and very fast subsidence rates, to estimate the total economic cost of construction based on risk categories and the economic cost of building that overpass the Limit States to differential subsidence. We used an

InSAR vertical velocity field (2014-2022), the cadastral land and construction values, and the Limit States of the current Mexico City building code to compute the differential subsidence economic risk evaluation.

## 2 Methodology

We applied a three-stage methodology to evaluate the economic risk of civil structures to differential subsidence. In the first stage, we used Mexico City's cadastral information, the 2020 Households and Population Census data (INEGI 2020), the 2022 Fiscal Code (Congreso de la Ciudad de Mexico 2021), the *Directorio Estadístico Nacional de Unidades Económicas* (DENUE; INEGI 2022), and building height (Esch et al. 2022) to obtain the cadastral value per city block (Fig. 1). In the second stage, the Mexico City's Sentinel-1 A/B (ascending/descending) 2014-2022 Single Look Complex (SLC) scenes were used to generate vertical velocity, angular distortion, and differential subsidence maps (Fig. 1). In this stage, we also calibrated the results by comparing the InSAR time series with GPS time series from 4 stations (Fig. 1). In the last stage, the products of stage I (i.e., cadastral value per city block) and stage II (i.e., differential subsidence map) are combined to obtain the differential subsidence per city block (Fig. 1). Then, we used the Limit States of differential subsidence using the Mexico City's building code to obtain the city blocks exceeding allowable differential subsidence. Finally, we calculated the risk based on a risk matrix where the vertical axis is building volume from Esch et al. (2022), and the horizontal axis represents the number of times the Limit States values are exceeded.

### 2.1 Stage I, Cadastral values

To obtain the cadastral values of each land parcel of land, we assigned its building use, building's number of floors, and class (Fig. 1), using Mexico City's Fiscal Code to get the value per square meter of each property (Congreso de la Ciudad de Mexico 2021; see Supplementary file 1).

For the building use assignments, we used the cadastral information (Agencia Digital de Innovación Pública), DENUE (INEGI 2022), and the Census data (INEGI 2020) (see Fig. 1); we then merged building uses of these three data sources to match them with the tables of construction values from the Mexico City's Fiscal code using the official building use definitions from Secretaría de Administración y Finanzas (2023) (Supplementary file 2). When there is no match between building uses for the three data sources, we used the building uses from DENUE, because this data source is the most up-to-date (INEGI 2022). The DENUE registers all economic activities within a property (e.g., a shopping mall with many stores may have several DENUE's building uses such as commerce, office, and health care, among others). Therefore, we established a hierarchical order to assign one building use per parcel of land. The hierarchical order is consecutively commerce, hotel, sport activities, office, health care, household, industry, warehouse, culture, communication, education, parking and squares, garden, and cemetery. This criterion is based on the average construction values per square meter (Congreso de la Ciudad de Mexico 2021). In cases where parcels of land do not have a specific building use, we assigned a household use because this is the most common use for civil structures in Mexico City (see Fig. 3a).

For each building's number of floor assignment, we used the cadastral information (Agencia Digital de Innovación Pública). In this case, renaming the building floor data to match the Mexico City Fiscal Code was unnecessary. However, for the properties without building floor information, we replaced assigned Range 2 (i.e., buildings with 1 or 2 levels), as these constructions are the most common throughout the city (Fig. 3c).

Building class refers to a set of features of a civil structure, such as special building facilities, services, and quality of construction finishes (Congreso de la Ciudad de Mexico 2021). The class value is a unique value per property, and it can range from 1 to 7, where the higher the class value, the better the structure's physical conditions, and it is reflected in its assigned construction unit cost value (see Supplementary file 1). Building class values were calculated based on the Characteristic Matrix from the Mexico City building code using the cadastral information and building height (Fig. 1; Supplementary file 3). For the household and household use adapted to office, hotel, commerce, health care, education, or communication, the construction total area categories from the Characteristic Matrix were used to define classes (Supplementary file 3). The number of floor categories from the Characteristic Matrixes were utilized for office, hotel, commerce, health care, education, or communication use. In cases where the building uses are industrial, warehouse, cultural, or sport, the categories from the Characteristic Matrixes based on height values were employed (Supplementary file 3).

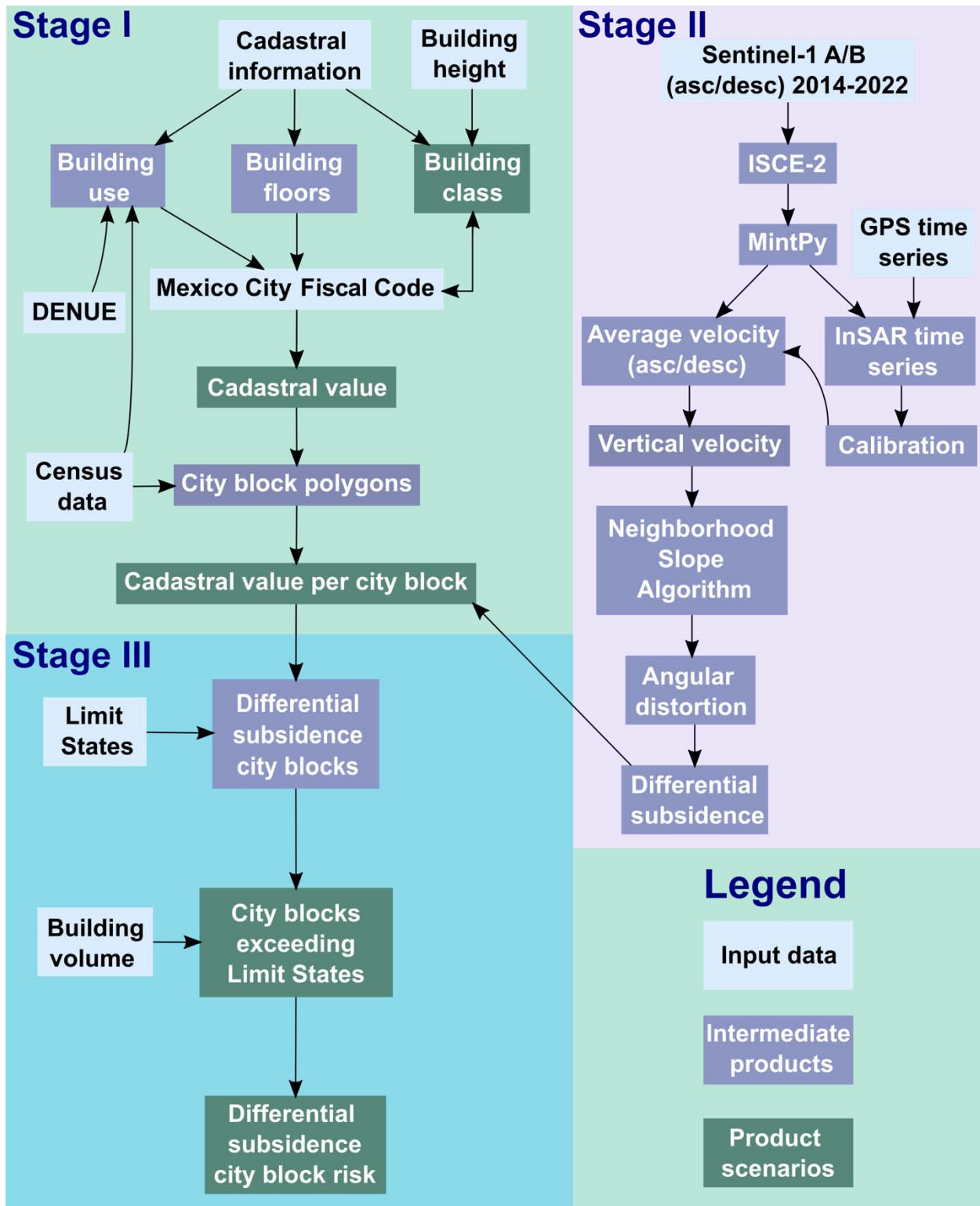


**Fig. 1** Workflow to calculate the economic risk due to differential subsidence in Mexico City

To compute the cadastral value per land parcel, we applied a six-step methodology (Agencia Digital de Innovación Pública) (Fig. 2). In the first step, we computed the land value (LV) of each property as the multiplication of the unit LV per square meter by its total land area (Fig. 2). Then, property building use, floors, and class and the unit value

per m<sup>2</sup> tables from Mexico City Fiscal Code (Congreso de la Ciudad de Mexico 2021) were used to determine the unit construction value (CV) per square meter. Then, each unit construction value was multiplied by the construction area to obtain its construction value. In the third step, depreciation (TD) was calculated by multiplying 0.8% by the construction age. Next, we evaluated if the TD was higher than the 40% of the CV; in this case, we assigned the 40% of the construction value as the TD; in other cases, we kept the TD value. In the fifth step, we assessed if the building has special facilities (e.g., electric stairs, air conditioning, heating system) using the cadastral data. In cases where the building has special facilities, the construction value increases by 8%; else, the construction value remains the same. In the last step, the cadastral value per parcel of land was calculated as the sum of the final CV (considering TD and special facilities) and the LV (Fig. 2).

To have the cadastral value information in a spatial resolution compatible with the 80x80 m<sup>2</sup> pixel size of the Sentinel-1 SBAS velocity maps, we calculated the cadastral value per city block using the Mexico City's city blocks shapefile from the geostatistical framework from INEGI (2020). We then calculated the cadastral price in US dollars per city block as the sum of all parcels of land inside each city block, assuming an exchange rate of \$20 Mexican pesos/US dollar.

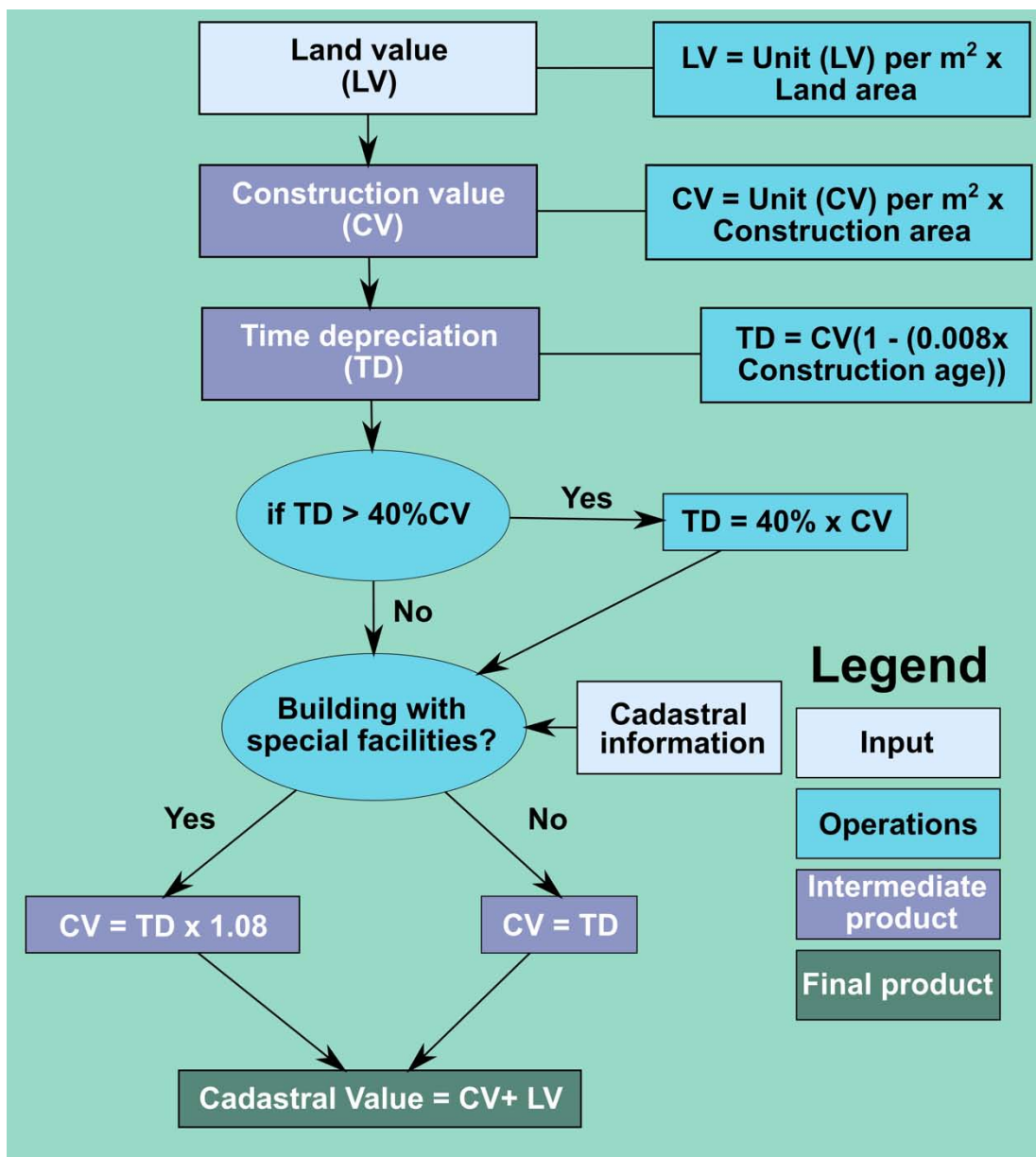


**Fig. 2 Workflow to calculate the cadastral value per parcel of land**

## 2.2 Stage II, InSAR subsidence velocity maps

### 2.2.1 InSAR descending and ascending average velocity maps

For generating the deformation maps, we used Sentinel-1 A/B SLC scenes downloaded from ESA's Copernicus Sentinel-1 archive using the Alaska Satellite Facility (ASF) and the Copernicus Open Access hub. The Sentinel-1 A/B data set consists of 907 SLCs, which were acquired using orbits 143 and 78 in descending (543 SLCs) and ascending (354 SLCs) modes (Table 1), respectively, and covering the time window from October 3, 2014, to June 11, 2022. The Interferometric Synthetic Aperture Radar Scientific Computing Environment (ISCE-2; Rosen et al. 2012) software was used for processing SLCs using the Small Baseline Subsets approach (SBAS; Berardino et al. 2002). For the ISCE-2's setup parameters, we used the Network-Based Enhanced Spectral Diversity (NESD; Fattahi et al. 2017), interferogram network with three connections, and the Statistical-cost Network-flow Algorithm for PHase Unwrapping (SNAPHU; Hooper 2009) for co-registering the SLCs scenes, generating the interferometric network and unwrapping the phase, respectively. We also applied a 5 by 20 multilook, in azimuth and range direction, to improve the spatial coherence, resulting in a pixel size of  $\sim 80 \times 80 \text{ m}^2$  (Table 1). The ISCE-2 final products were 1,137 and 969 unwrapped interferograms in descending and ascending modes, respectively (Table 1).

The time series and average velocity maps were generated using the ISCE-2's unwrapped interferograms and the Miami INsar Time-series Python software (MintPy; Yunjun et al. 2019). In MintPy software, the geographic coordinate of the TNGF cGPS station ( $19.327^\circ, -99.176^\circ$ ) was set up as the reference point for both descending and ascending velocity maps (Supplementary file 4). The reference point was chosen mainly for three reasons. First, the reference pixel is in a null deformation area (i.e., geotechnical hill zone); spatial coherence larger than 0.85; and it shows comparable velocity fields for both acquisition geometries. We employed the empirical relationship between topography and the troposphere to correct the phase tropospheric delay component (Doin et al. 2009).

**Table 1.** SAR data

Mode	Descending	Ascending
Sensor	Sentinel-1 A/B	Sentinel-1 A/B
Relative orbit	143	78
# SLC	543	364
# Interferograms	1,137	969
Looks (azimuth x range)	5x20	5x20
Pixel size (m)	80x80	80x80
Period	2014/10/03-2022/06/11	2014/10/23-2022/06/07

### 2.2.2 Vertical velocity, angular distortion, and differential subsidence

Vertical and horizontal velocity calculation based on ascending and descending InSAR-velocity fields may allow a higher accurate measurement of differential subsidence than using the vertical velocity calculated without subtracting the East-West velocity contribution (i.e., projecting LOS velocity into vertical using the incidence angle). We did not consider the North-South component because the near-polar Sentinel-1 orbits considerably reduce the sensor sensibility to measure land deformation in that direction (Torres et al. 2012).

To calculate each pixel's average vertical  $V_{U(i)}$  and horizontal  $V_{E(i)}$ , velocities, we used equations 1, 2, 3, and 4 (e.g., Cigna et al. 2021). Where the subindexes  $D(i)$  and  $A(i)$  represent each velocity pixel in the descending or ascending (LOS) satellite acquisition mode.  $V_{D(i)/A(i)}$  are the descending or ascending (LOS) velocities,  $\alpha_{A(i)/D(i)}$ , and  $\theta_{A(i)/D(i)}$  are the incidence angles and the azimuth angles, respectively.

$$V_{U(i)} = \frac{E_{Di} * V_{Ai} - E_{Ai} * V_{Di}}{E_{Di} * U_{Ai} - E_{Ai} * U_{Di}} \quad (1)$$

$$V_{E(i)} = \frac{U_{Ai} * V_{Di} - U_{Di} * V_{Ai}}{E_{Di} * U_{Ai} - E_{Ai} * U_{Di}} \quad (2)$$

$$U_{D(i)/A(i)} = \cos(\alpha_{A(i)/D(i)}) \quad (3)$$

$$E_{D(i)/A(i)} = -\cos\left(\theta_{\frac{A(i)}{D(i)}}\right) \sin\left(\alpha_{\frac{A(i)}{D(i)}}\right) \quad (4)$$

To evaluate civil infrastructure damage severity due to land subsidence, we can use subsidence-related intensity parameters such as angular distortion and differential subsidence (e.g., Skempton and Macdonald 1956; Burland and Wroth 1975). Angular distortion ( $\beta$ ) is a structural engineering parameter that measures the slope between differential subsidence ( $ds$ ) and their respective distance ( $l$ ) (e.g., distance between the columns of a building) (see eq. 5). To compute  $\beta$ , we used the vertical velocity based on ascending and descending InSAR-velocity fields for the 2014-2022-time window as input raster (Fig. 5a), we then applied the Neighborhood Slope Algorithm (NSA) from Burrough et al. (2015). The NSA algorithm measures the maximum change rate between a central pixel and its closest neighbors in the horizontal ( $dz/dx$ ) and vertical ( $dz/dy$ ) directions (see eq. 6). The NSA algorithm was applied in the QGIS spatial analysis software using the Slope tool, which considers a mobile window of 3 by 3 pixels length and has to posse at least seven valid values to calculate a no NAN  $\beta$  value. The angular distortion values were computed in radians to compare with Limit States values of  $\beta$  (e.g., Skempton and Macdonald 1956). Finally, the differential subsidence raster map (i.e.,  $ds$ ) was computed by multiplying the ( $\beta$ ) value of each cell by the pixel size of the vertical velocity raster ( $l$ ) (i.e., 80 m; eq. 5) (e.g., Cigna and Tapete 2021a). The resulting angular distortion and differential subsidence calculated under this methodology only shows the civil structure diferential deformation for the 2014-2022 period.

$$\beta = \frac{ds}{l} \quad (5)$$

$$\beta = \sqrt{(dz/dx)^2 + (dz/dy)^2} \quad (6)$$

### 2.2.3 InSAR time series calibration

To calibrate the 2014-2022 InSAR velocity maps, we compared the time series from InSAR with four GPS stations (MXAZ, ICMX, MMX1, and UFXN; Supplementary file 4) using the descending and ascending velocity fields in LOS and 3D GPS time series (i.e., Vertical, North-South, East-West components), respectively. To perform the calibration, we first obtained the time series information of four Mexico City's GPS stations with position information in the 2014-2022 time span (Blewitt et al. 2018; Cabral-Cano et al. 2018). Then, we projected all the GPS time series into LOS, considering the incidence angle of each GPS's station pixel and using the information from InSAR descending and ascending acquisition geometries. Finally, we calculated the slope of both InSAR and GPS time series as the better linear regression adjustment (see Supplementary file 4).

## 2.3 Stage III, Economic risk

### 2.3.1 City block exceeding Limit States due to differential subsidence

The economic exposure for each of Mexico City's civil structure due to differential subsidence was calculated following a four steps methodology, which are:

1. We joined the differential subsidence map (see Stage II, Fig. 1) with the cadastral value per city block (see Stage I, Fig. 1).
2. The mean differential subsidence per city block was computed.
3. We compared the city blocks' mean differential subsidence with the Limit State values from Mexico's City Building Code (Table 2).
4. Finally, we calculated the cadastral value of the city blocks exceeding the Limit State values under two scenarios, including or excluding the land value.

The Limit States values represent maximum tolerable differential subsidence based on building typologies and Mexico City’s building code; however, the information on typologies for each of Mexico City’s building does not exist. Therefore, to evaluate each city’s street block exceeding the Limit States value due to differential subsidence, we assumed two scenarios. The first assumes Mexico City only has masonry constructions with less than 2 floors high and the second assumes that all constructions of the city are made of steel frames with less than 4 floors. These two scenarios are representative because most of the Mexico City constructions have 4 or fewer floors (Fig. 3c), and masonry and steel frame constructions are frequent typologies in the city.

**Table 2** Limit states for differential subsidence in structures (modified from GCDMX 2017)

Type of structure	Differential subsidence (limit value)
Masonry constructions (MC) (lower than 2 stories)	0.002 m to 0.003 m
Steel frame constructions (SFC) (lower than 4 stories)	0.006 m

### 2.3.2. Differential subsidence city block risk

A risk matrix is used to compute the differential subsidence city block risk. In the vertical axis of this matrix, we used the building volume developed by the German Aerospace Center (Esch et al. 2022). We use three threshold values to define this axis. The first threshold corresponds to those city blocks with a building volume lower than 55,000 m<sup>3</sup>; this volume value results from multiplying the average city block area by the average building height. The second threshold upper value is two times the city block average value, and the last upper value is the highest. The matrix horizontal axis is defined by the Limit States values, the first value (D0) or null risk are city blocks not exceeding the Limit State values, the D1, D2, and D3 represent city blocks exceeding between 1 to 2, 2 and 3, and more than 3 times the Limit States values, respectively. In the risk matrix, R0, R1, R2, R3, and R4 represent null, low, intermediate, high, and very high risk due to differential subsidence.

## 3 Results and discussion

### 3.1 Cadastral values

#### 3.1.1 Building use, class, and floors distribution

Building uses were assigned using the DENU, the 2020 Household and Population Census, and Cadastral information, as explained in section 2.1. Fig. 3a shows the building use distribution per parcel of land in Mexico City. As a result, we observe that more than 95% of the parcels of land have households (HS; 48.5%) and commerce (CO; 46.9%) uses, where the sum of both HS and CO represent 1,021,314 out of 1,069,900 properties.

For class values calculation, the Characteristic Matrix of Mexico City’s Fiscal Code was used, resulting in intermediate classes (4, 3, and 5), the most common in Mexico City (Fig. 3b). The sum of classes 3, 4, and 5 is equal to 720,900 parcels of land out of a total of 1,069,900, representing 67.3%. The properties within classes 4, 3, and 5 are 251,236, 248,390, and 221,274, respectively (Fig 3b). Therefore, most of the buildings in Mexico City have intermediate conditions regarding their construction finishes, services, and materials.

To determine the number of floors per land parcel, we used Mexico City’s Cadastral Information (Agencia Digital de Innovación Pública; see previous section 2.2). The Cadastral Information reports the number of levels in 8 categories based on the number of levels (i.e., R1, R2, R5, R10, R15, R20, R99, RU; Fig. 3c) except for the RU category, which does not depend on the number of floors but building use (see Supplementary file 1). We can observe that R2 (1-2 levels high) and R5 (3-5 levels high) are the most common number of building’s floors in Mexico City, representing more than 96% of Mexico City’s constructions. In other words, in Mexico City, 9.6 out of 10 buildings have a total height equal to or lower than 12.2 m. Assuming each story has an average height of 2.44 m, where 77.5% and 19% of buildings have 1-2 floors and 3-5 floors, respectively (Fig. 3c). The obtained average buildings height match with previous research (e.g., Esch et al. 2022).

#### 3.1.2 Cadastral values per city block

The cadastral value per property is the result of the sum of land value (LV) and construction value (CV), considering time depreciation and special building facilities (Fig. 2; see section 2.1). Then, cadastral values were grouped into city blocks using polygons from Mexico City's census (INEGI 2020), obtaining cadastral value per city block (Fig. 4a). The cadastral values per city blocks are presented with or without land value, and these are grouped into five categories considering the city block cadastral values as follows: a)  $\leq 5$  million USD, b)  $5 - 10$  million USD, c)  $10 - 30$  million USD, e)  $30 - 50$  million USD, and f)  $\geq 50$  million USD (Figs. 4a and 4b).

In 2022, Mexico City has a total cadastral value of \$171.3 billion USD, where \$113.1 billion USD corresponds to the construction value and \$58.2 billion USD accounts for land value. Only 4.5% of city blocks have a cadastral value higher than \$10 million USD, and the top three municipalities with cadastral values are Iztapalapa \$21.1 billion USD, Gustavo A Madero \$19.3 billion USD, and Cuauhtémoc \$19 billion USD. In contrast, municipalities with the lower cadastral value are Milpa Alta \$854.9 million USD, Tlalpan \$3.1 billion USD, and Magdalena Contreras \$3.4 billion USD (Fig 4b). Municipalities with the higher percentage of city blocks with a cadastral value exceeding \$10 million USD are Cuauhtémoc, Miguel Hidalgo, and Cuajimalpa, with 19.2%, 19.1%, and 11.8%, respectively. Novelo-Casanova et al. (2022) found that Mexico City's western sector has a lower socioeconomic vulnerability. Our research may suggest that a possible reason for a lower socioeconomic vulnerability in the western Mexico City portion is due to the proportionally higher construction cadastral value.

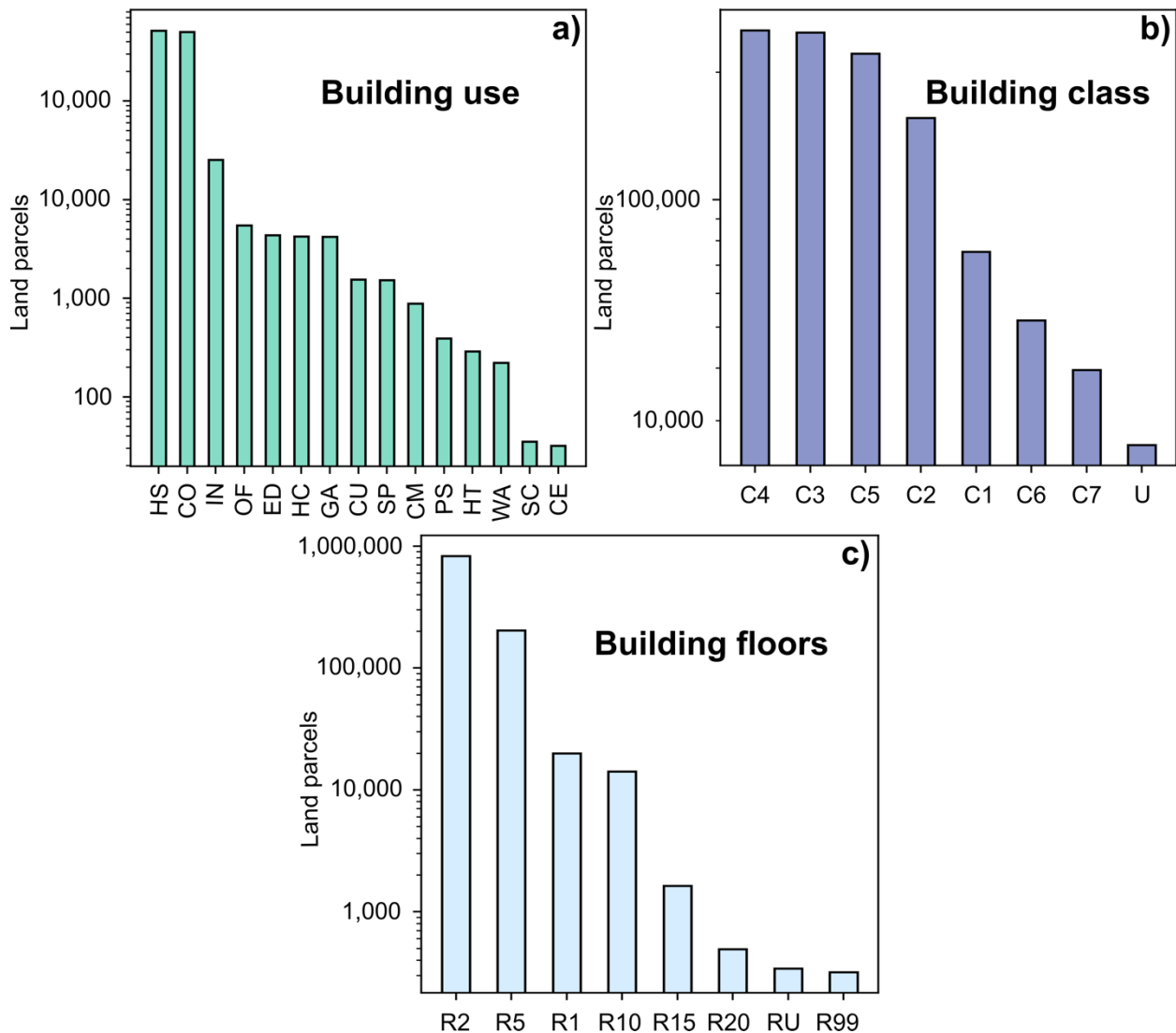




**Fig. 3** Input elements to determine the cadastral value per parcel of land. a) Building use, b) building class, and c) building floors. HS: household, CO: commerce, IN: industry, OF: office, ED: education, HC: health care, GA: garden, CU: culture, SP: sport, CM: communications, PS: parking and squares, HT: hotel, WA: warehouses, SC: sport centers, CE: cemetery. C1: class 1, C2: class 2, C3: class 3, C4: class 4, C5: class 5, C6: class 6, C7: class 7, U: Unique. R1: Range 1 (1 floor), R2: Range 2 (1-2 floors), R5: Range 5 (3-5 floors), R10: Range 10 (6-10 floors), R15: Range 15 (11-15 floors), R20: Range 20 (16-20 floors), R99: Range 99 (>21 floors), RU: Range Unique

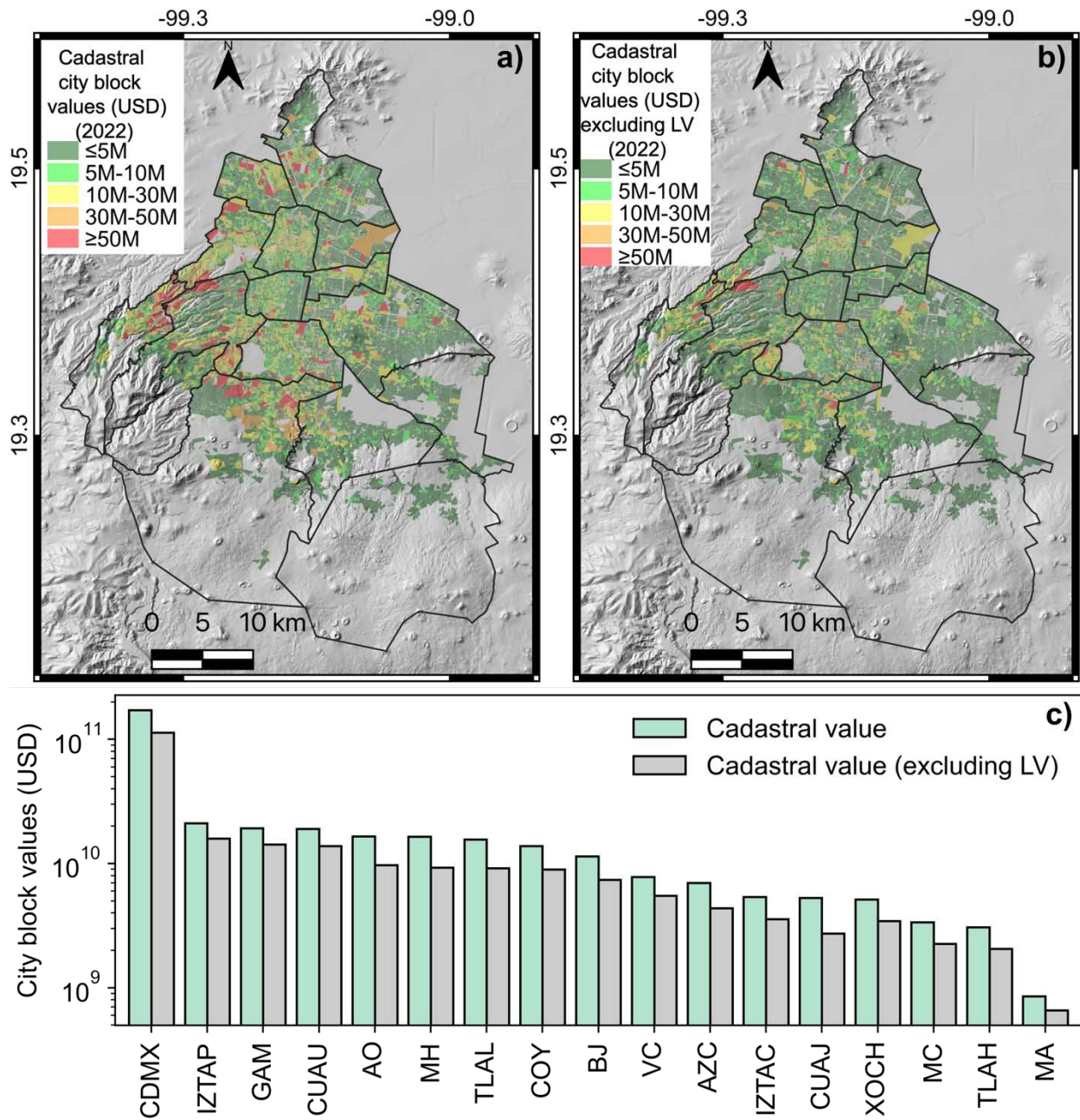


**Fig. 4** Cadastral value per city block. a) Considering construction and land value. b) Only construction values. c) Cadastral values of Mexico City (CDMX) and its municipalities considering land and construction values (green polygons) and excluding land value (grey polygons). IZTAP: Iztapalapa, GAM: Gustavo A. Madero, CUAU: Cuauhtémoc, AO: Álvaro Obregón, MH: Miguel Hidalgo, TLAL: Tlalpan, COY: Coyoacán, BJ: Benito Juárez, VC: Venustiano Carranza, AZC: Azcapotzalco, IZTAC: Iztacalco, CUAJ: Cuajimalpa, XOCH: Xochimilco, MC: Magdalena Contreras, Tlah: Tláhuac, MA: Milpa Alta

## 3.2 Mexico City subsidence

### 3.2.1 Vertical and horizontal velocity maps

Ascending and descending InSAR LOS velocity maps are obtained by processing Sentinel-1 A/B SLCs scenes covering October 2014 to June 2022 (see section 2.2.1; Supplementary file 4). In order to calculate the vertical and horizontal E-W velocity fields, we combine the ascending and descending velocity fields and their acquisition geometries (see section 2.2.2; Figs. 5a and 5b). Mexico City presents two well-defined areas where ground subsidence rates can exceed tens of centimeters per year.

The largest vertical subsidence footprint is in the central northeast sector of the city (Fig. 5a). This footprint follows an approximate northeast-southwest orientation, a maximum length of ~28 km, and is located within the Lake (Zone III) geotechnical zoning. The fastest vertical velocity within this subsidence footprint is almost in the middle of this sector (point 5, Fig. 5a), in the surroundings of Caseta de Cobro Peñón-Texcoco, Nezahualcóyolt municipality, State of Mexico, where the vertical subsidence velocity is -52.3 cm/yr, the highest subsidence velocity recorded in the Mexico City Metropolitan Area, which matches the highest vertical subsidence and spatial location reported in previous research (Chaussard et al. 2021). Some of the city's most significant historical and strategic buildings are in this vertical subsidence patch. For instance, the Angel of Independence (1), Monument to the Revolution (2), the Mexico City Cathedral (3), and the Mexico City International Airport (4) have maximum vertical subsidence of -1.3 cm/yr, -2.4 cm/yr, -6.6 cm/yr and -24 cm/yr, respectively (Fig. 5a, points 1, 2, 3, and 4).

The second vertical subsidence footprint is located between the southern flank of the Sierra Santa Catarina and borders the northern flank of the Sierra Chichinautzin (Fig. 5a). This zone has an east-west orientation, and its maximum length can be up to 24 km. Within this footprint, the fastest observed vertical subsidence rate is -43.8 cm/yr in the suburb of Bosque de Xico, Valle de Chalco municipality, State of Mexico (Fig. 5a; point 6).

At the municipality level, the top five metropolitan area municipalities with the fastest recorded vertical velocity are Nezahualcóyolt (-26.6 cm/yr), Venustiano Carranza (-18.2 cm/yr), Valle de Chalco (-17.5 cm/yr), Iztacalco (-15.2 cm/yr), and Tláhuac (-12.9 cm/yr). The municipality ranking with the fastest maximum subsidence rate is Nezahualcóyolt (-52.3 cm/yr), Texcoco (-46.6 cm/yr), Valle de Chalco (-43.8 cm/yr), Tláhuac (-41.1 cm/yr), and Xochimilco (-38.8 cm/yr).

The high subsidence rates recorded in Mexico City may intensify the effects of other natural hazards, such as the seismic response of subsoil (Ermert et al. 2023), and increase the flooding potential. In the case of seismic activity, ground subsidence has generated shortening of the vibration periods of soil (Avilés et al. 2006; Avilés and Pérez-Rocha 2010; Albano et al. 2016), rapid slip along subsidence associated faulting (Solano-Rojas et al. 2020a), and the increase of vulnerability to earthquakes in constructions over some parts of the Transition geotechnical zone (Ovando-Shelley et al. 2003). The high-ground subsidence velocities recorded in Mexico City have modified the terrain relief, promoting the development of negative relief areas susceptible to flooding events when extreme rain occurs (Novelo-Casanova et al. 2022). Precipitation could also collapse the drainage network, which has lost its optimal capacity due to the slope decrease of pipelines due to land subsidence, increasing the flooding potential affecting the central and northern parts of Mexico City (Novelo-Casanova et al. 2022).

Mexico City's rapid subsidence velocity has induced changes in the subsoil properties, and in the silty clay upper aquitard. Ovando-Shelley et al. (2003) found that water content, density, strength, and compressibility are the subsoil properties that are more susceptible to changes due to land subsidence in Mexico City, which can produce a rearrangement of lacustrine volcanic components of the upper aquitard producing inelastic ground subsidence (Chaussard et al. 2021).

Mexico City's subsidence may also produce migration of salts and other contaminants from the upper aquitard to the productive aquifer, causing a reduction in water quality, producing the potential for a water crisis in coming years (e.g., Ortega-Guerrero et al. 1993; Hernández-Espriú et al. 2014). Chaussard et al. (2021) forecasted that within 150 years, the upper aquitard would be completely compacted, which could eliminate the current natural protection of the productive aquifer from the contaminants due to urban activity and contribute to at least an additional 30 m of subsidence.

In the horizontal rates field, we can observe that the E-W velocities are comparatively lower than the vertical subsidence values (Figs. 5a and 5b). However, some municipalities in the eastern sector of the Mexico City metropolitan area show significant horizontal velocities. The maximum recorded horizontal velocities are in the surroundings of Caseta de Cobro Peñón-Texcoco, Texcoco (-10.1 cm/yr), Mexico City International Airport, Venustiano Carranza (-8.6 cm/yr), and the north flank of Peñón del Marqués, Iztapalapa (-8.3 cm/yr), (Fig. 5b points, 1, 2, and 3, respectively). Our results are similar to those obtained by Cigna and Tapete (2021a).

We also observe that at the south flank of Sierra de Santa Catarina and the north flank of Sierra de Chichinautzin, their predominant horizontal velocities are toward the west and east, respectively, which suggests some topographic control of the horizontal movement in this portion of the city. The obtained horizontal velocity field may suggest that although the land subsidence in Mexico City is predominantly vertical, there is indeed a horizontal component of motion. The horizontal velocity could be due to groundwater extraction and tectonic movement (Osmanoğlu et al. 2011). Our results only show the East-West horizontal field because Sentinel-1 has a nearly polar acquisition path, considerably reducing the capability to detect North-South deformation (Torres et al. 2012).

To corroborate the precision of our velocity maps, they were calibrated by comparing the InSAR-SBAS LOS in ascending and descending acquisition modes with four GPS stations (MXAZ, MMX1, ICMX, and UFXN, see Supplementary file 4). In this calibration, we found a mean velocity difference of 0.3 cm/yr, and 0.4 cm/yr between ascending and descending velocity (LOS) time series and the cGGPS (LOS) time series. Therefore, we assume that the obtained velocity fields are accurate.

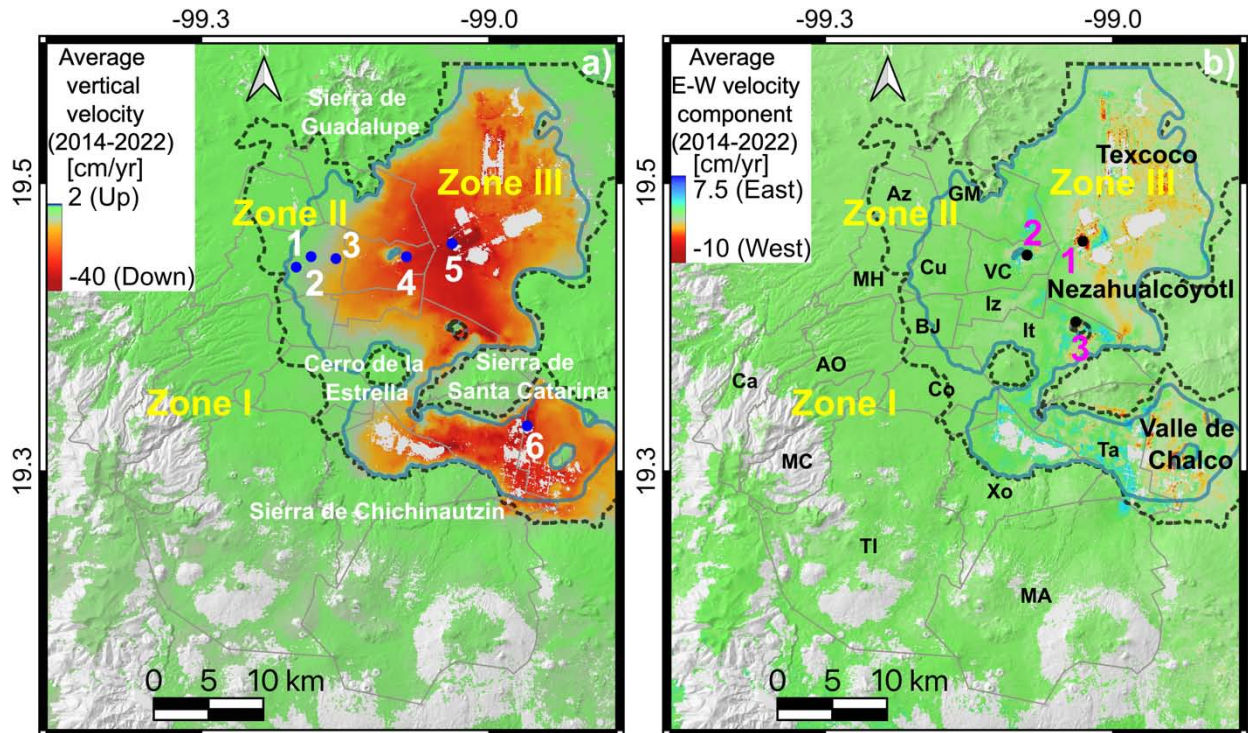


**Fig. 5** Mexico City's InSAR velocity using Sentinel-1 A/B scenes for the period 2014-2022. a) Vertical velocity field; 1: The Angel of Independence, 2: Monument to the Revolution, 3: Cathedral, 4: Mexico City International Airport, 5 and 6: locations of maximum vertical velocity in patch 1 and 2, Ciudad Nezahualcōyōtl and Valle de Chalco municipalities, respectively. Zone I: Hill, Zone II: Transition, Zone III: Lake geotechnical zones (GCDMX 2017). b) horizontal velocity map; 1 (Texcoco), 2 (Mexico City International Airport), and 3 (Peñón del Marqués) represent locations of maximum horizontal velocity. Az: Azcapotzalco, GM: Gustavo A. Madero, MH: Miguel Hidalgo, Cu: Cuauhtémoc, VC: Venustiano Carranza, Ca: Cuajimalpa, AO: Álvaro Óbregon, BJ: Benito Juárez, Iz: Iztacalco, MC: Magdalena Contreras, Co: Coyoacán, It: Iztapalapa, TI: Tlapan, Xo: Xochimilco, Ta: Tláhuac, MA: Milpa Alta. Light grey polygons are the municipalities of Mexico City

### 3.2.2 Angular distortion and differential subsidence

We use the InSAR-vertical velocity (2014-2022) as input to the Neighborhood Slope Algorithm (NSA) to calculate angular distortion and differential subsidence. The NSA algorithm allows measuring the vertical and horizontal maximum change rate (see equations 5 and 6, section 2.2.2) and the angular distortion ( $\beta$ ) and differential subsidence ( $ds$ ). In Mexico City, the maximum differential vertical velocity change occurs in the eastern sector of the city, around the contact of the stable volcanic structures (e.g., Sierra de Chichinautzin, Sierra de Santa Catarina, Peñón del Marqués, Peñón de Los Baños; see Figs. 6a and 6b). Mexico City's municipalities with the higher mean differential subsidence are Tháhuac ( $ds = 0.8$  cm), Iztapalapa ( $ds = 0.6$  cm), Venustiano Carranza ( $ds = 0.5$  cm), Iztacalco ( $ds = 0.4$  cm), and Xochimilco ( $ds = 0.4$  cm). The three locations with the highest differential subsidence are in the surrounding of Line A, Peñón Viejo subway station, Iztapalapa ( $ds = 7.2$  cm), between Line 12, Nopalera and Zapotitlán subway stations, Tháhuac ( $ds = 5.4$  cm), and Tlalmelac, Xochimilco ( $ds = 4.4$  cm) (Fig. 6b; locations 1, 2, and 3, respectively). On the other hand, the municipalities with the lower mean differential subsidence are Azcapotzalco ( $ds = 0.05$  cm), Miguel Hidalgo ( $ds = 0.06$  cm), and Álvaro Obregón ( $ds = 0.07$  cm).

Our results show that in Mexico City, high values of differential subsidence and angular distortion are located along the contact between volcanic structures and lacustrine compressible deposits. Previous research has demonstrated that abrupt transition between materials with dissimilar mechanical behavior (i.e., volcanic, and lacustrine deposits) could be the leading cause of differential subsidence (e.g., Carreón-Freyre and Cerca 2006; Carreón-Freyre and Rodríguez-Quiroz 2010). Carreón-Freyre et al. (2006) pointed out that an additional contribution to differential deformation is also observed inside the silty clay aquitard sediments due to lateral and vertical heterogeneities in the geomechanical behavior that the mineralogical heterogeneity may produce, which could be controlled by the paleoenvironmental history of the sediments.

High values of differential subsidence promote large tensile stress in the ground, increasing the vulnerability to developing subsidence-associated faulting (e.g., Holzer 1984; Rojas et al. 2002; Cabral-Cano et al. 2008; Carreón-Freyre 2010; Sarychikhina et al. 2011; Solano-Rojas et al. 2020c; Cigna and Tapete 2021b; Fernández-Torres et al. 2022). Faulting associated with differential subsidence is responsible for considerable damages to constructions in Mexico City, including the subway system, urban infrastructure, historical buildings, and houses (e.g., Auvinet-Guichard et al. 2013, 2017b; Solano-Rojas et al. 2020b). In this context, Ovando-Shelley et al. (2003) suggest a scenario where most of the architectural heritage buildings of Mexico City may be severely damaged in the coming decades at the current differential subsidence rate.

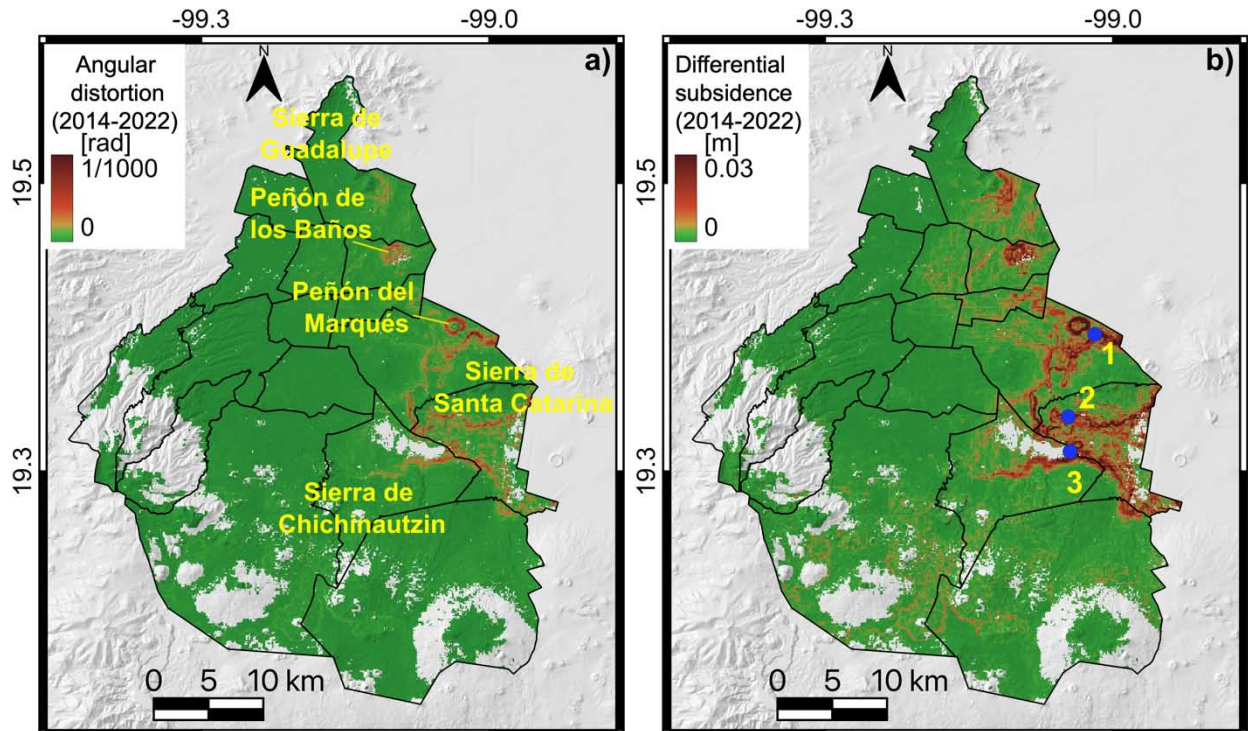


**Fig. 6** Angular distortion and differential subsidence based on InSAR vertical velocity (2014-2020), in Mexico City. a) Angular distortion; b) differential subsidence. Blue circles represent the three locations with the highest differential subsidence in Mexico City. 1: Peñón Viejo Line A subway station, Iztapalapa ( $ds = 7.2$  cm), 2: between Nopalera and Zapotitlán Line 12 subway stations, Tháhuac ( $ds = 5.4$  cm), and 3: Tlalmelac, Xochimilco ( $ds = 4.4$ )

### 3.3 Economic risk

#### 3.3.1 City blocks exceeding Limit States due to differential subsidence

We combine city blocks' cadastral value with the differential subsidence field to compute and compare the results with the Limit States under two assumptions (Fig. 1). In scenario 1, all city street blocks have masonry constructions with less than two floors, and scenario 2, civil structures are made of steel frame constructions less than four floors (see section 2.3.1; Table 2; Figs. 7a, 7b, 7c, and 7d).

In scenario 1, we found that 24.6% of city blocks overpass the construction code differential subsidence Limit State value (0.0025 m; Table 2; Fig. 7a). This implies a cadastral value exposure of 44.4 billion and 32 billion USD if only constructions are considered. We also found that the municipalities with the higher number of city blocks exceeding tolerable differential subsidence assuming masonry constructions with less than two floors are Iztapalapa (5,517), Gustavo A. Madero (2,712), and Tláhuac (1,796), and the municipalities with the lower number of city blocks that exceed the differential subsidence limit states are Miguel Hidalgo (0), Magdalena Contreras (4), and Azcapotzalco (5) (Fig. 7a). The top 3 municipalities with the highest cadastral values exceeding Limit States assuming masonry constructions typology are Iztapalapa \$12.4 billion USD, Cuauhtémoc \$7.7 billion USD, and Gustavo A. Madero \$7.6 billion USD (Fig. 7c).

For scenario 2, we observed that 9.7% of Mexico City's blocks exceed 0.006 m of differential subsidence (Table 2; Fig. 7b). The cadastral value of city blocks exceeding 0.006 m is \$13.6 billion USD, where \$9.9 billion USD represents only the civil structure cost. Municipalities with a higher number of city blocks exceeding 0.006 m are Iztapalapa (2,908), Tláhuac (1,368), and Gustavo A. Madero (857). The municipalities with the highest cadastral value exceeding 0.006 m are Iztapalapa, Gustavo A. Madero, and Tláhuac with \$5.5 billion, \$2.1 billion, and \$2 billion USD, respectively (Fig. 7d).

In scenarios 1 and 2, we obtained that \$44 billion USD and \$13.6 billion USD are the cadastral cost of city blocks exceeding Limit States, respectively. As a consequence, the economic exposure due to differential subsidence that exceeds the construction code Limit States represents 3.1% and 0.9% of the 2022 Mexico PIB (\$1.41 trillion USD; the 14th largest economy of the world; World Bank 2023) for scenarios 1 and 2, respectively.

The obtained cadastral value exceeding the Limit States considers the differential deformation of construction for the 2014-2022 period, which is a small time window of the more than 100 years that Mexico City has undergone land subsidence (Gayol 1925). Therefore, the cadastral cost scenarios of civil structures exposed to differential subsidence are underestimated.

We used two scenarios to evaluate the city blocks exceeding the Limit States due to differential subsidence (i.e., masonry  $\leq 2$  floors and steel frame constructions  $\leq 4$  floors) because the information on building typologies is unavailable in Mexico City. However, civil structures with four or fewer floors (Fig. 3c) and masonry materials are the most common buildings in Mexico City. Therefore, the two typologies' scenarios are representative of the city's civil structures. Our assessment was performed at the city block level because of the Sentinel-1 spatial resolution limitations, which may produce an underestimation of the Limit States due to differential subsidence.

Other Mexican cities, such as San Luis Potosi, Morelia, and Toluca, have evaluated the economic losses due to differential subsidence (Julio-Miranda et al. 2012; Hernández-Madriral et al. 2015; Camacho-Sanabria et al. 2020). These studies did not consider the velocity and differential velocity fields. Instead, they used the spatial proximity to faulting associated with ground subsidence as the unique criteria to identify the properties with the highest exposure and only assumed an average construction cost, except for Camacho-Sanabria et al. (2020) in Santa Ana Tlapatlán Toluca, where they used the land and construction cadastral costs in their estimation of the economic losses due to differential subsidence.

### 3.3.2 Economic risk due to differential subsidence

A risk matrix based on average city block volume and a multiple of the Limit State threshold value was used to compute economic risk due to differential subsidence (Figs. 8 and 9). Five categories are defined to evaluate risk, which are null (R0), low (R1), intermediate (R2), high (R3), and very high (R4).

If the scenario is based on the assumption that civil structures on all city blocks are masonry with 1-2 floors, we found that 7.6% of city blocks are under a high and very high risk. The number of properties and people living in those high and very high-risk city blocks are 215,000 and 738,000, respectively. As a consequence, the cost of civil structures at high and very high economic risk due to differential subsidence is \$10.5 billion USD or 6.1% of Mexico City's cadastral value (Figs. 8a, 8b, 8c, 8d).

When we assume that city blocks are made of constructions with steel frames with 4 or less floors, 2% of city blocks reach high economic risk, where 1.6% (48 thousand) and 1.9% (169 thousand) of Mexico City's total households and population, reach high economic risk due to differential subsidence. In economic terms, \$2.5 billion USD is the total cadastral value of city blocks with high risk or 1.4% of Mexico City's cadastral value (Figs. 9a, 9b, 9c, 9d).

In Mexico City, other methodologies have been applied to evaluate risk due to land subsidence. Fernández-Torres et al. (2022) used a formula that includes socioeconomic vulnerability, vertical land subsidence, and subsidence horizontal gradient to determine socioeconomic risk due to land subsidence, and Cigna and Tapete (2021a) used a risk matrix that consists of properties density and angular distortion to compute subsidence-induced surface faulting. Both previous risk evaluations were made at AGEBA level (i.e., a group of city blocks defined by INEGI), and in Cigna and Tapete (2021a), the analysis included adjacent municipalities of the State of Mexico.

Our results estimate the economic value of the civil structures that exceed the Limit States, based on Mexico City's current construction code, and is most useful to compare the economic impact of differential subsidence with other phenomena such as seismic or volcanic activity. In addition, using the risk matrix, the building volumes instead of the property's density considered the actual dimensions, including the civil structure height and not only the property amount. Our risk maps allow us to describe with higher spatial resolution the properties at high and very high economic risk.

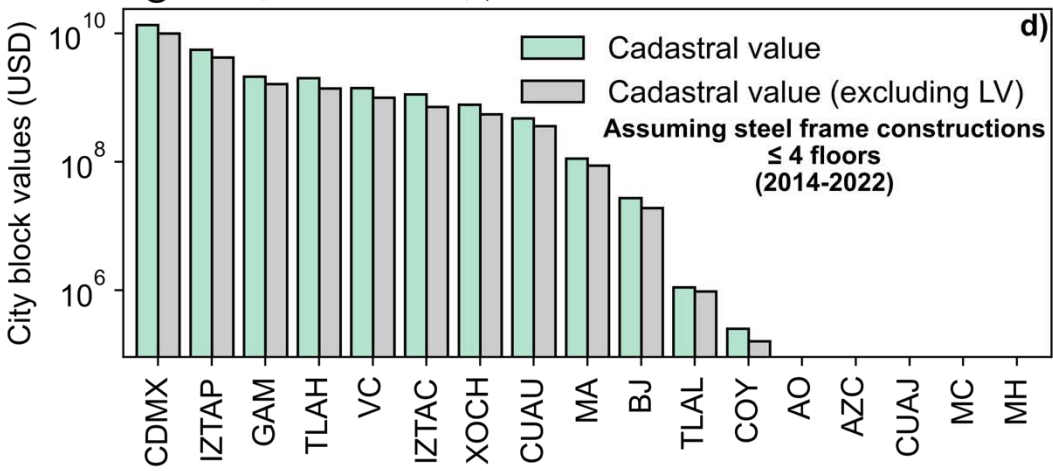
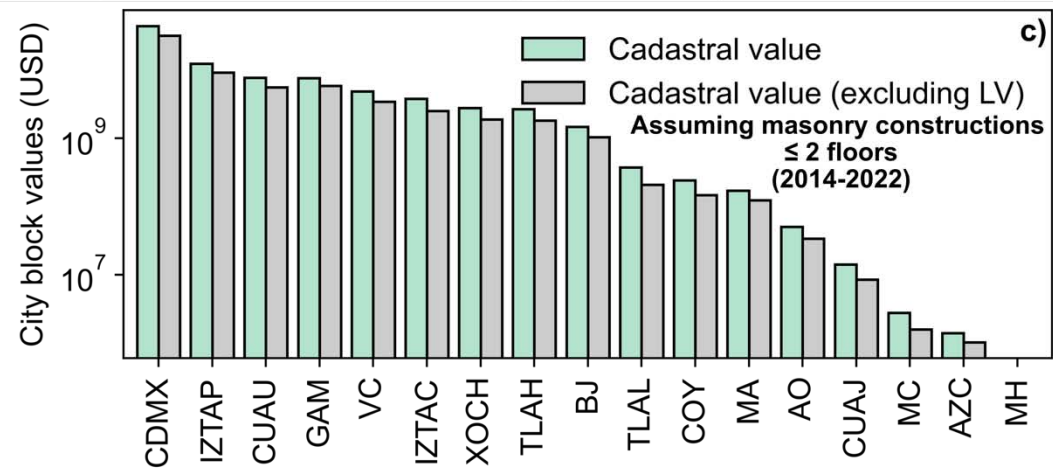
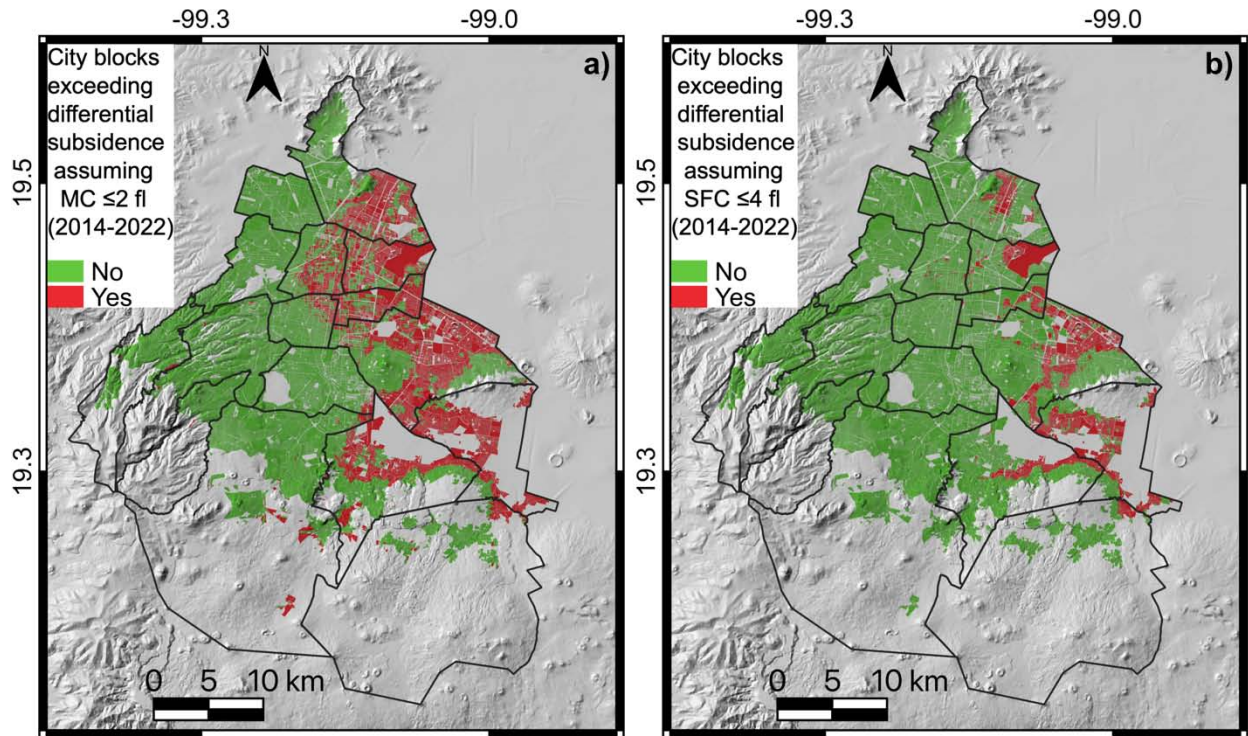


**Fig. 7** City blocks exceeding the Limit States due to differential subsidence. City blocks and city block values that exceed differential subsidence Limit States assuming masonry structures with less than 2 floors, a) and c) respectively. City block and city block values that exceed differential subsidence Limit States assuming steel frame structures with less than 4 floors b and d, respectively. In panels a) and b) red and green polygons represents city blocks exceeding or not the Limit States, respectively

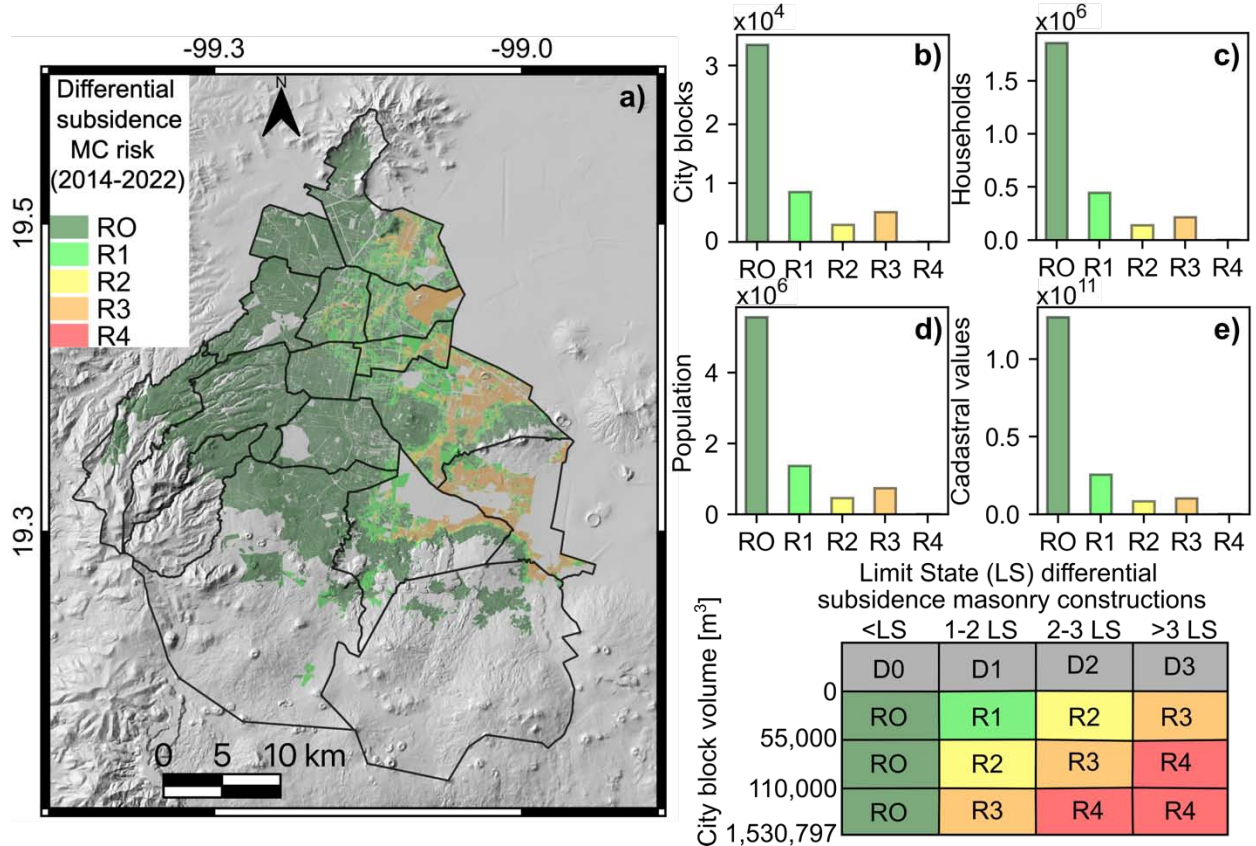


**Fig. 8** Economic risk due to differential subsidence assuming masonry construction with 2 or less floors. a) City blocks with the economic risk value. b) City blocks distribution per risk category. c) Household distribution per risk category. e) Cadastral values per risk category



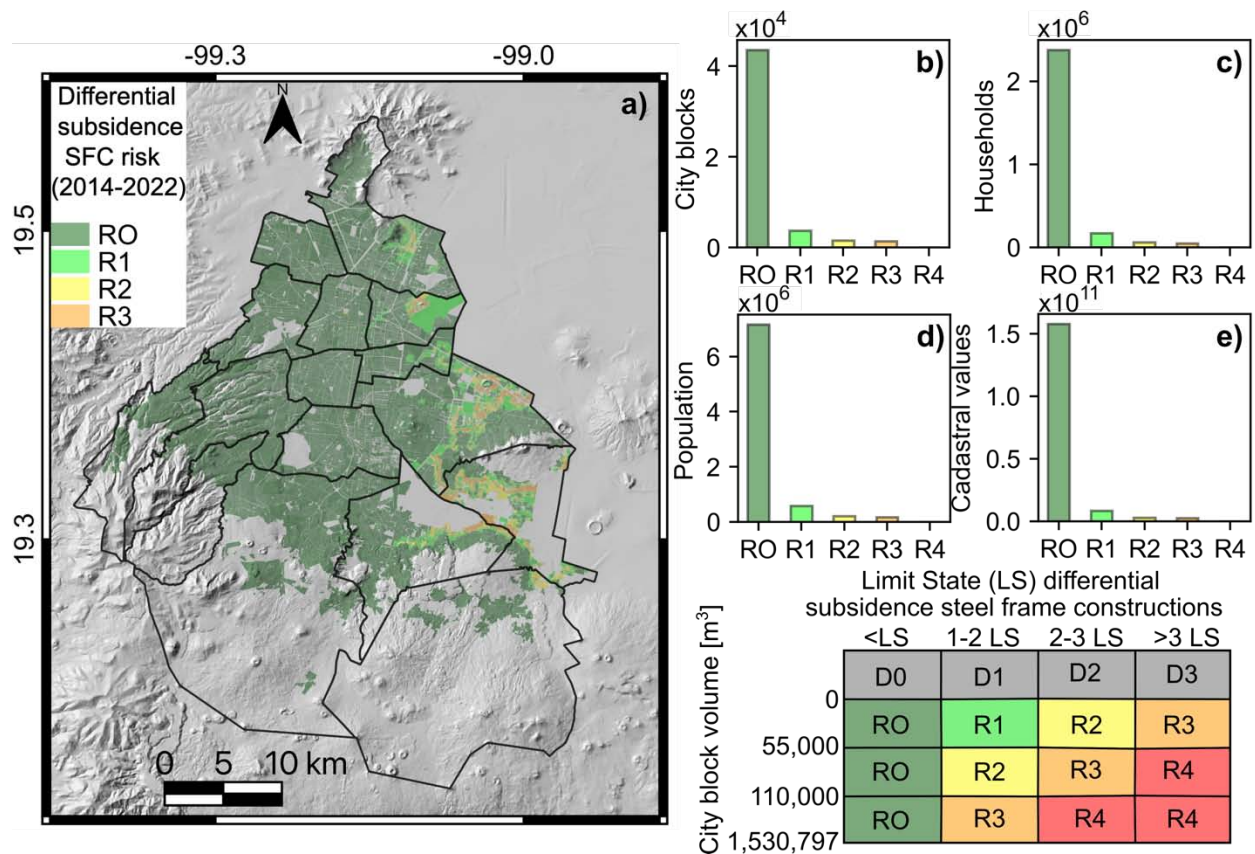


**Fig. 9** Economic risk due to differential subsidence assuming steel frame constructions with 4 or less floors. a) City blocks with the economic risk value. b) City blocks distribution per risk category. c) Household distribution per risk category. e) Cadastral values per risk category.

#### 4 Conclusion

This study evaluated the economic risk due to differential land subsidence under two scenarios using different construction typologies. These two scenarios assumed that Mexico City constructions are built using masonry materials with 1-2 floors or steel frame constructions with 1-4 floors. In the first scenario, we obtained that 7.6% of the city blocks of Mexico City are at high and very high economic risk, exposing 738,000 people and 215,000 properties, which have a cadastral cost of \$10.5 billion USD, which is equivalent to 6.1% of the Mexico City total cadastral value (i.e., \$171.3 billion USD). For scenario 2, we obtained that the cadastral value of properties at very high risk is \$2.5 billion USD or 1.4% of Mexico City's total cadastral value, exposing 2% of Mexico City's blocks, 48,000 properties, and 169,000 people.

The obtained vertical velocity spatial distribution presents two well-defined areas where the subsidence rate is faster than -10 cm/yr toward the eastern and southeastern sector of the Mexico City metropolitan area with a maximum vertical velocity of -52.3 cm/yr within the Nezahualc6yolt municipality, State of Mexico, coinciding with previous research (Cabral-Cano et al. 2008; Chaussard et al. 2021; Cigna and Tapete 2021a). On the other hand, we detect that the metropolitan area undergoes horizontal velocities faster than -8 cm/yr in places like Texcoco, the Mexico City International Airport, and Pe6n6n del Marqu6s in Iztapalapa, suggesting that although the vertical velocity is the main velocity component, a horizontal component is also present in some places of the city as was previously reported by Cigna and Tapete (2021a). We also confirm that the highest values of differential subsidence are along the sharp boundaries between compressible lacustrine deposits and stable volcanic structures where the three locations with the highest differential subsidence are in the surroundings of Line A Pe6n6n Viejo subway station, Iztapalapa ( $ds = 7.2$  cm), between Line 12's Nopalera and Zapotitl6n subway stations, Th6huac ( $ds = 5.4$  cm), and Tlalmelac, Xochimilco ( $ds = 4.4$  cm).

This study illustrates the economic cost and risk due to differential land subsidence for the first time in Mexico City, one of the cities in the world with the highest land subsidence rate, population exposure, and longer subsidence history.

## Statements & Declarations

### Acknowledgments

We acknowledge Copernicus Sentinel-1 IW SAR data retrieved from the Alaska Satellite Facility and the Copernicus Open Access Hub. GPS data was provided by several data providers, including the Trans-boundary, Land and Atmosphere Long-term Observational and Collaborative Network (TLALOCNet) operated by Servicio de Geodesia Satelital (SGS) at the Instituto de Geofísica-Universidad Nacional Autónoma de México (UNAM) in collaboration with GAGE operated by the Earthscope Consortium, US Federal Aviation Administration, and other unknown providers whose metadata is unavailable at the University of Nevada Reno Nevada Geodetic Laboratory where GPS solutions were accessed. InSAR processing was performed at the UNAM-Dirección General de Cómputo y de Tecnologías de Información y Comunicación (DGTIC) Miztli high-performance computer under project LANCAD-DGTIC 362 to ECC. The ISCE and MintPy are open-source code freely available from GitHub.

### Funding

Eaft was funded by Consejo Nacional de Ciencia y Tecnología (CONACyT) for his doctoral studies. ECC acknowledges support from UNAM-Programa de Apoyo a Proyectos de Investigación e Innovación Tecnológica (PAPIIT) project IN107321.

### Declaration of interests

The authors declare that they have no known competing financial interests or personal relationships that could have appeared to influence the work reported in this paper.

### Author contributions

Eaft and ECC conceptualized the research and developed the methodology. Eaft processed the data and provided formal analysis and writing of the original draft under the supervision of ECC. ECC and DSR supervised the InSAR processing. Eaft and LST generated GPS data and its analysis under the supervision of ECC. ECC and DSR contributed to the data validation. All authors revised the manuscript.

### Supplementary information

*Supplementary file 1* contains the table of building value per  $m^2$  based on the 2022 Fiscal Code of Mexico City. *Supplementary file 2* has the tables to rename building uses based on the 2022 Fiscal Code of Mexico City. *Supplementary file 3* poses the Characteristic matrixes to compute building classes. *Supplementary file 4* contains Mexico City's InSAR SAB velocity LOS (2014-2022) in ascending and descending paths and the comparison between GPS and InSAR time series in LOS.

### References

- Agencia Digital de Innovación Pública Sistema Abierto de Información Geográfica (SIGCDMX). <http://sig.cdmx.gob.mx/>. Accessed 2 May 2021
- Albano M, Polcari M, Bignami C, et al (2016) An innovative procedure for monitoring the change in soil seismic response by InSAR data: application to the Mexico City subsidence. *International Journal of Applied Earth Observation and Geoinformation* 53:146–158. <https://doi.org/10.1016/j.jag.2016.08.011>
- Arce JL, Layer PW, Macías JL, et al (2019) Geology and stratigraphy of the Mexico Basin (Mexico City), central Trans-Mexican Volcanic Belt. *Journal of Maps* 15:320–332. <https://doi.org/10.1080/17445647.2019.1593251>
- Auvinet-Guichard G, Méndez E, Juárez M (2013) Soil fracturing induced by land subsidence in Mexico City. In: *In Proceedings of the 18th International Conference on Soil Mechanics and Geotechnical Engineering*. Paris, France, pp 2921–2924
- Auvinet-Guichard G, Méndez E, Juárez M (2017a) Recent information on Mexico City subsidence. In: *International Society for Soil Mechanics and Geotechnical Engineering*. p 5
- Auvinet-Guichard G, Méndez E, Moises J (2017b) El Subsuelo de la Ciudad de México. In *Instituto de Ingeniería, UNAM III*:
- Avilés J, Pérez-Rocha LE (2010) Regional subsidence of Mexico City and its effects on seismic response. *Soil Dynamics and Earthquake Engineering* 30:981–989. <https://doi.org/10.1016/j.soildyn.2010.04.009>

- Avilés J, Pérez-Rocha LE, Aguilar HR (2006) Influence of ground water extraction in the seismic hazard of Mexico City. In: *Geo-Environment and Landscape Evolution II: Monitoring, Simulation, Management and Remediation*. WIT Press, Rhodes, Greece, pp 457–466
- Berardino P, Fornaro G, Lanari R, Sansosti E (2002) A new algorithm for surface deformation monitoring based on small baseline differential SAR interferograms. *IEEE Trans Geosci Remote Sensing* 40:2375–2383. <https://doi.org/10.1109/TGRS.2002.803792>
- Bjerrum L (1963) *Allowable Settlement of Structures*. Wiesbaden, 2, Brighton, England, pp 135–137
- Blewitt G, Hammond W, Kreemer C (2018) Harnessing the GPS Data Explosion for Interdisciplinary Science. In: *Eos*, 99. <https://doi.org/10.1029/2018EO104623>. Accessed 16 Jun 2021
- Blong R (2003) *A New Damage Index*. Natural Hazards
- Bürgmann R, Rosen PA, Fielding EJ (2000) Synthetic Aperture Radar Interferometry to Measure Earth's Surface Topography and Its Deformation. *Annu Rev Earth Planet Sci* 28:169–209. <https://doi.org/10.1146/annurev.earth.28.1.169>
- Burland J, Wroth C (1975) *Settlement of Buildings and Associated Damage*. Building Research Establishment 65
- Burrough PA, McDonnell RA, Lloyd CD (2015) *Principles of Geographical Information Systems*. OUP Oxford
- Cabral-Cano E, Dixon T, Miralles-Wilhelm F, et al (2008) Space geodetic imaging of rapid ground subsidence in Mexico City. *Geological Society of America Bulletin - GEOL SOC AMER BULL* 120:1556–1566. <https://doi.org/10.1130/B26001.1>
- Cabral-Cano E, Pérez-Campos X, Azúa B, et al (2018) TLALOCNet: A continuous GPS-met backbone in Mexico for seismotectonic and atmospheric research. *Seismological Research Letters* 89:. <https://doi.org/10.1785/0220170190>
- Calderhead AI, Therrien R, Rivera A, et al (2011) Simulating pumping-induced regional land subsidence with the use of InSAR and field data in the Toluca Valley, Mexico. *Advances in Water Resources* 34:83–97. <https://doi.org/10.1016/j.advwatres.2010.09.017>
- Camacho-Sanabria R, Camacho Sanabria JM, Balderas Plata MÁ, Hernández Madrigal VM (2020) Cuantificación Espacial del Daño Socioeconómico por Subsistencia Diferencial en Santa Ana Tlapaltitlán, Toluca, México. *REDER* 4:95. <https://doi.org/10.55467/reder.v4i1.44>
- Carreón-Freyre D (2010) Land subsidence processes and associated ground fracturing in central Mexico. In: *IAHS-AISH*
- Carreón-Freyre D, Hidalgo-Moreno CM, Hernández-Marin M (2006) Mecanismos de fracturamiento de depósitos arcillosos en zonas urbanas. Caso de deformación diferencial en Chalco, Estado de México. *Boletín de la Sociedad Geológica Mexicana* 58:237–250. <https://doi.org/10.18268/bsgm2006v58n2a6>
- Carreón-Freyre D, Rodríguez-Quiroz JC (2010) Guidelines for the design of a unit of urban risk prevention for subsurface fracturing in the Municipality of Iztapalapa in Mexico City. In: *IAHS-AISH*
- Carreón-Freyre DC, Cerca M (2006) Fracturing phenomena in two urban areas of Mexico. *IAEG* 291:1–10
- Chaussard E, Havazli E, Fattahi H, et al (2021) Over a Century of Sinking in Mexico City: No Hope for Significant Elevation and Storage Capacity Recovery. *Journal of Geophysical Research: Solid Earth* 126:1–18. <https://doi.org/10.1029/2020JB020648>
- Cigna F, Esquivel Ramírez R, Tapete D (2021) Accuracy of Sentinel-1 PSI and SBAS InSAR Displacement Velocities against GNSS and Geodetic Leveling Monitoring Data. *Remote Sensing* 13:4800. <https://doi.org/10.3390/rs13234800>
- Cigna F, Tapete D (2021a) Present-day land subsidence rates, surface faulting hazard and risk in Mexico City with 2014–2020 Sentinel-1 IW InSAR. *Remote Sensing of Environment* 112161. <https://doi.org/10.1016/j.rse.2020.112161>
- Cigna F, Tapete D (2021b) Satellite InSAR survey of structurally-controlled land subsidence due to groundwater exploitation in the Aguascalientes Valley, Mexico. *Remote Sensing of Environment* 254:112254. <https://doi.org/10.1016/j.rse.2020.112254>
- Cigna F, Tapete D (2022) Urban growth and land subsidence: Multi-decadal investigation using human settlement data and satellite InSAR in Morelia, Mexico. *Science of The Total Environment* 811:152211. <https://doi.org/10.1016/j.scitotenv.2021.152211>
- Congreso de la Ciudad de Mexico (2021) *Código Fiscal de la Ciudad de Mexico*
- Díaz-Rodríguez JA (2003) Characterisation and engineering properties of Mexico City lacustrine soils. In: *Characterization and engineering properties of Mexico City lacustrine soils*. Swets & Zeitlinger, Lisse
- Doin M-P, Lasserre C, Peltzer G, et al (2009) Corrections of stratified tropospheric delays in SAR interferometry: Validation with global atmospheric models. *Journal of Applied Geophysics* 69:35–50. <https://doi.org/10.1016/j.jappgeo.2009.03.010>
- Ermert LA, Cabral-Cano E, Chaussard E, et al (2023) Probing environmental and tectonic changes underneath Mexico City with the urban seismic field. *Solid Earth* 14:529–549. <https://doi.org/10.5194/se-14-529-2023>
- Esch T, Brzoska E, Dech S, et al (2022) World Settlement Footprint 3D - A first three-dimensional survey of the global building stock. *Remote Sensing of Environment* 270:112877. <https://doi.org/10.1016/j.rse.2021.112877>
- Fattahi H, Agram P, Simons M (2017) A Network-Based Enhanced Spectral Diversity Approach for TOPS Time-Series Analysis. *IEEE Transactions on Geoscience and Remote Sensing* 55:777–786. <https://doi.org/10.1109/TGRS.2016.2614925>
- Fernández-Torres E, Cabral-Cano E, Solano-Rojas D, et al (2020) Land Subsidence risk maps and InSAR based angular distortion structural vulnerability assessment: an example in Mexico City. In: *Proceedings of the International Association of Hydrological Sciences*. Copernicus GmbH, pp 583–587
- Fernández-Torres EA, Cabral-Cano E, Novelo-Casanova DA, et al (2022) Risk assessment of land subsidence and associated faulting in Mexico City using InSAR. *Nat Hazards* 112:37–55. <https://doi.org/10.1007/s11069-021-05171-0>
- Ferrari L (2000) Avances en el conocimiento de la Faja Volcánica Transmexicana durante la última década. *Boletín de la Sociedad Geológica Mexicana* LIII:84–92
- Ferretti A, Prati C, Rocca F (2001) Permanent scatterers in SAR interferometry. *IEEE Transactions on Geoscience and Remote Sensing* 39:8–20. <https://doi.org/10.1109/36.898661>
- Figueroa-Vega GE (1976) Subsidence of the city of Mexico; a historical review. In: *Anaheim Symp. USA*, pp 35–38
- García-Palomo A, Macías JL, Garduño VH (2000) Miocene to Recent structural evolution of the Nevado de Toluca volcano region, Central Mexico. *Tectonophysics* 318:281–302. [https://doi.org/10.1016/S0040-1951\(99\)00316-9](https://doi.org/10.1016/S0040-1951(99)00316-9)
- Gayol R (1925) Estudio de las perturbaciones que en el fondo de la Ciudad de México ha producido el drenaje de las aguas del subsuelo, por las obras del desagüe y rec-tificación de los errores a que ha dado lugar una incorrecta interpretación de los efectos producidos. *Revista Mexicana de Ingeniería y Arquitectura* III:96–132
- GCDMX (2017) (Gobierno de la Ciudad de Mexico) *Reglamento de Construcciones para el Distrito Federal*
- Hanssen RF (2001) *Radar Interferometry Data Interpretation and Error Analysis*. Kluwer Academic Publishers, Estados Unidos
- Hernández-Espriú A, Reyna-Gutiérrez JA, Sánchez-León E, et al (2014) The DRASTIC-Sg model: An extension to the DRASTIC approach for mapping groundwater vulnerability in aquifers subject to differential land subsidence, with application to Mexico City. *Hydrogeology Journal* 22:1469–1485. <https://doi.org/10.1007/s10040-014-1130-4>

- Hernández-Madrigal VM, Lázaro NF, Reyes CIV, Jauregui JAM (2015) Impacto económico producido por subsidencia diferencial en zonas urbanas. Caso de estudio Morelia, Michoacán. *Ciencia Nicolaita* 78–94. <https://doi.org/10.35830/cn.vi65.267>
- Hernández-Madrigal VM, Muñoz-Jauregui JA, Garduño-Monroy VH, et al (2014) Depreciation factor equation to evaluate the economic losses from ground failure due to subsidence related to groundwater withdrawal. *NS* 06:108–113. <https://doi.org/10.4236/ns.2014.63015>
- Holzer TL (1984) Ground failure induced by ground-water withdrawal from unconsolidated sediment. In: *Reviews in Engineering Geology*. Geological Society of America, pp 67–106
- Hooper A (2009) A statistical-cost approach to unwrapping the phase of InSAR time series. 6
- Hu L, Navarro-Hernández MI, Liu X, et al (2022) Analysis of regional large-gradient land subsidence in the Alto Guadalupe Basin (Spain) using open-access aerial LiDAR datasets. *Remote Sensing of Environment* 280:113218. <https://doi.org/10.1016/j.rse.2022.113218>
- INEGI (2020) Censo Población y Vivienda 2020. In: *Censo Población y Vivienda 2020*. <https://www.inegi.org.mx/programas/ccpv/2020/default.html>. Accessed 2 Dec 2021
- INEGI (2022) Directorio Nacional de Unidades Económicas. DENU. In: *Censos Económicos 2022*. <https://www.inegi.org.mx/app/mapa/denu/default.aspx>. Accessed 8 Nov 2022
- Julio-Miranda P, Ortiz-Rodríguez AJ, Palacio-Aponte AG, et al (2012) Damage assessment associated with land subsidence in the San Luis Potosí-Soledad de Graciano Sánchez metropolitan area, Mexico, elements for risk management. *Nat Hazards* 64:751–765. <https://doi.org/10.1007/s11069-012-0269-3>
- Lanari R, Mora O, Manunta M, et al (2004) A small-baseline approach for investigating deformations on full-resolution differential SAR interferograms. *IEEE Transactions on Geoscience and Remote Sensing* 42:1377–1386. <https://doi.org/10.1109/TGRS.2004.828196>
- Manunta M, De Luca C, Zinno I, et al (2019) The Parallel SBAS Approach for Sentinel-1 Interferometric Wide Swath Deformation Time-Series Generation: Algorithm Description and Products Quality Assessment. *IEEE Transactions on Geoscience and Remote Sensing* 57:6259–6281. <https://doi.org/10.1109/TGRS.2019.2904912>
- Marsal RJ, Mazari M (1959) El subsuelo de la Ciudad de México, 1er Congreso Panamericano de Mecánica de Suelos e Ingeniería de Cimentaciones, Facultad de Ingeniería. UNAM, México
- Massonnet D, Rossi M, Carmona C, et al (1993) The displacement field of the Landers earthquake mapped by radar interferometry. *Nature* 364:138–142. <https://doi.org/10.1038/364138a0>
- Novelo-Casanova DA, Suárez G, Cabral-Cano E, et al (2022) The Risk Atlas of Mexico City, Mexico: a tool for decision-making and disaster prevention. *Nat Hazards* 111:411–437. <https://doi.org/10.1007/s11069-021-05059-z>
- Ortega-Guerrero A, Cherry JA, Rudolph DL (1993) Large-Scale Aquitard Consolidation Near Mexico City. *Groundwater* 31:708–718. <https://doi.org/10.1111/j.1745-6584.1993.tb00841.x>
- Osmanoğlu B, Dixon TH, Wdowinski S, et al (2011) Mexico City subsidence observed with persistent scatterer InSAR. *International Journal of Applied Earth Observation and Geoinformation* 13:1–12. <https://doi.org/10.1016/j.jag.2010.05.009>
- Ovando-Shelley E, Romo MP, Contreras N, Giralt A (2003) Effects on soil properties of future settlements in downtown Mexico City due to ground water extraction. *Geofísica Internacional* 42:185–204
- Rojas E, Arzate J, Arroyo M (2002) A method to predict the group fissuring and faulting caused by regional groundwater decline. *Engineering Geology* 65:245–260. [https://doi.org/10.1016/S0013-7952\(01\)00135-1](https://doi.org/10.1016/S0013-7952(01)00135-1)
- Rosen PA, Gurrola E, Sacco GF, Zebker H (2012) The InSAR scientific computing environment. In: *EUSAR 2012; 9th European Conference on Synthetic Aperture Radar*. pp 730–733
- Sarychikhina O, Glowacka E, Mellors R, Vidal FS (2011) Land subsidence in the Cerro Prieto Geothermal Field, Baja California, Mexico, from 1994 to 2005: An integrated analysis of DInSAR, leveling and geological data. *Journal of Volcanology and Geothermal Research* 204:76–90. <https://doi.org/10.1016/j.jvolgeores.2011.03.004>
- Secretaría de Administración y Finanzas (2023) Valores unitarios. In: *DEFINICIONES*. [https://servidoresx3.finanze.cdmx.gob.mx/tesoreria/v\\_unitarios/definiciones.html](https://servidoresx3.finanze.cdmx.gob.mx/tesoreria/v_unitarios/definiciones.html). Accessed 20 Jun 2023
- Skempton AW, Macdonald DH (1956) The allowable settlements of buildings. *Proceedings of the Institution of Civil Engineers* 5:727–768. <https://doi.org/10.1680/ipeds.1956.12202>
- Solano-Rojas D, Cabral-Cano E, Fernández-Torres E, et al (2020a) Remotely triggered subsidence acceleration in Mexico City induced by the September 2017  $M_w$  7.1 Puebla and the  $M_w$  8.2 Tehuantepec September 2017 earthquakes. In: *Proceedings of the International Association of Hydrological Sciences*. Copernicus GmbH, pp 683–687
- Solano-Rojas D, Cabral-Cano E, Hernández-Espriú A, et al (2015) The relationship of InSAR-GPS land subsidence and the groundwater level decrease in wells of the Mexico City Metropolitan Area. *Boletín de la Sociedad Geológica Mexicana* 67:273–283
- Solano-Rojas D, Wdowinski S, Cabral-Cano E, Osmanoğlu B (2020b) Detecting differential ground displacements of civil structures in fast-subsiding metropolises with interferometric SAR and band-pass filtering. *Scientific Reports* 10:15460. <https://doi.org/10.1038/s41598-020-72293-z>
- Solano-Rojas DE, Wdowinski S, Cabral-Cano E, et al (2020c) A multiscale approach for detection and mapping differential subsidence using multi-platform InSAR products. *Proc IAHS* 382:173–177. <https://doi.org/10.5194/piahs-382-173-2020>
- Torres R, Snoeij P, Geudtner D, et al (2012) GMES Sentinel-1 mission. *Remote Sensing of Environment* 120:9–24. <https://doi.org/10.1016/j.rse.2011.05.028>
- World Bank (2023) World Bank Open Data. In: *World Bank Open Data*. <https://data.worldbank.org>. Accessed 8 Aug 2023
- Yunjun Z, Fattahi H, Amelung F (2019) Small baseline InSAR time series analysis: Unwrapping error correction and noise reduction. *Computers & Geosciences* 133:1–67. <https://doi.org/10.1016/j.cageo.2019.104331>

## Capítulo 5.5 Land Subsidence risk maps and InSAR based angular distortion structural vulnerability assessment: an example in Mexico City

### Contents

---

#### **Abstract**

#### **1 Introduction**

#### **2 Methodology**

##### **2.1 Land subsidence velocity and subsidence horizontal gradient maps**

##### **2.2 Land Subsidence Risk assessment**

##### **2.3 Structural vulnerability analysis of the civil due to angular distortion and exposition of critical infrastructure of the city**

#### **3 Results**

#### **4 Conclusion**

#### **References**

---

**Fernández-Torres E**, Cabral-Cano E, Solano-Rojas D, et al (2020) Land Subsidence risk maps and InSAR based angular distortion structural vulnerability assessment: an example in Mexico City. In: Proceedings of the International Association of Hydrological Sciences. Copernicus GmbH, pp 583–587



## Land Subsidence risk maps and InSAR based angular distortion structural vulnerability assessment: an example in Mexico City

Enrique Fernández-Torres<sup>1</sup>, Enrique Cabral-Cano<sup>1</sup>, Dario Solano-Rojas<sup>2</sup>, Emre Havazli<sup>3,a</sup>, and Luis Salazar-Tlaczani<sup>1</sup>

<sup>1</sup>Instituto de Geofísica, Universidad Nacional Autónoma de México, México CDMX, 04510, Mexico

<sup>2</sup>Facultad de Ingeniería, Universidad Nacional Autónoma de México, México CDMX, 04510, Mexico

<sup>3</sup>Rosenstiel School of Marine and Atmospheric Science, University of Miami, Miami, Florida, USA

<sup>a</sup>now at: Jet Propulsion Laboratory, California Institute of Technology, Pasadena, CA, USA

**Correspondence:** Enrique Fernández-Torres (enrique.30065@gmail.com)

Published: 22 April 2020

**Abstract.** Land subsidence is a phenomenon present in several cities in central Mexico, and results from a combination of groundwater resources' overexploitation and the local stratigraphic nature. Furthermore, subsidence occurs inhomogeneously in space, producing differential vertical displacements, which affect both the natural media, as well as human-built structures. Subsidence associated structural-vulnerability assessments usually rely on direct field measurements to determine parameters such as angular distortion. However, the large areas in which land subsidence occurs (city-scale) in Mexico City hinders a direct quantification of differential displacements for all buildings and structures present in it. A Sentinel-1 based subsidence analysis shows that the highest velocities are located on the eastern sector of the city. This velocity map was used as the basis for a population density weighted land subsidence correlation analysis. Our Land Subsidence Risk assessment indicates that 15.43 % of the population of Mexico City live in intermediate, high and very-high risk zones which corresponds to 1 358 873 inhabitants. Therefore, a significant percentage of Mexico City's population is vulnerable to suffering damage in their housing structures due to land subsidence. Furthermore, the lower income inhabitants share a proportionally greater economic cost due to land subsidence and associated shallow faulting. The structural vulnerability analysis of the civil structures in the city was performed using angular distortion maps derived from the subsidence velocity gradient between October 2014–October 2017 period. These maps indicate that within this time window, ~ 12 % of the total urbanized area in Mexico City had already exceeded a 0.002 radian angular distortion threshold; above which damage in civil structures is more likely to occur. In fact, more than 1 million people have already suffered damages in their houses due to the differential ground subsidence and the resulting structural angular distortion. With these results, we can evaluate correspondence between angular distortion map and critical infrastructure of the city, as a result, we found that between 0 % and 12.84 % of these buildings have undergone over 0.002 radian angular distortion.

## 1 Introduction

Mexico's central region has the higher population density of all the country (INEGI, 2011) therefore this condition creates an accelerated demand of public services among them potable water. In the case of Mexico City, more than 70 % of this water come from the aggressive exploitation of the underground aquifer of the basin (Santoyo-Villa et al., 2005). The intense underground extraction produces piezometric reduction and an increase of the effective stresses within the subsoil that generates compaction and causes land subsidence velocities of outstanding magnitude (e.g. Carrillo, 1948; Cabral-Cano et al., 2008, 2011).

Ground subsidence risk maps are a valuable decision element to help local authorities design better risk management, land use and mitigation strategies for cities under intense subsidence. In Mexico City, methodology to create risk an hazard maps have been refined for the past years (Cabral-Cano et al., 2011, 2015; Solano-Rojas, 2013) to help create an adequate characterization of subsidence velocity and its associated surface faulting as well as the spatial relationship between those process and the population density (e.g. Solano-Rojas, 2013).

Continuous ground subsidence results in severe damage to urban infrastructure and civil infrastructure. Angular distortion is a valid alternative to evaluate damages of civil infrastructure caused by land subsidence. This parameter measures the difference of subsidence of two adjacent supports relative to the distance between them (Skempton and MacDonald, 1956), and threshold limits of angular distortion beyond which it is expected that there will be damage to civil structures. This analysis can be useful as a criterion for evaluation of the impact of differential subsidence over the civil structures in Mexico City.

This work is aimed toward the use of InSAR-derived products to obtain ground subsidence velocity map and subsidence horizontal gradient map combined with population density to generate a land subsidence hazard map. Furthermore, these products were also used for a structural vulnerability analysis of the civil structures in the city using an angular distortion estimation derived from the subsidence horizontal gradient map, this methodology allowed the evaluation of critical infrastructure due to angular distortion.

## 2 Methodology

### 2.1 Land subsidence velocity and subsidence horizontal gradient maps

Ground subsidence velocity and subsidence horizontal gradient maps are based on space-based Synthetic Aperture Radar (SAR) acquisitions processed using Interferometric SAR (InSAR) techniques. Other InSAR products include time series and velocity maps, obtained from an SBAS analysis.

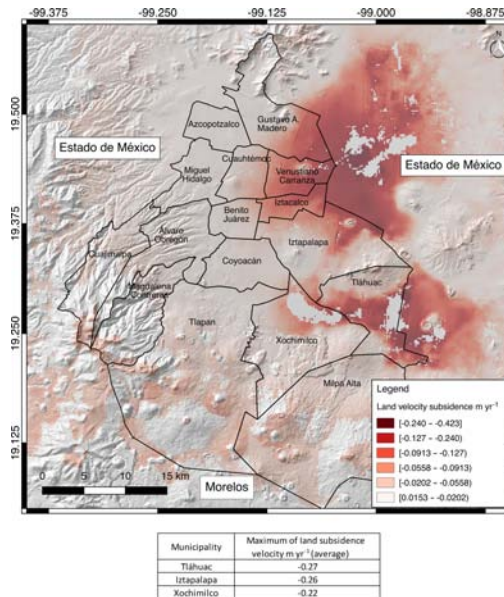


**Figure 1.** Velocity of Land Subsidence (LOS) of Mexico City (October 2014–October 2017). The shaded topographic base layer is taken from Continuo de Elevaciones Mexicano 3.0. © Instituto Nacional de Estadística Geografía e Informática (INEGI).

For this job, InSAR processing from Sentinel 1a and b data was used to obtain an SBAS derived subsidence velocity map (Fig. 1). Subsidence horizontal gradient was calculated (Cabral-Cano et al., 2011), using a slope algorithm, available in QGIS v 2.18 (Fig. 2).

Both maps land subsidence velocity and subsidence gradient were divided into five categories using the algorithm Natural Break (Jenks, 2007) as the criterion of classification in order to better discriminate among classes.

### 2.2 Land Subsidence Risk assessment

A Risk map was computed using algebra maps by multiplying the sum of land subsidence velocity and subsidence horizontal gradient with the population density (INEGI, 2011, 2012). To better estimate the distribution of the city regions where most people are affected by these processes. To define of relative weight of the previously mentioned variables that defined hazard due to land subsidence and associated faulting we considered the relative importance of each parameter as shown on Eq. (1). We assigned three times more weight to subsidence horizontal gradient than land subsidence because subsidence gradient represents differential ground displacement of civil structures and as a result, the higher subsidence gradient, the higher shear stress and the consequent develop-

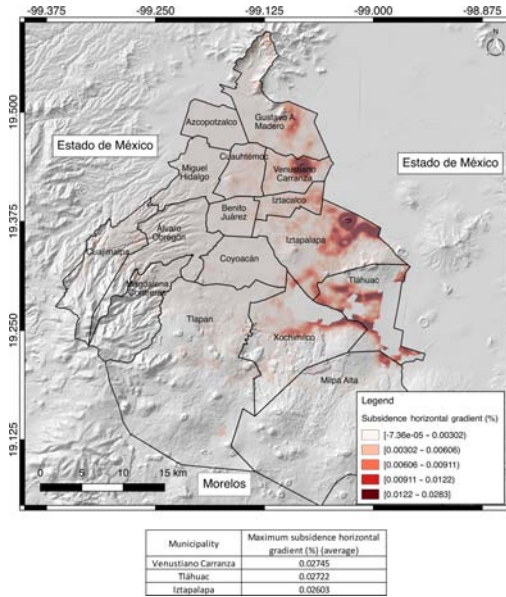


**Figure 2.** Subsidence Horizontal Gradient of Mexico City. The shaded topographic base layer is taken from Continuo de Elevaciones Mexicano 3.0. © Instituto Nacional de Estadística Geografía e Informática (INEGI).

ment of faults and damage to structures (Cabral-Cano et al., 2015). On the other hand, if the magnitude of land subsidence velocity is spatially homogeneous on an area, the probability of damage in urban infrastructure is reasonably lower. The equation that define the risk due to land subsidence and associated faulting is the following:

$$\text{Risk} = ((3 \times \text{SHG}) + V_{\text{sub}}) \times \text{Pop}_{\text{den}} \quad (1)$$

Where SHG is the subsidence horizontal gradient,  $V_{\text{sub}}$  is the land subsidence velocity and  $\text{Pop}_{\text{den}}$  is the population density of Mexico City.

Finally, we divided risk map (Fig. 3) into five categories by using the Natural Break algorithm (Jenks, 2007) and counting the population inside each category.

### 2.3 Structural vulnerability analysis of the civil due to angular distortion and exposition of critical infrastructure of the city

To compute the angular distortion map we used the raster calculator available in QGIS v2.18 to transform the subsidence horizontal gradient from percentage into radians. This map expressed in radians let us to evaluate the places of the city that are above the 0.002 radian threshold that is the recommended value to avoid damage in urban infrastructure

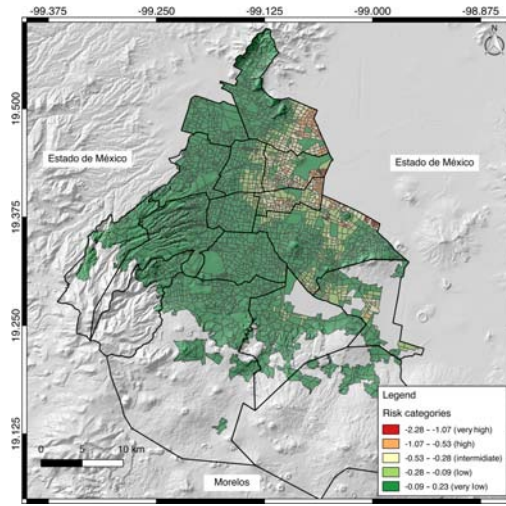


**Figure 3.** Hazard zonation for surface faulting associated to ground subsidence in the Mexico City. The shaded topographic base layer is taken from Continuo de Elevaciones Mexicano 3.0. © Instituto Nacional de Estadística Geografía e Informática (INEGI).

(Skempton and MacDonald, 1956; Bjerrum, 1963; Zhang and Ng, 2007). The next stage was the evaluation of structural vulnerability by counting the area and population which are affected their infrastructure due to angular distortion for this propose the information of the 2010 Mexico’s population census was used (INEGI, 2011, 2012).

To evaluate the structural vulnerability of critical infrastructure of the Mexico we mapped these discrete points over the angular distortion layer and recorded the of angular distortion value for each point or polyline by using the add raster value to feature tool available in QGIS 2.18.

## 3 Results

The eastern sector of Mexico City is undergoing rapid subsidence due to overexploitation of ground water resources and the consequent compaction of clay-rich lacustrine sediment (Osmanoğlu et al., 2011). According to our land subsidence velocity map (Fig. 1) the municipalities with higher land subsidence velocities are Tláhuac ( $-0.27 \text{ m yr}^{-1}$ ), Iztapalapa ( $-0.26 \text{ m yr}^{-1}$ ), and Xochimilco ( $-0.22 \text{ m yr}^{-1}$ ). These areas show the highest values of land subsidence because of combination of lacustrine deposits with high ground water extraction rates.

The subsidence horizontal gradient map show that municipalities with highest values are Venustiano Carranza (0.02745 %), Tláhuac (0.02722 %), and Iztapalapa (0.02603 %) (see Fig. 2). Moreover, as the highest values



of subsidence gradient represents potential areas of surface, the horizontal gradient is an excellent proxy for assessing potential structural damage to civil structures and other hydraulic infrastructure. The development of higher values of subsidence gradient (Fig. 2) is controlled by the sharp transition between highly compressible lacustrine deposits and volcanic structures (Auvinet, et al., 2017).

The hazard map due to land subsidence and associated faulting combines risk elements represented by the velocity of land subsidence and subsidence gradient. On the other hand, local density population represents the vulnerability indicator. After applying map algebra using Eq. (1) we found that municipalities with higher area and population that fall under intermediate, high and very high risks categories are Gustavo A. Madero (18.25 km<sup>2</sup>, 369 387 inhabitants), Venustiano Carranza (18.25 km<sup>2</sup>, 329 338 inhabitants), Iztacalco (13.21 km<sup>2</sup>, 292 241 inhabitants.), and Iztapalapa (11.49 km<sup>2</sup>, 262 892 inhabitants) (Fig. 3). This underscores the presence of high land subsidence velocities and differential subsidence rates with higher density of population. The land subsidence hazard map is a valuable decision element to help local authorities design the best hazard mitigation and management strategies for cities under intense subsidence.

The angular distortion map shows that the eastern portion of the city is where civil structures have exceeded 0.002 radian which is the recommended threshold to avoid damage in urban infrastructure (Skempton and MacDonald, 1956; Bjerum, 1963; Zhang and Ng, 2007). According to our angular distortion map (Fig. 4), more than 12 % of the area and 13 % of the population of Mexico City which corresponds to an area of 97.47 km<sup>2</sup> and a population of 1 110 790 inhabitants which are affected.

Our assessment of Mexico City's critical infrastructure of between 0 % and 12.84 % of these buildings overcome 0.002 radians of angular distortion (Fig. 5). This analysis is of further importance in case of occurrence of other phenomena such as earthquakes.

#### 4 Conclusions

Our land subsidence risk analysis in Mexico City shows that this process affects the eastern portion of the city. The angular distortion product is a valuable tool to assess the structural vulnerability and allowed us to estimate areas with the highest structural damage. The angular distortion map may be an excellent proxy to help local authorities design the best risk mitigation and management strategies.

**Data availability.** Sentinel 1a and b SAR data used on this work was provided by the European Space Agency (ESA) through the Alaska Satellite Facility SAR Data Center (ASF SDC) at <https://www.asf.alaska.edu/> (Alaska Satellite Facility SAR Data Center, 2020).

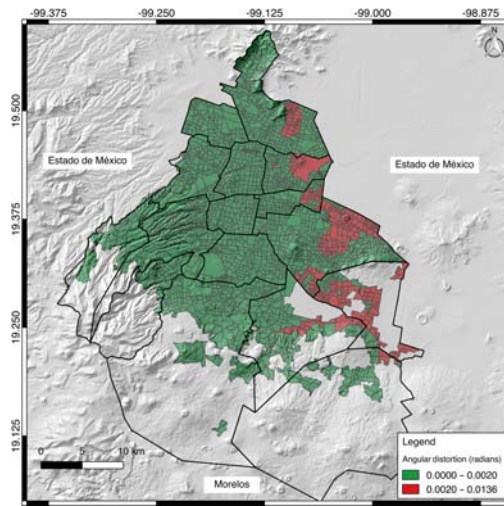


**Figure 4.** Angular distortion map of Mexico City. The shaded topographic base layer is taken from Continuo de Elevaciones Mexicano 3.0. © Instituto Nacional de Estadística Geografía e Informática (INEGI).

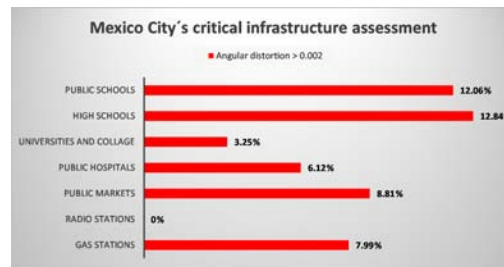


**Figure 5.** Mexico City's critical infrastructure assessment.

**Author contributions.** EFT provided formal analysis, investigation, methodology and writing of original draft. ECC provided conceptualization of the project, investigation, resources and writing of original draft and supervision, DSR provided formal analysis and review and editing of draft, EH provided formal analysis and methodology, LST provided investigation and validation.

**Competing interests.** The authors declare that they have no conflict of interest.

**Special issue statement.** This article is part of the special issue "TISOLS: the Tenth International Symposium On Land Subsidence – living with subsidence". It is a result of the Tenth Inter-

national Symposium on Land Subsidence, Delft, the Netherlands, 17–21 May 2021.

**Acknowledgements.** Enrique Fernández-Torres acknowledges support from CONACyT during his MS dissertation. Darío Solano-Rojas acknowledges support from CONACyT and Fulbright-García Robles. SAR data was kindly provided by the European Space Agency (ESA). Part of the InSAR processing was done on UNAM-DGTIC's Miztli supercomputing facility with processing time granted by LANCAD and CONACyT.

**Financial support.** This research has been supported by the Universidad Nacional Autónoma de México, Dirección General de Asuntos del Personal Académico, DGAPA-PAPIIT projects IV100215 and IN104818-3 and Consejo Nacional de Ciencia y Tecnología (CONACyT) projects 256012 and 005955 to Enrique Cabral-Cano.

## References

- Alaska Satellite Facility SAR Data Center: Sentinel-1 Interferometric Wide swath Track 143, Frame 3203, descending mode, acquired between 3/10/2014 and 29/10/2017, available at: <https://www.asf.alaska.edu>, last access: 14 April 2020.
- Auvinet, G., Méndez, E., and Juárez, M.: El Subsuelo de la Ciudad de México, Instituto de Ingeniería, UNAM, Vol. III, 2017, México CDMX, México, 2017.
- Bjerrum, L.: Discussion, Proc. European Conference on Soil Mechanics and Foundation Engineering, Wiesbaden, Germany, vol. III, p. 135, 1963.
- Cabral-Cano, E., Dixon, T. H., Miralles-Wilhelm, F., Sainchez-Zamora, O., Díaz-Molina, O., and Carande, R. E.: Space Geodetic Imaging of Rapid Ground Subsidence in México City, *B. Am. Geol. Soc.*, 120, 1556–1566, <https://doi.org/10.1130/B26001.1>, 2008.
- Cabral-Cano, E., Díaz Molina, O., and Delgado-Granados, H.: Subsistencia y Mapas de Peligro por Fallamiento Superficial: Un Ejemplo en el área Nororiental de la Zona Metropolitana de la Ciudad de México, *Bol. Soc. Geol. Mex.*, 63, 53–60, 2011.
- Cabral-Cano, E., Solano-Rojas, D., Oliver-Cabrera, T., Wdowinski, S., Chaussard, E., Salazar-Tlaczani, L., Cigna, F., DeMets, C., and Pacheco-Martínez, J.: Satellite geodesy tools for ground subsidence and associated shallow faulting hazard assessment in central Mexico, *Proc. IAHS*, 372, 255–260, <https://doi.org/10.5194/piahs-372-255-2015>, 2015.
- Carrillo, N.: Influence of Artesian Wells on the Sinking of Mexico City, Proceedings, Second International Conference on Soil Mechanics and Foundation Engineering, 21–30 June 1948, Rotterdam, the Netherlands, vol. 2, 156–159, 1948.
- INEGI: Conteos de población y vivienda 2010: INEGI, available at: <https://www.inegi.org.mx/programas/ccpv/2010/> (last access: 14 April 2020), 2011.
- INEGI: Vectorial de localidades amanzandas y números exteriores, Urbanas. Cierre de planeación del Censo de Población y Vivienda, available at: <https://www.inegi.org.mx/app/mapas/default.html> (last access: 14 April 2020), 2012.
- Jenks, G. F.: Natural Breaks, Release 9.2, Last modified August 15, 2007. ESRI, ArcGIS 9.2 Desktop Help, available at: [http://webhelp.esri.com/arcgisdesktop/9.2/index.cfm?topicname=natural\\_breaks\\_\(jenks\)](http://webhelp.esri.com/arcgisdesktop/9.2/index.cfm?topicname=natural_breaks_(jenks)) (last access: 14 April 2020), 2007.
- Osmanoğlu, B., Dixon, T. H., Wdowinski, S., Cabral-Cano, E., and Jiang, Y.: Mexico City Subsidence Observed with Persistent Scatterer InSAR, *Int. J. Appl. Earth Obs.*, 13, 1–12, <https://doi.org/10.1016/j.jag.2010.05.009>, 2011.
- Santoyo-Villa, E., Ovando, E., Mooser, E., and León, E.: Síntesis Geotécnica de la Cuenca del Valle de México, Publicaciones TGC, México, CDMX, México, 2005.
- Skempton, A. W. and MacDonald, D. H.: Allowable settlement of buildings, *Proc. Inst. Civ. Engrs.*, Part III, 5, 727–768, 1956.
- Solano-Rojas, D. E.: Evaluaciones de Riesgo por Fallamiento Asociado a Subsistencia de INSAR, (Tesis de licenciatura), Universidad Nacional Autónoma de México, Ciudad de México, México, 2013.
- Zhang, L. M. and Ng, A. M. Y.: Limiting Tolerable Settlement and Angular Distortion for Building Foundations, Geo-Denver 2007, 18–21 February 2007, Denver, Colorado, USA, American Society of Civil Engineers, 1–11, [https://doi.org/10.1061/40914\(233\)18](https://doi.org/10.1061/40914(233)18), 2007.

## 6 Discusión

En esta investigación se identificó que la subsidencia del terreno en áreas urbanas no está limitada al centro de México, sino que también está presente al norte de México y a lo largo de las zonas costeras. Considerando un umbral de detección de  $-2.8$  cm/a y una pendiente promedio del terreno máxima de 5 grados, determinamos que  $3,797$  km<sup>2</sup> es el área urbana de México expuesta a subsidencia de terreno con potencial afectaciones a la infraestructura. En consecuencia, 21.4 millones de personas y 6.9 millones de viviendas están expuestas a velocidades de subsidencia significativas que pueden alcanzar las varias decenas de centímetros al año. Estas zonas con subsidencia representan 853 localidades urbanas, las cuales agrupamos en 29 regiones.

También identificamos que las zonas urbanas con subsidencia se encuentran preferentemente sobre depósitos compresibles, con acuíferos estresados y sin disponibilidad de agua. Los resultados obtenidos muestran similitudes importantes con el mapa de Subsidencia Potencial Global en cuanto a la distribución espacial (Herrera-García et al. 2021). La mayor densidad de localidades urbanas con subsidencia en México se concentra a lo largo de la Faja Volcánica Mexicana, dado que esta zona se concentra la mayor extracción de agua, la cual es destinada principalmente para fines agrícolas y el consumo de las áreas urbanas. Adicionalmente, un importante número de las ciudades ubicadas en la Faja Volcánica Mexicana se encuentran sobre planicies, con considerable espesor de sedimentos lacustres y aluviales que favorecen a la subsidencia del terreno (p. ej. Figueroa-Miranda et al. 2018).

Con relación a las velocidades máximas de subsidencia, obtuvimos valores similares a investigaciones previas realizadas en el centro de México y Baja California (p. ej. Chaussard et al. 2014; Sarychikhina et al. 2018; Cigna and Tapete 2022a; Pérez-Falls et al. 2022). Algunas de las velocidades de subsidencia urbana medidas en este trabajo se encuentran entre las más altas del mundo (p. ej. Galloway and Burbey 2011), registrando, en algunos casos, varias decenas de centímetros por año (p. ej. Ciudad Nezahualcóyotl [42.8 cm/a], Chaparrosa, Zacatecas [19.3 cm/a], Jocotepec, Jalisco [16.5 cm/a], La Partida, Coahuila [14.3 cm/a]). También se realizó una comparación de series de tiempo InSAR y cGPS, utilizando las series de tiempo GPS de 100 estaciones, obteniéndose una diferencia promedio de velocidades de  $-1$  mm/a, lo que indica que las velocidades del terreno medidas son precisas, siendo esta la calibración InSAR-cGPS más extensa realizada en México.

Adicionalmente, podemos señalar que la subsidencia del terreno en México es causada principalmente por la extracción intensiva de agua subterránea, lo que ha llevado que la tasa de extracción sobrepase a la recarga en 105 de los 653 sistemas acuíferos (CONAGUA 2020). Sin embargo, en México existen otras causas que generaran subsidencia del terreno, tales como lo son la extracción de fluido geotérmico y de hidrocarburos (p. ej. Sarychikhina et al. 2018; Cigna et al. 2020; Pérez-Falls et al. 2022).

En esta investigación también se estimó el riesgo socioeconómico por subsidencia y fallamiento asociado en la Ciudad de México. Obteniéndose que las áreas urbanas con mayor vulnerabilidad socioeconómica coinciden espacialmente, en muchos casos, con los mayores valores de subsidencia del terreno y gradiente horizontal de subsidencia. Por tanto, obtuvimos que 9% del área urbanizada de la Ciudad de México presenta riesgo socioeconómico alto y muy alto, lo que corresponde a  $70.7$  km<sup>2</sup>, donde 12.6% de la población de la ciudad vive, según datos del Censo de Población y Vivienda de 2010 (INEGI 2010). Adicionalmente, determinamos que el 40.4% de la longitud total del fallamiento asociado a subsidencia del terreno se encuentra en zonas con gradiente horizontal de subsidencia alto y muy alto. Este trabajo presenta la primera determinación del riesgo socioeconómico en México, lo que representa una herramienta de utilidad a los tomadores de decisiones para la identificación de las zonas en las que la población se ve afectada por subsidencia de terreno y donde la capacidad para sobreponerse a dichos efectos es menor, dado su vulnerabilidad socioeconómica. A su vez, corroboramos que el gradiente horizontal de subsidencia es una herramienta de utilidad para la determinación de áreas potenciales para el desarrollo de fallamiento asociado a subsidencia, como ya ha sido determinado en otras investigaciones (p. ej. Cabral-Cano et al. 2008; Solano-Rojas et al. 2020c).

En la Ciudad de México también estudiamos por primera vez el riesgo económico por subsidencia diferencial, utilizando los Estados Límites de la reglamentación de construcciones vigente y el valor catastral de los predios. La estimación del riesgo económico se realizó para dos escenarios de tipologías. El primer escenario consistió en edificaciones de mampostería de hasta dos niveles y el segundo en construcciones de armazón de acero de hasta cuatro niveles. Se tomaron estos escenarios considerando que la Ciudad de México, la mayoría de las construcciones son de 1 a 5 niveles y mampostería y armazón de acero son tipologías comunes en la ciudad. Para el primer escenario de

riesgo económico obtuvimos que el valor catastral de las edificaciones ubicadas en zonas de riesgo alto y muy alto es de 10,500 millones de dólares, lo que expondría 215,000 propiedades y 738,000 habitantes. Para el escenario dos obtuvimos que 2,500 millones de dólares es valor catastral de las propiedades con riesgo económico alto debido a subsidencia diferencial, exponiendo 48,000 propiedades y 169,000 personas. Los resultados obtenidos representan la primera evaluación en términos económicos de la subsidencia diferencial en la Ciudad de México, una de las ciudades con mayor densidad poblacional, velocidad e historia de subsidencia del terreno por extracción de agua. Investigaciones previas realizadas en otras ciudades de México (p. ej. Morelia, Toluca, San Luis Potosí) estimaron pérdidas económicas por subsidencia del terreno, utilizando un factor de demérito en función de las cercanías de las fallas asociadas a subsidencia diferencial y evaluación de daños en campo. Estas investigaciones previas no utilizaron los estados límites definidos en la reglamentación de construcción, ni el campo de velocidades de subsidencia del terreno, ni llegaron a la estimación del riesgo económico (Julio-Miranda et al. 2012; Hernández-Madrigal et al. 2014, 2015; Camacho-Sanabria et al. 2020).

Otro de los avances de este trabajo es la generación de un mapa de distorsión angular mediante el uso del campo de velocidades verticales InSAR. La distorsión angular es un parámetro de la ingeniería estructural que permite evaluar la intensidad de daños relacionados con la subsidencia del terreno (p. ej. Skempton and Macdonald 1956; Burland and Wroth 1975). Este parámetro ingenieril ha sido utilizado en otros países (p. ej. Países Bajos, Estados Unidos, China), y ha permitido establecer relaciones entre intensidad de daños y valores de distorsión angular para edificaciones con distintas características tipológicas, cimentaciones y características del subsuelo (p. ej. Skempton and Macdonald 1956; Zhang and Ng 2007; Peduto et al. 2017). En este estudio, realizamos una estimación de las construcciones expuestas a subsidencia diferencial y potencial fallamiento. Obtuvimos que el 12% del área urbanizada de la Ciudad de México excede 0.002 radianes de distorsión angular, exponiendo a más de un millón de habitantes a posibles daños de sus construcciones. También, fue evaluada la distorsión angular en construcciones críticas tales como: centros educativos, hospitales, mercados públicos y estaciones de gasolina, obteniéndose que entre el 3% y 12% de las mismas presentan distorsión angular mayor a 0.002 radianes, lo que representaría una potencial afectación a estas construcciones. El valor de corte de la distorsión angular fue obtenido de tablas de referencia de artículos publicados, en los cuales indican que a partir de 0.002 radianes de distorsión angular las edificaciones tienen el potencial de sufrir daños (p. ej. Skempton and Macdonald 1956; Bjerrum 1963; Zhang and Ng 2007). Posterior a la publicación de este trabajo, otros autores han utilizado la distorsión angular calculada bajo la metodología presentada para evaluar el potencial daño de las edificaciones y la estimación de exposición por subsidencia diferencial en la Ciudad de México y otras ciudades del centro de México (p. ej. Cigna and Tapete 2021a, b, 2022b).

En las investigaciones realizadas en este trabajo se generaron avances en campo de detección de localidades urbanas con subsidencia, riesgo económico y socioeconómico y determinación de distorsión angular. Productos que presentan una potencial aplicación para la determinación de las zonas urbanas de México que requieren la ejecución de medidas que fomenten la mitigación de la subsidencia del terreno.

A pesar de los avances presentados en la detección de subsidencia y evaluación de su riesgo, existen ciertas limitaciones que se pretenden cubrir en próximas investigaciones. Como los son la evaluación de la subsidencia del terreno de México utilizando escenas SAR adquiridas en órbitas ascendentes y descendentes y series de tiempo InSAR más largas (p. ej. 7 o más años) lo que permitirá la separación de la velocidad del terreno en la componente vertical y este-oeste y la evaluación de la evolución temporal de la subsidencia. La separación de las componentes de velocidad del terreno permitirá la determinación del gradiente horizontal de subsidencia a nivel país, para conseguir zonas de potencial desarrollo de fallas, así como áreas con deformación horizontal. También es necesario realizar evaluaciones en campo de las nuevas zonas urbanas con subsidencia del terreno detectadas en esta investigación. Las evaluaciones en campo podrían incluir la evaluación del cambio en los niveles piezométricos, estudio de las propiedades mecánicas del subsuelo, la cartografía de fallamiento en caso de existir, la evaluación de los daños en las construcciones y modelación de la subsidencia diferencial y del comportamiento del sistema acuífero. También se propone la evaluación de la deformación diferencial de las construcciones que presentan mayor gradiente horizontal de subsidencia mediante el uso del algoritmo PSI y escenas SAR de banda X. Estos estudios SAR con mayor resolución espacial permitirán la generación de perfiles de deformación de las edificaciones y cuyos daños deben ser corroborados en campo con el fin de generar curvas de fragilidad y vulnerabilidad estructural. También se propone incluir en próximos censos de población y vivienda la información de tipología y acabados de las construcciones (p. ej. tipos de muros, recubrimientos, tipos de pisos), ya que esto permitirá la evaluación del riesgo estructural y económico no solo por subsidencia sino por otros peligros geológicos.

## 7 Conclusiones

A partir de los resultados de esta investigación determinamos que la subsidencia urbana en México no solo está limitada al centro del país, sino también a lo largo de las costas y en la zona norte y noroeste. Se localizaron 853 localidades urbanas expuestas a subsidencia del terreno más rápidas que 2.8 cm/a (1.5 desviaciones estándar de la velocidad), lo que representa una exposición del 17% de la población del país, 6.9 millones viviendas y un área urbana total de 3,797 km<sup>2</sup>. Adicionalmente, se determinó que la subsidencia urbana en México ocurre en zonas donde los sistemas acuíferos se encuentran estresados, donde la tasa de extracción sobrepasa a la recarga y sobre sedimentos no consolidados.

En esta investigación también se determinó que, en la Ciudad de México, las mayores tasas de subsidencia y gradiente horizontal de subsidencia presentan una correlación espacial con las zonas de mayor vulnerabilidad socioeconómica. Por lo tanto, 12.6% de la población se encuentra expuesta a riesgo socioeconómico alto y muy alto. Además, se encontró, que las fallas asociadas a subsidencia presentan una correlación espacial de 40.4% con los valores de gradiente horizontal de subsidencia. Por tanto, el gradiente horizontal de subsidencia es una herramienta de gran utilidad para determinar las áreas potenciales para el desarrollo de fallamiento asociado a subsidencia. Los resultados obtenidos permiten conocer las zonas de la ciudad que necesitan una pronta intervención para reducir el impacto de la subsidencia, así como las zonas que debería ser destinadas a otros usos, evitando la construcción de viviendas que puedan ser afectadas en el corto y mediano plazo.

En cuanto al riesgo económico por subsidencia diferencial en la Ciudad de México, se obtuvo que el costo catastral de las propiedades que se encuentran en riesgo económico alto y muy alto es de 1,5 mil millones USD o el 6.1% del valor catastral de la Ciudad de México, exponiendo 738,000 personas y 215,000 viviendas para el escenario de edificaciones de mampostería y de hasta dos niveles. Para el caso de edificaciones de estructuras de marcos de acero de hasta 4 niveles, se determinó que el costo catastral de propiedades que se encuentran en riesgo alto es de USD 2,500 millones o 1.4% del valor catastral de la Ciudad de México, generando una exposición de 48,000 viviendas y 169,000 personas. También se encontró que el costo catastral de la Ciudad de México es de 171.3 mil millones USD y que el valor catastral de las propiedades que sobrepasan los Estados Límite para edificaciones de mampostería es de USD 44,000 millones USD y para el caso de edificaciones con marcos de acero es 13,600 millones USD. Estos resultados permiten obtener la primera evaluación en términos monetarios de las implicaciones del proceso de subsidencia en la Ciudad de México, lo que hace posible comparar con otros fenómenos naturales y estimular el desarrollo y aplicación de estrategias que permitan la mitigación de los efectos de la subsidencia.

En relación con el análisis de exposición de las construcciones por subsidencia mediante la utilización de un mapa de distorsión angular basado en un análisis InSAR, obtuvimos que el 12% del área urbana de la Ciudad de México excede el valor de 0.002 radianes de distorsión angular, lo que pudiese ocasionar daños en la infraestructura y vivienda, afectando a más de 1 millón de personas. Por tanto, la distorsión angular es una herramienta que puede ayudar a las autoridades locales la determinación de áreas de interés para el diseño de mejores estrategias de mitigación de daños y administración y gestión de los recursos hídricos.

El trabajo aquí desarrollado pretende servir como un marco de referencia para el desarrollo de futuras investigaciones relacionadas con la subsidencia del terreno en México, así como una herramienta de consulta para las autoridades y tomadores de decisiones con fines de estimular la mitigación de la subsidencia mediante un manejo eficiente de la extracción de agua y planeación urbana.

## 8 Referencias

- Acuña-Lara F, Pacheco-Martínez J, Luna-Villavicencio H, et al (2020) Infiltration of surface water through subsidence failure assessment applying electric prospecting, case Aguascalientes Valley, Mexico. In: Proceedings of IAHS. Copernicus GmbH, pp 5–9
- Aguilar-Pérez LA, Ortega-Guerrero MA, Lugo-Hubp J, Ortiz-Zamora D del C (2006) Análisis numérico acoplado de los desplazamientos verticales y generación de fracturas por extracción de agua subterránea en las proximidades de la Ciudad de México. *Revista mexicana de ciencias geológicas* 23:247–261
- Alaniz-Álvarez SA, Nieto-Samaniego AF, Morán-Zenteno DJ, Alba-Aldave L (2002) Rhyolitic volcanism in extension zone associated with strike-slip tectonics in the Taxco region, southern Mexico. *Journal of Volcanology and Geothermal Research* 118:1–14. [https://doi.org/10.1016/S0377-0273\(02\)00247-0](https://doi.org/10.1016/S0377-0273(02)00247-0)

- Albano M, Polcari M, Bignami C, et al (2016) An innovative procedure for monitoring the change in soil seismic response by InSAR data: application to the Mexico City subsidence. *International Journal of Applied Earth Observation and Geoinformation* 53:146–158. <https://doi.org/10.1016/j.jag.2016.08.011>
- Auvinet-Guichard G, Méndez E, Juárez M (2013) Soil fracturing induced by land subsidence in Mexico City. In: *Proceedings of the 18th International Conference on Soil Mechanics and Geotechnical Engineering*. Paris, France, pp 2921–2924
- Auvinet-Guichard G, Méndez-Sánchez E, Juárez-Camarena M (2015) New information on regional subsidence and soil fracturing in Mexico City Valley. *Proceedings of IAHS* 372:39–44. <https://doi.org/10.5194/piahs-372-39-2015>
- Ávila-Olivera JA, Farina P, Garduño-Monroy VH (2010) Land subsidence monitored by satellite interferometry in Mexican cities. In: *IAHS-AISH*
- Ávila-Olivera JA, Farina P, Garduño-Monroy VH (2008) Integration of InSAR and GIS in the Study of Surface Faults Caused by Subsidence-Creep-Fault Processes in Celaya, Guanajuato, Mexico. In: *AIP Conference Proceedings*. pp 200–211
- Avilés J, Pérez-Rocha LE (2010) Regional subsidence of Mexico City and its effects on seismic response. *Soil Dynamics and Earthquake Engineering* 30:981–989. <https://doi.org/10.1016/j.soildyn.2010.04.009>
- Avilés J, Pérez-Rocha LE, Aguilar HR (2006) Influence of ground water extraction in the seismic hazard of Mexico City. In: *Geo-Environment and Landscape Evolution II: Monitoring, Simulation, Management and Remediation*. WIT Press, Rhodes, Greece, pp 457–466
- Bamler R, Hartl P (1998) Synthetic aperture radar interferometry. *Inverse Problems* 14:R1–R54. <https://doi.org/10.1088/0266-5611/14/4/001>
- Barajas-Nigoche LD, Carreon-Freyre D, Mata-Segura JL, et al (2010) Geological and geophysical characterization of fracturing in granular deposits associated with land subsidence in San Luis Potosí City, Mexico. In: *IAHS-AISH/IAHS-AISH*. IAHS-AISH
- Berardino P, Fornaro G, Lanari R, Sansosti E (2002) A new algorithm for surface deformation monitoring based on small baseline differential SAR interferograms. *IEEE Trans Geosci Remote Sensing* 40:2375–2383. <https://doi.org/10.1109/TGRS.2002.803792>
- Bignami C, Brunori CA, Murgia F, Tolomei C (2018) Multi-sensor monitoring of Ciudad Guzman (Mexico) ground subsidence. *Procedia Computer Science* 138:362–365. <https://doi.org/10.1016/j.procs.2018.10.051>
- Bjerrum L (1963) *Allowable Settlement of Structures*. Wiesbaden, 2, Brighton, England, pp 135–137
- Blong R (2003) *A New Damage Index*. *Natural Hazards*
- Brunori C, Bignami C, Albano M, et al (2015a) Land subsidence, Ground Fissures and Buried Faults: InSAR Monitoring of Ciudad Guzmán (Jalisco, Mexico). *Remote Sensing* 7:8610–8630. <https://doi.org/10.3390/rs70708610>
- Brunori CA, Bignami C, Zucca F, et al (2015b) Ground Fracturation in Urban Area: Monitoring of Land Subsidence Controlled by Buried Faults with InSAR Techniques (Ciudad Guzmán: Mexico). In: Lollino G, Manconi A, Guzzetti F, et al. (eds) *Engineering Geology for Society and Territory - Volume 5*. Springer International Publishing, pp 1027–1031
- Bürgmann R, Rosen PA, Fielding EJ (2000) Synthetic Aperture Radar Interferometry to Measure Earth's Surface Topography and Its Deformation. *Annu Rev Earth Planet Sci* 28:169–209. <https://doi.org/10.1146/annurev.earth.28.1.169>
- Burland J, Wroth C (1975) *Settlement of Buildings and Associated Damage*. Building Research Establishment 65:
- Burrough PA, McDonnell RA, Lloyd CD (2015) *Principles of Geographical Information Systems*. OUP Oxford
- Cabral-Cano E, Arciniega-Ceballos A, Diaz-Molina O, et al (2010a) Is there a tectonic component to the subsidence process in Morelia, Mexico? In: *IAHS*. IAHS, Querétaro, Mexico
- Cabral-Cano E, Diaz Molina O, Delgado Granados H (2011) Subsidence and hazard maps: An example in the northeast of Mexico City Metropolitan Zone. *Boletín de la Sociedad Geologica Mexicana* 63:53–60
- Cabral-Cano E, Dixon T, Miralles-Wilhelm F, et al (2008) Space geodetic imaging of rapid ground subsidence in Mexico City. *Geological Society of America Bulletin - GEOL SOC AMER BULL* 120:1556–1566. <https://doi.org/10.1130/B26001.1>
- Cabral-Cano E, Osmanoglu B, Dixon T, et al (2010b) Subsidence and fault hazard maps using PSInSAR and permanent GPS networks in central Mexico. In: *In: D. Carreón-Freyre et al. (ed.) IAHS Press*, pp 255–259
- Calderhead AI, Martel A, Alasset P-J, et al (2010) Land subsidence induced by groundwater pumping, monitored by D-InSAR and field data in the Toluca Valley, Mexico. *Canadian Journal of Remote Sensing* 36:9–23. <https://doi.org/10.5589/m10-024>
- Calderhead AI, Martel R, Garfias J, et al (2012) Sustainable Management for Minimizing Land Subsidence of an Over-Pumped Volcanic Aquifer System: Tools for Policy Design. *Water Resour Manage* 26:1847–1864. <https://doi.org/10.1007/s11269-012-9990-7>
- Calderhead AI, Martel R, Rivera A, et al (2009) C-band D-InSAR and field data for calibrating a groundwater flow and land subsidence model. In: *2009 IEEE International Geoscience and Remote Sensing Symposium*. p IV-149–IV-152
- Calderhead AI, Therrien R, Rivera A, et al (2011) Simulating pumping-induced regional land subsidence with the use of InSAR and field data in the Toluca Valley, Mexico. *Advances in Water Resources* 34:83–97. <https://doi.org/10.1016/j.advwatres.2010.09.017>
- Camacho-Sanabria R, Camacho Sanabria JM, Balderas Plata MÁ, Hernández Madrigal VM (2020) Cuantificación Espacial del Daño Socioeconómico por Subsistencia Diferencial en Santa Ana Tlapaltitlán, Toluca, México. *REDER* 4:95. <https://doi.org/10.55467/reder.v4i1.44>
- Cárdenas-Soto M, Escobedo-Zenil D, Tejero-Andrade A, et al (2020) Exploring a near-surface subsidence over a rehabilitated underground mine through ambient seismic noise tomography in combination with other geophysical methods. *Near Surface Geophysics* 18:483–495. <https://doi.org/10.1002/nsg.12108>
- Carnec C, Fabriol H (1999) Monitoring and modeling land subsidence at the Cerro Prieto geothermal field, Baja California, Mexico, using SAR interferometry. *Geophysical Research Letters* 26:1211–1214. <https://doi.org/10.1029/1999GL900062>
- Carreón-Freyre D (2010) Land subsidence processes and associated ground fracturing in central Mexico. In: *IAHS-AISH*
- Carreón-Freyre D, Cerca M, Gutierrez-Calderon R, Huerta-Ladrón M (2010) Monitoring of land subsidence and fracturing in Iztapalapa, Mexico City. In: *IAHS-AISH*
- Carreón-Freyre D, Cerca M, Ochoa-González G, et al (2016) Shearing along faults and stratigraphic joints controlled by land subsidence in the Valley of Queretaro, Mexico. *Hydrogeol J* 24:657–674. <https://doi.org/10.1007/s10040-016-1384-0>
- Carreón-Freyre D, González-Hernández M, Martínez-Alfaro D, et al (2015) Analysis of the variation of the compressibility index (Cc) of volcanic clays and its application to estimate subsidence in lacustrine areas. *Proceedings of IAHS* 372:273–279. <https://doi.org/10.5194/piahs-372-273-2015>
- Carreón-Freyre D, Rodríguez-Quiroz JC (2010) Guidelines for the design of a unit of urban risk prevention for subsurface fracturing in the Municipality of Iztapalapa in Mexico City. In: *IAHS-AISH*
- Carreón-Freyre DC, Cerca M (2006) Integration of geological properties in the study of the subsidence and fracturing phenomena in two urban areas of Mexico. In: *IAEG*. The Geological Society of London

- Carrillo N (1948) Influence of Artesian Wells on the Sinking of Mexico City. *Proceedings, second International Conference on Soil Mechanics and Foundation Engineering* 2:156–159
- Castellazzi P, Garfías J, Martel R, et al (2017) InSAR to support sustainable urbanization over compacting aquifers: The case of Toluca Valley, Mexico. *International Journal of Applied Earth Observation and Geoinformation* 63:33–44. <https://doi.org/10.1016/j.jag.2017.06.011>
- Castellazzi P, Garfías J, Martel R (2021a) Assessing the efficiency of mitigation measures to reduce groundwater depletion and related land subsidence in Querétaro (Central Mexico) from decadal InSAR observations. *International Journal of Applied Earth Observation and Geoinformation* 105:102632. <https://doi.org/10.1016/j.jag.2021.102632>
- Castellazzi P, Garfías J, Martel R (2021b) Mitigation of Land Subsidence Due to Groundwater Extraction in Queretaro, Mexico. In: 2021 IEEE International Geoscience and Remote Sensing Symposium IGARSS. pp 6036–6039
- Castellazzi P, Martel R, Rivera A, et al (2016) Groundwater depletion in Central Mexico: Use of GRACE and InSAR to support water resources management. *Water Resources Research* 52:5985–6003. <https://doi.org/10.1002/2015WR018211>
- Cavalié O, Doin M-P, Lasserre C, Briole P (2007) Ground motion measurement in the Lake Mead area, Nevada, by differential synthetic aperture radar interferometry time series analysis: Probing the lithosphere rheological structure. *Journal of Geophysical Research: Solid Earth* 112:. <https://doi.org/10.1029/2006JB004344>
- CEA Querétaro (2016) Acueducto II. In: Comisión Estatal de Aguas Querétaro. <https://www.ceaqueretaro.gob.mx/cultura-del-agua/acueducto-ii/>. Accessed 27 Jun 2023
- CENAPRED (2017) Análisis de la Vulnerabilidad Física a la Subsistencia y Agrietamiento en la Ciudad de México. Mexico, p 23
- Centeno-Salas FA, Carreón-Freyre D, Flores-García WA, Gutiérrez-Calderón RI (2015) Application of high resolution geophysical prospecting to assess the risk related to subsurface deformation in Mexico City. *Proceedings of IAHS* 372:267–272. <https://doi.org/10.5194/piahs-372-267-2015>
- Cerca M, Carreón-Freyre D, Gutiérrez R (2010) Instability of the urbanized flank of El Peñón del Marques volcanic edifice and its relation to land subsidence in Mexico City. In: IAHS-AISH. IAHS-AISH
- Chaussard E, Havazli E, Fattahi H, et al (2021) Over a Century of Sinking in Mexico City: No Hope for Significant Elevation and Storage Capacity Recovery. *Journal of Geophysical Research: Solid Earth* 126:1–18. <https://doi.org/10.1029/2020JB020648>
- Chaussard E, Wdowinski S, Cabral-Cano E, Amelung F (2014) Land subsidence in central Mexico detected by ALOS InSAR time-series. *Remote Sensing of Environment* 140:94–106. <https://doi.org/10.1016/j.rse.2013.08.038>
- Chen CW, Zebker HA (2002) Phase unwrapping for large SAR interferograms: statistical segmentation and generalized network models. *IEEE Transactions on Geoscience and Remote Sensing* 40:1709–1719. <https://doi.org/10.1109/TGRS.2002.802453>
- Cigna F, Esquivel Ramírez R, Tapete D (2021) Accuracy of Sentinel-1 PSI and SBAS InSAR Displacement Velocities against GNSS and Geodetic Leveling Monitoring Data. *Remote Sensing* 13:4800. <https://doi.org/10.3390/rs13234800>
- Cigna F, Osmanoğlu B, Cabral-Cano E, et al (2012) Monitoring land subsidence and its induced geological hazard with Synthetic Aperture Radar Interferometry: A case study in Morelia, Mexico. *Remote Sensing of Environment* 117:146–161. <https://doi.org/10.1016/j.rse.2011.09.005>
- Cigna F, Tapete D (2022a) Land Subsidence and Aquifer-System Storage Loss in Central Mexico: A Quasi-Continental Investigation With Sentinel-1 InSAR. *Geophysical Research Letters* 49:e2022GL098923. <https://doi.org/10.1029/2022GL098923>
- Cigna F, Tapete D (2020) Sentinel-1 InSAR Assessment of Present-Day Land Subsidence Due to Exploitation of Groundwater Resources in Central Mexico. In: IGARSS 2020 - 2020 IEEE International Geoscience and Remote Sensing Symposium. pp 4215–4218
- Cigna F, Tapete D (2021a) Present-day land subsidence rates, surface faulting hazard and risk in Mexico City with 2014–2020 Sentinel-1 IW InSAR. *Remote Sensing of Environment* 112161. <https://doi.org/10.1016/j.rse.2020.112161>
- Cigna F, Tapete D (2022b) Urban growth and land subsidence: Multi-decadal investigation using human settlement data and satellite InSAR in Morelia, Mexico. *Science of The Total Environment* 811:152211. <https://doi.org/10.1016/j.scitotenv.2021.152211>
- Cigna F, Tapete D (2021b) Satellite InSAR survey of structurally-controlled land subsidence due to groundwater exploitation in the Aguascalientes Valley, Mexico. *Remote Sensing of Environment* 254:112254. <https://doi.org/10.1016/j.rse.2020.112254>
- Cigna F, Tapete D, Garduño-Monroy VH, et al (2019) Wide-Area InSAR Survey of Surface Deformation in Urban Areas and Geothermal Fields in the Eastern Trans-Mexican Volcanic Belt, Mexico. *Remote Sensing* 11:2341. <https://doi.org/10.3390/rs11202341>
- Cigna F, Tapete D, Muñoz-Jauregui JA, et al (2020) Wide-area observations of surface deformation in Mexican urban areas and geothermal fields using ENVISAT InSAR. *IOP Conf Ser: Earth Environ Sci* 509:012007. <https://doi.org/10.1088/1755-1315/509/1/012007>
- CONAGUA (2020) Sistema Nacional de Información del Agua | SINA. In: Acuíferos (nacional). <http://sina.conagua.gob.mx/sina/index.php>. Accessed 2 Dec 2021
- Corona EP (2004) Geotechnical Analysis of the Formation of Earth Fissures at Ciudad Guzman, Jalisco. New York, NY, p 6
- Costantini M, Falco S, Malvarosa F, Minati F (2008) A New Method for Identification and Analysis of Persistent Scatterers in Series of SAR Images. In: IGARSS 2008 - 2008 IEEE International Geoscience and Remote Sensing Symposium. IEEE, Boston, MA, p II-449-II–452
- Crosetto M, Devanathéry N, Cuevas-González M, et al (2015) Exploitation of the full potential of PSI data for subsidence monitoring. *Proceedings of IAHS* 372:311–314. <https://doi.org/10.5194/piahs-372-311-2015>
- De Zan F, Monti Guarnieri A (2006) TOPSAR: Terrain Observation by Progressive Scans. *IEEE Trans Geosci Remote Sensing* 44:2352–2360. <https://doi.org/10.1109/TGRS.2006.873853>
- Díaz-Rodríguez JA (2003) Characterisation and engineering properties of Mexico City lacustrine soils. In: *Characterization and engineering properties of Mexico City lacustrine soils*. Swets & Zeitlinger, Lisse
- Doin M-P, Lasserre C, Peltzer G, et al (2009) Corrections of stratified tropospheric delays in SAR interferometry: Validation with global atmospheric models. *Journal of Applied Geophysics* 69:35–50. <https://doi.org/10.1016/j.jappgeo.2009.03.010>
- Du Z, Ge L, Ng AH-M, et al (2019a) Long-term subsidence in Mexico City from 2004 to 2018 revealed by five synthetic aperture radar sensors. *Land Degradation & Development* 30:1785–1801. <https://doi.org/10.1002/ldr.3347>
- Du Z, Ge L, Ng AH-M (2019b) InSAR Reveals the Long Term Subsidence and Potential Landdegradation in Mexico City from 2004 to 2018 with Five Sar Sensors. In: IGARSS 2019 - 2019 IEEE International Geoscience and Remote Sensing Symposium. IEEE, Yokohama, Japan, pp 421–424
- Farina P, Avila-Olivera JA, Garduño-Monroy VH, Catani F (2008) DInSAR analysis of differential ground subsidence affecting urban areas along the Mexican Volcanic Belt (MVB). *Italian Journal of Remote Sensing / Rivista Italiana di Telerilevamento* 40:103–113
- Farr TG, Rosen PA, Caro E, et al (2007) The Shuttle Radar Topography Mission. *Reviews of Geophysics* 45:. <https://doi.org/10.1029/2005RG000183>

- Fattahi H, Agram P, Simons M (2017) A Network-Based Enhanced Spectral Diversity Approach for TOPS Time-Series Analysis. *IEEE Transactions on Geoscience and Remote Sensing* 55:777–786. <https://doi.org/10.1109/TGRS.2016.2614925>
- Fattahi H, Amelung F (2013) DEM Error Correction in InSAR Time Series. *Geoscience and Remote Sensing, IEEE Transactions on* 51:4249–4259. <https://doi.org/10.1109/TGRS.2012.2227761>
- Fernández-Torres E, Cabral-Cano E, Solano-Rojas D, et al (2020) Land Subsidence risk maps and InSAR based angular distortion structural vulnerability assessment: an example in Mexico City. In: *Proceedings of the International Association of Hydrological Sciences. Copernicus GmbH*, pp 583–587
- Fernández-Torres EA, Cabral-Cano E, Novelo-Casanova DA, et al (2022) Risk assessment of land subsidence and associated faulting in Mexico City using InSAR. *Nat Hazards* 112:37–55. <https://doi.org/10.1007/s11069-021-05171-0>
- Ferretti A, Monti-Guarnieri A, Prati C, Rocca F (2007) *InSAR Principles: Guidelines for SAR Interferometry Processing and Interpretation*. ESA
- Ferretti A, Prati C, Rocca F (2001) Permanent scatterers in SAR interferometry. *IEEE Transactions on Geoscience and Remote Sensing* 39:8–20. <https://doi.org/10.1109/36.898661>
- Figueroa-Miranda S, Hernández-Madrigal VM, Tuxpan-Vargas J, Villaseñor-Reyes CI (2020) Evolution assessment of structurally-controlled differential subsidence using SBAS and PS interferometry in an emblematic case in Central Mexico. *Engineering Geology* 279:105860. <https://doi.org/10.1016/j.enggeo.2020.105860>
- Figueroa-Miranda S, Tuxpan-Vargas J, Ramos-Leal JA, et al (2018) Land subsidence by groundwater over-exploitation from aquifers in tectonic valleys of Central Mexico: A review. *Engineering Geology* 246:91–106. <https://doi.org/10.1016/j.enggeo.2018.09.023>
- Fletcher K, European Space Agency (eds) (2012) *Sentinel-1: ESA's radar observatory mission for GMES operational services*. ESA Communications, Noordwijk, The Netherlands
- Franceschini A, Teatini P, Janna C, et al (2015) Modelling ground rupture due to groundwater withdrawal: applications to test cases in China and Mexico. *Proceedings of IAHS* 372:63–68. <https://doi.org/10.5194/piahs-372-63-2015>
- Galloway DL, Burbey TJ (2011) Review: Regional land subsidence accompanying groundwater extraction. *Hydrogeol J* 19:1459–1486. <https://doi.org/10.1007/s10040-011-0775-5>
- Gayol R (1925) Estudio de las perturbaciones que en el fondo de la Ciudad de México ha producido el drenaje de las aguas del subsuelo, por las obras del desagüe y rectificación de los errores a que ha dado lugar una incorrecta interpretación de los efectos producidos. *Revista Mexicana de Ingeniería y Arquitectura* III:96–132
- GCDMX (2017) (Gobierno de la Ciudad de México) *Reglamento de Construcciones para el Distrito Federal*
- GDF (2004) *Normas Técnicas Complementarias para Diseño y Construcción de Cimentaciones para el Distrito Federal*,
- Glowacka E, Sarychikhina O, Nava FA (2005) Subsidence and Stress Change in the Cerro Prieto Geothermal Field, B. C., Mexico. *Pure appl geophys* 162:2095–2110. <https://doi.org/10.1007/s00024-005-2706-7>
- Glowacka E, Sarychikhina O, Suárez F, et al (2010) Anthropogenic subsidence in the Mexicali Valley, Baja California, Mexico, and slip on the Saltillo fault. *Environ Earth Sci* 59:1515–1524. <https://doi.org/10.1007/s12665-009-0137-y>
- González-Hernández M, Carreón-Freyre D, Gutiérrez-Calderon R, et al (2015) Mass movement processes triggered by land subsidence in Iztapalapa, the eastern part of Mexico City. *Proceedings of IAHS* 372:261–265. <https://doi.org/10.5194/piahs-372-261-2015>
- Gutiérrez-Yurrita PJ (2010) Land subsidence and environmental law in Mexico: A reflection on civil liability for environmental damage. In: *AHS-AISH*
- Hernández-Espriú A, Reyna-Gutiérrez JA, Sánchez-León E, et al (2014) The DRASTIC-Sg model: An extension to the DRASTIC approach for mapping groundwater vulnerability in aquifers subject to differential land subsidence, with application to Mexico City. *Hydrogeology Journal* 22:1469–1485. <https://doi.org/10.1007/s10040-014-1130-4>
- Hernández-Madrigal VM, Lázaro NF, Reyes CIV, Jauregui JAM (2015) Impacto económico producido por subsidencia diferencial en zonas urbanas. Caso de estudio Morelia, Michoacán. *Ciencia Nicolaita* 78–94. <https://doi.org/10.35830/cn.vi65.267>
- Hernández-Madrigal VM, Muñoz-Jáuregui JA, Garduño-Monroy VH, et al (2014) Depreciation factor equation to evaluate the economic losses from ground failure due to subsidence related to groundwater withdrawal. *NS* 06:108–113. <https://doi.org/10.4236/ns.2014.63015>
- Hernandez-Marin M, Esquivel-Ramirez R, Zermelo-De-Leon ME, et al (2020) Ongoing research on the pumping-induced land deformation in the Aguascalientes Valley: an analysis of the recent data of vertical deformation, groundwater level variations and local seismicity. In: *Proceedings of IAHS. Copernicus GmbH*, pp 99–102
- Hernandez-Marin M, Pacheco-Martínez J, Burbey TJ, et al (2017) Evaluation of subsurface infiltration and displacement in a subsidence-reactivated normal fault in the Aguascalientes Valley, Mexico. *Environ Earth Sci* 76:812. <https://doi.org/10.1007/s12665-017-7163-y>
- Hernandez-Marin M, Pacheco-Martínez J, Ramirez-Cortes A, et al (2014) Evaluation and analysis of surface deformation in west Chapala basin, central Mexico. *Environ Earth Sci* 72:1491–1501. <https://doi.org/10.1007/s12665-014-3054-7>
- Herrera-García G, Ezquerro P, Tomás R, et al (2021) Mapping the global threat of land subsidence. *Science* 371:34. <https://doi.org/10.1126/science.abb8549>
- Herrera-Zamarrón GS, González-Hita L, Cardona-Benavides A, et al (2006) *Modelo hidrodinámico del acuífero de la zona metropolitana de la Ciudad de México, Informe Final*. Secretaría del Medio Ambiente, Gobierno del Distrito Federal. Volumen I., Ciudad de México
- Hooper A, Zebker H, Segall P, Kampes B (2004) A new method for measuring deformation on volcanoes and other natural terrains using InSAR persistent scatterers. *Geophysical Research Letters* 31:. <https://doi.org/10.1029/2004GL021737>
- INEGI (2010) *Censo de Población y Vivienda 2010*. In: INEGI. <https://www.inegi.org.mx/programas/ccpv/2010/>. Accessed 5 Apr 2021
- Ju J, Hong S-H (2021) Monitoring of a Time-series of Land Subsidence in Mexico City Using Space-based Synthetic Aperture Radar Observations. *Korean Journal of Remote Sensing* 37:1657–1667. <https://doi.org/10.7780/kjrs.2021.37.6.1.14>
- Julio-Miranda P, Ortiz-Rodríguez AJ, Palacio-Aponte AG, et al (2012) Damage assessment associated with land subsidence in the San Luis Potosi-Soledad de Graciano Sanchez metropolitan area, Mexico, elements for risk management. *Nat Hazards* 64:751–765. <https://doi.org/10.1007/s11069-012-0269-3>
- Kalia AC, Frei M, Lege T (2017) A Copernicus downstream-service for the nationwide monitoring of surface displacements in Germany. *Remote Sensing of Environment* 202:234–249. <https://doi.org/10.1016/j.rse.2017.05.015>
- Kampes BM (2006) *Radar interferometry: persistent scatterer technique*. Springer, Dordrecht, the Netherlands
- León WHH, Martínez JP, Marín MH, et al (2018) *LAND SUBSIDENCE AND ITS EFFECTS ON THE URBAN AREA OF TEPIC CITY, MEXICO*. Alicante, Spain, pp 369–380
- López-Quiroz P, Doin MP, Tupin F, et al (2010) Mexico City subsidence analysis assisted by InSAR. In: *IAHS-AISH*



- López-Quiroz P, Doin M-P, Tupin F, et al (2009) Time series analysis of Mexico City subsidence constrained by radar interferometry. *Journal of Applied Geophysics* 69:1–15. <https://doi.org/10.1016/j.jappgeo.2009.02.006>
- Luna-Villavicencio H, Pacheco-Martínez J, Ochoa-González GH, et al (2023) Determination of Susceptibility to the Generation of Discontinuities Related to Land Subsidence Using the Frequency Ratio Method in the City of Aguascalientes, Mexico. *Remote Sensing* 15:2597. <https://doi.org/10.3390/rs15102597>
- Marsal RJ (1992) Hundimiento de la Ciudad de México. Ciudad de México
- Marsal RJ, Mazari M (1959) El subsuelo de la Ciudad de México, 1er Congreso Panamericano de Mecánica de Suelos e Ingeniería de Cementaciones, Facultad de Ingeniería. UNAM, México
- Marsal RJ, Mazari M, Auvinet G, et al (2016) El subsuelo de la Ciudad de México: con una revisión de los avances en el conocimiento del subsuelo de la Ciudad de México (1959-2016). Vol. 3: ..., 3a. edición con revisión a avances. UNAM, Instituto de Ingeniería, Ciudad de México
- Matínez-Reyes J, Mitre-Salazar LM (2010) Geological setting of active faulting associated with land subsidence at the Aguascalientes and Querétaro valleys, Mexico. In: IAHS-AISH. IAHS-AISH
- Moreira A, Prats-Iraola P, Younis M, et al (2013) A tutorial on synthetic aperture radar. *IEEE Geosci Remote Sens Mag* 1:6–43. <https://doi.org/10.1109/MGRS.2013.2248301>
- Murgia F, Bignami C, Brunori CA, et al (2019) Ground Deformations Controlled by Hidden Faults: Multi-Frequency and Multitemporal InSAR Techniques for Urban Hazard Monitoring. *Remote Sensing* 11:2246. <https://doi.org/10.3390/rs11192246>
- Muro-Ortega JA, de Jesús Escalona-Alcázar F, Bluhm-Gutiérrez J, et al (2021) Geological risk assessment by a fracture measurement procedure in an urban area of Zacatecas, Mexico. *Nat Hazards*. <https://doi.org/10.1007/s11069-021-04997-y>
- Navarro-Hernández MI, Tomás R, Lopez-Sanchez JM, et al (2020) Spatial Analysis of Land Subsidence in the San Luis Potosi Valley Induced by Aquifer Overexploitation Using the Coherent Pixels Technique (CPT) and Sentinel-1 InSAR Observation. *Remote Sensing* 12:3822. <https://doi.org/10.3390/rs12223822>
- Navarro-Hernández MI, Valdes-Abellan J, Tomás R, et al (2022) ValInSAR: A Systematic Approach for the Validation of Differential SAR Interferometry in Land Subsidence Areas. *IEEE Journal of Selected Topics in Applied Earth Observations and Remote Sensing* 15:3650–3671. <https://doi.org/10.1109/JSTARS.2022.3171517>
- Novelo-Casanova DA, Suárez G, Cabral-Cano E, et al (2022) The Risk Atlas of Mexico City, Mexico: a tool for decision-making and disaster prevention. *Nat Hazards* 111:411–437. <https://doi.org/10.1007/s11069-021-05059-z>
- Ochoa-González GH, Carreón-Freyre D, Franceschini A, et al (2018) Overexploitation of groundwater resources in the faulted basin of Querétaro, Mexico: A 3D deformation and stress analysis. *Engineering Geology* 245:192–206. <https://doi.org/10.1016/j.enggeo.2018.08.014>
- Ochoa-Gonzalez GH, Teatini P, Carreon-Freyre D, Gambolati G (2013) Modeling the deformation of faulted volcano-sedimentary sequences associated to groundwater withdrawal in the Querétaro Valley, Mexico. In: Piantadosi, J., Anderssen, R.S. and Boland J. (eds) MODSIM2013, 20th International Congress on Modelling and Simulation. Modelling and Simulation Society of Australia and New Zealand (MSSANZ), Inc.
- O’Riordan N, Canavate-Grimal A, Kumar S, Ciruela-Ochoa F (2018) Analysis of friction piles in consolidating soils. In: Cardoso AS, Borges JL, Costa PA, et al. (eds) 1st edn. CRC Press, pp 981–987
- Ortega-Guerrero A, Cherry JA, Rudolph DL (1993) Large-Scale Aquitard Consolidation Near Mexico City. *Groundwater* 31:708–718. <https://doi.org/10.1111/j.1745-6584.1993.tb00841.x>
- Ortega-Guerrero A, Rudolph DL, Cherry JA (1999) Analysis of long-term land subsidence near Mexico City: Field investigations and predictive modeling. *Water Resources Research* 35:3327–3341. <https://doi.org/10.1029/1999WR900148>
- Ortiz-Zamora D del C, Ortega-Guerrero MA (2007) Origen y evolución de un nuevo lago en la planicie de Chalco: implicaciones de peligro por subsidencia e inundación de áreas urbanas en Valle de Chalco (Estado de México) y Tláhuac (Distrito Federal). *Investigaciones geográficas* 26–42
- Osmanoğlu B, Dixon TH, Wdowski S, et al (2011) Mexico City subsidence observed with persistent scatterer InSAR. *International Journal of Applied Earth Observation and Geoinformation* 13:1–12. <https://doi.org/10.1016/j.jag.2010.05.009>
- Osmanoğlu B, Sunar F, Wdowski S, Cabral-Cano E (2016) Time series analysis of InSAR data: Methods and trends. *ISPRS Journal of Photogrammetry and Remote Sensing* 115:90–102. <https://doi.org/10.1016/j.isprsjprs.2015.10.003>
- Ovando-Shelley E, Pinto Oliveira MO, Santoyo Villa E, Hernández V (2008) Mexico City: Geotechnical Concerns in the Preservation of Monuments. *International Journal of Architectural Heritage* 2:60–82. <https://doi.org/10.1080/15583050701612887>
- Ovando-Shelley E, Romo MP, Contreras N, Giralte A (2003) Effects on soil properties of future settlements in downtown Mexico City due to ground water extraction. *Geofísica Internacional* 42:185–204
- Pacheco J, Arzate J, Rojas E, et al (2006) Delimitation of ground failure zones due to land subsidence using gravity data and finite element modeling in the Querétaro valley, México. *Engineering Geology* 84:143–160. <https://doi.org/10.1016/j.enggeo.2005.12.003>
- Pacheco-Martínez J, Arzate-Flores J, López-Doncel R, et al (2010) Zoning map of ground failure risk due to land subsidence of San Luis Potosí, Mexico. *IAHS* 339:1
- Pacheco-Martínez J, Cabral-Cano E, Wdowski S, et al (2015a) Application of InSAR and Gravimetry for Land Subsidence Hazard Zoning in Aguascalientes, Mexico. *Remote Sensing* 7:17035–17050. <https://doi.org/10.3390/rs71215868>
- Pacheco-Martínez J, Wdowski S, Cabral-Cano E, et al (2015b) Application of InSAR and gravimetric surveys for developing construction codes in zones of land subsidence induced by groundwater extraction: case study of Aguascalientes, Mexico. *Proceedings of IAHS* 372:121–127. <https://doi.org/10.5194/pias-372-121-2015>
- Palma A, Rivera A, Carmona R (2022) A Unified Hydrogeological Conceptual Model of the Mexico Basin Aquifer after a Century of Groundwater Exploitation. *Water* 14:1584. <https://doi.org/10.3390/w14101584>
- Peduto D, Nicodemo G, Maccabiani J, Ferlisi S (2017) Multi-scale analysis of settlement-induced building damage using damage surveys and DInSAR data: A case study in The Netherlands. *Engineering Geology* 218:117–133. <https://doi.org/10.1016/j.enggeo.2016.12.018>
- Pepe A, Lanari R (2006) On the Extension of the Minimum Cost Flow Algorithm for Phase Unwrapping of Multitemporal Differential SAR Interferograms. *IEEE Transactions on Geoscience and Remote Sensing* 44:2374–2383. <https://doi.org/10.1109/TGRS.2006.873207>
- Peréz-Cruz ZA (1988) Estudio sísmológico de reflexión del subsuelo de la Ciudad de México. Universidad Nacional Autónoma de México
- Pérez-Falls Z, Martínez-Flores G, Sarychikhina O (2022) Land Subsidence Detection in the Coastal Plain of Tabasco, Mexico Using Differential SAR Interferometry. *Land* 11:1473. <https://doi.org/10.3390/land11091473>

- Poreh D, Pirasteh S, Cabral-Cano E (2021) Assessing subsidence of Mexico City from InSAR and LandSat ETM+ with CGPS and SVM. *Geoenvironmental Disasters* 8:7. <https://doi.org/10.1186/s40677-021-00179-x>
- Raspini F, Caleca F, Del Soldato M, et al (2022) Review of satellite radar interferometry for subsidence analysis. *Earth-Science Reviews* 235:104239. <https://doi.org/10.1016/j.earscirev.2022.104239>
- Rivera A, Ledoux E (1991) Nonlinear modeling of groundwater flow and total subsidence of the Mexico City aquifer-aquitard system. *Land Subsidence (Proceedings of the Fourth International Symposium on LandSubsidence 29:A79)*. [https://doi.org/10.1016/0148-9062\(92\)92180-K](https://doi.org/10.1016/0148-9062(92)92180-K)
- Rodríguez-Castillo R, Schroeder-Aguirre A (2010) Structural control on the subsidence faults alignment in Irapuato - Mexico. *AQUAmundi 6*
- Rosen PA, Gurrrola E, Sacco GF, Zebker H (2012) The InSAR scientific computing environment. In: *EUSAR 2012; 9th European Conference on Synthetic Aperture Radar*. pp 730–733
- Saaty TL (1980) *The Analytical Hierarchy Process*. McGraw-Hill
- Samsonov SV, d'Oreye N (2017) Multidimensional Small Baseline Subset (MSBAS) for Two-Dimensional Deformation Analysis: Case Study Mexico City. *Canadian Journal of Remote Sensing* 43:318–329. <https://doi.org/10.1080/07038992.2017.1344926>
- Santoyo-Villa E, Ovando-Shelley E, Mooser F, León-Plata E (2005) Síntesis Geotécnica de la Cuenca del Valle de México. México
- Sarychikhina O, Glowacka E, Mellors R, Vidal FS (2011) Land subsidence in the Cerro Prieto Geothermal Field, Baja California, Mexico, from 1994 to 2005: An integrated analysis of DInSAR, leveling and geological data. *Journal of Volcanology and Geothermal Research* 204:76–90. <https://doi.org/10.1016/j.jvolgeores.2011.03.004>
- Sarychikhina O, Glowacka E, Robles B (2018) Multi-sensor DInSAR applied to the spatiotemporal evolution analysis of ground surface deformation in Cerro Prieto basin, Baja California, Mexico, for the 1993–2014 period. *Nat Hazards* 92:225–255. <https://doi.org/10.1007/s11069-018-3206-2>
- Schmidt DA, Bürgmann R (2003) Time-dependent land uplift and subsidence in the Santa Clara valley, California, from a large interferometric synthetic aperture radar data set: SANTA CLARA VALLEY INSAR TIME SERIES. *J Geophys Res* 108:. <https://doi.org/10.1029/2002JB002267>
- Siles GL, Alcérreca-Huerta JC, López-Quiroz P, Hernández JC (2015a) On the potential of time series InSAR for subsidence and ground rupture evaluation: application to Texcoco and Cuautitlan–Pachuca subbasins, northern Valley of Mexico. *Natural Hazards* 79:1091–1110. <https://doi.org/10.1007/s11069-015-1894-4>
- Siles GL, Alcérreca-Huerta JC, López-Quiroz P, Niemeier W (2015b) Long Term Subsidence Analysis and Soil Fracturing Zonation Based on InSAR Time Series Modelling in Northern Zona Metropolitana del Valle de Mexico. *Remote Sensing* 7:6908–6931. <https://doi.org/10.3390/rs70606908>
- Skempton AW, Macdonald DH (1956) The allowable settlements of buildings. *Proceedings of the Institution of Civil Engineers* 5:727–768. <https://doi.org/10.1680/ipeds.1956.12202>
- Solano-Rojas D, Cabral-Cano E, Fernández-Torres E, et al (2020a) Remotely triggered subsidence acceleration in Mexico City induced by the September 2017  $M_w$  7.1 Puebla and the  $M_w$  8.2 Tehuantepec September 2017 earthquakes. In: *Proceedings of the International Association of Hydrological Sciences*. Copernicus GmbH, pp 683–687
- Solano-Rojas D, Cabral-Cano E, Hernández-Espriú A, et al (2015) The relationship of InSAR-GPS land subsidence and the groundwater level decrease in wells of the Mexico City Metropolitan Area. *Boletín de la Sociedad Geológica Mexicana* 67:273–283
- Solano-Rojas D, Wdowinski S, Cabral-Cano E, Osmanoğlu B (2020b) Detecting differential ground displacements of civil structures in fast-subsiding metropolises with interferometric SAR and band-pass filtering. *Scientific Reports* 10:15460. <https://doi.org/10.1038/s41598-020-72293-z>
- Solano-Rojas DE, Wdowinski S, Cabral-Cano E, et al (2020c) A multiscale approach for detection and mapping differential subsidence using multi-platform InSAR products. *Proc IAHS* 382:173–177. <https://doi.org/10.5194/piahs-382-173-2020>
- Sowter A, Che Amat A, Cigna F, et al (2016) Mexico City land subsidence in 2014-2015 with Sentinel-1 IW TOPS: results using the Intermittent SBAS (ISBAS) technique. *International Journal of Applied Earth Observation and Geoinformation* 52:. <https://doi.org/10.1016/j.jag.2016.06.015>
- Strozzi T, Wegmuller U (1999) Land subsidence in Mexico City mapped by ERS differential SAR interferometry. In: *IEEE 1999 International Geoscience and Remote Sensing Symposium. IGARSS'99 (Cat. No.99CH36293)*. pp 1940–1942 vol.4
- Strozzi T, Wegmüller U, Tosi L, Spreckels V (2001) Land Subsidence Monitoring with Differential SAR Interferometry. *PHOTOGRAMMETRIC ENGINEERING* 10
- Strozzi T, Wegmuller U, Werner CL, et al (2003) JERS SAR interferometry for land subsidence monitoring. *IEEE Trans Geosci Remote Sensing* 41:1702–1708. <https://doi.org/10.1109/TGRS.2003.813273>
- Strozzi T, Werner C, Wegmüller U, Wiesmann A (2005) Monitoring land subsidence in Mexico city with ENVISAT ASAR interferometry. In: *European Space Agency, (Special Publication) ESA SP*. pp 935–939
- Sun Y, Wang D, Tsang DCW, et al (2019) A critical review of risks, characteristics, and treatment strategies for potentially toxic elements in wastewater from shale gas extraction. *Environment International* 125:452–469. <https://doi.org/10.1016/j.envint.2019.02.019>
- Terzaghi K (1925) Principles of soil mechanics: IV; settlement and consolidation of clay. *Erdbaummechanik* 95:874–878
- Tong-Minh DH, Ngo Y-N (2021) ComSAR: A new algorithm for processing Big Data SAR Interferometry. In: *2021 IEEE International Geoscience and Remote Sensing Symposium IGARSS*. pp 820–823
- Torres R, Snoeij P, Geudtner D, et al (2012) GMES Sentinel-1 mission. *Remote Sensing of Environment* 120:9–24. <https://doi.org/10.1016/j.rse.2011.05.028>
- Tracy J, Chang W, St George Freeman S, et al (2022) Enabling dynamic emulation of high-dimensional model outputs: Demonstration for Mexico City groundwater management. *Environmental Modelling & Software* 147:105238. <https://doi.org/10.1016/j.envsoft.2021.105238>
- Trugman DT, Borsa AA, Sandwell DT (2014) Did stresses from the Cerro Prieto Geothermal Field influence the El Mayor-Cucapah rupture sequence? *Geophysical Research Letters* 41:8767–8774. <https://doi.org/10.1002/2014GL061959>
- Usai S (2003) A least squares database approach for SAR interferometric data. *IEEE Transactions on Geoscience and Remote Sensing* 41:753–760. <https://doi.org/10.1109/TGRS.2003.810675>
- Vázquez-Guillén F, Auvinet-Guichard G (2019) Injection into the shallow aquifer-aquitard system beneath Mexico City for counteracting pore pressure declines due to deeper groundwater withdrawals: Analysis of one injection well. *Geofísica internacional* 58:81–99

- Villaseñor-Reyes CI, Hernández-Madrigal VM, Figueroa-Miranda S (2022) Identification and assessment of land subsidence development in rural areas using PS interferometry: a case study in Western Michoacan, Mexico. *Environ Earth Sci* 81:417. <https://doi.org/10.1007/s12665-022-10545-z>
- Wegmüller U, Strozzi T, Tosi L (2000) ERS and ENVISAT differential SAR interferometry for subsidence monitoring. In: European Space Agency, (Special Publication). pp 203–210
- Werner C, Wegmüller U, Strozzi T, Wiesmann A (2003) Interferometric point target analysis for deformation mapping. In: IEEE International Geoscience and Remote Sensing Symposium. Proceedings. IEEE, pp 4362–4364
- Werner C, Wegmüller U, Strozzi T, Wiesmann A (2000) GAMMA SAR AND INTERFEROMETRIC PROCESSING SOFTWARE. In: ERS - ENVISAT Symposium. p 9
- Yalvac S (2020) Validating InSAR-SBAS results by means of different GNSS analysis techniques in medium- and high-grade deformation areas. *Environ Monit Assess* 192:120. <https://doi.org/10.1007/s10661-019-8009-8>
- Yunjun Z, Fattahi H, Amelung F (2019) Small baseline InSAR time series analysis: Unwrapping error correction and noise reduction. *Computers & Geosciences* 133:1–67. <https://doi.org/10.1016/j.cageo.2019.104331>
- Zapata-Norberto B, Morales-Casique E, Herrera GS (2018) Nonlinear consolidation in randomly heterogeneous highly compressible aquitards. *Hydrogeol J* 26:755–769. <https://doi.org/10.1007/s10040-017-1698-6>
- Zebker HA, Rosen PA, Hensley S (1997) Atmospheric effects in interferometric synthetic aperture radar surface deformation and topographic maps. *J Geophys Res* 102:7547–7563. <https://doi.org/10.1029/96JB03804>
- Zebker HA, Villaseñor J (1992) Decorrelation in interferometric radar echoes. *IEEE Transactions on Geoscience and Remote Sensing* 30:950–959. <https://doi.org/10.1109/36.175330>
- Zhang L, Ng AMY (2007) Limiting Tolerable Settlement and Angular Distortion for Building Foundations. In: Probabilistic Applications in Geotechnical Engineering. American Society of Civil Engineers, Denver, Colorado, United States, pp 1–11